

**Measurement of the Electric Form Factor of the  
Neutron at Low Momentum Transfers Using a Vector  
Polarized Deuterium Gas Target at BLAST**

by

Vitaliy Ziskin

Submitted to the Department of Physics  
in partial fulfillment of the requirements for the degree of

Doctor of Philosophy

at the

MASSACHUSETTS INSTITUTE OF TECHNOLOGY

April 2005

© Massachusetts Institute of Technology 2005. All rights reserved.

Author .....  
Department of Physics  
April 27, 2005

Certified by .....  
Richard Milner  
Professor  
Thesis Supervisor

Accepted by .....  
Thomas J. Greytak  
Chairman, Department Committee on Graduate Students

# Measurement of the Electric Form Factor of the Neutron at Low Momentum Transfers Using a Vector Polarized Deuterium Gas Target at BLAST

by

Vitaliy Ziskin

Submitted to the Department of Physics  
on April 27, 2005, in partial fulfillment of the  
requirements for the degree of  
Doctor of Philosophy

## Abstract

Elastic form factors are fundamental quantities that characterize the electromagnetic structure of the nucleon. High precision measurements of these quantities are essential in understanding the structure of hadronic matter.

Although the proton elastic form factors are well known, knowledge of the neutron form factors has been limited due to the lack of pure neutron targets. Few nucleon targets, deuterium in particular, are typically used to study the electromagnetic structure of the neutron. Cross section measurements are not sufficient for high precision determination of the electric form factor of the neutron,  $G_E^n$ , due to its small value. Recently, experiments using polarization observables which are proportional to the product of the electric and magnetic form factors of the neutron have been used instead. Such measurements require highly polarized electron beams and either a vector polarized neutron target (typically  $^2H$ ) or else a neutron final state polarimeter.

The Bates Large Acceptance Spectrometer Toroid (BLAST) provides a unique opportunity to measure the shape of the neutron electric form factor at low momentum transfers. BLAST combines a high duty-factor polarized electron beam in the South Hall Ring (SHR), an Atomic Beam Source (ABS) target of highly polarized deuterium atoms and a large acceptance detector. This work reports the results of measurements of the neutron electric form factor using the  $^2\vec{H}(\vec{e}, e'n)p$  reaction at five 4-momentum transfer squared,  $Q^2$ , points of 0.14, 0.20, 0.29, 0.38 and 0.50  $(\text{GeV}/c)^2$  using data taken in 2004. The experimental setup is discussed in detail and the results for  $G_E^n$  are presented and discussed in the context of various theoretical predictions.

A fit to the world's data including new BLAST data determines  $G_E^n$  to  $\pm 6.5\%$  over  $0 < Q^2 < 1$   $(\text{GeV}/c)^2$ . The best fit includes contributions from a low  $Q^2$  bump and a smooth dipole term.

Thesis Supervisor: Richard Milner  
Title: Professor

# Acknowledgments

First and foremost I would like to thank my wife, Alla, for her love and patient support throughout my long tenure as a graduate student. Her presence in my life gave me the strength and resolve to see my graduate work to its completion. Most importantly, she taught me to find joy in life outside of academics.

I would like to thank my parents for their love and constant encouragement. They have sacrificed so much to come to this country and give me an opportunity to achieve.

I would like to thank incredibly my thesis adviser, Prof. Richard Milner. As an adviser, Richard has always been supportive of me, and, on occasion, I know that it was not easy for him. I appreciate all of his help and advice. I always admire his enthusiasm about our field of science. He is a great role model for all young scientists.

I would like to thank Dr. Evgeni Tsentalovich. Genya, more than anybody, taught me what it takes to be a scientist. He is a great scientist with a keen understanding of the way experimental science works. His advice was invaluable to my research.

I would like to acknowledge Dr. Tancredi Botto and Dr. Michael Kohl for their help with my thesis work. Both Tancredi and Michael are wise “beyond their years”, and I feel fortunate to absorb some of their wisdom. I hope to have such a tremendous work ethic in my academic carrier as they do. I thank them for their support and, most of all, for their friendship.

I would like to thank all of the Bates scientific staff. Dr. Karen Dow was always ready to patiently answer all of my questions. Dr. Townsend Zwart always had useful suggestions on how to achieve my experimental goals faster and more efficiently. Townsend has a tremendous physics curiosity, and I enjoyed our frequent discussions of his “revolutionary” ideas. Dr. William Turchinets was always willing to share his enormous knowledge of nuclear physics with us, the graduate students. I would like to thank Brian McAllister for his invaluable help with my work on ABS EPICS controls.

This work would not have been possible had it not been for the hard work and dedication of the Bates staff. In particular, I would like to acknowledge the mechanical engineering group. I spent countless hours in the South Hall with this group of great engineers and technicians. The successful operation of the Atomic Beam Source is a testimony to their

professionalism and commitment. I would like to thank Ernest Ihloff for his willingness to be my mentor and also my friend. I have learned a lot from Ernie about experimental physics, mechanical engineering and, most importantly, life. Special thanks go to Peter Binns, Brian O'Rourke and Steve Ciacera. These guys are true professionals and fun to work with.

The Bates operations group deserves special acknowledgment for successful operation of the stored polarized electron beam in the South Hall Ring under the difficult conditions created by the BLAST experiment. Under the leadership of Dr. Chris Tschalär and Dr. Manouchehr Farkhondeh, the operations group consistently produced stored beam with a quality which exceeded the BLAST design requirements. Special thanks to Dr. Wilbur Franklin for his work on the polarized electron source and the Compton polarimeter.

I would like to acknowledge Prof. Ricardo Alarcon for helping to cement my understanding of my research topic. I am thankful to Dr. Douglas Hasell for his help and guidance in my research. I would also like to acknowledge a tremendous amount of help from Dr. William Donnelly. Bill is a great teacher who is willing to spend hours sharing his keen insight into the subtleties of nuclear physics. I am grateful to Dr. Hartmuth Arenhövel for making his calculations available in a timely fashion. These calculations are instrumental to the analysis of the deuterium data from BLAST.

Last but certainly not least, I would like to acknowledge my fellow graduate students working on the BLAST experiment. Their hard, backbreaking labor made BLAST work. Chris Crawford and Chi Zhang were my "go to" guys for all of the data analysis questions. I am thankful to Nikolas Meitanis for all of his help with my ABS work. I am grateful to Aaron Maschinot for helping me develop my analysis code. Special thanks to Jason Seely, Benjamin Clasia, Adam DeGrush, Peter Karpus, Adrian Sindile, Octavian Filoti, Eugene Geis, Yuan Xiao and the rest of the BLAST collaboration for their contribution in constructing and running the BLAST experiment. I am grateful to Bradley Plaster for making the details of his analysis and his collection of the world's form factor data available to me.

# Contents

<b>1</b>	<b>Introduction</b>	<b>14</b>
<b>2</b>	<b>Theoretical Background</b>	<b>17</b>
2.1	Unpolarized Elastic Electron-Nucleon Scattering . . . . .	17
2.1.1	Form Factor Data from Unpolarized Scattering . . . . .	22
2.2	Polarized Elastic Electron-Nucleon Scattering . . . . .	25
2.2.1	Proton Elastic Form Factors from Polarization Measurements . . . . .	28
2.3	Polarized Elastic Electron-Deuteron Scattering . . . . .	30
2.3.1	Deuteron Ground State Wave Function . . . . .	30
2.3.2	The Elastic Form Factors of the Deuteron . . . . .	33
2.3.3	Elastic Electron-Deuterium Scattering . . . . .	34
2.3.4	Extraction of the Elastic Form Factor of the Neutron from the Elastic Form Factors of the Deuteron . . . . .	39
2.4	Polarized Quasielastic Electron-Deuteron Scattering . . . . .	43
2.4.1	Differential Cross Section For Polarized Electro-Disintegration of the Deuteron . . . . .	46
2.4.2	Extraction of $G_E^n$ from the ${}^2\vec{H}(\vec{e}, e'n)p$ Reaction . . . . .	49
2.5	Theoretical Models of the Elastic Form Factors of the Nucleon . . . . .	54
2.5.1	Scaling and pQCD . . . . .	55
2.5.2	Lattice QCD . . . . .	56
2.5.3	Dispersion Theory . . . . .	57
2.5.4	Vector Meson Dominance . . . . .	57
2.5.5	Chiral Quark Soliton Model . . . . .	59

2.5.6	Relativistic Constituent Quark Model . . . . .	60
2.5.7	Cloudy Bag Model . . . . .	61
2.5.8	Phenomenological Models . . . . .	62
2.5.9	Diquark Model . . . . .	63
2.5.10	Summary . . . . .	63
<b>3</b>	<b>Polarized Hydrogen/Deuterium Gas Target</b>	<b>67</b>
3.1	The RF Dissociator . . . . .	70
3.1.1	Performance of the RF Dissociator . . . . .	74
3.2	Focusing in a Sextupole Magnet System . . . . .	75
3.2.1	ABS Sextupole Magnet System at BLAST . . . . .	79
3.3	Polarization Techniques . . . . .	83
3.3.1	Hyperfine States of Hydrogen and Deuterium . . . . .	83
3.3.2	RF Transitions . . . . .	89
3.3.3	Polarization States in the Target . . . . .	94
3.4	The RF Transition Units . . . . .	96
3.4.1	MFT . . . . .	96
3.4.2	WFT . . . . .	100
3.4.3	SFT . . . . .	100
3.5	The Scattering Chamber . . . . .	101
3.5.1	Gas in the Storage Cell . . . . .	102
3.5.2	Polarized Atomic Gas in the Storage Cell . . . . .	105
3.5.3	Target Magnetic Holding Field . . . . .	110
3.5.4	Breit-Rabi Polarimeter . . . . .	113
3.6	ABS Performance . . . . .	115
3.6.1	Intensity . . . . .	115
3.6.2	Polarization . . . . .	117
<b>4</b>	<b>The BLAST Experiment</b>	<b>120</b>
4.1	The Stored Polarized Electron Beam in the South Hall Ring . . . . .	120
4.2	The BLAST Toroid Magnet . . . . .	123

4.3	The BLAST Detector . . . . .	124
4.3.1	The Drift Chambers . . . . .	127
4.3.2	Reconstruction Resolution of the Drift Chambers . . . . .	128
4.3.3	Čerenkov Detectors . . . . .	130
4.3.4	Time-of-Flight Scintillators . . . . .	134
4.3.5	Neutron Detector System . . . . .	135
4.4	The BLAST Trigger . . . . .	140
4.5	Charge Particle Veto . . . . .	142
4.6	BLAST Monte-Carlo . . . . .	144
<b>5</b>	<b>Data Analysis</b>	<b>149</b>
5.1	Overview of the Experiment . . . . .	149
5.2	Identification of the ${}^2\vec{H}(\vec{e}, e'n)p$ events . . . . .	151
5.2.1	Vertex cuts . . . . .	152
5.2.2	Neutron-photon separation . . . . .	152
5.2.3	Electron Quasielastic Cut . . . . .	154
5.2.4	Missing Mass Cut . . . . .	154
5.3	$Q^2$ Bin Selection . . . . .	156
5.4	Reconstructed Kinematic Variables . . . . .	157
5.5	Raw Experimental Asymmetry . . . . .	158
5.6	Background Corrected Asymmetry . . . . .	165
5.6.1	Unpolarized Background from the Target Cell . . . . .	165
5.6.2	Polarized Background . . . . .	168
5.7	Extraction of $G_E^n/G_M^n$ from the Background Corrected Asymmetry . . . . .	172
5.8	Systematic Uncertainties . . . . .	174
5.8.1	Target Polarization Angle . . . . .	175
5.8.2	Product of the Beam and Target Polarizations . . . . .	177
5.8.3	Reconstruction . . . . .	179
5.8.4	Value of $G_M^n$ . . . . .	180
5.8.5	Cut Dependence . . . . .	181
5.8.6	Radiative Corrections . . . . .	183

5.8.7	False Asymmetries . . . . .	184
<b>6</b>	<b>Discussion and Conclusion</b>	<b>186</b>
6.1	Discussion of the Results . . . . .	186
6.1.1	Phenomenological Fit . . . . .	186
6.1.2	Charge Density of the Neutron . . . . .	190
6.1.3	Nucleon Effective QCD Models . . . . .	193
6.2	Conclusion . . . . .	193
<b>A</b>	<b>Boosts and Rotations at BLAST</b>	<b>196</b>
A.1	Variable Naming Convention . . . . .	196
A.2	Kinematic Variable Listing . . . . .	198
A.3	Kinematic Relations . . . . .	200
A.4	Lorentz Transformations . . . . .	202
A.5	Jacobians and Cross Sections . . . . .	205

# List of Figures

2-1	Electron-Nucleon Elastic Scattering . . . . .	18
2-2	Elastic Form Factors of the Proton from the Unpolarized Electron Scattering Experiments . . . . .	23
2-3	World Data on $G_M^n$ . . . . .	24
2-4	Diagram of the Polarized Electron-Nucleon Elastic Scattering . . . . .	25
2-5	Proton's $\mu_p G_E^p / G_M^p$ from Polarization Experiments . . . . .	29
2-6	Deuteron's Wave Functions . . . . .	31
2-7	$A(Q^2)$ World's Data . . . . .	35
2-8	$B(Q^2)$ World's Data . . . . .	36
2-9	$T_{20}(Q^2)$ World's Data . . . . .	38
2-10	Contribution to $A(Q^2)$ . . . . .	40
2-11	Platchkov <i>et al</i> best fits . . . . .	42
2-12	$G_E^n$ extraction by Schiavilla and Sick . . . . .	43
2-13	Diagram of the Polarized Quasielastic Scattering . . . . .	44
2-14	Polarization of the Nucleons with Respect to the Direction of Target Polarization	49
2-15	$A_{ed}^V(\frac{\pi}{2}, 0)$ Comparison . . . . .	50
2-16	$A_{ed}^V(\frac{\pi}{2}, 0)$ Plotted with Various $G_E^n$ . . . . .	51
2-17	Model Dependence of $A_{ed}^V(\frac{\pi}{2}, 0)$ . . . . .	53
2-18	Potential Model Dependence of $A_{ed}^V(\frac{\pi}{2}, 0)$ . . . . .	54
2-19	Pion Cloud Model . . . . .	61
2-20	$\mu G_E^n / G_M^n$ World's Data with Theory . . . . .	65
2-21	$G_E^n$ World's Data with Theory . . . . .	66
3-1	ABS Schematic . . . . .	68

3-2	RF Dissociator . . . . .	70
3-3	Polarized Gas Feed System . . . . .	71
3-4	Unpolarized Gas Feed System . . . . .	73
3-5	Relative QMA Detection Probability $\kappa_{det}$ . . . . .	75
3-6	$\alpha_{H/D}$ of the Atomic Beam from the Dissociator . . . . .	76
3-7	Radial Component of the Sextupole Force Acting on Atom in the Presence of External Magnetic Field . . . . .	78
3-8	Effect of the External Field on 6-pole Focusing . . . . .	80
3-9	Sextupole Magnet . . . . .	81
3-10	Ray Tracing in the ABS . . . . .	82
3-11	Hyperfine structure of hydrogen and deuterium . . . . .	87
3-12	Hydrogen Polarizations in the External Magnetic Field . . . . .	88
3-13	Deuterium Vector Polarizations in the External Magnetic Field . . . . .	89
3-14	Deuterium Tensor Polarization in the External Field . . . . .	90
3-15	MFT and WFT RF transitions . . . . .	92
3-16	SFT RF transitions . . . . .	94
3-17	BLAST Magnetic Field along the Path of the Atomic Beam . . . . .	97
3-18	MFT magnetic shield and coils . . . . .	98
3-19	MFT RF . . . . .	99
3-20	WFT/SFT RF . . . . .	101
3-21	SFT magnetic shield and coils . . . . .	102
3-22	Storage Cell . . . . .	103
3-23	Cell on a Frame . . . . .	105
3-24	Holding Field Magnet . . . . .	111
3-25	Holding Field Map . . . . .	112
3-26	Breit-Rabi Polarimeter . . . . .	113
3-27	MFT Scan with SFT2-6 On . . . . .	115
3-28	Attenuation of the Atomic Beam in the ABS . . . . .	116
3-29	Vector Polarization of the Deuterium Target as a Function of Time . . . . .	118
3-30	Tensor Polarization of the Deuterium Target as a Function of Time . . . . .	119

3-31	Vector Polarization of the Hydrogen Target as a Function of Time . . . . .	119
4-1	South Hall Ring . . . . .	121
4-2	Compton Polarimeter . . . . .	122
4-3	Polarization of a Stored Beam . . . . .	123
4-4	BLAST Toroidal Magnet . . . . .	124
4-5	$B_y$ Produced by the BLAST Toroid . . . . .	125
4-6	BLAST Detector . . . . .	126
4-7	Electron Geometrical Acceptance of BLAST . . . . .	127
4-8	e-p Event in Single Event Display . . . . .	129
4-9	BLAST Resolutions . . . . .	131
4-10	BLAST Resolutions . . . . .	132
4-11	Čerenkov ADC Spectrum . . . . .	133
4-12	Čerenkov Efficiency . . . . .	134
4-13	Single Event Display . . . . .	136
4-14	Neutron Timing Calibration From Cosmic Rays . . . . .	138
4-15	The Reconstructed Position inside of Neutron Detectors . . . . .	139
4-16	Time-Walk Correction . . . . .	141
4-17	BLAST First Level Trigger Logic Diagram . . . . .	143
4-18	BLAST Second Level Trigger Logic Diagram . . . . .	144
4-19	BLASTMC Acceptance . . . . .	145
5-1	Target Polarization States . . . . .	151
5-2	Cut on Time-of-Flight Spectrum of Neutral Events . . . . .	153
5-3	Cut on Quasi-Free Neutron Knock-out Kinematics . . . . .	155
5-4	Missing Mass Cut . . . . .	156
5-5	Neutron Yields . . . . .	157
5-6	Reconstructed Kinematic Variables in the $Q^2 = 0.14$ (GeV/c) <sup>2</sup> Bin . . . . .	159
5-7	Reconstructed Missing Variables in the $Q^2 = 0.14$ (GeV/c) <sup>2</sup> Bin . . . . .	160
5-8	Reconstructed Kinematic Variables in the $Q^2 = 0.20$ (GeV/c) <sup>2</sup> Bin . . . . .	161
5-9	Reconstructed Missing Variables in the $Q^2 = 0.20$ (GeV/c) <sup>2</sup> Bin . . . . .	162
5-10	Reconstructed Kinematic Variables in the $Q^2 = 0.29$ (GeV/c) <sup>2</sup> Bin . . . . .	163

5-11	Reconstructed Missing Variables in the $Q^2 = 0.29$ (GeV/c) <sup>2</sup> Bin . . . . .	164
5-12	Vector Asymmetry not Corrected for the Background . . . . .	166
5-13	Correction Factor to the Vector Asymmetry Due to Scattering on Cell Walls	167
5-14	Correction Factor to the Vector Asymmetry Due to Scattering on Cell Walls with Hydrogen Gas in the Cell . . . . .	169
5-15	Vector Asymmetry Corrected for the Background . . . . .	171
5-16	$\chi^2$ Fit for the Best $G_E^n$ Value . . . . .	173
5-17	$\theta_D^*$ . . . . .	175
5-18	Target Angle Calculation Using the Tensor Asymmetry . . . . .	176
5-19	Target Spin Angle Profile . . . . .	177
5-20	Extraction of the $hP_z$ from ${}^2\vec{H}(\vec{e}, e'p)n$ Reaction . . . . .	178
5-21	Extraction of the $hP_z$ from ${}^2\vec{H}(\vec{e}, e'n)p$ Reaction in the Parallel Kinematics .	179
5-22	Friedrich and Walcher $G_M^n$ Parametrization . . . . .	181
5-23	Cut Dependence of the Extracted $G_E^n$ . . . . .	182
5-24	Effect of the Radiative Corrections on Vector Beam-Target Polarization Ob- servable . . . . .	184
5-25	False Asymmetries . . . . .	185
6-1	$G_E^n$ Results . . . . .	187
6-2	Contributions to $G_E^n$ from the different terms in the phenomenological para- metrization . . . . .	190
6-3	$\Delta G_E^n / G_E^n$ of the BLAST fit . . . . .	191
6-4	Ratio of the World's data to the Galster parametrization . . . . .	192
6-5	Contributions to Charge Density of the Neutron . . . . .	193
6-6	Charge Density of the Neutron . . . . .	194
6-7	$\mu_n G_E^n / G_M^n$ Results . . . . .	195

# List of Tables

2.1	Static Properties of a Deuterium . . . . .	33
3.1	Pole-tip Fields . . . . .	81
3.2	Distances from the Nozzle in the ABS . . . . .	83
3.3	RF Transitions in ABS . . . . .	96
3.4	Cell Geometry . . . . .	104
3.5	Diffusive Flow Quantities . . . . .	110
3.6	ABS Intensity . . . . .	116
3.7	Polarization Results . . . . .	118
4.1	SHR Design Parameters . . . . .	120
4.2	Electron Resolution at BLAST . . . . .	130
4.3	Neutron Detector Geometry . . . . .	137
4.4	BLAST Trigger Definitions and Rates . . . . .	142
5.1	Experimental Parameters . . . . .	150
5.2	Number of (e,e'n) events in Each $Q^2$ bin . . . . .	158
5.3	Extracted Background Corrected $A_{ed}^V(\frac{\pi}{2}, 0)$ Values . . . . .	170
5.4	Measured Values of $G_E^n/G_D^n$ . . . . .	174
5.5	Contributions to the Systematic Uncertainties . . . . .	174
6.1	Global Phenomenological Fit to the $G_E^n$ data . . . . .	189

# Chapter 1

## Introduction

The discovery of the neutron and subsequent study of the deuterium atom have played a key role in the development of the theory of nuclear force. In the 1932, right before the discovery of a neutron, there was no acceptable theory explaining the structure of a nucleus. The atoms were shown by Rutherford to consist of a massive core, nucleus, and super light particles, electrons, "orbiting around" the nucleus. The nuclei themselves were also shown by Rutherford to consist of positively charged particles named protons. However, there was a discrepancy between the mass and the charge of those nuclei. To account for this problem a proton-electron pair inside of the nucleus was introduced.

In 1932 J. Chadwick [1] discovered a neutral particle, then thought to be that proton-electron pair. By scattering  $\alpha$ -particles from the beryllium target he observed a signal consistent with an emission of a neutral particle. The energy conservation relation led him to conclude that the emitted particle had a mass 1 (in atomic units). However, in a series of papers Heisenberg showed from quantum mechanics that there cannot be a neutral spin- $\frac{1}{2}$  proton-electron pair [2, 3]. Instead, this was an elementary particle with no charge and a spin of  $1/2$ . At this point the picture of an atom's nucleus became clearer. It consisted of positively charged protons and neutrally charged neutrons.

However, two mysteries still remained. The first mystery had to do with an experiment that was conducted by R.Frisch and O. Stern [4]. They found that the magnetic moment of a proton deviated strongly from the simple magnetic moment of a structureless spin- $\frac{1}{2}$  particle. The only satisfactory explanation was that a proton had a finite structure. The

second mystery was the existence of the neutron itself. The electromagnetic force will cause the nucleons inside of a nucleus to be repelled since there are only positively and neutrally charged particles. Clearly, there had to be another, stronger, force that was responsible for containing protons and neutrons together. This force had to be electric charge neutral, which meant that the nucleons had to have an additional quantum number(s) to couple to this unknown force.

To further study these problems it was important to find a source of free or quasi-free neutrons. This was the dipion or as it is known now deuterium, discovered by H. Urey [5]. The deuteron is the only known bound two nucleon system. After physicists had developed a way to isolate the isotope of deuterium, Chadwick and Goldhaber conducted the first photo-disintegration experiment [6]. By measuring the energy of a recoiled proton and knowing the energy of the photon, they were able to measure the deuteron binding energy of 2.1 MeV and determine the mass of a neutron to be  $1.008 \pm 0.0005$  amu (atomic mass units). Moreover, Chadwick and Goldhaber showed the feasibility of using deuterium as a source of quasi-free neutrons. From this moment deuteron became a heavily studied N-N system. Most of the current knowledge about the neutron was obtained from studies on the deuteron.

It is now known that the nucleons (proton and neutron) are extended objects consisting of quarks and gluons. Quantum Chromodynamics, the standard model theory of the strong force points to a complex electromagnetic distribution inside of a nucleon. The precise knowledge of these distributions constrains quark-gluon models making them more precise and more realistic. Better knowledge of the electromagnetic structure of a nucleon also benefits better description of the nucleon-nucleon forces in deuterium and heavier nuclei.

The structure of the nucleon is principally studied by high energy electromagnetic probes. The most popular of these probes are the lepton beams (electrons or muons), since leptons are structureless elementary particles. The lepton probes are called “clean probes” since their electromagnetic interactions are well understood from QED. In lepton scattering the nucleon is probed by a single *virtual photon* in a one photon exchange approximation which is emitted by a lepton. The size of the four-momentum transfer,  $Q$  of a virtual photon determines the scale at which a nucleon is probed. The de Broglie wavelength of the virtual photon  $\lambda \approx 1/Q$  has to be of the order of the size of a nucleon,  $\sim 1$  fm in order to be sensitive

to the internal structure of the nucleon .

Today, medium energy electron scattering experiments are used as a tool to study the nucleon structure at the Jefferson Laboratory, Mainz and the Bates Linear Accelerator Center. Also, high energy lepton scattering is used to study nuclear interactions in the perturbative regime at the HERA Ring in Germany and the COMPASS muon scattering experiment at CERN.

# Chapter 2

## Theoretical Background

In this chapter, the theoretical framework for determination of the neutron's electric form factor,  $G_E^n$  is reviewed. Initially the theoretical description of elastic electron-nucleon scattering is presented. Both unpolarized and polarized elastic scattering are discussed. Then the theoretical description of the deuteron is introduced by discussing the latest models of the nucleon-nucleon bound state (Bonn and V18) and their relation to the static ( $Q^2 = 0$ ) and dynamic ( $Q^2 > 0$ ) properties of the deuteron. The model dependent extraction of  $G_E^n$  from elastic electron-deuteron scattering follows. Next, the determination of  $G_E^n$  in polarized electron-deuteron quasielastic scattering is described. In conclusion, an overview of the latest progress in the theory of the electromagnetic properties of the nucleon is presented.

### 2.1 Unpolarized Elastic Electron-Nucleon Scattering

An electron with initial four-momentum,  $K^\mu = (\mathcal{E}, \vec{k})$  acquires recoil momentum,  $K'^\mu = (\mathcal{E}', \vec{k}')$  when it scatters off a nucleon by exchanging a virtual photon with four-momentum  $Q^\mu = (\omega, \vec{q}) = K^\mu - K'^\mu = (\mathcal{E} - \mathcal{E}', \vec{k} - \vec{k}')$ . The four-momentum of the recoil nucleon is defined as  $P_f^\mu = Q^\mu + P_i^\mu$ , where  $P_i^\mu$  is the initial four-momentum of the nucleon. The initial three-momentum of the nucleon in the fixed target experiments is  $\vec{p}_i = 0$  in a lab frame and the initial energy,  $\mathcal{E}_i$  is equal to the nucleon mass,  $M_i$ .

Following Bjorken and Drell [7] the most general differential cross section can be written as

$$d\sigma = \frac{m_e^2}{|\vec{k}|} \frac{d^3\vec{k}'}{\mathcal{E}'(2\pi)^3} \frac{d^3\vec{p}_f}{E_f(2\pi)^3} M_i \sum_{if} |\mathcal{M}_{fi}|^2 (2\pi)^4 \delta^4(K^\mu + P_i^\mu - K'^\mu - P_f^\mu), \quad (2.1)$$

where  $m_e$  is the mass of the electron. By integrating over the final three-momentum,  $\vec{p}_f$  and

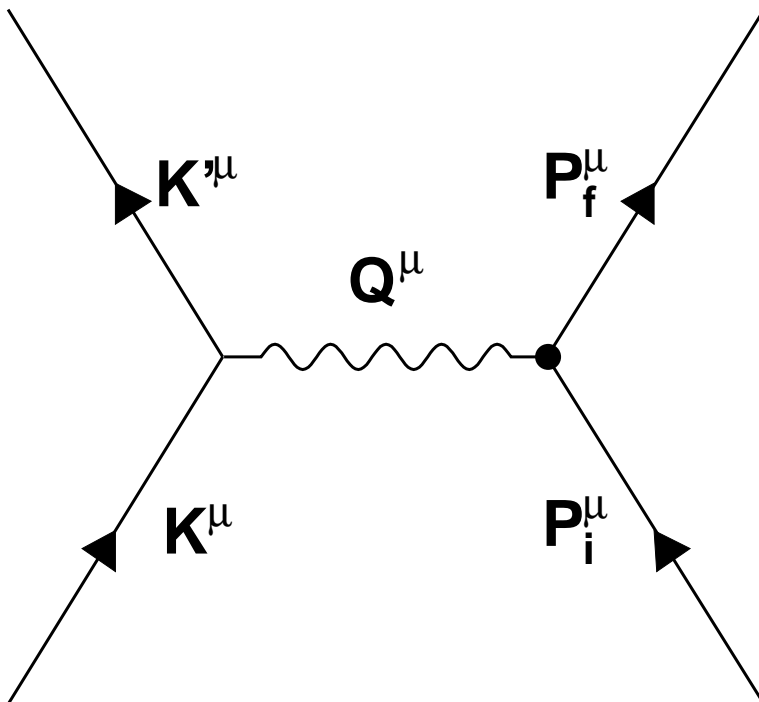


Figure 2-1: The tree-level Feynman diagram of electron-nucleon elastic scattering.

by using the differential form  $d^3\vec{k}' = k'^2 dk' d\Omega_e$ , the differential cross section becomes<sup>1</sup>

$$\frac{d\sigma}{d\Omega_e} = \frac{m_e^2 \mathcal{E}'}{4\pi^2 \mathcal{E}} f_{rec}^{-1} \sum_{if} |\mathcal{M}_{fi}|^2, \quad (2.2)$$

where  $f_{rec}$  is a nuclear recoil factor given in the extreme relativistic limit ( $m_e \ll \mathcal{E}'$ ) by

$$f_{rec} = 1 + \frac{2\mathcal{E}}{M_i} \sin^2\left(\frac{\theta_e}{2}\right). \quad (2.3)$$

The sum in eqn. 2.2 is the average over the initial leptonic and hadronic states and the sum over all final states.  $\mathcal{M}_{fi}$  is the invariant matrix element representing the factorized product

---

<sup>1</sup>Here the four-momentum conserving delta-function is used with the identity  $\frac{\partial k'}{\partial \mathcal{E}'} = \frac{\mathcal{E}'}{k'}$

of the leptonic and hadronic currents,  $j_e^\mu(K', K)$  and  $J^\mu(P_f, P_i)$ , respectively. Accordingly,

$$\mathcal{M}_{fi} = \frac{ie}{Q^2} j_e^\mu(K'^\mu, K^\mu) J_\mu(P_f^\mu, P_i^\mu), \quad (2.4)$$

where the leptonic current represents the electron vertex in the tree-level Feynman scattering diagram (fig 2-1). Since the electron is a structureless, spin- $\frac{1}{2}$  particle, the current  $j_e^\mu$  is simply expressed by combination of the Dirac spinors,  $u_e$  and  $\bar{u}_e$ ,

$$j_e^\mu(K'^\mu, S'; K^\mu, S) = \bar{u}_e(K'^\mu, S') \gamma^\mu u_e(K^\mu, S), \quad (2.5)$$

where  $S$  and  $S'$  are the spins of the incident and scattered electron, respectively.

If the nucleon is also a structureless point particle, its current can be defined in a similar fashion,

$$J_n^\mu(P_f^\mu, S_f; P_i^\mu, S) = \bar{u}_n(P_f^\mu, S_f) \gamma^\mu u_n(P_i^\mu, S), \quad (2.6)$$

The differential cross section of the electron scattered by the structureless spin- $\frac{1}{2}$  particle is obtained by combining eqns. 2.2, 2.4, 2.5 and 2.6.

$$\frac{d\sigma}{d\Omega_e} = \left( \frac{d\sigma}{d\Omega_e} \right)_M f_{rec}^{-1} \left\{ 1 + 2\tau \tan^2 \left( \frac{\theta_e}{2} \right) \right\}, \quad (2.7)$$

where  $\tau$  is the convenient kinematic variable, defined as  $\tau \equiv Q^2/(4M_n^2)$  and  $Q^2$  is defined as the negative of the 4-momentum squared of the virtual photon ( $Q^2 \equiv -Q_\mu Q^\mu$ ). The quantity  $\left( \frac{d\sigma}{d\Omega_e} \right)_M$  is the Mott cross section, which is the extension of the Rutherford cross section to the scattering of a relativistic, spin- $\frac{1}{2}$  particle [8, 9]

$$\left( \frac{d\sigma}{d\Omega_e} \right)_M = \frac{\alpha^2 \cos^2 \left( \frac{\theta_e}{2} \right)}{4\mathcal{E}^2 \sin^4 \left( \frac{\theta_e}{2} \right)}, \quad (2.8)$$

where  $\alpha$  is the fine-structure constant. The last term in the equation 2.7 reflects the fact that the target nucleon is the spin- $\frac{1}{2}$  particle.

However, the scattering formalism needs to be extended to a nucleon with an extended internal structure. The most complete form of the electromagnetic hadronic current that

satisfies current and parity conservation<sup>2</sup> is

$$J^\mu(P_f^\mu, S_f, \eta; P_i^\mu, S) = \bar{u}(P_f^\mu, S_f, \eta_f) \{ \gamma^\mu F_1^\eta(Q^2) + \frac{i}{2M_i} \sigma^{\mu\nu} Q_\nu F_2^\eta(Q^2) \} u(P_i^\mu, S_i, \eta_i), \quad (2.9)$$

where  $\eta$  is the isospin quantum number and the functions  $F_1(Q^2)$  and  $F_2(Q^2)$  represent the unknown extended electromagnetic structure of the nucleon. The Dirac form factor,  $F_1(Q^2)$  represents the charge distribution, whereas the Pauli form factor,  $F_2(Q^2)$  represents the magnetization distribution inside of the nucleon. Accordingly, the boundary conditions of the form factors are defined by the static electromagnetic properties of a nucleon with an isospin  $\eta$ ,

$$F_1^\eta(Q^2 = 0) = \begin{cases} 1 & \eta = +\frac{1}{2} \leftrightarrow \text{proton} \\ 0 & \eta = -\frac{1}{2} \leftrightarrow \text{neutron} \end{cases} \quad (2.10)$$

$$F_2^\eta(Q^2 = 0) = \begin{cases} k_p = 1.79 & \eta = +\frac{1}{2} \leftrightarrow \text{proton} \\ k_n = -1.91 & \eta = -\frac{1}{2} \leftrightarrow \text{neutron} \end{cases} \quad (2.11)$$

The differential cross section in terms of these structure function has well known Rosenbluth form [10]:

$$\frac{d\sigma}{d\Omega_e} = \left( \frac{d\sigma}{d\Omega_e} \right)_M f_{rec}^{-1} \left\{ (F_1^2 + \tau F_2^2) + 2\tau(F_1 + F_2)^2 \tan^2 \left( \frac{\theta_e}{2} \right) \right\} \quad (2.12)$$

A more convenient form for the nucleon elastic form factors has been suggested by Sachs et al. [11]. By moving to a special frame defined by the following kinematic condition,

$$\begin{aligned} \mathcal{E}' &= \mathcal{E} \\ \vec{k} &= -\vec{k}', \end{aligned} \quad (2.13)$$

the Dirac spinor in eqn. 2.9 can be re-written as

$$P_f^\mu = -P_i^\mu \implies \bar{u}(P_f^\mu, S_f, \eta_f) = \bar{u}(-P_i^\mu, S_f, \eta_f) \quad (2.14)$$

This frame is known as the Breit or the ‘‘brick wall’’<sup>3</sup> frame where the energy transfer,

<sup>2</sup>Current conservation is expressed as  $Q_\mu J^\mu = 0$ .

<sup>3</sup>The name ‘‘brick wall’’ comes from the fact that the electron behaves kinetically like a ball bouncing off

$\omega = 0$ . In the Breit frame, the Sachs electric and magnetic form factors  $G_E(Q^2)$  and  $G_M(Q^2)$  associated with the transfer of zero and one unit of the angular momentum along the direction of the virtual photon are the true representation of the electric and magnetic distributions of the nucleon. The Dirac and Pauli form factors can be written as a linear combination of the Sachs form factors as

$$\left. \begin{aligned} F_1 &= \frac{1}{1+\tau} [G_E + \tau G_M] \\ F_2 &= \frac{1}{1+\tau} [G_M - G_E] \end{aligned} \right\} \left\{ \begin{aligned} G_E &= F_1 - \tau F_2 \\ G_M &= F_1 + F_2 \end{aligned} \right. , \quad (2.15)$$

The Rosenbluth cross section in eqn. 2.12 in terms of the Sachs form factors becomes

$$\frac{d\sigma}{d\Omega_e} = \left( \frac{d\sigma}{d\Omega_e} \right)_M f_{rec}^{-1} \left\{ \frac{G_E^2 + \tau G_M^2}{1+\tau} + 2\tau G_M^2 \tan^2 \left( \frac{\theta_e}{2} \right) \right\} \quad (2.16)$$

In the non-relativistic limit, the Sachs form factors are interpreted as the Fourier transforms of spacial distributions of charge,  $\rho_{charge}(\vec{r})$  and magnetization,  $\rho_{mag}(\vec{r})$  inside of the nucleon,

$$G_E(Q^2) = \int \rho_{charge}(\vec{r}) e^{-i\vec{q}\cdot\vec{r}} d^3r \quad (2.17)$$

$$G_M(Q^2) = \int \mu \rho_{mag}(\vec{r}) e^{-i\vec{q}\cdot\vec{r}} d^3r, \quad (2.18)$$

where  $\mu$  is the nucleon dipole magnetic moment ( $\mu_p = 1 + \kappa_p$  and  $\mu_n = \kappa_n$ ). In this context, it is possible to define the nucleon charge and magnetization mean square radius by Taylor expansion of eqns. 2.17 and 2.18 around  $Q^2 = 0$ . The expectation values of the charge and magnetic radii are defined as

$$\langle r_{charge}^2 \rangle = \int r^2 \rho_{charge}(\vec{r}) d^3r = -6 \frac{dG_E}{dQ^2} \Big|_{Q^2 \rightarrow 0} \quad (2.19)$$

$$\langle r_{mag}^2 \rangle = \int r^2 \rho_{mag}(\vec{r}) d^3r = -\frac{6}{\mu} \frac{dG_M}{dQ^2} \Big|_{Q^2 \rightarrow 0} \quad (2.20)$$

The interpretation of the mean square charge radius of the proton and especially of the neutron has been a point of much discussion in the literature. The neutron square charge radius can be written [12] as a sum of the square radius associated with the neutron rest

---

a brick wall

frame charge distribution,  $r_{1,n}^2$  and the Foldy term [13],  $r_{Foldy,n}^2$ . The Foldy term arises from the relativistic corrections associated with the neutron magnetic moment. Isgur [12] showed that in certain models the Foldy term is canceled exactly by the contribution from the Dirac form factor  $F_1$ . Thus,  $r_{charge}$  as defined in eqn. 2.19 predicts exactly the rest frame charge distribution of the neutron.

### 2.1.1 Form Factor Data from Unpolarized Scattering

The proton electric and magnetic form factors have been measured extensively in unpolarized electron scattering using the Rosenbluth separation technique. In the Rosenbluth separation scheme, the differential cross section 2.16 is re-written in the following form

$$\left(\frac{d\sigma}{d\Omega_e}\right) / \left(\frac{d\sigma}{d\Omega_e}\right)_M \left(\frac{(1+\tau)\epsilon}{\tau}\right) = \frac{\epsilon}{\tau} (G_E^p)^2 + (G_M^p)^2, \quad (2.21)$$

where  $\epsilon$  is a measure of the longitudinal polarization of the virtual photon. If the value of  $Q^2$  is fixed, this quantity is a function of electron scattering angle,  $\theta_e$  only, i.e.

$$\epsilon = \left[1 + 2(1 + \tau) \tan^2\left(\frac{\theta_e}{2}\right)\right]^{-1} \quad (2.22)$$

$$0 \leq \epsilon \leq 1$$

The form factors are extracted from the linear fits in  $\epsilon$ , by keeping the momentum transfer constant. The electric form factor term in eqn. 2.21 is inversely proportional to  $Q^2$  through the kinematic factor,  $\tau$ . Thus, at a low momentum transfer the Rosenbluth measurement is very sensitive to  $(G_E^p)^2$ , whereas at large  $Q^2$  it is dominated by  $(G_M^p)^2$ .

$G_E^p$  is well known from Rosenbluth separation measurements in the range of  $Q^2$  up to 5 (GeV/c)<sup>2</sup> and  $G_M^p$  is known up to 30 (GeV/c)<sup>2</sup>. Compiled in fig. 2-2 are the present data on the electromagnetic form factors of the proton measured in unpolarized electron scattering experiments. The electric and magnetic form factors of the proton can be reasonably described by the dipole form factor,  $G_D$  over a large momentum transfer range. The dipole form is most commonly written as

$$G_E^p \approx G_M^p / \mu_p \approx G_D \equiv \frac{1}{(1 + Q^2/\Lambda)^2} \quad (2.23)$$

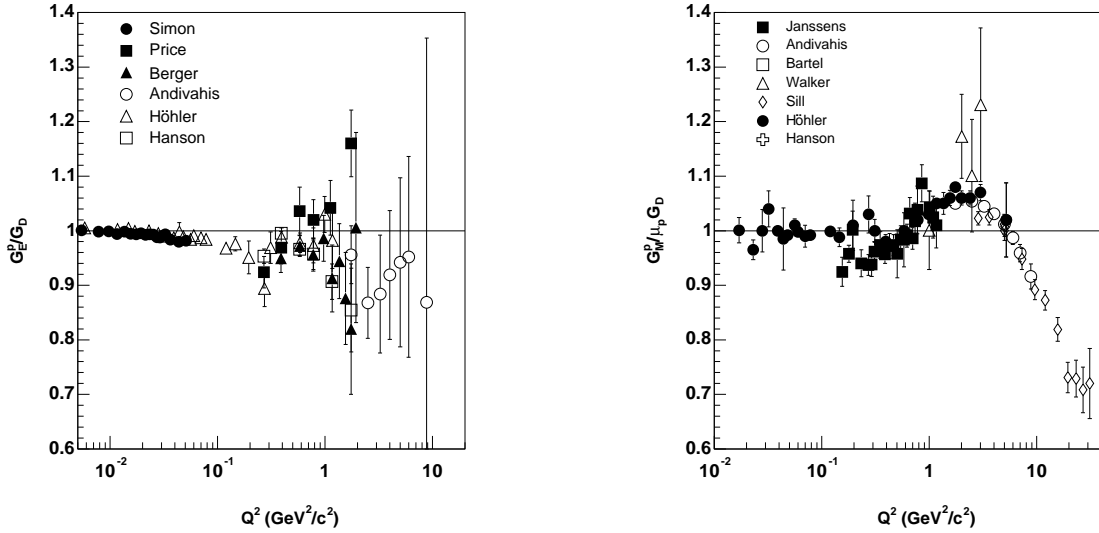


Figure 2-2: Elastic electric (left) and magnetic (right) form factors of the proton from the unpolarized electron scattering experiments plotted as a ratio to the dipole form factor.  $G_E^p$  data are taken from references [14, 15, 16, 17, 18, 19].  $G_M^p$  data are taken from references [20, 17, 21, 22, 18, 23, 19].

where  $\Lambda = 0.71$  (GeV/c)<sup>2</sup> is the global dipole fit parameter to the data. The dipole form factor is a Fourier transform of the exponential, radially symmetric charge and magnetization distributions [24],

$$G_D = \frac{\Lambda^{3/2}}{2\pi} \int e^{-\sqrt{\Lambda}r} \frac{\sin(qr)}{q} r dr \quad (2.24)$$

Since there is no free neutron target, the magnetic form factor of the neutron is typically measured with <sup>2</sup>H and more recently <sup>3</sup>He targets. Because  $G_M^n$  is almost two orders of magnitude larger than the  $G_E^n$ , the exclusive<sup>4</sup> quasielastic scattering cross section is almost purely determined by the magnetic form factor. However, there are two difficulties with the  $X(e, e'n)$  cross section measurement. Firstly, the cross section is modified by the finite motion of the neutron in the nuclear target and by the final state interaction of the recoil nucleons<sup>5</sup>

The second difficulty stems from the uncertainty in the absolute cross section measure-

<sup>4</sup>The neutron is detected in the final state to insure that the electron scatters off the neutron.

<sup>5</sup>The issue of initial and final interactions is further discussed in section 2.4.2.

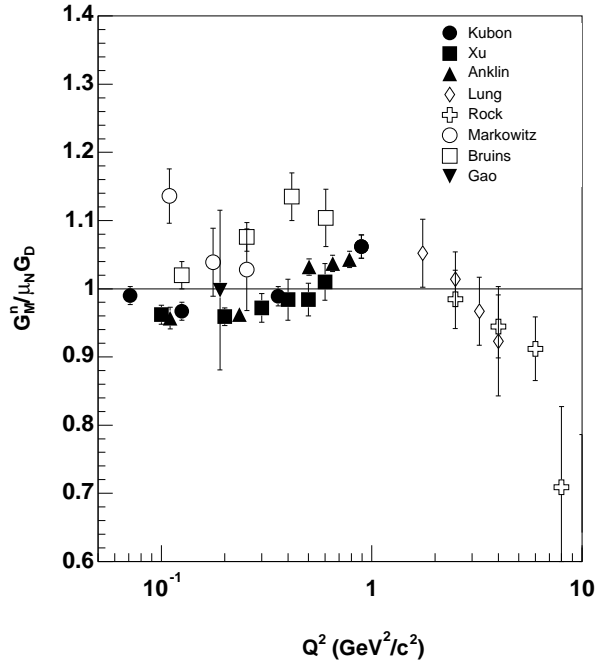


Figure 2-3: World data on the elastic magnetic form factor of the neutron. Data are taken from references [25, 26, 27, 28, 29, 30, 31, 32, 33, 34]. Open points are the cross section measurements and where the neutron detection efficiency was determined from a known nuclear reaction and filled points are the polarization measurements or experiments where the neutron detection efficiency was measured with the neutron beams.

ment due to the neutron detection efficiency. This difficulty can be overcome by using polarized scattering, where the detection efficiency cancels out to the first order.

For completeness, fig. 2-3 combines all the unpolarized and polarized measurements of  $G_M^n$ . Although the data are still lacking, it appears that neutron's magnetic form factor can also be parametrized with the dipole form factor in eq. 2.24. There is a significant discrepancy between most polarization and cross section measurements of  $G_M^n$  where the neutron detection efficiency was calibrated using a known nuclear reaction. Jourdan and collaborators [35] published a paper critiquing the method used by Bruins et al. [33] to calculate the neutron efficiency in the cross section measurement, thus casting doubt on their results for  $G_M^n$  which is in significant disagreement with the polarization experimental data.

Due to the smallness of the neutron's electric form factor, for a long time the only reliable unpolarized data on  $G_E^n$  were extracted from the unpolarized elastic scattering on deuterium. These experiments will be discussed in detail in section 2.4.

## 2.2 Polarized Elastic Electron-Nucleon Scattering

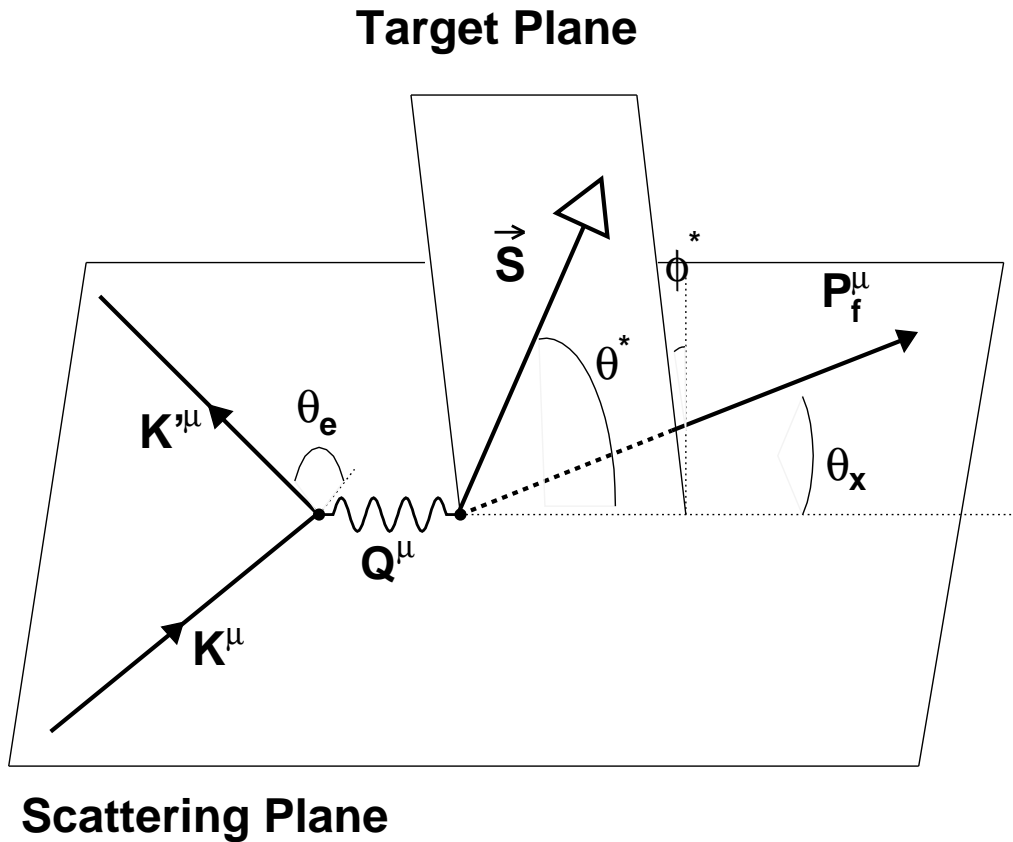


Figure 2-4: Schematic representation of polarized electron-nucleon scattering in the limit of single photon exchange.

The discussion of polarized electron-nucleon scattering is largely based on the review articles by Donnelly and Raskin [36, 37] and by Arenhövel, Leidemann and Tomusiak [38].

Figure 2-4 shows the schematic representation of this type of scattering. The kinematic variables are defined in the same way as in the unpolarized case. However, for each po-

larization vector, an additional kinematic plane needs to be defined to fully describe the reaction mechanism. In the case of a longitudinally polarized electron the *Scattering Plane* is introduced (see fig. 2-4). Typically this plane's definition follows the so-called Madison convention, defined by the following identities

$$\hat{z} \equiv \frac{\vec{q}}{|\vec{q}|} \quad , \quad \hat{y} \equiv \frac{\vec{k} \times \vec{k}'}{|\vec{k}||\vec{k}'|} \quad , \quad \hat{x} \equiv \hat{y} \times \hat{z}. \quad (2.25)$$

With a polarized target, there is another kinematic plane added. It is denoted as the *Target Plane* in fig. 2-4. The target plane is defined by the target polarization vector  $\vec{S}$ , with respect to the scattering plane as

$$\vec{S} = (\sin\theta^* \cos\phi^*, \sin\theta^* \sin\phi^*, \cos\theta^*), \quad (2.26)$$

where  $\theta^*$  is the polar angle between the target spin vector and the three-momentum transfer vector and  $\phi^*$  is the azimuthal angle of the target spin direction relative to the scattering plane.

In the one-photon approximation the most general differential cross section is given by

$$\frac{d\sigma}{d\Omega_e} = C \{ \rho_L f_L + \rho_T f_T + \rho_{LT} f_{LT} + \rho_{TT} f_{TT} + h P_z (\rho'_{LT} f'_{LT} + \rho'_T f'_T) \}, \quad (2.27)$$

where  $h$  is the electron polarization,  $P_z$  is the target polarization and  $C = \frac{\alpha}{6\pi^2} \frac{\mathcal{E}'}{\mathcal{E}Q^2}$ . The virtual photon density matrices,  $\rho_{\mu\mu}$  have to be boosted into the inertial frame in which the structure functions,  $f_{\mu\mu}$  are evaluated

$$\begin{aligned} \rho_L &= -\beta^2 Q^2 \frac{\xi^2}{2\eta} & , & \quad \rho_{LT} = -\beta^2 Q^2 \frac{\xi}{\eta} \sqrt{\frac{\xi + \eta}{8}} \\ \rho_T &= -\frac{1}{2} Q^2 \left\{ 1 + \frac{\xi}{2\eta} \right\} & , & \quad \rho_{TT} = Q^2 \frac{\xi}{4\eta} \\ \rho'_{LT} &= -\frac{1}{2} \beta Q^2 \frac{\xi}{\sqrt{2\eta}} & , & \quad \rho'_T = -\frac{1}{2} Q^2 \sqrt{\frac{\xi + \eta}{\eta}}, \end{aligned} \quad (2.28)$$

where,

$$\beta = \frac{|\vec{q}^{tab}|}{|\vec{q}^{breit}|} = \sqrt{1 + \tau} \quad , \quad \xi = \frac{Q^2}{|\vec{q}^{tab}|^2} \quad , \quad \eta = \tan^2 \left( \frac{\theta_e}{2} \right) \quad (2.29)$$

In the Breit frame, the structure functions can be explicitly written in term of the nucleon

electromagnetic current,  $J_\mu$  and the initial nucleon density matrix,  $\rho_N$ . These quantities are defined in terms of the Sachs form factors, Pauli matrices and the target polarization vector as

$$J_\mu = (G_E, i\frac{q}{2M\beta}G_M\sigma_x, -i\frac{q}{2M\beta}\sigma_y, 0) \quad (2.30)$$

$$\rho_N = \frac{1}{2}(1 + P_z\vec{S} \cdot \vec{\sigma}) \quad (2.31)$$

where  $M$  is the mass of a nucleon,  $\beta$  is defined in eq. 2.29 and  $\vec{\sigma}$  is the vector of Pauli matrices in the coordinate system defined in eq. 2.25.

Using eqns. 2.30 and 2.31 along with the known properties of Pauli matrices, the structure functions,  $f_{\mu\mu}$  can be written as [38]

$$f_L = \text{Tr}(J_0\rho_N J_0^\dagger) = G_E^2 \quad (2.32)$$

$$f_T = \text{Tr}(J_x\rho_N J_x^\dagger) + \text{Tr}(J_y\rho_N J_y^\dagger) = 2\tau G_M^2 \quad (2.33)$$

$$f_{LT} = -\sqrt{2}\{\text{Tr}(J_0\rho_N J_x^\dagger) + \text{Tr}(J_x\rho_N J_0^\dagger)\} = 0 \quad (2.34)$$

$$f_{TT} = -\text{Tr}(J_x\rho_N J_x^\dagger) + \text{Tr}(J_y\rho_N J_y^\dagger) = 0 \quad (2.35)$$

$$f'_{LT} = \sqrt{2}\{\text{Tr}(J_0\rho_N J_y^\dagger) + \text{Tr}(J_y\rho_N J_0^\dagger)\} = -2\sqrt{2\tau}G_E G_M S^\perp \quad (2.36)$$

$$f'_T = -i\{\text{Tr}(J_x\rho_N J_y^\dagger) + \text{Tr}(J_y\rho_N J_x^\dagger)\} = -2\tau G_M^2 S^\parallel \quad (2.37)$$

The differential cross section in eqn. 2.27 can be rewritten by combining eqns. 2.28 and 2.32-2.37 as

$$\frac{d\sigma}{d\Omega_e} = \Sigma_0 \{1 + hP_z\vec{S} \cdot \vec{A}_{eN}\}, \quad (2.38)$$

where,

$$\Sigma_0 = C(\rho_L G_E^2 + 2\tau\rho_T G_M^2) \quad (2.39)$$

is the unpolarized elastic cross section. The polarized term in the cross section can be expressed by the components of  $\vec{A}_{eN}$  associated with the direction of the target polarization

vector,  $\vec{S}$  as

$$A_{eN}^{\parallel} = -C \frac{2\tau \rho'_T G_M^2}{\Sigma_0} \quad (2.40)$$

$$A_{eN}^{\perp} = -C \frac{2\sqrt{2}\tau \rho'_{LT} G_E G_M}{\Sigma_0} \quad (2.41)$$

$$A_{eN}^{oop} = 0 \quad (2.42)$$

The asymmetry measured in *parallel kinematics*, where the momentum transfer is parallel to the target spin vector, is proportional to the nucleon's magnetic form factor squared. The asymmetry in *perpendicular kinematics* is proportional to the product of the magnetic and electric form factors.

If the asymmetries in both kinematic regimes are measured simultaneously, one can build a so-called *super ratio* as

$$\frac{A_{eN}^{\perp}}{A_{eN}^{\parallel}} = \sqrt{\frac{2}{\tau}} \frac{\rho'_{LT} G_E}{\rho'_T G_M}. \quad (2.43)$$

In the super ratio measurement, the beam and target polarizations drop out. Therefore, this measurement is less sensitive to the systematic uncertainties of the product of beam and target polarizations,  $hP_z$ .

It follows from equation 2.38 that polarized beam alone does not produce additional information about the structure of the nucleon in elastic electron-nucleon scattering as compared to unpolarized scattering. The target also has to be polarized.

## 2.2.1 Proton Elastic Form Factors from Polarization Measurements

The measurement of the asymmetry in the double polarized electron-nucleon scattering is a very sensitive method to determine the nucleon electromagnetic form factors. However, these experiments are difficult since they require highly polarized electron beam and target. Alternatively, a technique was developed by Milbrath et al. [39, 40], where the polarization of the recoiling proton is measured in a polarized electron scattering on an unpolarized  $^1H$  target. It can be shown that such a polarization transfer measurement also probes the nucleon form factors in a similar fashion as in eqns. 2.40 and 2.41.

High precision data on  $\mu_p G_E^p/G_M^p$  became available within the last five years from measurements using the recoil proton polarimeters at Jefferson Lab [41, 42, 43]. These measurements consistently show a step decrease of the  $\mu_p G_E^p/G_M^p$  ratio at  $Q^2 > 1$  (GeV/c)<sup>2</sup> (see fig. 2-5). The decrease of the form factor ratio is in strong disagreement with the unpolarized

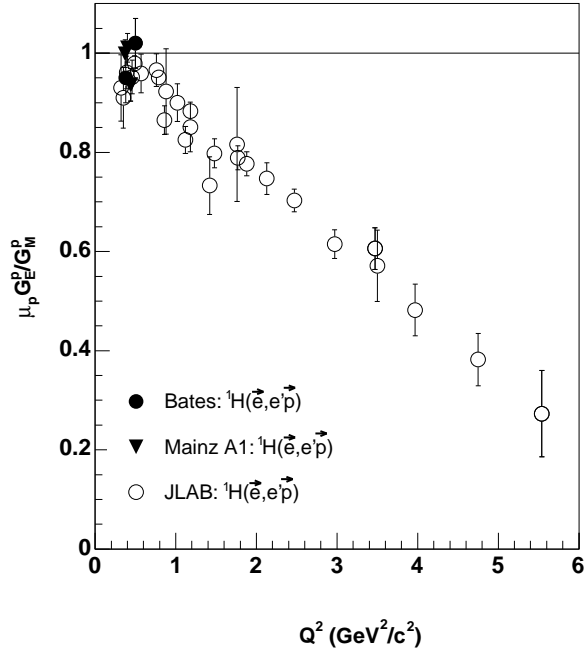


Figure 2-5: Proton form factor ratio,  $\mu_p G_E^p/G_M^p$  from recoil polarization experiments. Data points are taken from [40, 41, 42, 44, 43].

measurements, as noted by Arrington [45]. A possible explanation could be a correction due to the two-photon contribution to the unpolarized scattering becoming significant at large momentum transfer. However, it appears that the two-photon contribution to the polarized measurement is small [46].

## 2.3 Polarized Elastic Electron-Deuteron Scattering

### 2.3.1 Deuteron Ground State Wave Function

The deuterium nucleus is the only known bound state of two nucleons. The neutron and proton, both spin- $\frac{1}{2}$  particles, combine to form a spin-1 bound nucleon-nucleon state with a positive parity. This indicates the presence of a spin and orbital angular momentum dependent force in the nucleon-nucleon potential (i.e. spin-spin, spin-orbit and tensor) [47]. The most general form of the non-relativistic Hamiltonian can be written as [48]

$$H = \sum_i -\frac{\hbar^2}{2m} \nabla_i^2 + \sum_{i<j} V_{ij}, \quad (2.44)$$

A non relativistic wave function of the deuteron in coordinate space can be written in general as [49]

$$\Psi_M(\vec{r}) = \frac{u(r)}{r} Y_{00}(\hat{r}) |1, m_s\rangle + \frac{w(r)}{r} Y_{00}(\hat{r}) \sum_{m_s} Y_{2m-m_s}(\hat{r}) \langle 21m - m_s m_s | 1m \rangle |1, m_s\rangle, \quad (2.45)$$

where the  $Y_{lm_l}$  are spherical harmonic wave functions and states  $|1, m_s\rangle$  represent a spin-1 multiplets for  $m_s = \pm 1, 0$ . In eqn. 2.45  $u(r)/r$  and  $w(r)/r$  represent the spatial components of the reduced  $S$ - and  $D$ -wave functions in coordinate space<sup>6</sup>. These wave functions are Fourier transformed into the momentum space using Bessel's functions,  $j_l(pr)$  as

$$\begin{aligned} u(\vec{p}) &= \int_0^\infty r dr u(r) j_0(pr) \\ w(\vec{p}) &= \int_0^\infty r dr w(r) j_2(pr). \end{aligned} \quad (2.46)$$

The normalization condition for the  $u(r)$  and  $w(r)$  wave functions in terms of  $S$ - and  $D$ -wave probability densities is

$$P_S \left[ = \int_0^\infty dr u^2(r) \right] + P_D \left[ = \int_0^\infty dr w^2(r) \right] = 1. \quad (2.47)$$

While the angular properties of the wave function are explicitly dependent on the orbital

---

<sup>6</sup>Since the deuteron has a positive parity, only the wave functions with even angular momentum are allowed.

and total angular momenta, the radial wave function is determined by the choice of the potential  $V_{ij}$  in eqn. 2.44. In this work the emphasis is on the Bonn [50] potential. The choice of this potential is driven by the fact that all of the theoretical calculations performed for this work by H. Arenhövel were done using the Bonn potential. Figure 2-6 shows  $u(r)$  and  $w(r)$  radial wave function in coordinate space and the corresponding probability densities  $\rho_S(p)$  and  $\rho_D(p)$  in momentum space.

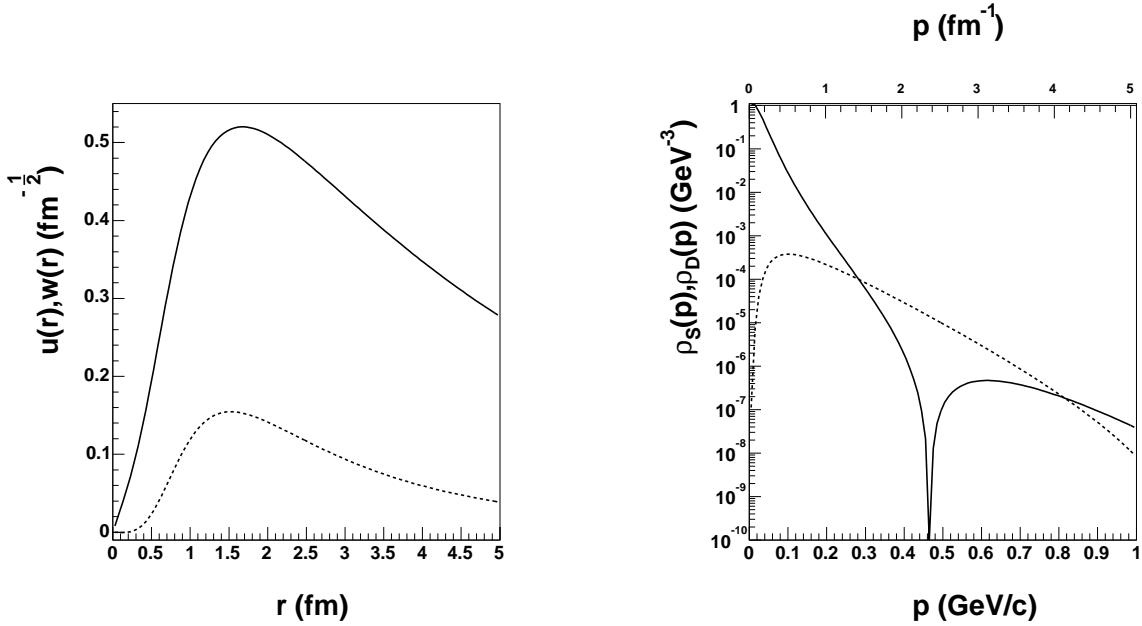


Figure 2-6: On the left are the  $S$ -wave (solid) and  $D$ -wave (dotted) components of a deuteron radial wave function determined with the Bonn [50] potential in the coordinate (left) multiplied by  $r^2$ . On the right are the densities of  $S$  (solid) and  $D$  (dotted) wave functions in the momentum space.

A successful nucleon-nucleon potential must be able to precisely predict the static properties of the deuteron. One of these static properties is the root mean square matter radius<sup>7</sup> of the deuteron,  $r_d$  defined as a half distance between two nucleons in the deuteron. The matter radius is expressed in terms of the wave function as

$$r_d = \frac{1}{2} \left\{ \int_0^\infty r^2 dr [u^2(r) + w^2(r)] \right\}^{\frac{1}{2}}. \quad (2.48)$$

This static quantity is not very sensitive to the  $D$ -wave component of the wave function,

<sup>7</sup>Not to be confused with a charge radius.

since the  $S$ -wave state is a significantly larger contributor to the integral in eqn. 2.48.

A more interesting static property of the deuteron is its electric quadrupole moment, written as

$$Q_d = \frac{1}{\sqrt{50}} \int_0^\infty r^2 dr w(r) \left[ u(r) - \frac{w(r)}{\sqrt{8}} \right] \quad (2.49)$$

This quantity is explicitly proportional to the size of the  $D$ -wave component in the wave function. Hence, its measurement is a very sensitive test for the deuteron model.

Analogously the magnetic dipole moment of the deuteron can be defined entirely in terms of the  $D$ -wave probability,  $P_D$  [47]

$$\mu_d = (\mu_p + \mu_n) \left(1 - \frac{3}{2} P_D\right) + \frac{3}{4} P_D = 0.8798 - 0.5697 P_D, \quad (2.50)$$

where  $\mu_p$  and  $\mu_n$  are the magnetic moments of the proton and neutron respectively.

Another interesting static property of the deuteron is the asymptotic behavior of the wave function as  $r \rightarrow \infty$ <sup>8</sup>. In this limit the wave functions are parametrized as [50].

$$\begin{cases} u(r \rightarrow \infty) \rightarrow A_S e^{-\gamma r} \\ w(r \rightarrow \infty) \rightarrow A_D e^{-\gamma r} \left(1 + \frac{3}{\gamma r} + \frac{3}{\gamma^2 r^2}\right), \end{cases} \quad (2.51)$$

where  $\gamma = \sqrt{4M_p^2 M_n^2 - (M_d^2 - M_p^2 - M_n^2)^2} / 2M_d = 0.2315380 \text{ fm}^{-1}$  with  $M_d$ ,  $M_n$  and  $M_p$  being the masses of a deuteron, neutron and proton, respectively. The ratio of the asymptotic normalization factors  $A_S$  and  $A_D$  is a good test of the theoretical models, since it explicitly establishes the relative sizes of  $S$  and  $D$ -wave function in the  $p \rightarrow 0$  limit.

The relative size of the  $D$ -wave component is still uncertain. Also, the interpretation of the  $D$ -wave contributions to the dipole and the quadrupole moments is subject to relativistic corrections and meson exchange currents.

Table 2.1 shows the experimental measurements of these static properties and the calculations using the Bonn [50] potential and another modern potential, Argonne V18 [51]. Calculations using both potentials predict the static properties of the deuteron relatively well. However, some discrepancies still remain. One of these discrepancies is due to the fact that both potentials underestimate the size of the electric quadrupole moment, while cor-

---

<sup>8</sup>This corresponds to the asymptotic behavior at  $p \rightarrow 0$  in the momentum space.

Properties	Recent data	AV18	Bonn
$\mu_d$	$0.8574382284(98)\mu_N$	$0.871\mu_N$ <sup>9</sup>	$0.852\mu_N$ <sup>10</sup>
$Q_d$	$0.2859(3)fm^2$	$0.275fm^2$ <sup>9</sup>	$0.270fm^2$ <sup>10</sup>
$A_D/A_S$	$0.0256(4)$	$0.0250$	$0.0256$
$r_d$	$1.975(3)fm$	$1.967fm$	$1.966fm$
$\mathcal{E}_d$	$2.22456612MeV$	$2.224575MeV$	$2.224575MeV$

Table 2.1: Comparison between recent data on the static properties of the deuteron and theoretical predictions by the Argonne V18 [51] and Bonn [50] potentials. The table is taken from the review paper by Garçon [47]. Refer to this paper for all citations.

rectly predicting the size of the magnetic dipole moment. These inconsistencies indicate that despite the successes of the modern nucleon-nucleon potentials, there is still some theoretical work that remains to be done.

### 2.3.2 The Elastic Form Factors of the Deuteron

In addition to its static properties, the deuteron has a dynamical electromagnetic structure. The observables that correspond to the internal properties of the deuteron are best measured in the elastic electron scattering. These observables are of the great interest, since they can potentially access the density distributions of the  $S$ - and  $D$ -wave functions in the momentum space. Similarly to electron-nucleon scattering, the electron-deuteron scattering amplitude is a product of the leptonic (eqn. 2.5) and hadronic currents. The most general form of the deuteron hadronic current in terms of the elastic form factors is [52]

$$\begin{aligned}
J_d^\mu(P_f^\mu, S_f; P_i^\mu, S_i) = & -G_1(Q^2) \left[ \xi_{S_f}^{\mu*}(P_f) \cdot \xi_{S_i}^\mu(P_i)(P_f + P_i)^\mu \right] \\
& -G_2(Q^2) \left[ \xi_{S_i}^\mu(P_i)(\xi_{S_f}^{\mu*}(P_f) \cdot (P_f - P_i)^\mu) - \xi_{S_f}^{\mu*}(P_f)(\xi_{S_i}^\mu(P_i) \cdot (P_f - P_i)^\mu) \right] \\
& +G_3(Q^2) \frac{1}{2M_d^2} \left[ \xi_{S_f}^{\mu*}(P_f) \cdot (P_f - P_i)^\mu (\xi_{S_i}^\mu(P_i) \cdot (P_f - P_i)^\mu)(P_f + P_i)^\mu \right],
\end{aligned} \tag{2.52}$$

where  $P_i$  and  $P_f$  are the initial and final momenta of the deuteron respectively and  $\xi_{S_i}^\mu$  and  $\xi_{S_f}^\mu$  are the initial and final polarization four-vectors. The form factors  $G_1$  and  $G_2$  are analogous to the Dirac and Pauli form factors of the nucleon. The additional form factor,  $G_3$ , is due to the deuteron being a spin-1 particle. In direct analogy with the nucleon Sachs form factors, the deuteron elastic form factors can be identified with the charge, magnetic

<sup>9</sup>Corrected for relativistic effects and meson exchange currents (MEC)

<sup>10</sup>Not corrected for relativistic effects and MEC

and an additional electric quadrupole form factor. These quantities are written in terms of the form factors  $G_i$  in eqn. 2.52 as [52]

$$\begin{aligned}
G_C(Q^2) &= G_1(Q^2)\left(\frac{2}{3}\eta + 1\right) - \frac{2}{3}\eta G_2(Q^2) + \frac{2}{3}\eta(1 + \eta)G_3(Q^2) \\
G_M(Q^2) &= G_2(Q^2) \\
G_Q(Q^2) &= G_1(Q^2) - G_2(Q^2) + (1 + \eta)G_3(Q^2),
\end{aligned}
\tag{2.53}$$

where  $\eta$  is the kinematic parameter equivalent to the parameter  $\tau$  in the elastic electron-nucleon scattering,  $\eta = Q^2/(4M_d)^2$ .

The measurements of the deuteron form factors provide an additional constraint on the theoretical models of the deuteron.

### 2.3.3 Elastic Electron-Deuterium Scattering

In the simplest case of the elastic scattering of the unpolarized electron beam from the unpolarized deuterium target, the form of the differential cross section is similar to the elastic electron-nucleon unpolarized cross section in eqn. 2.16.

$$\frac{d\sigma}{d\Omega_e} = \left(\frac{d\sigma}{d\Omega_e}\right)_M f_{rec}^{-1} \left\{ A(Q^2) + B(Q^2)\tan^2\left(\frac{\theta_e}{2}\right) \right\}
\tag{2.54}$$

Therefore, the technique of the Rosenbluth separation introduced earlier in this chapter, can be applied to electron-deuteron elastic scattering cross section in eqn. 2.54 in order to determine elastic form factors,  $A(Q^2)$  and  $B(Q^2)$  separately. These elastic form factor are the linear combination of the three electromagnetic form factors  $G_C$ ,  $G_M$  and  $G_Q$  introduced in eqn. 2.53.

$$\begin{aligned}
A(Q^2) &= G_C^2(Q^2) + \frac{8}{9}\eta^2 G_Q^2(Q^2) + \frac{2}{3}\eta G_M^2(Q^2) \\
B(Q^2) &= \frac{4}{3}\eta(1 + \eta)G_M^2(Q^2)
\end{aligned}
\tag{2.55}$$

Both  $A(Q^2)$  and  $B(Q^2)$  are reasonably well-determined quantities<sup>11</sup> up to a momentum transfer of  $Q^2 = 4$  (GeV/c)<sup>2</sup>. However, the unpolarized elastic scattering observables by themselves are not sufficient to independently determine all three electromagnetic form fac-

---

<sup>11</sup>A 10 % discrepancy in  $A(Q^2)$  remains between separate experimental data sets.

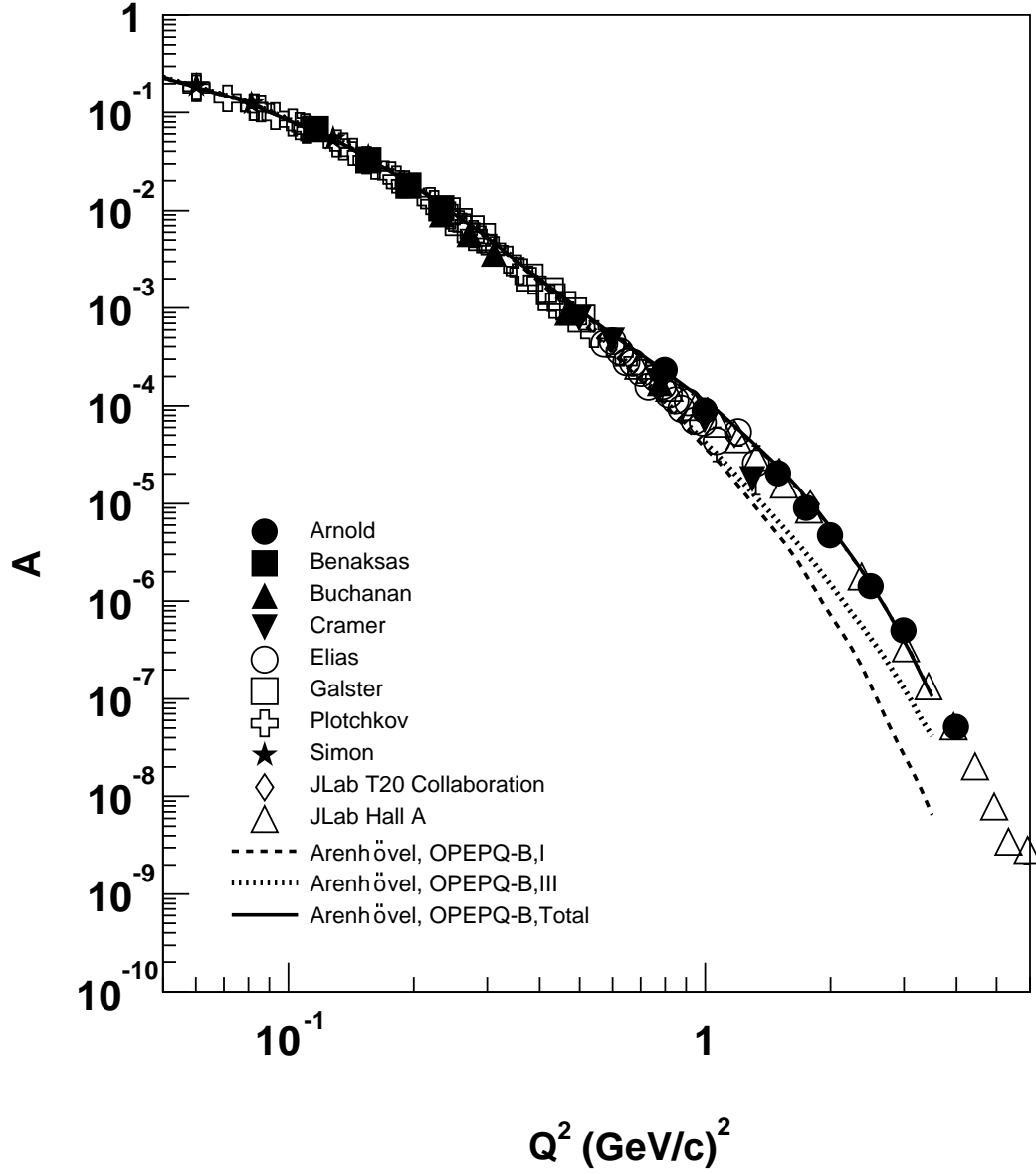


Figure 2-7: World's data for the observable  $A(Q^2)$ . The data were compiled by the Jefferson Lab Hall C T<sub>20</sub> collaboration [53] from references [54, 55, 56, 57, 58, 59, 60, 61, 62, 63]. The curves are theoretical predictions based on the Bonn OBEPQ-B potential [64] with non relativistic nucleon current (dashed), relativistic nucleon current (dotted), relativistic nucleon current with  $\pi$ ,  $\rho$  and heavy meson exchange currents (solid).

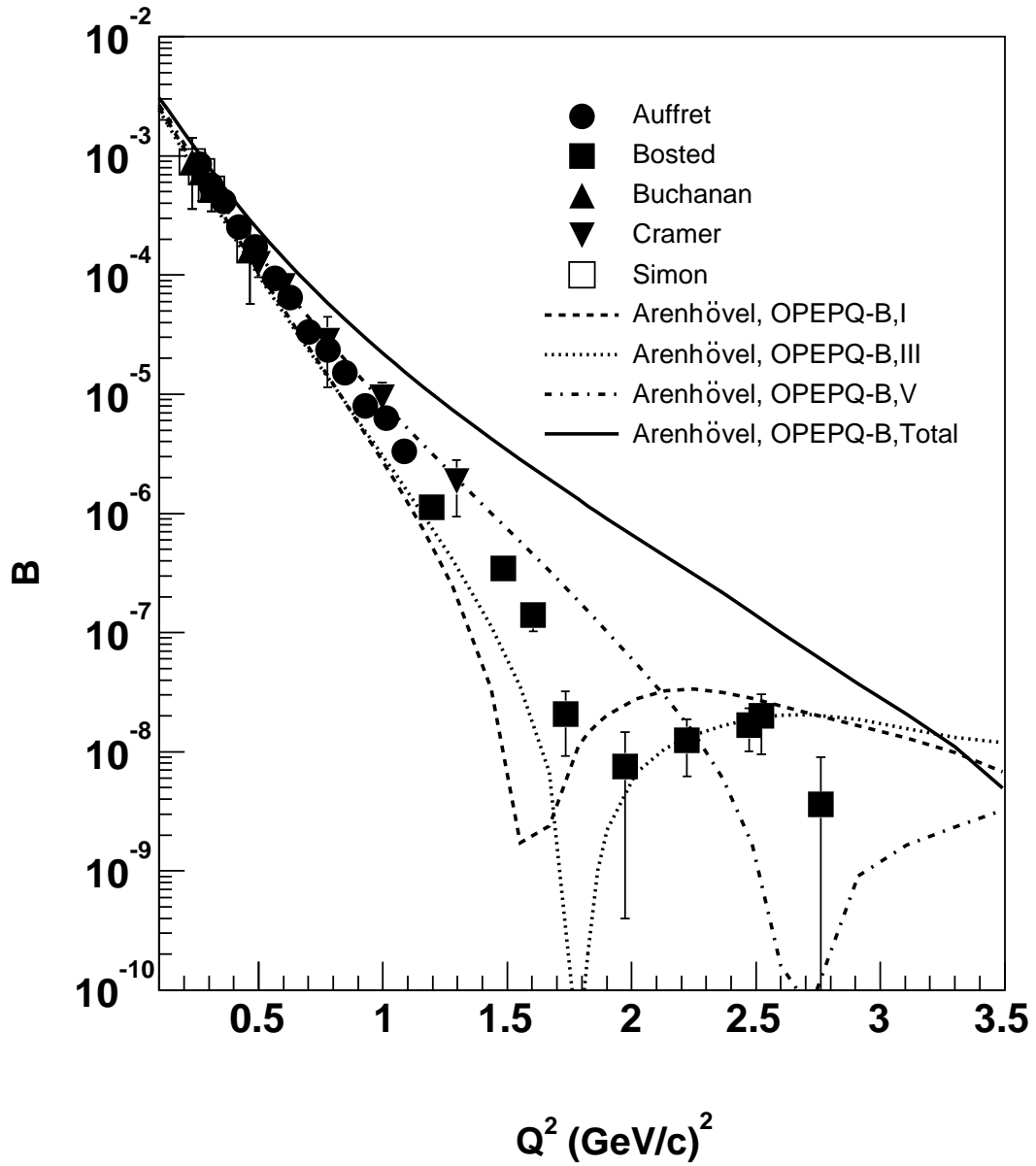


Figure 2-8: World's data for the observable  $B(Q^2)$ . The data were compiled by the Jefferson Lab Hall C  $T_{20}$  collaboration [53] from references [54, 61, 65, 60, 66]. The curves are theoretical predictions based on the Bonn OBEPQ-B potential [64] with non relativistic nucleon current (dashed), relativistic nucleon current (dotted), relativistic  $\pi$ -meson exchange currents (dot-dashed), relativistic nucleon currents and  $\pi$ ,  $\rho$  and heavy meson exchange currents (solid).

tors of the deuteron. Hence, at least one more observable is needed.

The new observables are introduced by using a tensor polarized target in elastic scattering. Using Donnelly and Raskin formalism [36], the polarized differential cross section is expressed as <sup>12</sup>.

$$\begin{aligned} \frac{d\sigma}{d\Omega_e} &= \left( \frac{d\sigma}{d\Omega_e} \right)_M f_{rec}^{-1} R_0 \left[ 1 + \frac{1}{\sqrt{2}} P_{zz} P_2^0(\cos\theta^*) T_{20}(Q^2) - \frac{1}{\sqrt{3}} P_{zz} P_2^1(\cos\theta^*) \cos\phi^* T_{21}(Q^2) + \right. \\ &\quad \left. + \frac{1}{2\sqrt{3}} P_{zz} P_2^2(\cos\theta^*) \cos 2\phi^* T_{22}(Q^2) \right] \\ R_0 &= A(Q^2) + B(Q^2) \tan^2 \left( \frac{\theta_e}{2} \right), \end{aligned} \quad (2.56)$$

where  $P_{zz}$  is the tensor polarization of the deuterium target,  $\theta^*$  and  $\phi^*$  are the angles of the target polarization vector with respect to the momentum transfer direction and  $P_l^i$  are associated Legendre polynomials. The tensor polarization observables,  $T_{ij}$  are written in term of the electromagnetic form factors as

$$\begin{aligned} T_{20} &= -\frac{1}{\sqrt{2}R_0} \left[ \frac{8}{3} \eta G_C(Q^2) G_Q(Q^2) + \frac{8}{9} \eta^2 G_Q^2(Q^2) + \frac{1}{3} \eta \left( 1 + 2(1 + \eta) \tan^2 \left( \frac{\theta_e}{2} \right) \right) G_M^2(Q^2) \right] \\ T_{22} &= -\frac{1}{2\sqrt{3}R_0} \eta G_M^2(Q^2) \\ T_{21} &= -\frac{2}{\sqrt{3}R_0} \eta \left[ \eta + \eta(1 + \eta) \tan^2 \left( \frac{\theta_e}{2} \right) \right]^{\frac{1}{2}} G_M(Q^2) G_Q(Q^2) \end{aligned} \quad (2.57)$$

Since it is the largest of the three tensor polarization observables,  $T_{20}$  is typically the third elastic scattering observable of choice used to separate  $G_C$ ,  $G_M$  and  $G_Q$ . Figures 2-7, 2-8 and 2-9 show the world's data on the unpolarized elastic scattering observables  $A(Q^2)$  and  $B(Q^2)$  and tensor polarized observable  $T_{20}(Q^2)$  compiled by the Jefferson Lab  $T_{20}$  collaboration [62, 67]. The availability of high precision  $T_{20}$  data is still lacking. The precision in the determination of  $G_C$ ,  $G_M$  and  $G_Q$  form factors is limited by the inadequate knowledge of the  $T_{20}$  polarization observable.

---

<sup>12</sup>The electron beam's polarization is taken to be zero for simplicity of discussion.

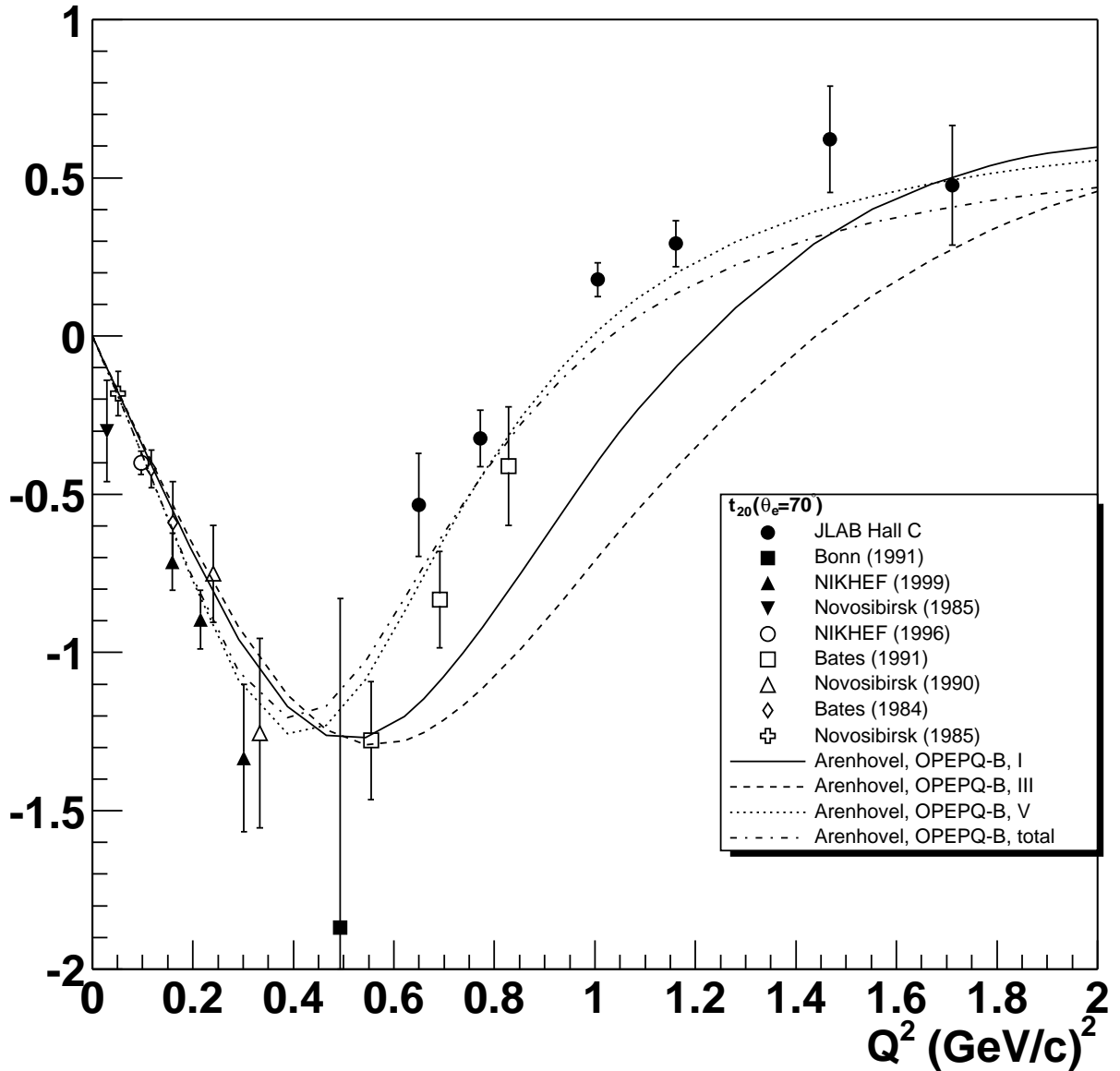


Figure 2-9: World's data for the  $T_{20}(Q^2)$ . The data were compiled by the Jefferson Lab Hall C  $T_{20}$  collaboration [67] from [62, 68, 69, 70, 71, 72, 73, 74, 75]. The curves are theoretical predictions based on the Bonn OBEPQ-B potential [64] with non relativistic nucleon current (solid), relativistic nucleon current(dashed), relativistic nuclear currents and  $\pi$ -meson exchange currents (dotted), relativistic nuclear current and  $\pi$ ,  $\rho$  and heavy meson exchange currents (dot-dashed).

### 2.3.4 Extraction of the Elastic Form Factor of the Neutron from the Elastic Form Factors of the Deuteron

In the non-relativistic limit and in the absence of exchange currents, the electromagnetic form factors of the deuteron can be expressed in terms of the isoscalar nucleon form factors  $G_i^s$  defined as

$$\begin{aligned} G_E^s &= \frac{1}{2}(G_E^p + G_E^n) \\ G_M^s &= \frac{1}{2}(G_M^p + G_M^n), \end{aligned} \quad (2.58)$$

weighted by the so-called *body form factors*,  $D_i$  [76, 49].

$$\begin{aligned} G_C(Q^2) &= G_E^s(Q^2)D_C(Q^2) \\ G_M(Q^2) &= \frac{m_d}{2m_p} \left\{ G_M^s(Q^2)D_M(Q^2) + G_E^s(Q^2)D_E(Q^2) \right\} \\ G_Q(Q^2) &= G_E^s(Q^2)D_Q(Q^2), \end{aligned} \quad (2.59)$$

where the body form factors are the Fourier transforms of the  $S$ - and  $D$ -wave function densities, defined as

$$\begin{aligned} D_C(Q^2) &= \int_0^\infty (u^2(r) + w^2(r))j_0(Qr)dr \\ D_M(Q^2) &= \int_0^\infty \left[ (2u^2(r) - w^2(r))j_0(Qr) + (\sqrt{2}u(r)w(r) + w^2(r))j_2(Qr) \right] dr \\ D_E(Q^2) &= \frac{3}{2} \int_0^\infty [j_0(Qr) + j_2(Qr)] w^2(r)dr \\ D_Q(Q^2) &= \int_0^\infty w(r) \left( u(r) - \frac{w(r)}{\sqrt{8}} \right) j_2(Qr)dr. \end{aligned} \quad (2.60)$$

In the static limit, as  $Q^2 \rightarrow 0$ , the body form factors are determined by the static properties of the deuteron in eqns. 2.48, 2.49 and 2.50,

$$\begin{aligned} G_C(0) &= 1 \\ G_M(0) &= \frac{m_d}{m_p} \mu_d \\ G_Q(0) &= m_d^2 Q_d. \end{aligned} \quad (2.61)$$

Figure 2-10 shows contributions from  $G_C$ ,  $G_M$  and  $G_Q$  to the  $A(Q^2)$  observable, calculated by Arenhövel using the Bonn potential. At low momentum transfer the contribution from

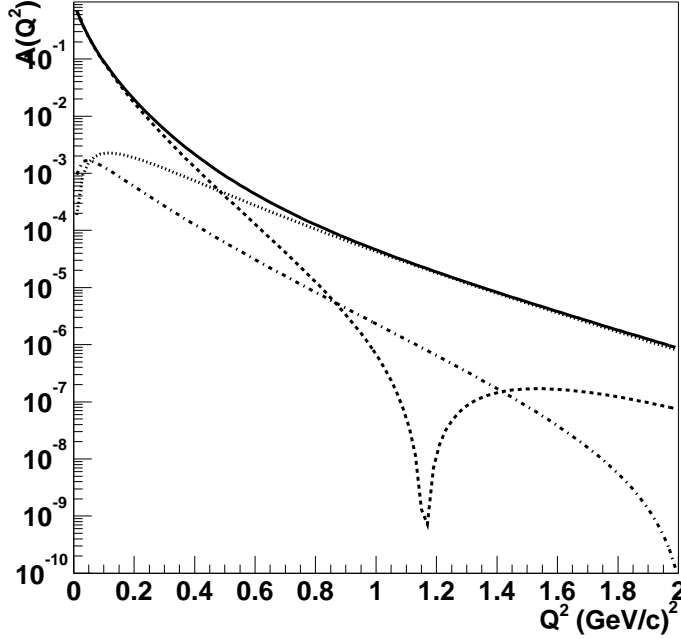


Figure 2-10: Contribution to the observable  $A(Q^2)$  (solid line) from  $G_C$  (dashed),  $G_M$  (dotted) and  $G_Q$  (dot-dashed) using the Bonn OBEPQ-B Total potential [50].

the charge form factor,  $G_C$  dominates by several orders of magnitude the contributions from  $G_M$  and  $G_Q$ . Thus, by measuring  $A(Q^2)$  one can infer the value for the isoscalar nucleon form factor,  $G_E^s$ . By using the fact that  $G_E^p$  is a well known quantity in this  $Q^2$  region, it is possible to deduce the value of the neutron elastic form factor,  $G_E^n$ . Since this measurement involves a calculation of the body form factors, the extraction of  $G_E^n$  from  $A(Q^2)$  depends heavily on the choice of a nucleon-nucleon potential. Also, relativistic corrections and meson exchange currents have to be handled correctly in this calculation.

The first such analysis was done by Galster *et al* [59]. Using the best available potential in 1971, Galster and collaborators extracted the best fit to their parametrization of choice for  $G_E^n$  (known as the *Galster parametrization*). The resulting Galster form is

$$G_E^{Galster,n} = -\frac{\mu_n \tau}{1 + b\tau} G_D, \quad (2.62)$$

where  $\mu_n$  is the magnetic moment of the neutron,  $b$  is an arbitrary fit parameter and  $G_D$  is the dipole form factor. The best fit was obtained for  $b = 5.6$  using the Feshbach-Lomon potential.

It is worth noting that the Galster formulation of the neutron electric form factor is purely phenomenological and has no physical meaning. However, it seems to fit the data rather well. It predicts behavior at low  $Q^2$  corresponding to the neutron's mean charge radius squared of

$$\langle r_n^2 \rangle_{Galster}^{ch} = -6 \frac{dG_E^n}{dQ^2} \Big|_{Q^2=0} = \frac{3\mu_n}{2M_n^2} = -0.125 fm^2.$$

This value coincides with the value of the Foldy term,  $\langle r_{Foldy,n}^2 \rangle = -0.126 fm^2$ . However, it seems to be in contradiction to the best experimental value of the neutron radius. Table I in reference [77] summarizes the best known experimental data for the charge radius of the neutron, determined from scattering of thermal neutrons by atomic electrons. Although, some discrepancy remains between these data, the best experimental value of the charge radius is [77]

$$\langle r_n^2 \rangle_{exp}^{ch} = -0.115 \pm 0.003 \pm 0.004.$$

This type of an analysis was extended by Platchkov and collaborators [58] in 1990. By using more modern potentials and introducing a second multiplicative fitting parameter,  $a$  to the Galster formula, they refitted the existing and newly measured  $A(Q^2)$  data to the Platchkov's  $G_E^n$  parametrization, expressed as

$$G_E^{Platchkov,n} = -a \frac{\mu_n \tau}{1 + b\tau} G_D, \quad (2.63)$$

An introduction of a second fit parameter had produced a better fit. The result of the fit varied greatly with the choice of a nucleon-nucleon potential, as can be seen from fig. 2-11. The most commonly quoted values of  $a = 1.25 \pm 0.13$  and  $b = 18.3 \pm 3.4$  were obtained with the Paris potential. However, this fit violates the low  $Q^2$  behavior governed by the neutron charge radius measurements<sup>13</sup>. The value of  $a = 0.98$  is the closest to the correct  $Q^2 = 0$  slope, extracted with the Reid Soft Core (RSC) potential. All of these parameters carry a strong theoretical uncertainty due to the lack of a precise knowledge of

---

<sup>13</sup>A value of  $a = 0.90$  is required for the Platchkov parametrization to correctly match the slope at  $Q^2 = 0$  predicted by the the neutron charge radius [77].

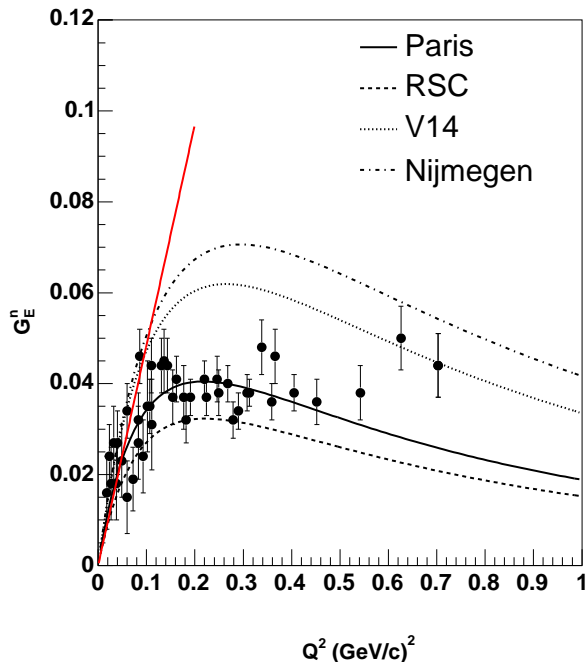


Figure 2-11: Platchkov et al. best fit [58] results for  $G_E^n$  (circles) from the  $A(Q^2)$  data using Paris potential. The curves represent the values of  $G_E^n$  derived from  $A(Q^2)$  data using various potentials. The thin red line has the slope according to the neutron's charge radius as measured by the thermal neutron scattering [77].

the nucleon-nucleon potential.

Recently, Schiavilla and Sick used the world's data on the elastic quadrupole form factor of the deuteron to determine  $G_E^n$  [78] over a larger  $Q^2$  range. At large momentum transfer,  $G_C$  and  $G_Q$  have equal strength, hence model dependence becomes even stronger. The authors tried to avoid this problem by using only data on the electric quadrupole form factor. However, the major difficulty with this analysis at large  $Q^2$  is the lack of high precision  $T_{20}$  data. Also, some model dependence remains, as noted by the authors.

Due to the theoretical difficulties, the measurements of the neutron's electric form factor from elastic electron-deuteron scattering have not produced results matching the precision of other nucleon elastic form factors. Also, this measurement is limited to a small region of momentum transfer. There is a possibility that better knowledge of the individual elastic electromagnetic form factors of the deuteron can constrain  $G_E^n$  with less uncertainty. How-

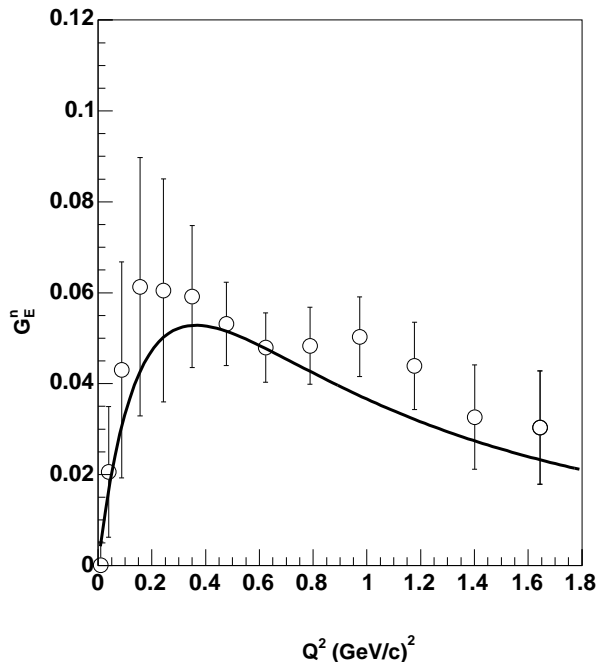


Figure 2-12:  $G_E^n$  extraction by Schiavilla and Sick (circles) along with the Galster parametrization (solid line).

ever, a far more effective and less model dependent method to measure  $G_E^n$  over a larger momentum transfer range is by using polarized quasielastic scattering on deuterium.

## 2.4 Polarized Quasielastic Electron-Deuteron Scattering

Quasielastic scattering refers to the scattering of a lepton from a single nucleon inside of an  $A \geq 2$  nuclear system, where either the lepton is detected alone (*inclusive*) or in coincidence with a recoiling nucleon (*exclusive*). In the *Born Approximation*, the incoming lepton exchanges a single virtual photon with the nucleon inside of the nucleus. If the momentum transfer is large enough the scattering can be described by the *Plane Wave Impulse Approximation* (PWIA) in which the knocked-out nucleon does not interact with the spectator  $A - 1$  recoil system which is not involved in reaction. However, the PWIA turns out to

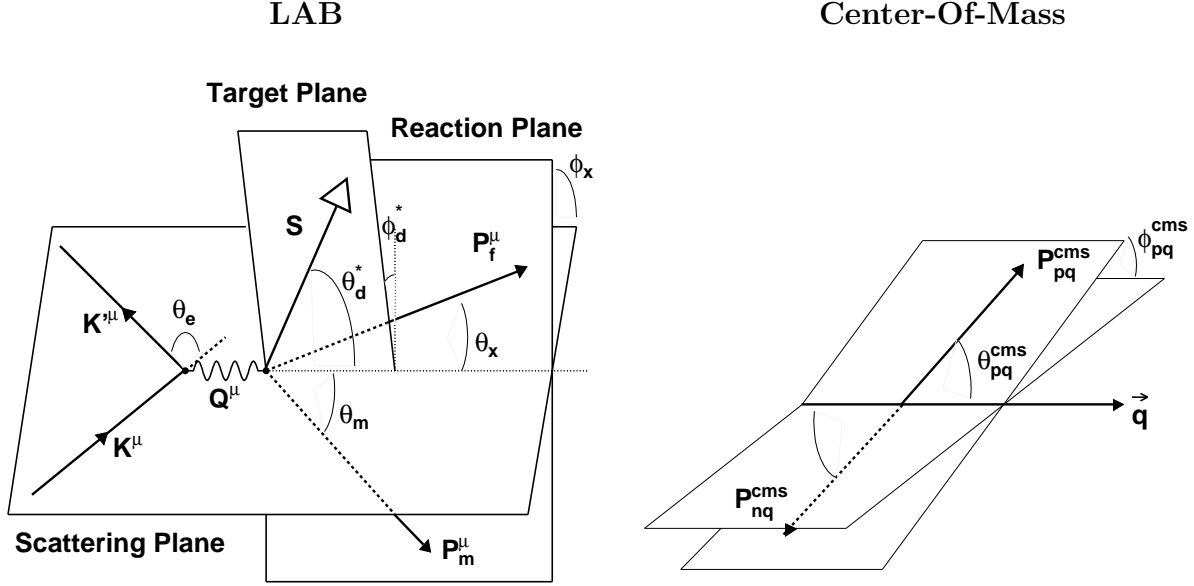


Figure 2-13: Schematic representation of the polarized quasielastic scattering.

be a crude approximation especially in the medium energy scattering regime. At the same time the assumption of the PWIA is not required to work out a full quasielastic scattering formalism. The formalism developed by Arenhövel et al. [79] for the electro-disintegration of the deuteron is followed in this section. This treatment includes the initial motion of the nucleon inside of the deuterium nucleus and the interactions between the recoil nucleons.

As in the case of the elastic scattering from a nucleon, the four-momentum of the virtual photon is  $Q^\mu = (\omega, \vec{q}) = K^\mu - K'^\mu = (\mathcal{E} - \mathcal{E}', \vec{k} - \vec{k}')$ . However, it can no longer be assumed that the nucleon is originally at rest. Hence, the three-momentum and the energy of the recoil nucleon detected in coincidence with the scattered electron is defined as

$$\begin{aligned}\vec{p}_f &= \vec{q} - \vec{p}_m \\ E_f &= M_d + \omega - E_m,\end{aligned}\tag{2.64}$$

where,  $f$  corresponds to a neutron or proton detected in the final state,  $\vec{p}_m$  and  $E_m$  are the momentum and energy of the recoil system which is not measured<sup>14</sup>. The energy of the undetected recoil system is

$$E_m = \sqrt{M_r^2 + p_m^2} + \mathcal{E}^*,\tag{2.65}$$

<sup>14</sup>These quantities are usually referred to as missing momentum and missing energy.

where  $M_r$  is the mass of the recoil system and  $\mathcal{E}^*$  is its excitation energy. In the deuterium two-body break up, where the undetected recoil nucleon is in the ground state, the excitation energy is simply the binding energy of a target nucleus,  $\mathcal{E}^* = E_b = 2.2$  MeV and the missing mass is simply the mass of the undetected nucleon,  $M_m = M_r$ .

The kinematic condition corresponding to the center of the *quasielastic peak* is characterized by the relation

$$\omega = \frac{Q^2}{2M_i} \quad (2.66)$$

At the top of the quasielastic peak the undetected recoil nucleon is at rest before and after the quasielastic knock-out. However, it would be a mistake to think that the top of the quasielastic peak corresponds to the PWIA reaction, since the effects of the initial and final state interactions are present in all kinematic regimes.

In the electro-disintegration reaction the virtual photon can be absorbed by either the proton or the neutron. A more natural way to describe the kinematics of either nucleon being knocked out is consider the opening angle of a cone created by  $\vec{p}_f$  around  $\vec{q}$ . In the lab frame, this angle is defined as

$$\cos \theta_{pq} = \frac{q^2 + p_f^2 - p_m^2}{2qp_f}, \quad (2.67)$$

where  $\theta_{pq}$  can be Lorentz boosted into the *final state center-of-mass frame* where the cross section is evaluated [79]. In the center-of-mass frame the sum of all hadronic momenta is zero,  $\vec{p}_p + \vec{p}_n = 0$ . Please see Appendix A for the discussion of rotations and boosts from the lab (BLAST) frame into a *q-cms* inertial reference frame. The convenience of this kinematic quantity is that it describes simultaneously the quasielastic scattering on the proton and the neutron. That is,  $\theta_{pq}^{cms} = 0^\circ$  kinematics corresponds to the quasielastic knock-out of the proton and  $\theta_{pq}^{cms} = 180^\circ$  corresponds to the quasielastic neutron knock-out.

The final hadronic state is characterized by the kinetic energy of the final state system,  $E_{np}$ , defined as

$$E_{np} = W - M_n - M_p, \quad (2.68)$$

where  $W$  is the invariant mass defined in the lab system as

$$W = \sqrt{(\omega + M_d)^2 - \vec{q}^2}. \quad (2.69)$$

### 2.4.1 Differential Cross Section For Polarized Electro-Disintegration of the Deuteron

The derivation of the exclusive differential cross section for the electro-disintegration of the deuteron reaction follows all of the same steps outlined earlier for polarized elastic e-p scattering. However, since the final hadronic state consists of two nucleons, the phase space in which the cross section is defined is larger. The exclusive differential cross section is defined in the five-dimensional phase space ( $\omega$ ,  $\Omega_e$ , and  $\Omega_{pq}^{ems}$ ), due to the detected nucleon which is not integrated over in the final state. The additional nucleon vector in the final state introduces another kinematic plane, denoted as the *Reaction Plane* in fig. 2-13. The hadronic tensor is now expressed in terms of 41 structure functions representing 35 helicity amplitudes. It was shown [80] that these 35 helicity amplitudes represent the complete set of all polarization observables in the exclusive electro-disintegration of deuterium. The structure functions  $f_{\mu\mu}^{(\prime)IM}$  ( $\mu \in \{L, T\}$ ) contain the complete information about the dynamical structure of the transition from the deuteron to the final n-p system.

Similarly to the case of polarized elastic electron-nucleon scattering, the differential cross section is written in terms of the target polarization vector. The direction of the target polarization vector is rotated into the reaction plane introduced in eqn. 2.25 by

$$\vec{P}_{IM}^d = P_I^d e^{iM\phi_d^*} d_{M0}^I(\theta_d^*), \quad (2.70)$$

where  $\theta_d^*$  and  $\phi_d^*$  are the target polarization angles with respect to the scattering plane, where  $\hat{z}$  is in the direction of  $\vec{q}$ . The  $d_{M0}^I$  are the rotation matrices defined in eqn. 2.80.  $P_I^d$  is the deuterium target polarization tensor, written as

$$P_I^d = \delta_{I,0} + \sqrt{\frac{3}{2}} P_z \delta_{I,1} + \sqrt{\frac{1}{2}} P_{zz} \delta_{I,2}, \quad (2.71)$$

where  $I = \pm 1, 2$  and  $P_z$ ,  $P_{zz}$  are the vector and tensor polarizations respectively.

The differential cross section naturally breaks up into the components of the target polarization tensor in eqn. 2.71. The full differential cross section can be expressed as [79]

$$\frac{d^5\sigma}{d\omega d\Omega_e^{lab} d\Omega_{pq}^{cms}} = S(h, P_z, P_{zz}) = S(0, 0, 0) \left\{ 1 + \sqrt{\frac{3}{2}} P_z A_d^V + \sqrt{\frac{1}{2}} P_{zz} A_d^T + h \left( A_e + \sqrt{\frac{3}{2}} P_z A_{ed}^V + \sqrt{\frac{1}{2}} P_{zz} A_{ed}^T \right) \right\}, \quad (2.72)$$

where the unpolarized cross section  $S(0, 0, 0)$  and the asymmetries,  $A_i^j$  can be obtained in terms of the structure functions,  $f_{\mu\mu}^{(\prime)IM}$

$$S(0, 0, 0) = c \left\{ \rho_L f_L + \rho_T f_T + \rho_{LT} f_{LT} \cos \phi_{pq}^{cms} + \rho_{TT} f_{TT} \cos 2\phi_{pq}^{cms} \right\} \quad (2.73)$$

$$A_e = \frac{c}{S_0} \rho'_{LT} f'_{LT} \sin \phi_{pq}^{cms} \quad (2.74)$$

$$A_d^V = \frac{c}{S_0} \sum_{M=0}^1 [(\rho_L f_L^{1M} + \rho_T f_T^{1M} + \rho_{LT} f_{LT}^{1M+} \cos \phi_{pq}^{cms} + \rho_{TT} f_{TT}^{1M+} \cos 2\phi_{pq}^{cms}) \sin M\tilde{\phi} + (\rho_{LT} f_{LT}^{1M-} \sin \phi_{pq}^{cms} + \rho_{TT} f_{TT}^{1M-} \sin 2\phi_{pq}^{cms}) \cos M\tilde{\phi}] d_{M0}^1(\theta_d^*) \quad (2.75)$$

$$A_d^T = \frac{c}{S_0} \sum_{M=0}^2 [(\rho_L f_L^{2M} + \rho_T f_T^{2M} + \rho_{LT} f_{LT}^{2M+} \cos \phi_{pq}^{cms} + \rho_{TT} f_{TT}^{2M+} \cos 2\phi_{pq}^{cms}) \cos M\tilde{\phi} - (\rho_{LT} f_{LT}^{2M-} \sin \phi_{pq}^{cms} + \rho_{TT} f_{TT}^{2M-} \sin 2\phi_{pq}^{cms}) \sin M\tilde{\phi}] d_{M0}^2(\theta_d^*) \quad (2.76)$$

$$A_{ed}^V = \frac{c}{S_0} \sum_{M=0}^1 [(\rho'_T f_T^{1M} + \rho'_{LT} f_{LT}^{1M-} \cos \phi_{pq}^{cms}) \cos M\tilde{\phi} - \rho'_{LT} f_{LT}^{1M+} \sin \phi_{pq}^{cms} \sin M\tilde{\phi}] d_{M0}^1(\theta_d^*) \quad (2.77)$$

$$A_{ed}^T = \frac{c}{S_0} \sum_{M=0}^2 [(\rho'_T f_T^{2M} + \rho'_{LT} f_{LT}^{2M-} \cos \phi_{pq}^{cms}) \sin M\tilde{\phi} + \rho'_{LT} f_{LT}^{2M+} \sin \phi_{pq}^{cms} \cos M\tilde{\phi}] d_{M0}^2(\theta_d^*) \quad (2.78)$$

$$c = \frac{\alpha \mathcal{E}'}{6\pi^2 \mathcal{E} Q^4}, \quad (2.79)$$

where  $S_0 = S(0, 0, 0)$ ,  $\phi_{pq}^{cms}$  is the angle between the scattering and reaction planes. The angle  $\tilde{\phi}$  is defined as  $\tilde{\phi} = \phi_{pq}^{cms} - \phi_d^*$  (see fig 2-13). The virtual photon density matrices  $\rho_{\mu\mu}^{(\prime)IM}$  are introduced earlier in eqn. 2.28<sup>15</sup>.

---

<sup>15</sup>Here, the Lorentz boost is done into the center-of-mass frame, not the Breit frame. The Lorentz boost constant,  $\beta$ , is expressed as  $\beta = \frac{|\vec{q}^{ab}|}{|\vec{q}^{cms}|}$ .

The elements of the rotation matrix,  $d_{M0}^I$  are defined as

$$\begin{aligned}
d_{00}^1(\theta_d^*) &= \cos\theta_d^* & , & \quad d_{00}^2(\theta_d^*) = \frac{1}{2}(3\cos^2\theta_d^*) - 1 \\
d_{10}^1(\theta_d^*) &= -\sqrt{\frac{1}{2}}\sin\theta_d^* & , & \quad d_{10}^2(\theta_d^*) = -\sqrt{\frac{3}{2}}\cos\theta_d^*\sin\theta_d^* \\
& & & \quad d_{20}^2(\theta_d^*) = \frac{\sqrt{6}}{4}\sin^2\theta_d^*
\end{aligned} \tag{2.80}$$

In the Plain Wave Born Approximation (PWBA)<sup>16</sup>, the asymmetries  $A_d^V$  and  $A_{ed}^T$  are expected to equal zero, since these polarization observables are T-odd imaginary combinations of the deuteron electromagnetic current. However, with the addition of the final state interactions these quantities can acquire small, non-zero values.  $A_e$  is expected to be small, especially because in this experiment, all observables are integrated over all out-of-plane angles, thus  $\langle \sin\phi_{pq}^{cms} \rangle = 0$ .

The two significant polarization observables are  $A_{ed}^V$  and  $A_d^T$ . The tensor polarization observable,  $A_d^T$  is sensitive to the  $D$ -wave component of the deuteron wave function. It is expected to be small at low missing momentum<sup>17</sup>, where the  $S$ -wave dominates the total wave function.  $A_d^T$  becomes larger as the missing momentum increases.

The vector asymmetry,  $A_{ed}^V$  is sensitive to both  $S$ - and  $D$ -waves of the deuteron. At low missing momentum the proton and neutron are both in the  $S$ -state. In this state the spins of both nucleons point in the direction of the deuteron spin. Hence, both the proton and neutron in the deuterium target are polarized in the same direction as the target. However, as the missing momentum increases, the  $D$ -wave starts to contribute to the total wave function 2-6. In the  $D$ -state the spins of the nucleons must be anti-parallel to the spin of the deuteron in order to conserve total angular momentum. Thus, the direction of the nucleon polarization becomes opposite to the nuclear polarization. Correspondingly, the average projection of the nucleon spin along the quantization axis defined by the polarization vector of the target is expressed as

$$P_z^N(p_m) = \frac{\rho_S(p_m) - \rho_D(p_m)}{\rho_S(p_m) + \rho_D(p_m)}. \tag{2.81}$$

A graph of  $P_z^N(p_m)$  using the Bonn potential is plotted in fig. 2-14. It is safe to assume

---

<sup>16</sup>PWBA is defined as the PWIA in one photon exchange approximation.

<sup>17</sup>Missing momentum in this context is equivalent to the momentum of the nucleons due to the Fermi motion inside of the nucleus.

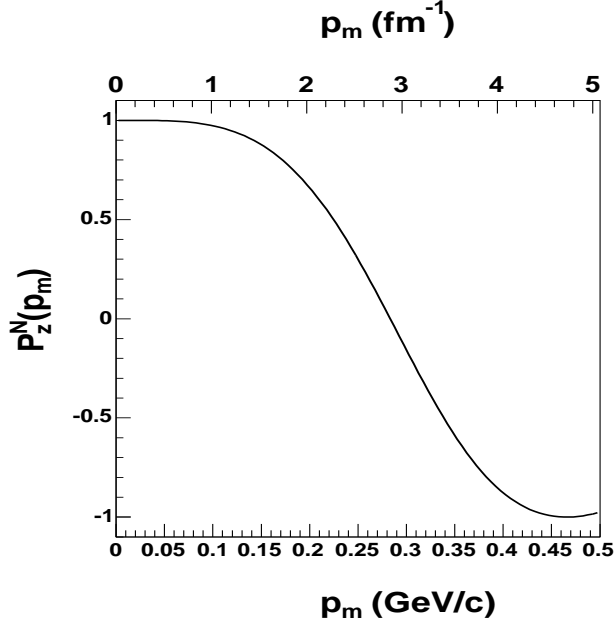


Figure 2-14: Average projection of the nucleon spin vector with respect to the deuterium target polarization vector.  $P_z^N(p_m)$  is calculated using the Bonn probability density functions,  $\rho_S(p)$  and  $\rho_D(p)$  (see fig. 2-6).

that the spin vector of the nucleon inside of deuteron is in the direction of the deuterium target polarization vector up to a missing momentum of 0.2 (GeV/c).

### 2.4.2 Extraction of $G_E^n$ from the ${}^2\vec{H}(\vec{e}, e'n)p$ Reaction

The influence of the neutron electric form factor on the polarized observables in the deuterium break-up reaction was originally investigated by Arenhövel, Leidemann and Tomusiak [38]. They found that the beam-target vector asymmetry in the perpendicular kinematics,  $A_{ed}^V(\theta_d^* = \frac{\pi}{2}, \phi_d^* = 0)$  was most sensitive to  $G_E^n$ . In the PWBA, electron scattering on the deuterium target can be approximated as an electron scattering on a single nucleon inside of the deuteron, where the nucleons do not interact with each other in the final state. The quasielastic proton knockout approximation corresponds to a center-of-mass angle,  $\theta_{pq}^{cms}$  of zero degrees. In the quasi-free neutron knockout approximation,  $\theta_{pq}^{cms} = 180^\circ$ . In this ap-

proximation  $A_{ed}^V(\frac{\pi}{2}, 0)$  becomes simply

$$\begin{aligned}
 A_{ed}^V(\frac{\pi}{2}, 0) &= -\frac{2\sqrt{2}\tau\rho'_{LT}G_E^n G_M^n}{\rho_L(G_E^n)^2 + 2\tau\rho_T(G_M^n)^2} & \left\{ \begin{array}{l} \text{for } \theta_{pq} = 180^\circ \\ \\ \text{for } \theta_{pq} = 0^\circ \end{array} \right. \\
 A_{ed}^V(\frac{\pi}{2}, 0) &= -\frac{2\sqrt{2}\tau\rho'_{LT}G_E^p G_M^p}{\rho_L(G_E^p)^2 + 2\tau\rho_T(G_M^p)^2} & \left\{ \begin{array}{l} \\ \\ \end{array} \right.
 \end{aligned} \tag{2.82}$$

This formula is identical to the perpendicular beam-target vector asymmetry from the elastic electron-proton scattering on a polarized hydrogen target,  $A_{eN}^\perp$  in eqn. 2.41 . Figure 2-15 shows a comparison between  $A_{e,p}^\perp$  and  $A_{ed}^V(\frac{\pi}{2}, 0)$  at  $\theta_{pq}^{cms} = 0^\circ$  in the PWBA approximation. This comparison shows that in the approximation described above, the observable  $A_{ed}^V(\frac{\pi}{2}, 0)$

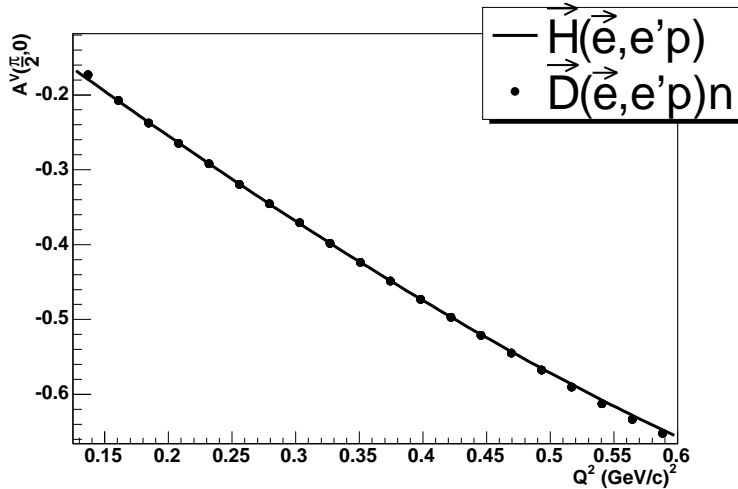


Figure 2-15: Comparison of theoretical  $A_{e,p}^\perp$  from  ${}^1\vec{H}(\vec{e}, e'p)$  (line) and  $A_{ed}^V(\frac{\pi}{2}, 0)$  from  ${}^2\vec{H}(\vec{e}, e'p)n$  (points). The asymmetry from the  $\vec{D}(\vec{e}, e'p)n$  reaction is taken at  $\theta_{pq}^{cms} = 0^\circ$  corresponding to a purely quasielastic scattering. The hydrogen asymmetry is calculated using Höhler [18] form factors and the deuterium asymmetry is calculated by Arenhövel et al. [79] using Bonn potential and PWBA formalism.

in the polarized electro-disintegration of deuterium where the proton is detected indeed follows the form predicted by the electromagnetic form factors of the proton. Analogously, the neutron asymmetry should follow the form factors of the neutron. This fact can be used in order to extract  $G_E^n/G_M^n$ .

Figure 2-16 shows the sensitivity to  $G_E^n$  at three out of five  $Q^2$  kinematic points considered in this work. The sensitivity increases near the quasielastic peak at  $\theta_{pq}^{cms} = 180^\circ$ . Away from the quasielastic kinematics the sensitivity rapidly gets smaller and completely disappears.

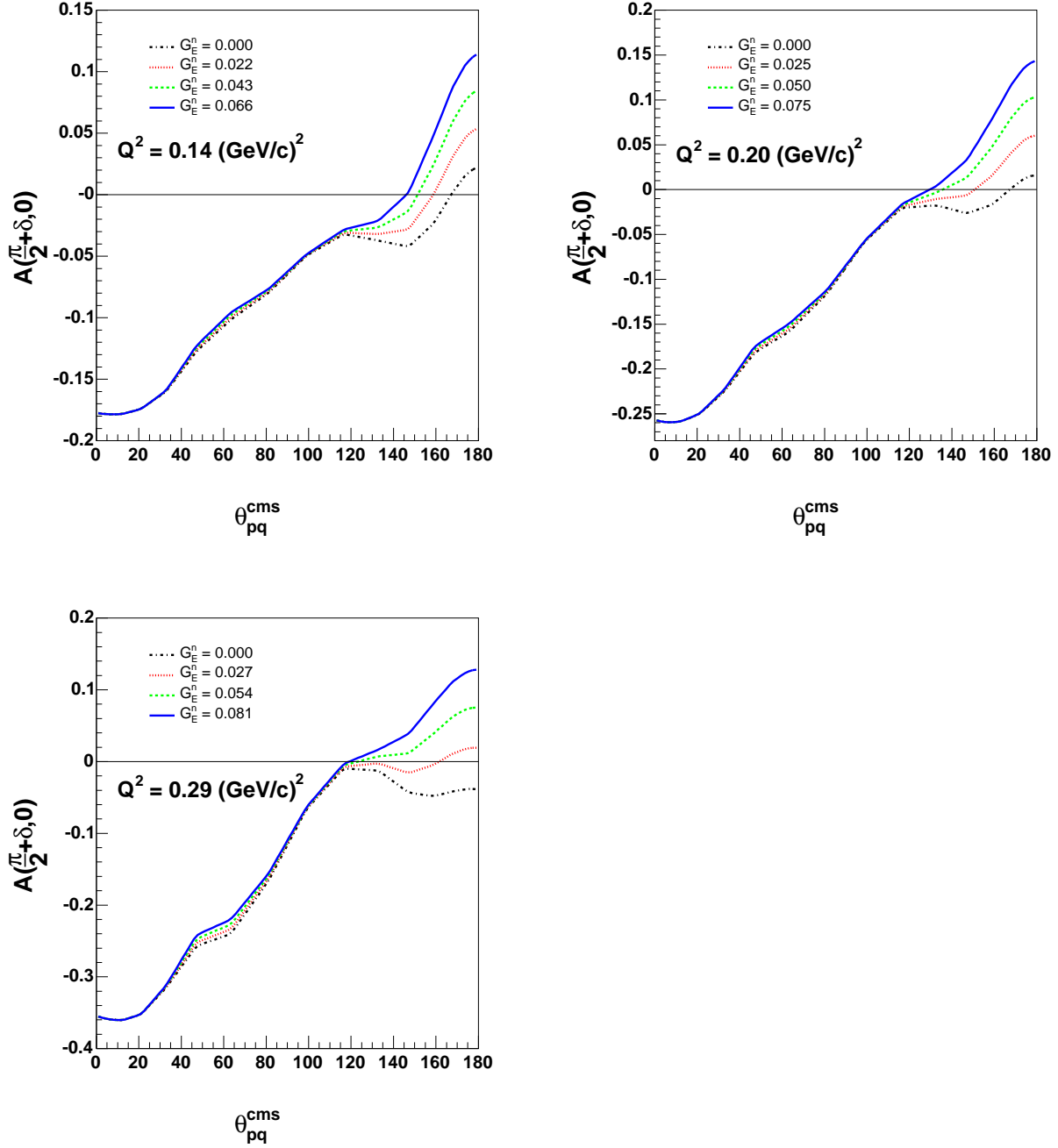


Figure 2-16: The spin-correlation parameter  $A_{ed}^V(\frac{\pi}{2}, 0)$  as a function of  $\theta_{pq}^{cms}$  for  $Q^2 = 0.14$  (top left),  $0.2$  (top right) and  $0.29$   $(\text{GeV}/c)^2$  (bottom). The angle of the target polarization is fixed at  $32^\circ$ , while the three-momentum transfer angle is changing with  $Q^2$ . Hence, angle,  $\theta_d^*$ , is not precisely set to  $\frac{\pi}{2}$ , but varies by small amount  $\delta = 10^\circ, 2^\circ$  and  $-3^\circ$  in each  $Q^2$  bin, respectively. The calculations were performed by Arenhövel using the Bonn potential. The Final state interactions (FSI), Meson Exchange Currents (MEC) and Isobar-Currents (IC) are included in the calculations.

Equation 2.82 indicates that in the PWBA the  $A_{ed}^V(\frac{\pi}{2}, 0)$  would vanish when  $G_E^n$  is zero. However, this is not true when the final and initial state interactions are considered. Also, as  $Q^2$  varies across the BLAST acceptance the perpendicular kinematics condition is slightly violated and  $\theta_d^*$  is no longer at exactly  $90^\circ$ . In this case the parallel asymmetry term, proportional to  $(G_M^n)^2$ , starts to contribute. Since the value of  $G_E^n$  is an order of magnitude smaller than that of  $G_M^n$ , any contribution from the parallel asymmetry is significant.

The quasielastic scattering on the neutron, even at the top of the quasielastic peak, where  $\theta_{pq}^{cms} = 180^\circ$ , is very sensitive to the reaction mechanism corrections. The largest correction is from the Final State Interactions (FSI). Other corrections include Meson Exchange Currents (MEC), Isobar-Currents (IC) and Relativistic Corrections (RC).

Figure 2-17 represents the reaction model dependence of  $A_{ed}^V(\frac{\pi}{2}, 0)$ . At the lowest momentum transfer,  $Q^2 = 0.14$  (GeV/c)<sup>2</sup>, the PWBA prediction deviates from the full model by almost 50% at  $\theta_{pq}^{cms} = 180^\circ$ . It is clear that the FSI play an important role in the asymmetry observables. At the same time, the MEC, IC and RC are small at this kinematic point. At  $Q^2 = 0.2$  (GeV/c)<sup>2</sup> the FSI become less of a factor at  $\theta_{pq}^{cms} = 180^\circ$ . However, FSI becomes more important as  $\theta_{pq}^{cms}$  moves away from  $180^\circ$ . At these kinematics inclusion of the MEC, IC and RC starts to significantly change the calculated asymmetry from the results for quasielastic kinematics. This trend continues at the  $Q^2 = 0.29$  (GeV/c)<sup>2</sup> kinematics. Here the PWBA and PWBA+FSI curves converge at the quasielastic peak. Away from the quasielastic peak, the MEC and IC modify values of the calculated asymmetry. The same follows for higher  $Q^2$  kinematic points.

Since the quasielastic cross section peaks strongly at  $\theta_{pq}^{cms} = 180^\circ$ <sup>18</sup>, the effects of the reaction mechanisms (MEC, IC and RC) on the vector polarization observable are small compared with sensitivity of the asymmetry to the size of  $G_E^n$ . However, the  $G_E^n$  measurements have to rely heavily on Arenhövel's description of the Final State Interactions.

At the same time the spin-correlation parameter  $A_{ed}^V(\frac{\pi}{2}, 0)$  is not sensitive to the choice of the nucleon-nucleon models, i.e. Bonn, Paris, V18 and V14 potentials (see fig. 2-18). Thus, the dependence on the choice of the potential which severely limited the precision of the Platchkov analysis, plays no role in the quasielastic scattering analysis.

---

<sup>18</sup>In fact the cross section peaks at  $\sim 175^\circ$  since the cross section is multiplied by the Jacobian which goes as  $\sin\theta_{pq}^{cms}$ . However, the Jacobian does alter the sensitivity to the reaction mechanism or  $G_E^n$ .

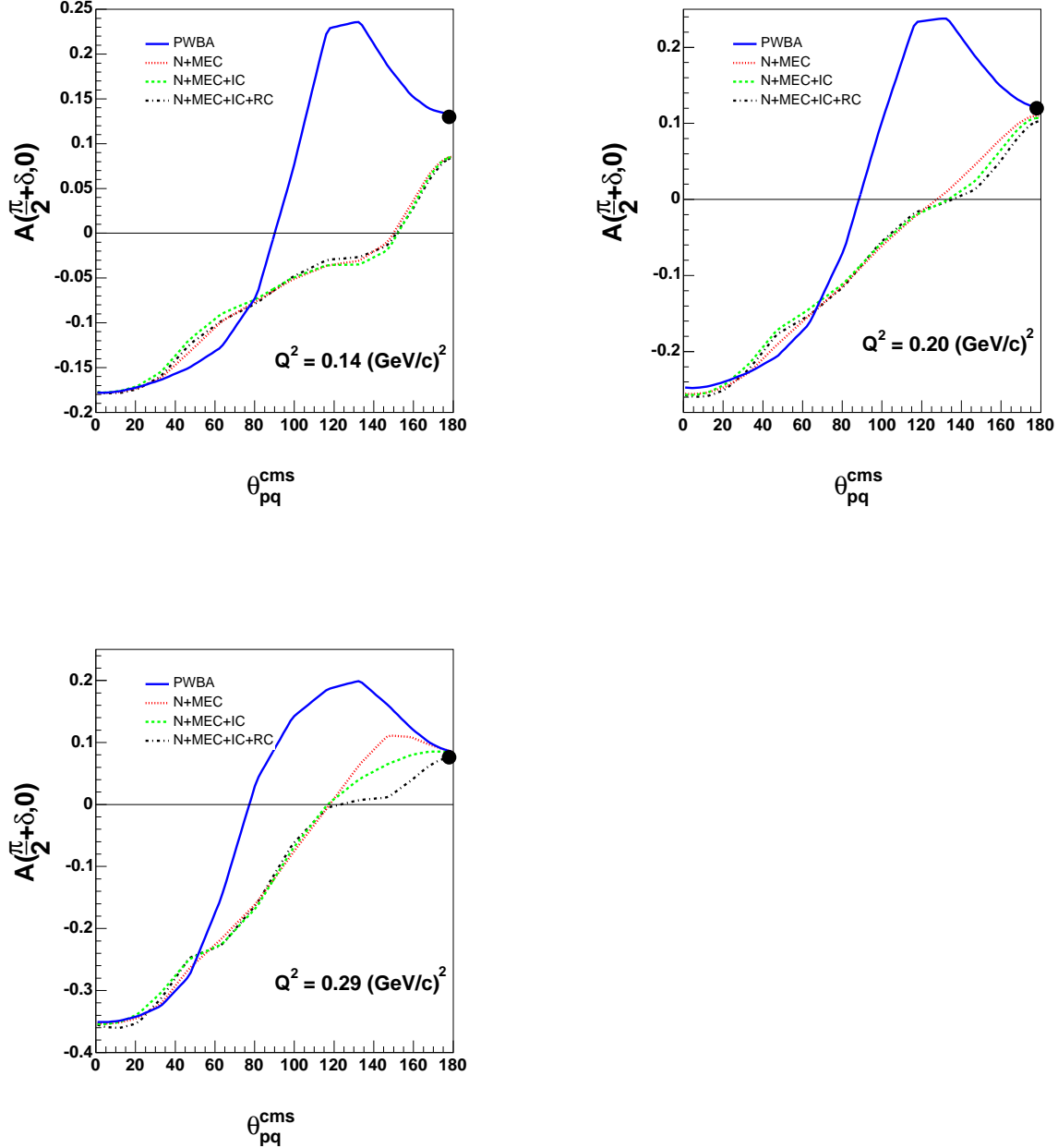


Figure 2-17: Effect of a reaction mechanism on the spin-correlation parameter  $A_{ed}^V(\frac{\pi}{2}, 0)$  for  $Q^2 = 0.14$  (top left),  $0.2$  (top right) and  $0.29 \text{ (GeV/c)}^2$  (bottom). Calculations were performed by Arenhövel for the BLAST kinematics using Bonn potential and  $G_E^n$  equals Galster. The solid circle represents the asymmetry from an electron-neutron elastic scattering with Galster-like neutron form factors. Model “N” is the PWBA+FSI.

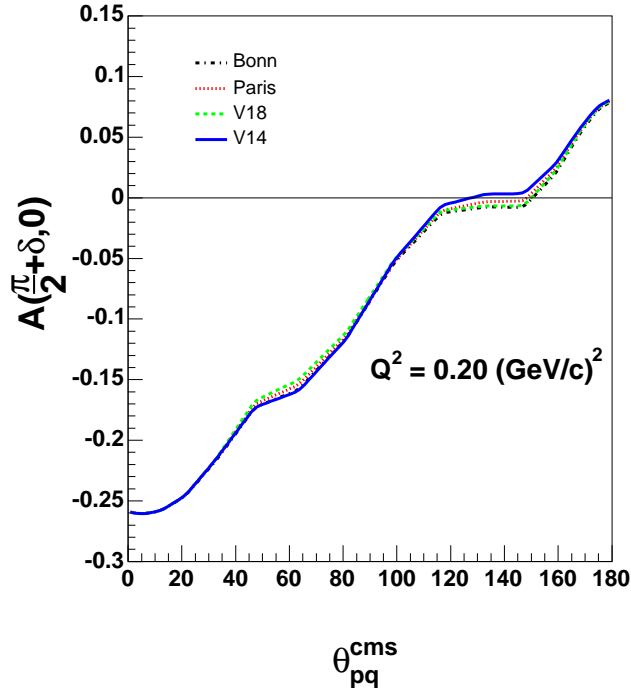


Figure 2-18: Effect of a N-N potential model on the spin-correlation parameter  $A_{ed}^V(\frac{\pi}{2}, 0)$  for  $Q^2 = 0.20 \text{ (GeV/c)}^2$ . Calculations were performed by Arenhövel for the BLAST kinematics using “Total” reaction mechanism and  $G_E^n$  equals Galster.

At  $\theta_{pq}^{cms} = 0$ ,  $A_{ed}^V$  shows little model or reaction mechanism dependence. This means that the quasielastic knock-out reaction on the proton inside of a deuteron is well described in terms of the electron-proton elastic scattering cross section. This allows the use of the  ${}^2\vec{H}(\vec{e}, ep)n$  reaction channel to measure a product of the beam and target vector polarizations,  $hP_z$ , with a high precision and little model uncertainty.

## 2.5 Theoretical Models of the Elastic Form Factors of the Nucleon

Ideally the internal electromagnetic structure of the nucleon should be calculated from the theory of the strong interactions, Quantum Chromo-Dynamics (QCD). So far, however, QCD has not been solved exactly. A large number of QCD inspired effective models were developed

over the past 30 years to describe the nucleon’s form factors at low  $Q^2$ . However, ab initio QCD calculations at low momentum transfer remain elusive. The overview of the theoretical models in this section uses a compilation of the latest model predictions in a review article by Gao [81]. The numerical values of the theoretical curves were compiled by Bradley Plaster [82].

### 2.5.1 Scaling and pQCD

Much work has been done to understand the electromagnetic form factors of the proton using the so-called perturbative QCD frame work. Perturbative QCD (pQCD) is the perturbation theory where the expansion is performed in terms of the strong coupling constant,  $\alpha_s$ . The parameter  $\alpha_s(Q^2)$  is a “running constant” that becomes small at a large momentum transfer.

In this framework, Brodsky and Farrar [83] developed the following scaling law governing the behavior of the Dirac and Pauli form factors,

$$F_1 \propto \frac{1}{Q^4} \quad \text{and} \quad F_2 \sim \frac{F_1}{Q^2}. \quad (2.83)$$

Using this scaling law the Sachs form factors have the same asymptotic behavior,  $G_{E,M} \sim 1/Q^4$ . The scaling predicts a constant Sachs form factor ratio,  $G_E^p/G_M^p$  at large  $Q^2$ .

Although the derivation of eqn. 2.83 was done using dimensional analysis, it was verified by a calculation using pQCD done by Brodsky and Lepage [84]. In their 1980 article they considered a proton in an infinite-momentum frame struck by a highly virtual photon with a large transverse momentum. The form factor is the probability of the proton to absorb a large transverse momentum while not breaking up. This probability is a product of three probability amplitudes: **a)** probability of finding a three-quark state in the proton, **b)** amplitude to produce a three-quark state with a collinear momenta and **c)** probability for the three-quark state to remain as a proton. In this framework the authors calculated the asymptotic behavior of the Sachs form factors of the proton.

$$G_m(Q^2) \rightarrow \frac{32\pi^2}{9} C \frac{\alpha_s^2(Q^2)}{Q^4} \left( \ln \frac{Q^2}{\Lambda^2} \right)^{-4/3\beta} (e_{||} - e_{-||}), \quad (2.84)$$

where  $\alpha_s$  and  $\Lambda$  are the strong coupling constants, and the exponent  $\beta = 11 - \frac{2}{3}n_{flavor}$ ,

where  $n_{flavor} = 3$  is the number of quark flavors in QCD.  $e_{||}$  and  $e_{-||}$  are the average charges of quarks with helicity parallel and anti-parallel to the spin of a nucleon, respectively. The average charges of the quarks inside the proton and neutron are

$$e_{||}^p = 1, \quad e_{-||}^p = 0, \quad e_{||}^n = e_{-||}^n = -\frac{1}{3} \quad (2.85)$$

Eqns. 2.84 and 2.85 predict at large  $Q^2$  that  $G_M^n/G_M^p = -2/3$ , assuming isospin-spin symmetry. The authors noted that this result is remarkably close to the value of  $\mu_n/(1 + \mu_p) = -0.685$ .

## 2.5.2 Lattice QCD

As mentioned before, the exact solution to the strong interaction theory is unattainable at this time. However, recently lattice QCD calculations present the possibility of determining observable properties of the nucleon from the full QCD Lagrangian [85]. Currently all lattice QCD calculations are done in the “heavy pion” regime. Initial efforts have been made to explore the chiral regime by extrapolating results from the “heavy pion” regime. However, the uncertainty in this extrapolation is rather large. Dunne et al. [86] were able to calculate the proton charge radius at the physical pion mass based on the lattice calculation in the “heavy pion” region, by expanding the charge radius around the chiral limit ( $m_\pi \rightarrow 0$ ).

$$\langle r_E \rangle = c_1 \pm \chi_N \log \frac{m_\pi}{\mu} + c_2 m_\pi^2, \quad (2.86)$$

where  $\mu$  is the mass scale and  $\chi_N = -(1 + 5g_A^2)/(4\pi f_\pi)^2$ , where  $g_A$  is the axial form factor and  $f_\pi$  is the pion decay constant. Ashley et al. [87] used the fact that in a dipole parametrization the mean square radius of a nucleon is defined in terms of the dipole fit parameter,  $\Lambda$  as

$$\langle r^2 \rangle = 12/\Lambda^2. \quad (2.87)$$

The authors used the present QCDSF lattice calculations [88] to fit for the dipole parameters,  $\Lambda$  for all nucleon form factors with a certain degree of success.

### 2.5.3 Dispersion Theory

Effective field theories of the strong interaction have been more successful, to date, in describing nucleon electromagnetic structure at medium and low momentum transfers. The first such effective field theory to be discussed in this chapter is the Dispersion Theory.

In the Dispersion Theory the isoscalar and isovector nucleon form factors can be written in a spectral representation as

$$\begin{aligned} F_{i,s}(Q^2) &= \frac{1}{\pi} \int_{9m_\pi}^{\infty} \frac{\text{Im}F_{i,s}(\mu^2)}{\mu^2 + Q^2} d\mu^2 \\ F_{i,v}(Q^2) &= \frac{1}{\pi} \int_{4m_\pi}^{\infty} \frac{\text{Im}F_{i,v}(\mu^2)}{\mu^2 + Q^2} d\mu^2, \end{aligned} \quad (2.88)$$

where  $i = 1, 2$  refer to the Dirac and Pauli form factors respectively. Meissner and collaborators have fitted the dispersion relation to the existing scattering data [89, 90] by choosing the residues of the vector meson pole so that the leading term would cancel in a  $1/Q^2$  expansion, thus preserving proper scaling in the pQCD regime. The minimum number of poles needed to fit the data was three isoscalar and three isovector poles. Of these two isovectors and three isoscalars could be identified with the physical vector meson masses.

### 2.5.4 Vector Meson Dominance

Vector Meson Dominance (VMD) is an approximation to the Dispersion Theory, when the eqn. 2.88 is parametrized as a sum over all possible vector mesons. In the VMD model a virtual photon couples to a nucleon through the vector mesons. A linear combination of the Dirac and Pauli form factors of the proton and neutron make up the isoscalar and isovector form factors

$$F_{i,s}(Q^2) = \frac{1}{2}(F_{i,p} + F_{i,n}) \quad \text{and} \quad F_{i,v}(Q^2) = \frac{1}{2}(F_{i,p} - F_{i,n}), \quad (2.89)$$

where  $i = 1, 2$  represents Dirac and Pauli form factors. These form factors are generally expressed as a sum over all mesonic contributions

$$F_i^{v,s}(Q^2) = \sum_{i=\text{mesons}} \frac{m_i a_i}{Q^2 + m_i^2} F_i(Q^2) \quad (2.90)$$

where  $a_i$  is the photon-meson coupling constant,  $m_i$  is the mass of a vector meson and  $F_i$  is the meson-nucleon coupling form factor. A sum over all vector mesons is done so that the exchanges of mesons with  $I = 0$  belong to the isoscalar form factors and exchanges of  $I = 1$  belong to isovector form factors. Eqn. 2.90 does not take into account the individual vector meson's mass distribution widths.

The Vector Meson Dominance model expressed in eqn. 2.90 violates the high  $Q^2$  behavior derived from the pQCD in eqn. 2.84, since  $F_2$  scales as  $1/Q^2$  and not as  $1/Q^6$  predicted by Brodsky, et al. Gari and Krümpelmann have worked out a “synthesis” of the VMD and the quark dynamics in the asymptotic pQCD limit [91, 92]. In this theory,  $\omega$ -mesons were used for  $I = 0$  vector mesons and  $\rho$ -mesons were used to represent  $I = 1$  vector mesons. Gari and Krümpelmann introduced a product of low  $Q^2$  VMD-like behavior,  $F_1 \sim F_2 \sim \frac{\Lambda_1^2}{Q^2 + \Lambda_1^2}$  and high  $Q^2$  behavior from eqn. 2.83 as

$$\begin{aligned} F_1 &= \frac{\Lambda_1^2}{\hat{Q}^2 + \Lambda_1^2} \times \frac{\Lambda_2^2}{\hat{Q}^2 + \Lambda_2^2} \\ F_2 &= \frac{\Lambda_1^2}{\hat{Q}^2 + \Lambda_1^2} \times \left[ \frac{\Lambda_2^2}{\hat{Q}^2 + \Lambda_2^2} \right]^2, \end{aligned} \quad (2.91)$$

where

$$\hat{Q}^2 = Q^2 \frac{\log\left(\frac{Q^2 + \Lambda_2^2}{\Lambda_{QCD}^2}\right)}{\log\left(\frac{\Lambda_2^2}{\Lambda_{QCD}^2}\right)}.$$

Here, if  $\Lambda_2^2 \gg \Lambda_1^2$ , then both the low and high momentum transfer behavior is conserved. If  $Q^2 \ll \Lambda_2^2$ , then the form factors are dominated by the meson dynamics and have a  $\Lambda_1^2/(Q^2 + \Lambda_1^2)$  form. If  $Q^2 \gg \Lambda_1^2$ , then the form factors are dominated by quark dynamics and have the proper  $Q^2$  scaling. Connecting low and high  $Q^2$  introduces two additional

fitting parameters, making a total of seven<sup>19</sup>. By fitting to all existing form factor data Gari and Krümpelmann obtained a  $\chi^2/Ndf$  of less than unity.

### 2.5.5 Chiral Quark Soliton Model

The Chiral Quark Soliton Model arises from consideration of the role of spontaneous chiral symmetry breaking in the dynamics of the bound state of a nucleon and the  $1/N_c$  expansion, where  $N_c$  is number of colors [93]. When chiral symmetry is spontaneously broken, the light<sup>20</sup> Goldstone bosons are expected to be present in the theory. In the Chiral Quark Soliton Model these bosons are in the form of pions, the lightest of all hadrons. The pion field can be written in terms of the  $(N_f^2 - 1) \times (N_f^2 - 1)$  unitary matrix

$$U(x) = \exp\left(i\frac{\tau^A\pi^A}{F_\pi}\right), \quad (2.92)$$

where  $\tau^A$  are the three SU(2) Pauli matrices (in case of  $N_f = 2$ ),  $F_\pi = 93$  MeV is the pion decay constant. The simplest chiral Lagrangian was suggested by Skyrme [94] as

$$\mathcal{L}_{skyrme}^\pi = \frac{F_\pi^2}{4} \left\{ \text{Tr} L_\mu L_\mu + M_\pi^2 \text{Tr}(U + U^\dagger) \right\} + \frac{1}{32e^2} \text{Tr} [L_\mu L_\mu]^2 \quad (2.93)$$

where  $L_\mu = U^\dagger \partial_\mu U$  is the gradient of a pion field,  $e = 4.25$  is the standard Skyrme parameter and  $M_\pi = 138$  MeV is the mass of a pion. Holzwarth [95] extended the pionic Lagrangian in eqn. 2.93 to include  $\rho$  and  $\omega$  vector meson fields explicitly as the dynamical degrees of freedom<sup>21</sup>, so that the total skyrmion Lagrangian is the sum of the three meson Lagrangians,

$$\mathcal{L}_{skyrme} = \mathcal{L}_{skyrme}^\pi + \mathcal{L}_{skyrme}^\rho + \mathcal{L}_{skyrme}^\omega \quad (2.94)$$

Holzwarth used this Lagrangian to obtain the results for the nucleon form factors.

---

<sup>19</sup>Masses in this theory are fixed.

<sup>20</sup>These bosons are massless in the pure Goldstone theory.

<sup>21</sup>Model B in reference [95]

## 2.5.6 Relativistic Constituent Quark Model

In the constituent quark model, the electromagnetic structure of a nucleon is understood purely in terms of the electromagnetic properties of constituent quarks. In a non-relativistic three constituent quark model the nucleon is an antisymmetric wave function of three spin- $\frac{1}{2}$  point quarks. The proton consists of two up quarks with the charge of  $+\frac{2}{3}$  and one down quark with the charge of  $-\frac{1}{3}$ , while the neutron consists of one up and two down quarks. The mass of a constituent quark in the non-relativistic model is  $\sim 1/3$  of a nucleon mass. Up and down quarks in the proton and neutron are related by the isospin symmetry,

$$\begin{aligned} u^p &= d^n \\ d^p &= u^n. \end{aligned} \tag{2.95}$$

This isospin symmetry is used in many model calculations.

The electromagnetic current of the nucleon,  $J^\mu$  can be approximately expressed as a sum of “one-body” quark currents,

$$J^\mu \approx J_1^\mu = \sum_{j=1}^N \left( f_1^j(Q^2) \gamma^\mu + f_2^j(Q^2) \frac{i\sigma^{\mu\nu} q_\nu}{2m_j} \right), \tag{2.96}$$

where  $f_1^j(Q^2)$  and  $f_2^j(Q^2)$  are the Dirac and Pauli form factors of the  $j$ th quark respectively and  $m_j$  is the mass of that quark<sup>22</sup>. To evaluate the form factor from the one body current the constituent quark wave function has to be constructed from a realistic quark potential.

Cardarelli and Simula [96, 97] have calculated the nucleon elastic form factors using a One-Gluon-Exchange (OGE) potential. The authors assumed valence quark dominance. The constituent quarks are then allowed to have structure, with the form factors of a given functional form. The constituent quark wave function is calculated by solving the three body Hamiltonian.

Wagenbrunn, Boffi et al. [98, 99] used the Goldstone-Boson-Exchange (GBE) potential with a single particle current operator for point-like constituent quarks. This formalism is called Point Form Spectator Approximation (PFSA), where a single quark is struck by a

---

<sup>22</sup>Remember that if the quarks are structureless point particles then Dirac and Pauli form factors become identically  $f_1^j = 1$  and  $f_2^j = 0$ .

photon, coherently or incoherently. The authors were able to achieve a good agreement with  $G_E^n$  at low  $Q^2$ . They postulate that  $G_E^n$  is driven by the small hyperfine components of the Hamiltonian and Lorentz boosts. The hyperfine components explicitly break the SU(6) symmetry in the quark interaction Hamiltonian<sup>23</sup>.

## 2.5.7 Cloudy Bag Model

In the cloudy bag model the three constituent quarks are surrounded by a cloud of pions. Here a distinction is made between the bare nucleon, consisting of constituent quarks and the physical nucleon observed in the elastic scattering. In this model an incident photon can

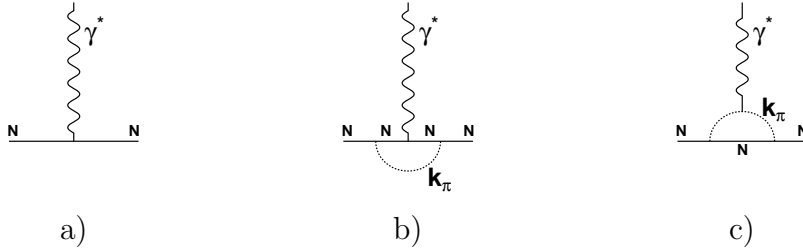


Figure 2-19: Diagram of a virtual photon interacting with a bare nucleon (a), nucleon in the presence of a pion (b) and a pion from cloud (c).

interact electromagnetically with the bare nucleon (fig. 2-19a), the nucleon in the presence of a pion (fig. 2-19b) or with a charged pion from the cloud (fig. 2-19c). The effect of the pion cloud is especially pronounced in the neutron electric form factor,  $G_E^n$ , due to the small contribution to the electromagnetic structure of the neutron from the constituent quarks.

Recently Miller [100] calculated the effect of the pion cloud in a relativistic framework to account for the latest data at large  $Q^2$ . The calculation was done in the Light Front formalism, similar to the approach of Cardarelli and Simula. The total nucleon form factor is expressed as a sum of three possible photon interaction form factors,

$$F_i^\alpha(Q^2) = Z \left[ F_i^{\alpha,0}(Q^2) + F_i^{\alpha,1}(Q^2) + F_i^{\alpha,2}(Q^2) \right], \quad (2.97)$$

where  $i = 1, 2$  and  $\alpha = p, n$ .  $F_i^{\alpha,0}(Q^2)$  is the bare nucleon form factor,  $F_i^{\alpha,1}(Q^2)$  is the form

<sup>23</sup>This was also noted by Cardarelli and Simula [96].

factor of the nucleon in a presence of a pion and  $F_i^{\alpha,2}(Q^2)$  is the photon-pion vertex form factor. The factor of  $Z$  is needed for a proper physical nucleon form factor normalization at  $Q^2 = 0$ .

### 2.5.8 Phenomenological Models

Kaskulov and Grabmayr [101, 102] used the pion cloud around a bare nucleon model to obtain the theoretical justification for the success of the Galster parametrization [59]. They showed that the pion cloud content of a nucleon under a set of approximations leads to the Galster-like  $Q^2$  dependence. Based on their work they propose a modified Galster parametrization,

$$G_E^n(Q^2) = a' \frac{b\tau}{1 + b\tau} G_D(Q^2), \quad (2.98)$$

where  $b = 4M_\pi^2/\Lambda_\pi^2$ ,  $\Lambda_\pi^2 = 0.53 \text{ GeV}^2$ ,  $a'$  is the value related to the pion-cloud content and  $G_D$  is the dipole form factor of a bare three quark core. By using this parametrization the authors were able, with a large degree of success, to unite data from pion electroproduction with the  $G_E^n$  measurements. A best  $\chi^2$  fit of the parametrization in eqn. 2.98 was found with  $b = 6.65$  and  $a' = 0.26$  being fixed by the pion data and  $\Lambda$  as the only free parameter.

Friedrich and Walcher [103] have phenomenologically parametrized the  $G_E^n$ . Their parametrization was inspired by the non-relativistic constituent quark model surrounded by a pion cloud. The contribution to the total nucleon form factor from each constituent quark,  $G^{qN}$  was parametrized with a dipole. The contribution from the pion cloud,  $G^\pi$  was parametrized with a Gaussian form.

$$\begin{aligned} G^{qN} &= \frac{a_0^{qN}}{(1 + Q^2/a_1^{qN})^2} \\ G^\pi &= a_0^\pi \left(1 - \frac{1}{6} Q^2/a_1^\pi\right) e^{-\left(\frac{Q}{2a_1^\pi}\right)^2}, \end{aligned} \quad (2.99)$$

where  $a_0^{qN}$  and  $a_0^\pi$  are given by quark and pion charges, respectively.

## 2.5.9 Diquark Model

In the quark spectator-diquark model a virtual photon incoherently strikes the constituent quark in the nucleon, with the remaining constituents treated as the quasi-particle spectators to supplement other quantum numbers of the nucleon. Ma and collaborators [104] have calculated the nucleon elastic form factors in the Light Front formalism. They took the mass of a quark to be  $m_q = 0.22$  GeV which is much less than the mass of a quark in the non-relativistic model (1/3 of a nucleon mass). The authors explained the lower constituent quark mass as the effect of relativity. The correct prediction of the neutron mean square charge radius was achieved by breaking SU(6) symmetry<sup>24</sup>. SU(6) was broken by the difference in the scalar and vector diquark parameters along with the Melosh rotation in the Light Front formalism.

### 2.5.10 Summary

The recently measured data on  $G_E^n$  at  $Q^2$  near or above 1 (GeV/c)<sup>2</sup> [105, 106, 107] have favored models based on constituent quarks surrounded by a pion cloud. In particular Cardarelli and Simula calculations at large  $Q^2$  seem to successfully predict a ratio of electric to magnetic form factors,  $\mu G_E^n/G_M^n$  in fig. 2-20, while they incorrectly predict a low  $Q^2$  behavior of  $G_E^n$ . They also predict an incorrect neutron charge radius. However, calculations by Miller show that the addition of a pion cloud around a bare nucleon generated by the constituent quarks can preserve the correct shape at large  $Q^2$  while being more accurate in predicting the small  $Q^2$  behavior.

The  $G_E^n$  data appear to show an enhancement at low momentum transfer,  $Q^2 \sim 0.25$  (GeV/c)<sup>2</sup>. In fact, the calculations based on the Chiral Soliton model, while misrepresenting the shape at large  $Q^2$ , seem to indicate an enhancement at small  $Q^2$ . Friedrich and Walcher have focused on this idea and used a phenomenological form to parametrize this enhancement as a long distance diffuse pion cloud. This contribution of the pion cloud appears to be connected to the deviation of the other three elastic form factors from the dipole parametrization at low momentum transfer.

There is still a sizable theoretical uncertainty in the calculation of the neutron electric

---

<sup>24</sup>Already indicated by Wagenbrunn and Boffi [98, 99] and Cardarelli and Simula [96, 97].

form factor at low  $Q^2$  partly due to lack of high quality  $G_E^n$  data. High precision data in this momentum transfer region would be very useful in constraining theoretical model predictions.

Precise knowledge of the neutron electric form factor will enhance the interpretation of results from parity-violating scattering experiments designed to probe the strangeness content of a nucleon. Recent parity-violation experiments [108] have indicated that the elastic form factors of the nucleons,  $G_E^n$  in particular, are one of the biggest contributions to the systematic uncertainty. The special interest of the parity-violating experiments is in the region of extremely low  $Q^2$ . This work should be of great value for such low momentum transfer experiments.

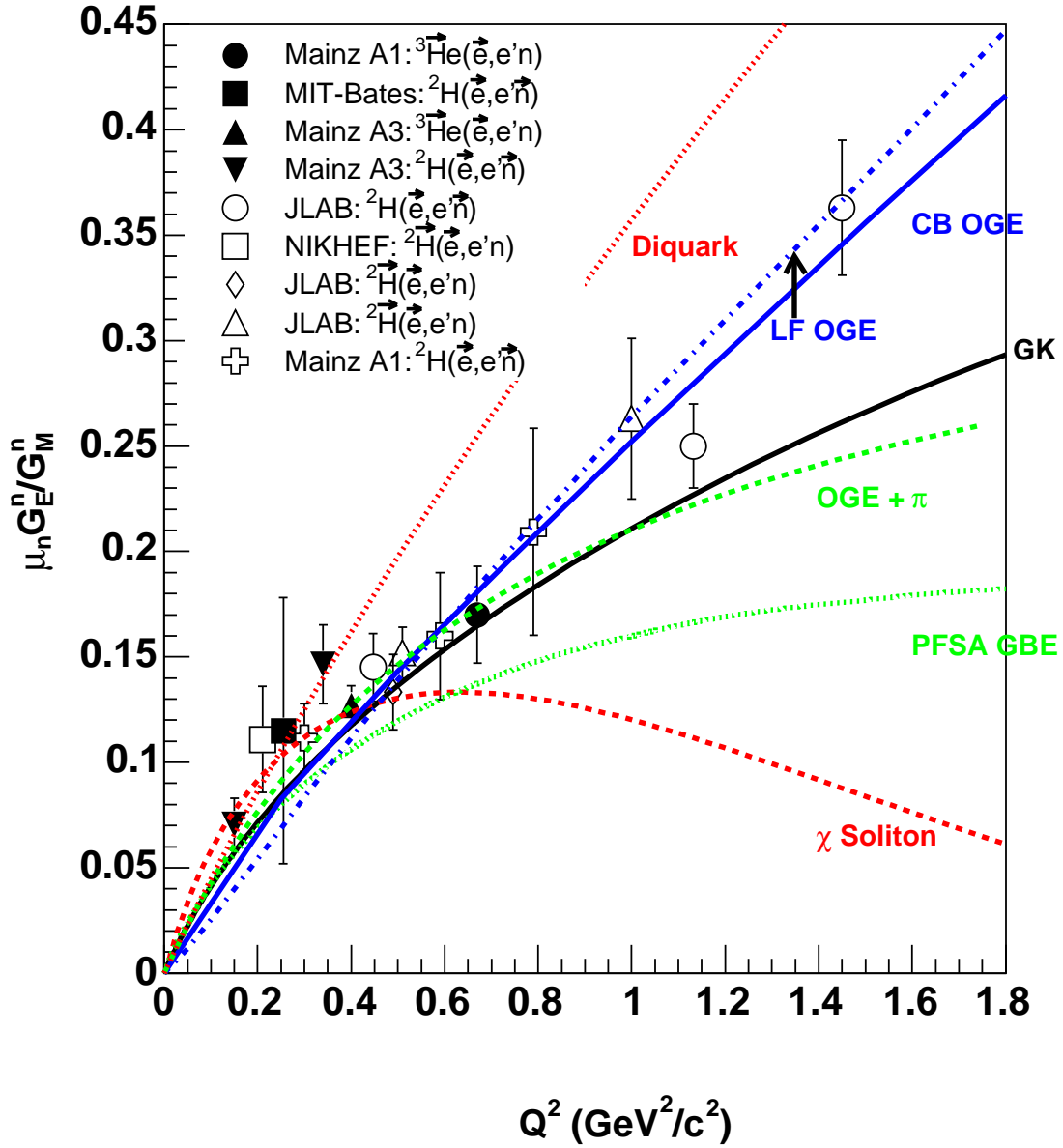


Figure 2-20: World's data on  $\mu G_E^n / G_M^n$  along with the theoretical calculations. The data are from references [109, 110, 111, 112, 113, 114, 115, 105, 116, 117, 106, 107]. The thin solid line marked as "GK" is a calculation by Lomon based on the extension of the Gari-Krümpelmann VMD+pQCD theory (section 2.5.4). The thin dashed line is a Chiral Soliton model calculation performed by Holzworth (section 2.5.5). The thin dot-dashed line marked as "LF OGE" is a calculation by Carderelli and Simula, the thin dotted line marked as "PFSA GBE" is a calculation by Wagenbrunn and Boffi. Both calculations are done with the constituent quark model (section 2.5.6). The thick solid line marked as "CB OGE" is a calculation by Miller performed in cloudy bag model using the One-Gluon-Exchange potential in a core nucleon (section 2.5.7). The thick dotted line is a calculation by Ma and collaborators using the Diquark model (section 2.5.9).

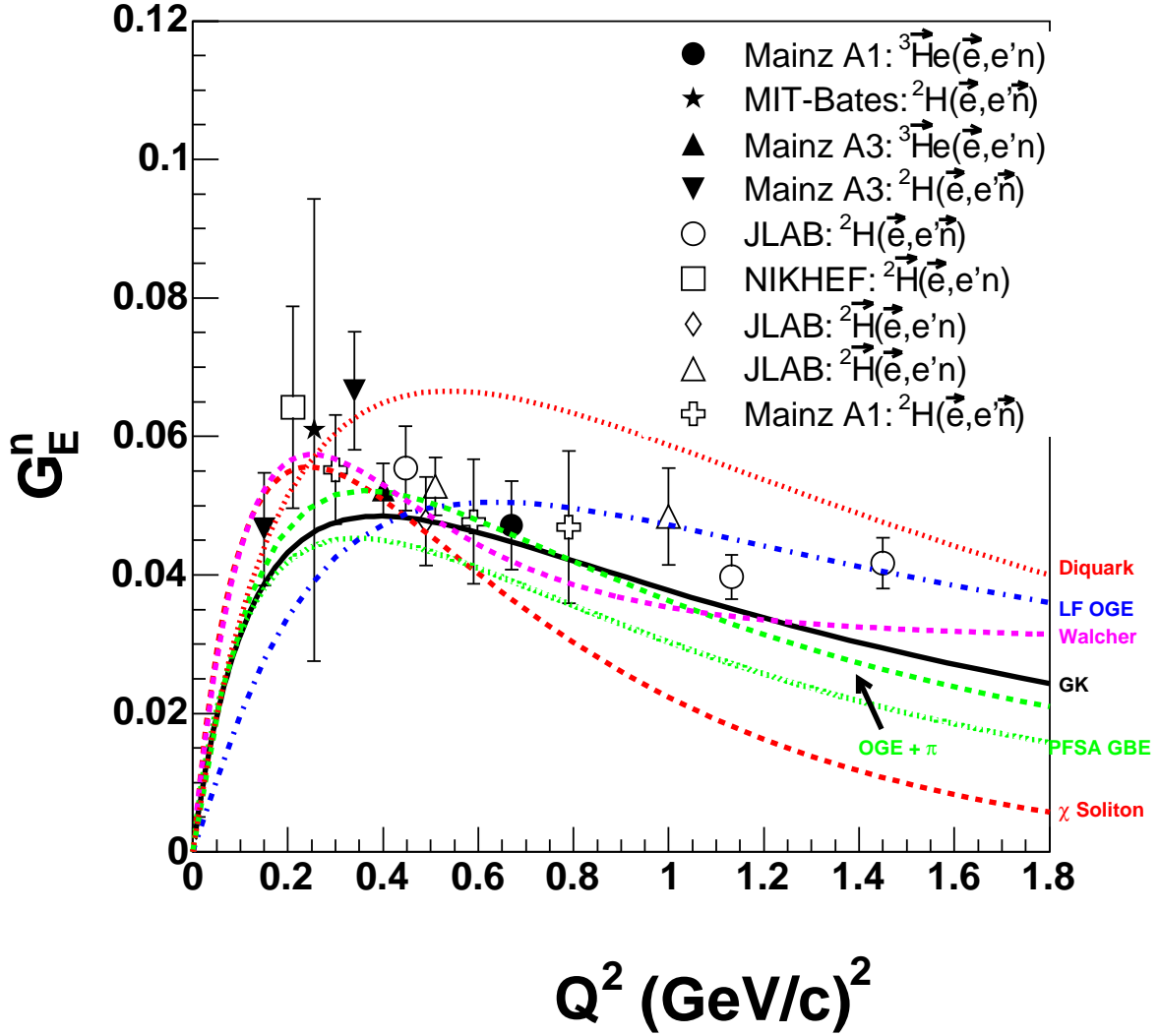


Figure 2-21: World's data on  $G_E^n$  along with theoretical calculations. The data are the same as in fig. 2-20. The theoretical calculations are the same as in fig. 2-20. Added to this plot is the Friedrich and Walcher parametrization marked as "Walcher" inspired by the non-relativistic constituent quark model.

# Chapter 3

## Polarized Hydrogen/Deuterium Gas Target

The success of an experiment in which the target polarization observables are measured is largely dependent upon the performance of the polarized target. Two types of targets are used in these kinds of experiments, solid and gaseous. Solid polarized targets, in the form of ammonia ( $\text{NH}_3$ ) or the deuterated ammonia ( $\text{ND}_3$ ) are used with the extracted beams [118] (e.g. CEBAF beam at Jefferson Laboratory). The advantage of a solid target is in its high density which, in combination with a high-duty factor CW beam, provides high luminosity. The maximum hydrogen atom polarization achieved with an ammonia target is 75 %. However, the polarization of deuterium atoms inside of the deuterated ammonia target is rather low,  $\sim 25$  %. Ammonia targets are not pure hydrogen or deuterium targets. This introduces backgrounds from scattering on other atomic species and the target's aluminum container.

A solid target cannot be used with a stored beam. Instead, a polarized gas produced by the Atomic Beam Source (ABS) and stored in the storage cell internal to a beam line is used as a target. The advantage of the polarized gas target is its high polarization, typically 85 %. Since the gas targets are pure, the scattering reaction is almost background free. The advantages of a polarized atomic gas target make it an excellent choice for the BLAST experiment.

The Atomic Beam Source used in BLAST was based on the source used in the AmPs

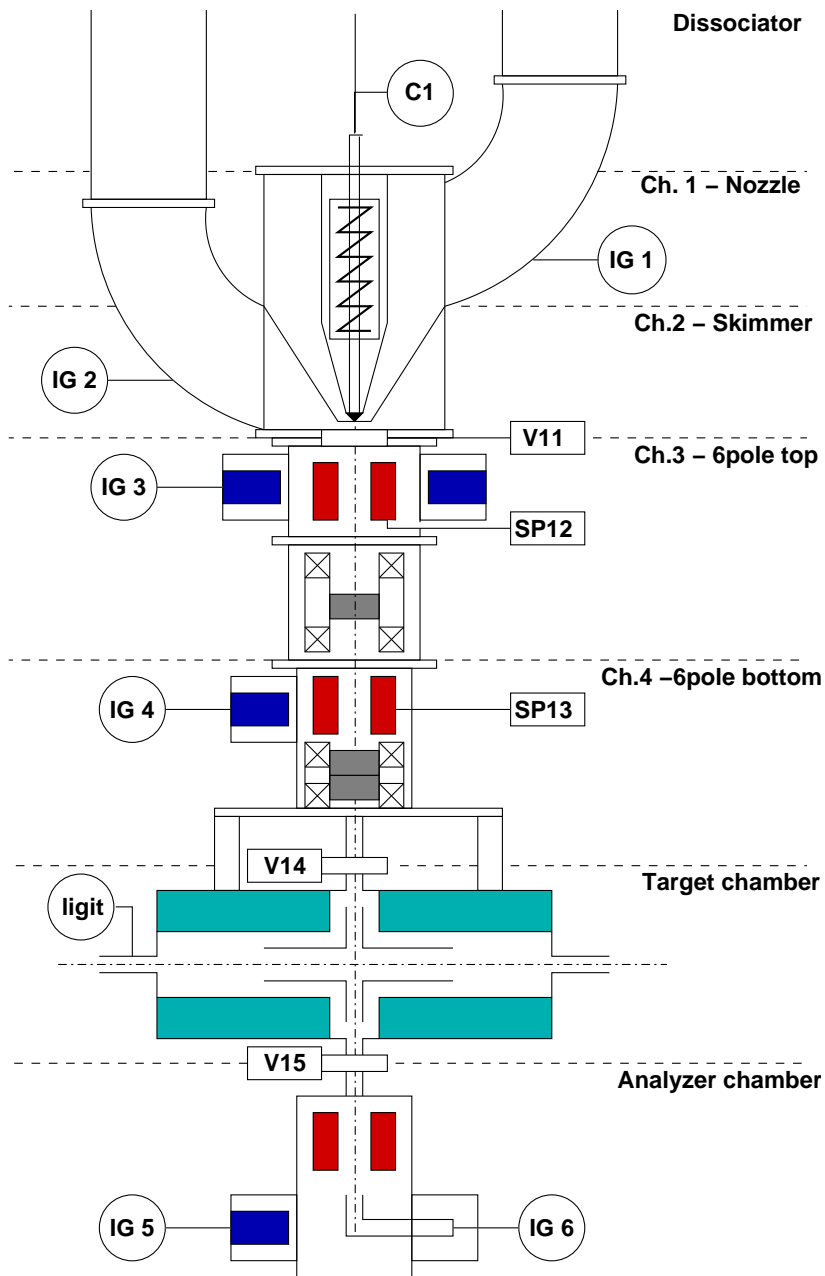


Figure 3-1: Schematic representation of the ABS. Gas is injected into the dissociator (C1). The Skimmer chamber is separated from the first sextupole vacuum chamber by the valve, V11. The first sextupole chamber is followed by the MFT transition unit vacuum chamber. The SFT and WFT transition units and the second sextupole system share the same vacuum chamber. The target chamber is separated from the ABS by a valve, V14. A Breit-Rabi polarimeter vacuum chamber is located underneath the target chamber and separated by a valve V15. All valves are remotely controlled. All vacuum chambers are equipped with ion gauges.

Ring at the NIKHEF laboratory [71]. The NIKHEF ABS was delivered to Bates in August, 2000. However, before the ABS could be installed into the South Hall Ring major differences between the AmPs and BLAST running conditions had to be addressed. These conditions are summarized below.

- **Space Consideration:** The ABS has to fit between the top two coils of the BLAST toroid (see fig. 4-4). The tight space requirements rendered some components of the NIKHEF ABS design unusable.
- **BLAST Field:** The ABS has to operate in the strong magnetic field (up to 3 kGauss) produced by the BLAST spectrometer magnet. Since all of the RF transitions in the ABS rely on the precise setting of the magnetic field, special consideration has to be given to shielding the magnetic components of the RF transition units from the BLAST field. The turbo pumps have to be either taken out of the high field region or replaced by pumps that can operate in a high magnetic field.
- **Reliability:** Due to limited access to the ABS during the experiment, the reliability is an important characteristic. The improvements to the ABS' reliability over the NIKHEF design are achieved by completely automating the ABS controls using the EPICS control system. Since the South Hall Ring control systems are all EPICS based it became easy to integrate the ABS operation into that of the South Hall Ring. The reliability of the RF transitions was improved by adding a magnetic feedback loop mechanism to the controls of the RF transition units.
- **Improved Figure-of-Merit:** The BLAST scientific program demands high figure-of-merit from the ABS target. Improvements over the NIKHEF design were made in order to raise the polarization of atoms in the target.
- **Multiple Modes of Operation:** The new ABS design allows for rapid switching between hydrogen and deuterium polarized targets, thus addressing one of the requirements of the BLAST experiment.

Figure 3-1 is a schematic representation of the ABS. Almost all of the components have been modified to some extent in order to satisfy the requirements of the ABS operation at BLAST.

### 3.1 The RF Dissociator

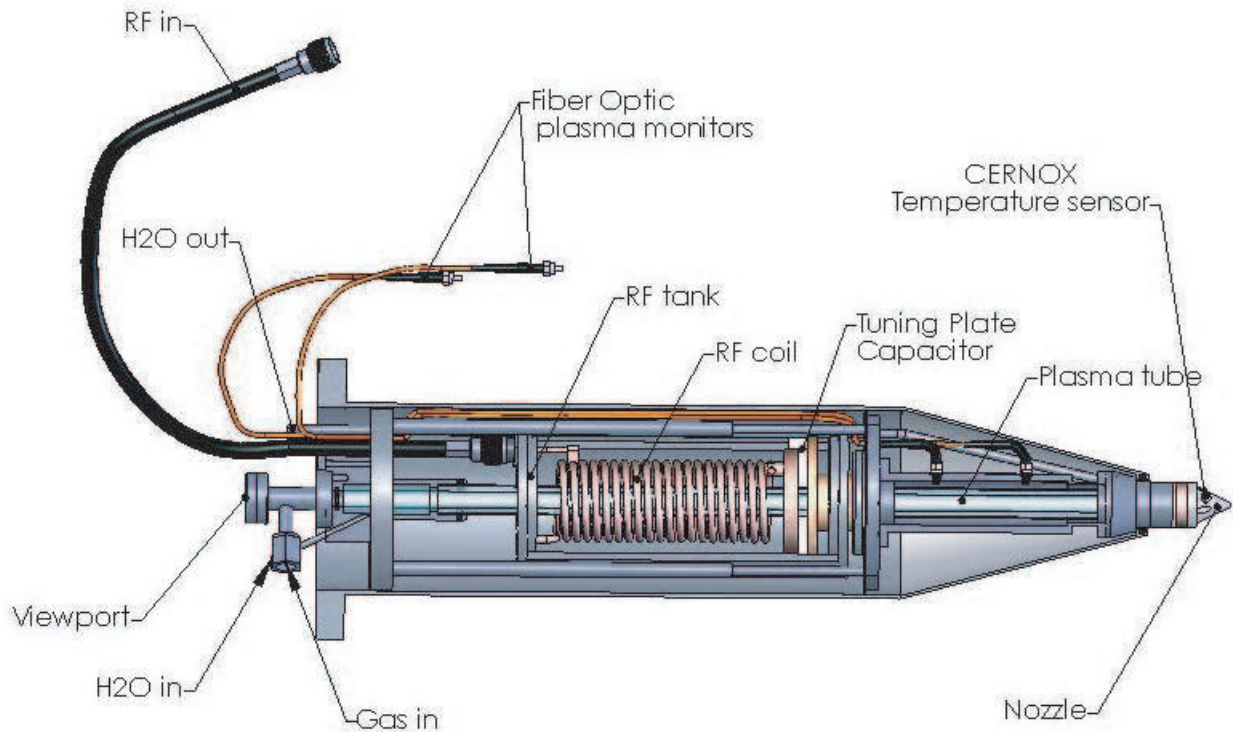


Figure 3-2: Diagram of the RF dissociator. The  $^1H_2$  or  $^2H_2$  is injected into the gas tube. The cooling water flows on the outside of the gas tube. The gas is dissociated by the RF field in the coil. The nozzle is cooled by the cold head connected to the nozzle by a copper braid.

An RF field with a fixed frequency of 27.12 MHz is used to dissociate the hydrogen (deuterium) molecules into atoms in the RF dissociator. The molecular gas is injected by the Polarized Gas Feed System (*PGFS*) into a 2 mm thick Pyrex glass tube with a 9 mm inner diameter. The PGFS is designed with the capability to switch quickly between injecting hydrogen and deuterium gases (see fig. 3-3). The PGFS also injects a small amount of oxygen gas into the gas tube to mix with hydrogen (deuterium) for reasons explained later.  $^1H_2$  and  $^2H_2$  gas flow rates are controlled by the MKS 1479A mass flow controller (*MFC*), with a dynamic range of 0 to 200 standard cubic centimeters per minute (sccm). The MFC with a dynamic range of 0 to 1 sccm is used for the  $O_2$  flow. The estimated accuracy of these devices is  $\sim 2-3\%$ .

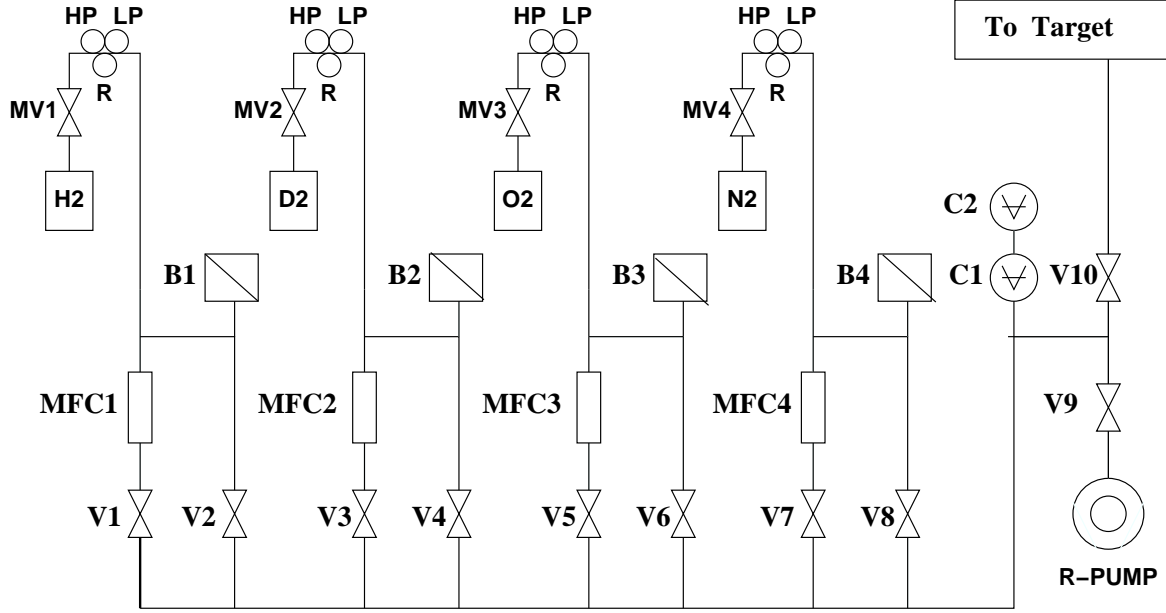


Figure 3-3: Polarized Gas Feed System (PGFS). The PGFS has four gas lines allowing quick switching between hydrogen ( $H_2$ ) and deuterium ( $D_2$ ) targets.  $N_2$  was not used during the experiment. The gas flow rate is regulated by the Mass Flow Controllers (MFC). The baratron (B) and convectron (C) gauges measure gas pressure in the PGFS lines. Valves V10 and V9 direct the gas flow either into the dissociator or the pump.

The gas tube is surrounded by a larger 4 mm thick and 16 mm inner diameter glass tube which is used to flow cooling water ( $CT$ ). The deionized (DI) cooling water is used to cool the plasma produced during the dissociation. It was found that the temperature of the cooling water has a significant effect on the performance of the dissociator. The temperature of the cooling water was kept constant at  $\sim 10$  °C.

The glass tube is surrounded by the RF coil ( $L$ ), which provides a resonant electromagnetic field needed to dissociate molecules into atoms. The RF coil is shielded by an aluminum can to reduce the amount of the RF field “leaking” into other ABS and BLAST detector components. A fixed frequency RF generator (ENI Genesis) is used to provide the RF field with power up to 500 Watts. The generator is located 130 meters away from the dissociator coil which results in  $\sim 40\%$  of RF power being dissipated in the semi-rigid RF cable. The actual power out of the supply used during the experiment is  $\sim 250$  W.

Since the RF field has the fixed frequency of 27.12 MHz, adjustments to the dissociator’s RF coil have to be made to maximize the Q-value of a resulting resonator at this particular frequency. The Q-value was optimized by properly choosing a tap point on the RF coil and

adjusting the capacitor inside of the aluminum can . The capacitor consists of a piece of dielectric placed between the bottom of the RF coil and the aluminum can which also serves as a ground. The coil (L), capacitor (C) and plasma (R) effectively create an LRC circuit.

In the Q-value maximization procedure, an RF signal in the range of 20 to 30 MHz is fed into the dissociator while the frequency response of the cavity is being measured by a pick-up coil. The capacitor inside of the can is adjusted until the peak of the frequency response is at 27.12 MHz. Then a small correction is made to account for the effect of the DI cooling water in the outer tube. It was discovered that the DI cooling water lowers the peak of the frequency response curve by  $\sim 1$  MHz. A Q-value of  $\sim 150$  was established for the dissociator resonant cavity .

The combination of two outside capacitors is used to minimize the power reflected from the dissociator RF circuit while maximizing the forward power. The “Load” capacitor is connected in series with the RF coil, and the “Tune” capacitor is in parallel. Both capacitors are remotely controlled. The Tune and Load capacitors are adjusted until a minimum reflected power is achieved. The minimum reflected power occurs when the load impedance of the effective dissociator RF circuit satisfies  $Re(Z) = 50 \Omega$  and  $Im(Z) = 0$ .

The atomic gas is ejected out of the dissociator into the ABS through a system of apertures, *nozzle-skimmer-collimator*. The diameters of the nozzle, skimmer and collimator are chosen to match the acceptance of the first sextupole system. The nozzle is cooled to 70 K in order to avoid the recombination of the dissociated atoms into molecules on its surface. Also, the cold nozzle cools the atomic beam, thus reducing the velocity of the individual atoms, which results in the cold atomic beam being focused more effectively in the sextupole system. The nozzle is cooled by a single stage GM type cold head with an external helium compressor which supplies 60 Watts at 80 K. The nozzle temperature is controlled by a heater-sensor combination connected to the PID controller. Four Cernox CX-1070-CU sensors are used to monitor and control the temperature on the cold head, nozzle and along the solid copper arm which connects the cold head to the nozzle.

To reduce the recombination rate further, a trace amount of  $O_2$  gas ( $\sim 0.5\%$  of the  $H_2$  flow) is injected into the dissociator. The oxygen molecules combine with the hydrogen (deuterium) atoms to form water which, in turn, freezes on the surface of the nozzle. The ice on

the nozzle provides a surface coating which reduces the probability of atomic recombination.

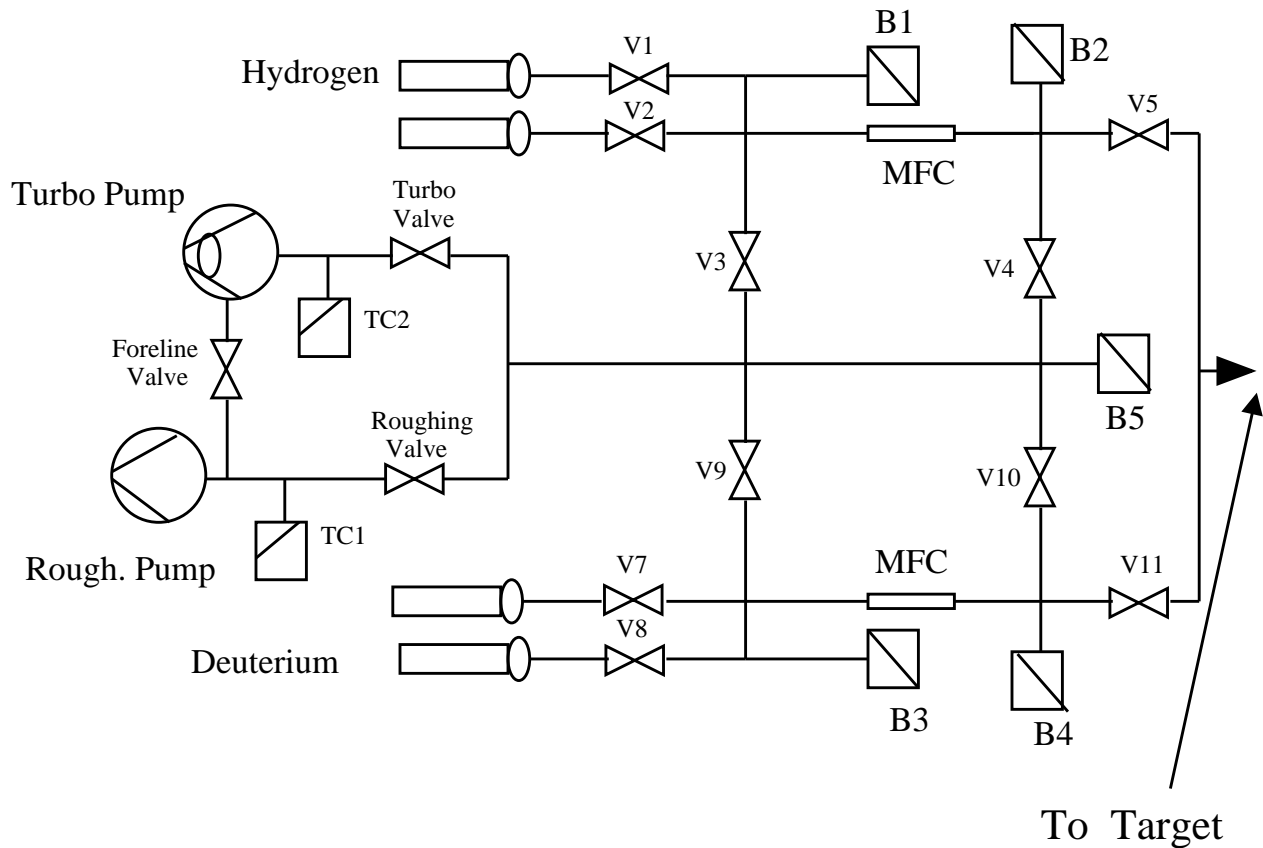


Figure 3-4: Unpolarized Gas Feed System (UGFS). The UGFS is capable of flowing both hydrogen and deuterium gases.

The BLAST target is also equipped with the Unpolarized Gas Feed System (UGFS). The UGFS is used for systematic false asymmetry measurements and luminosity calibrations. Both hydrogen and deuterium gases are fed by the UGFS directly into the target cell (see fig 3-4.) The flow rates in the UGFS are controlled by the MFCs. However, the precision of the MFC is not sufficient for the luminosity calibration purposes. For this reason a buffer system was attached to the UGFS to better monitor a gas flow into the target cell. The precision in the flow rate measurement with the buffer system is better than 1%.

### 3.1.1 Performance of the RF Dissociator

Before the RF dissociator was used in the full ABS configuration, its performance was studied with a Quadrupole Mass Analyzer (*QMA 200*). The vacuum chamber with the QMA inside was placed underneath the nozzle. The QMA vacuum chamber was separated from the nozzle by a set of apertures in order to limit the gas that scatters off the vacuum chamber walls from entering into the QMA. The atomic beam out of the nozzle was chopped by a chopper wheel in order to separate the atomic beam signal from background. Correspondingly, the lock-in amplifier was used to extract the AC component of the QMA analog signal.

The objective of this study was to measure the efficiency of the RF dissociator in breaking up the molecules into atoms which is described by the *degree of dissociation*,  $\alpha_{H/D}$ . Numerically  $\alpha_{H/D}$  is defined as

$$\alpha_{H/D} = \frac{P_{H/D}^1}{P_{H/D}^1 + 2\kappa_v P_{H/D}^2}, \quad (3.1)$$

where  $P_{H/D}^1$  and  $P_{H/D}^2$  are the partial pressures of the atomic and molecular gases, respectively. The correction factor  $\kappa_v \approx \frac{1}{\sqrt{2}}$  is due to the difference in the atomic and molecular velocities. The value of the degree of dissociation measured with the QMA can be redefined in terms of signal amplitudes in the QMA as

$$\alpha_{H/D} = \frac{S_{H/D}^1}{S_{H/D}^1 + 2\kappa_{det}\kappa_v S_{H/D}^2}, \quad (3.2)$$

where  $S_{H/D}^1$  and  $S_{H/D}^2$  are the respective atomic and molecular signals and  $\kappa_{det}$  is a relative detection probability in the QMA. The detection probability,  $\kappa_{det}$  is a function of the gas type and the QMA acceptance only. It should be constant over all flows and nozzle temperatures. Figure 3-5 shows the quantity  $\kappa_{det}$  measured for two different types of gases and various nozzle temperatures as a function of the gas flow into the dissociator. Parameter  $\kappa_{det}$  is constant over all flows and has two distinct values for hydrogen and deuterium gas.

The fraction of dissociation was measured for hydrogen and deuterium gas as a function of the RF power<sup>1</sup>. The dissociation fraction,  $\alpha_{H/D}^{max}$  of  $\sim 90\%$  was achieved for both gases<sup>2</sup> (see

---

<sup>1</sup>The RF power was measured at the output of the RF supply. However, there is close to 40% power loss in the cable.

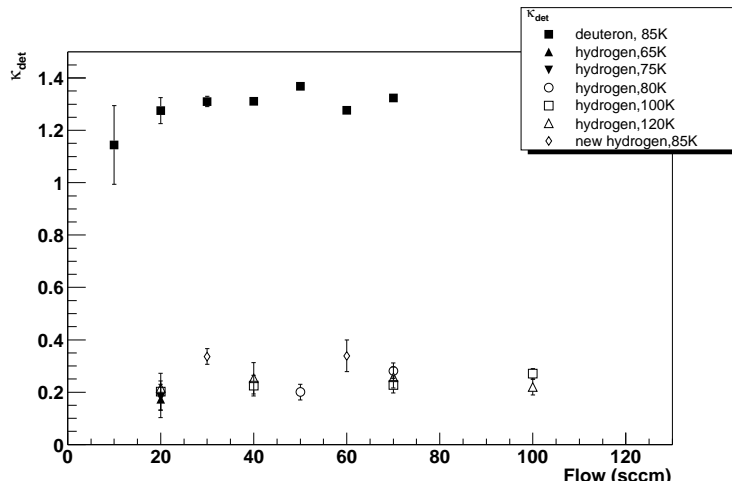


Figure 3-5: Relative QMA detection probability  $\kappa_{det}$  as function of the gas flow into the dissociator for deuterium (solid square) at 85 K and for hydrogen at 65 K (solid triangle), 75 K (solid upside-down triangle), 80 K (open circle), 100 K (open square), 120 K (open triangle), 85 K (open diamond).

fig. 3-6). As expected, a higher flow rate corresponding to a higher molecular density inside of the dissociator requires more RF power to reach a high level of dissociation. A slight difference in  $\alpha_{H/D}^{max}$  ( $< 10\%$ ) was observed as a function of the nozzle temperature within the range of 60-100 K. The optimal nozzle temperature was chosen to be 70 K. The optimal flow rate of oxygen gas was found to be 50 % higher for hydrogen gas than for deuterium.

## 3.2 Focusing in a Sextupole Magnet System

A set of sextupole magnets is used to focus and defocus atoms with the magnetic moments of  $\mu = \mu_B g_S m_S$ , where  $m_S = \pm \frac{1}{2}$  is the projection of an electron spin in the atom<sup>3</sup> and  $\mu_B$  is the Bohr magneton. The spin of an atom in the external magnetic field is oriented in the direction of that field,  $\vec{\mu} = \mu \hat{B}$ . Hence, the force on the atom passing through the magnetic field can classically be expressed as

$$\vec{F} = \vec{\nabla}(\vec{\mu} \cdot \vec{B}) = \mu \cdot \vec{\nabla} B. \quad (3.3)$$

<sup>2</sup>This measurement was done with the BLAST magnet off. The magnetic shield around the dissociator is installed to achieve the same performance with the BLAST magnet on.

<sup>3</sup>To a very good approximation, the nuclear magnetic moment is neglected in the magnetic focusing calculation, since  $\mu_B \gg \mu_N$ .

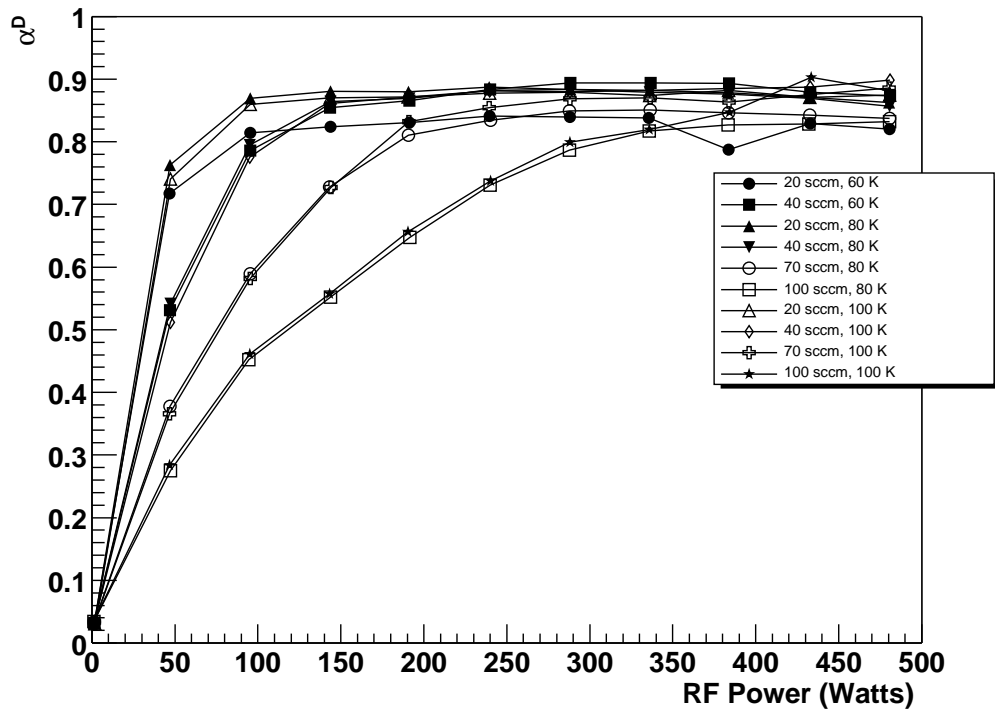
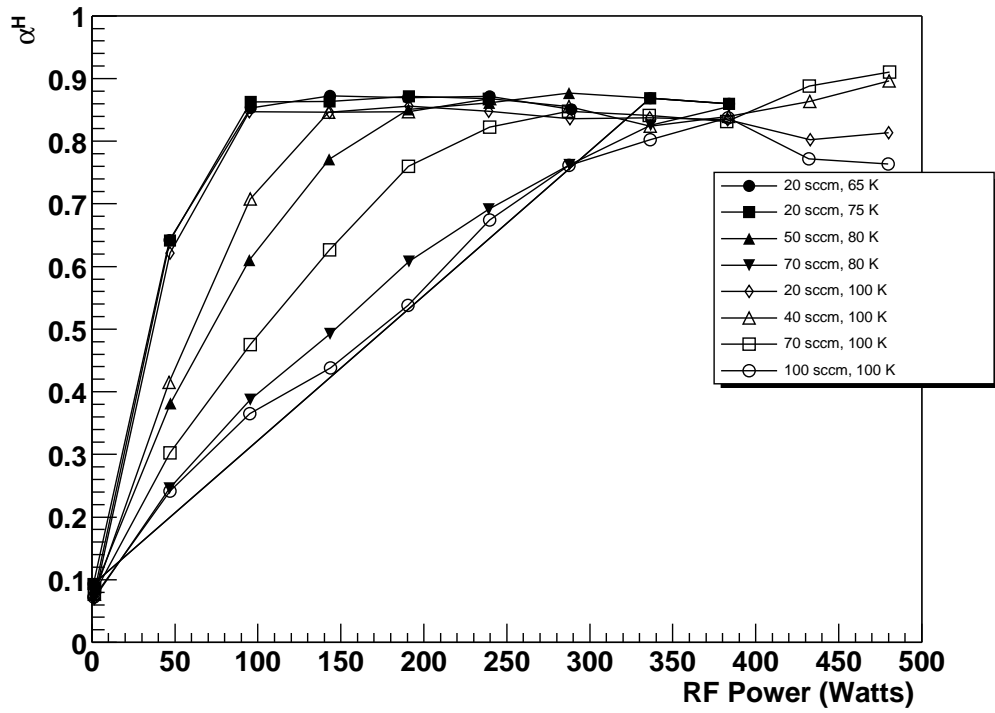


Figure 3-6: The atomic fraction of hydrogen (top) and deuterium (bottom) gas measured by the QMA immediately outside of the dissociator's nozzle as a function of the RF power.

The components of this force can be written in Cartesian coordinates as

$$\begin{aligned} F_x &= \mu \left( \frac{\partial B_x}{\partial x} \hat{B}_x + \frac{\partial B_y}{\partial x} \hat{B}_y \right) \\ F_y &= \mu \left( \frac{\partial B_x}{\partial y} \hat{B}_x + \frac{\partial B_y}{\partial y} \hat{B}_y \right), \end{aligned} \quad (3.4)$$

where the magnetic sextupole field is expressed in cylindrical coordinates as

$$\begin{aligned} B(r) &= B_0(z) \left( \frac{r}{r_0} \right)^2 \\ B_x &= B_0(z) \frac{x^2 - y^2}{r_0^2} \\ B_y &= -B_0(z) \frac{2xy}{r_0^2}, \end{aligned} \quad (3.5)$$

where the equality  $\vec{\nabla} \cdot \vec{B} = 0$  is used. The quantity  $B_0(z)$  is the amplitude of the pole-tip field of the sextupole magnet and  $r_0$  is the pole-tip radius. Using eqn. 3.3, the total force on the atom is

$$\vec{F} = 2\mu B_0 \frac{\vec{r}}{r_0^2}. \quad (3.6)$$

However, the ABS operates in the strong magnetic field created by the BLAST toroid. Following the established ABS coordinate system this field is generally in the  $\hat{x}$  direction. Hence, the x-component of the field,  $B_x$  in eqn. 3.5, is modified as

$$B'_x = B_x + B_{ext}. \quad (3.7)$$

Accordingly, the components of the magnetic forces on the atom are expressed in Cartesian coordinates as

$$\begin{aligned} F'_x &= \frac{2\mu B_0}{B'} x \left( B_0 \left( \frac{r}{r_0} \right)^2 + B_{ext} \right) \\ F'_y &= \frac{2\mu B_0}{B'} y \left( B_0 \left( \frac{r}{r_0} \right)^2 - B_{ext} \right), \end{aligned} \quad (3.8)$$

where

$$B' = \sqrt{B_x'^2 + B_y'^2}$$

The magnitude of the total magnetic force remains unchanged. However, the force,  $F'$ , is no

longer purely along  $\hat{r}$ . By using eqn. 3.8 the full expression for the radial component of the sextupole force exerted on the atoms in the external magnetic field is

$$\frac{\vec{F}'}{F} \cdot \frac{\vec{r}}{r} = \frac{1 + b \frac{r_0^2}{r^2} \cos(2\theta)}{\sqrt{1 + 2b \frac{r_0^2}{r^2} \cos(2\theta) + b^2 \frac{r_0^4}{r^4}}}, \quad (3.9)$$

where

$$b = \frac{B_{ext}}{B_0},$$

$$\tan(\theta) = \frac{y}{x},$$

and  $F$  is defined in eqn. 3.6.

The effect of the external magnetic field increases as the radius,  $r$ , goes to zero. This is due to the fact that the magnetic field in a sextupole magnet goes to zero at the origin. This means that a change in the external magnetic field,  $B_{ext}$ , the pole-tip field,  $B_0$ , or the radial position dependent,  $B(r)$ , produces the same effect on the radial component of the sextupole force and can be studied by simply varying the parameter  $b$ .

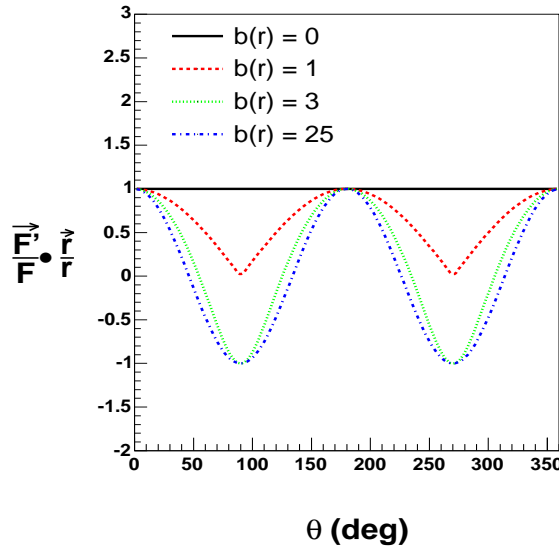


Figure 3-7: Radial component of the force,  $F'_r$ , acting on the atom inside of a sextupole magnet in the presence of the external magnetic field,  $B_{ext}$ , plotted for different values of  $b(r) = B_{ext}/B(r)$  vs. azimuthal coordinate,  $\theta$ .

Figure 3-7 shows a plot of the radial component of the magnetic sextupole field,  $F'_r$ ,

for different values of  $B_{ext}/B(r)$  vs. the azimuthal coordinate,  $\theta$ , of an atom inside of a cylindrical magnet. In the presence of a small, non-zero external magnetic field, the force on an atom in the sextupole system is reduced, but it remains in the proper direction. As the parameter  $b$  increases, the force changes sign in some intervals of  $\theta$ . At  $\theta = 0^\circ$  and  $180^\circ$  the magnetic force has a magnitude of 1 and points in the  $+\hat{r}$  direction, whereas at  $\theta = 90^\circ$  and  $270^\circ$  the force is exactly in the opposite direction. At the azimuthal angles of  $90^\circ$  and  $270^\circ$  the force on the atoms has only a  $y$ -component,  $F'_y$  from eqn. 3.8. Conversely, at  $\theta = 0^\circ$  and  $180^\circ$  the force is purely in the  $\hat{x}$  direction. Hence, in the strong external magnetic field limit, the  $F'_x$  component of the force remains the same as  $F_x$  (the field in the absence of  $B_{ext}$ ) while  $F'_y$  switches sign. When this happens, the sextupole focusing is significantly reduced and the atoms in those positions along the azimuthal direction get completely defocused.

This subtle effect was not observed in any other atomic beam sources, since all of them have been operated in the presence of only weak external fields. Once the significance of this phenomenon was realized<sup>4</sup> the external field value was accounted for in the ray trace program. The results are plotted in figure 3-8 [120]. The figure clearly shows a strong defocusing due to the external BLAST field. The transmission drops by almost a factor of two. The only way to reduce this effect is to add magnetic shielding to the sextupole magnet system. The result of shielding was a significant increase in the atomic beam intensity (see the discussion of the intensity results in section 3.6.1).

### 3.2.1 ABS Sextupole Magnet System at BLAST

The original sextupole magnet system was received from NIKHEF. However, it soon became apparent that the pole-tip fields of these magnets were not up to specifications. Most probably these permanent magnets were damaged at Bates during heat activation of the pumps in the area close to the magnets. A new set of magnets was ordered. The material for the new set was chosen to be *VAC Vacomax 225HR-2:17 samarium cobalt* which has better high temperature characteristics.

Each magnet consists of 24 individual segments (see fig. 3-9) that were assembled and epoxied together at Bates. In all there are seven sextupole magnets used in the ABS.

---

<sup>4</sup>It was first assumed that the effect had to be small due to the strength of the pole-tip field of the sextupole magnet.

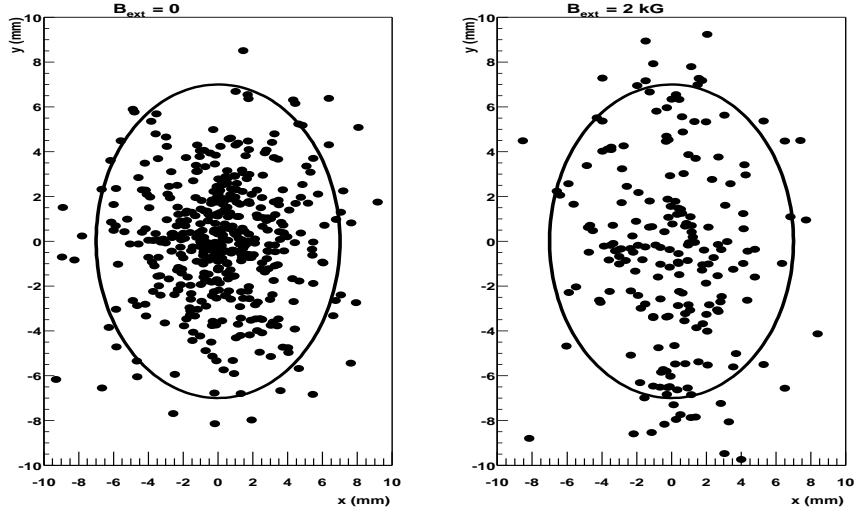


Figure 3-8: The effect of the external BLAST magnetic field on focusing in the sextupole system. The left panel shows focusing with no external field. The right panel shows focusing with a strong external magnetic field. The circle is the injection tube into the target cell. Due to the defocusing caused by the external magnetic field the transmission through the sextupole system is reduced by a factor of two.

Magnets 1, 2 and 3 have a tapered inner diameter design, whereas magnets 4, 5, 6 and 7 have a constant diameter.

The magnetic field of an untapered sextupole magnet is written in cylindrical coordinates as a function of its radius and length as [121]

$$\begin{aligned}
 B(r, z) &= B_0 \left( \frac{r}{r_0} \right)^2 \frac{1}{1 + e^s} \\
 s &= \sum_{n=0}^5 a_n d^n \\
 d &= \frac{z - L/2}{2r_0},
 \end{aligned} \tag{3.10}$$

where  $L$  is the length of a magnet,  $B_0$  and  $r_0$  are the pole-tip field and pole-tip radius of the magnet, respectively. In case of a magnet with a tapered inner diameter, the field has a

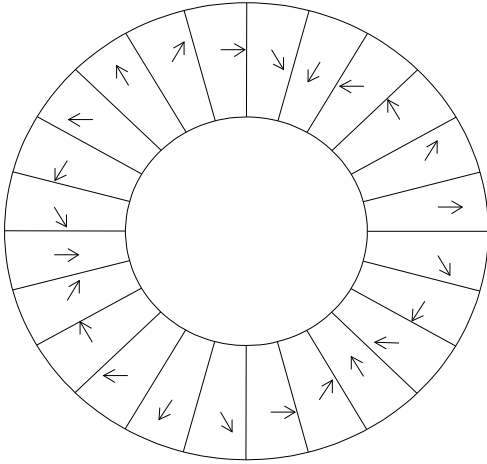


Figure 3-9: A diagram of a typical sextupole magnet used to focus/defocus atoms passing through the opening inside. A magnet consists of 24 permanent magnets epoxied together. The magnetic axis is rotated by  $45^\circ$  in each successive piece.

Magnet	NIKHEF Pole-tip Field, kG	BATES Pole-tip Field, kG
1	8.3	13.5
2	9.1	12.4
3	9.9	12.0
4	11.6	11.6
5	15.6	12.7
6	15.4	12.5
7	15.2	11.9

Table 3.1: Pole-tip field values of the individual sextupole magnets from NIKHEF and Bates. The strength of the first three magnets is improved.

more complex form

$$\begin{aligned}
 B(r, z) &= B_0 \left( \frac{r}{r_0} \right)^2 \frac{1}{1 + b_1 z + b_2 z^2} \frac{1}{1 + e^s} \\
 r_0 &= \frac{r_1 + r_2}{2} \\
 d &= \begin{cases} \frac{z-L/2}{2r_1} & \text{for } z < 0 \\ \frac{z-L/2}{2r_2} & \text{for } z > 0 \end{cases},
 \end{aligned} \tag{3.11}$$

where  $s$  is defined in equation 3.10,  $r_1$  and  $r_2$  are the inner radii at the top and bottom of the cylindrical magnet.

All seven new magnets were carefully mapped at Bates and the values were fitted for all parameters in eqns. 3.10 and 3.11. The pole-tip field values are listed in table 3.1. Even though magnets 4 through 7 show no improvement, the intensity is most sensitive to the

strength of the top three magnets (1, 2 and 3). The magnets were encased in steel to reduce the effect of the BLAST magnetic field described above.

The measured sextupole magnetic fields were used in a ray-tracing program (see fig. 3-10) which is capable of tracking hydrogen or deuterium atoms through the ABS volume. The velocity distribution of the atoms streaming from the nozzle is assumed to be Maxwellian

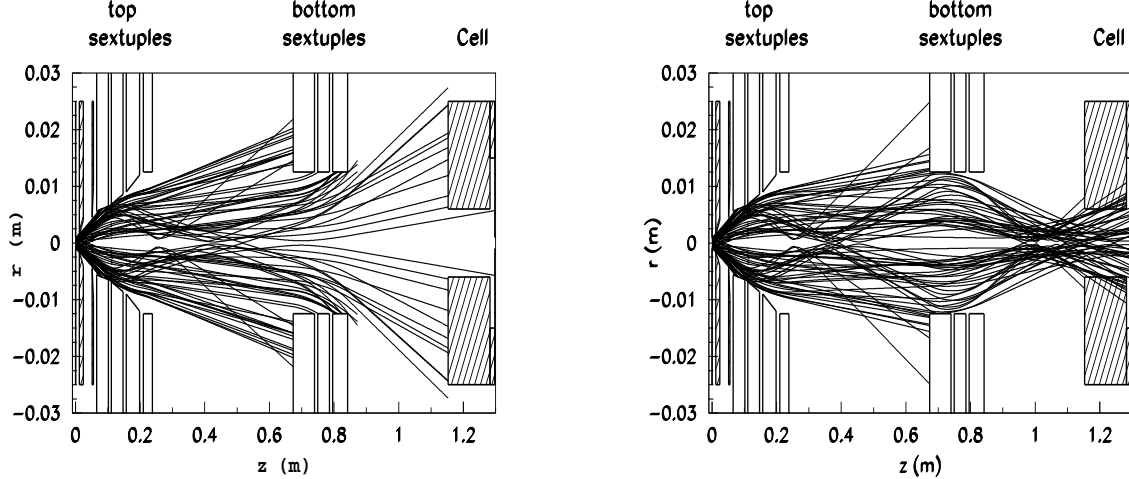


Figure 3-10: Ray tracing in the ABS. The atomic beam is moving from left to right. The top (very left) sextupole system focuses the atoms in hyperfine states with  $m_S = +\frac{1}{2}$ . In the left figure the atoms' electron spin of  $m_S = +\frac{1}{2}$  transition into  $m_S = -\frac{1}{2}$  between the top and bottom sextupole sets and get defocused in the bottom sextupole system. In the right figure the atoms keep their electron spin and get focused in the bottom sextupole set.

$$f(v) = \frac{\alpha}{v} \left( \frac{mv^2}{2k_B T} \right)^2 e^{-\frac{m(v-v_0)^2}{2k_B T}}, \quad (3.12)$$

where  $T$  is the temperature at the nozzle ( $\approx 70$  K),  $m$  is the mass of an atom,  $v$  is the velocity of an individual atom and  $v_0$  is the average velocity,  $\alpha$  is the arbitrary constant used for normalization and  $k_B$  is the Boltzmann constant. The distances between the ABS elements were optimized for the intensity and polarization simultaneously. The sextupoles were designed to focus all atoms in a hyperfine state with  $m_S = +\frac{1}{2}$  and defocus all atoms in  $m_S = -\frac{1}{2}$  states. The tracking simulation was used to optimize the focusing of the  $m_S = +\frac{1}{2}$  atoms in the top sextupole system and focusing/defocusing of the atoms in the bottom sextupole system. The defocusing in the bottom sextupole system was optimized for those

atoms in the simulation that change their hyperfine population from a  $m_S = +\frac{1}{2}$  to  $m_S = -\frac{1}{2}$  state between the top and bottom sextupoles systems<sup>5</sup> (see fig. 3-10). The focusing in the bottom sextupole was studied when there was no hyperfine population transition. Table 3.2

ABS Elements	Distances (mm)
Skimmer	12.0
Collimator	52.0
Sextupole #1	65.7
Sextupole #2	111.7
Sextupole #3	157.7
Sextupole #4	208.4
Sextupole #5	589.6
Sextupole #6	681.0
Sextupole #7	721.6
Cell Inlet	1056.0

Table 3.2: Distances from the nozzle of the focusing and collimating elements in the ABS.

shows the distances *from the nozzle* in the present ABS configuration.

## 3.3 Polarization Techniques

### 3.3.1 Hyperfine States of Hydrogen and Deuterium

The polarization technique in the Atomic Beam Source exploits the energy splitting in a single electron atom due to the hyperfine interaction, which arises from the interaction between the spins of the electron ( $\vec{S}$ ) and the nucleus ( $\vec{I}$ ). The pure hyperfine Hamiltonian has  $2S + 1$  distinct eigen-values. The hyperfine energy levels are further split when the spins of the electron and nucleus couple to the external magnetic field. In the presence of the external magnetic field,  $\vec{B}$ , the total hyperfine interaction Hamiltonian can be written as

$$\mathcal{H}_{HF}^{H/D} = h\nu_{HF}^{H/D} \vec{I} \cdot \vec{S} + \mu_B (g_I^{H/D} \vec{I} + g_S \vec{S}) \cdot \vec{B} \approx h\nu_{HF}^{H/D} \left( \vec{I} \cdot \vec{S} + \vec{S} \cdot \frac{\vec{B}}{B_c^{H/D}} \right), \quad (3.13)$$

where  $\mu_B$  is the Bohr magneton and  $g_I^{H/D}$  is the gyromagnetic factor of hydrogen ( $g_I^H = -0.00304$ ) or deuterium ( $g_I^D = -0.00047$ ) nuclei. The gyromagnetic factor  $g_I^{H/D}$  is orders of magnitude lower than that of the electron ( $g_S = 2.0023$ ). Thus, to a high degree of precision,

<sup>5</sup>The hyperfine population transitions will be discussed in section 3.3.2.

the external magnetic field only couples to the spin of the electron. The characteristic frequency of the hyperfine interaction in eqn. 3.13 is defined as

$$h\nu_{HF}^{H/D} = \mu_B (g_S + g_I) B_c^{H/D} \approx \mu_B g_S B_c^{H/D}, \quad (3.14)$$

where  $B_c^{H/D}$  is the “characteristic” magnetic field. The characteristic hyperfine quantities,  $\nu_{HF}^{H/D}$  and  $B_c^{H/D}$ , are known to high precision [122].

$$\nu_{HF}^H = 1.420GHZ \quad \text{and} \quad B_c^H = 507G \quad (3.15)$$

$$\nu_{HF}^D = 0.327GHZ \quad \text{and} \quad B_c^D = 117G$$

The expectation value of the interaction Hamiltonian,  $\mathcal{H}_{HF}^{H/D}$ , can be found by calculating the expectation values of  $\langle F, m_F; S, m_S | \vec{I} \cdot \vec{S} | I, m_I; F, m_F \rangle$  and  $\langle F, m_F; S, m_S | S_z | I, m_I; F, m_F \rangle$ , separately, where the direction of the magnetic field can be taken to be purely in the  $z$ -direction. The total angular momentum is defined as  $\vec{F} = \vec{I} + \vec{S}$  with  $m_F$  being its  $z$ -component.

In the matrix form the interaction Hamiltonian can thus be written for hydrogen as <sup>6</sup>

$$\mathcal{H}_{HF}^H = \frac{h\nu_{HF}^H}{4} \begin{pmatrix} 1 + 2x & 0 & 0 & 0 \\ 0 & -1 + 2x & 0 & 2 \\ 0 & 0 & 1 - 2x & 0 \\ 0 & 2 & 0 & -1 - 2x \end{pmatrix}, \quad (3.16)$$

---

<sup>6</sup>The details of the calculations can be found in reference [123].

where  $x = \frac{B}{B_c}$ . For deuterium, the interaction Hamiltonian has the form

$$\mathcal{H}_{HF}^D = \frac{h\nu_{HF}^D}{2} \begin{pmatrix} 1 + \frac{3}{2}x & 0 & 0 & 0 & 0 & 0 \\ 0 & \frac{3}{2}x & 0 & 0 & 0 & \sqrt{2} \\ 0 & 0 & -1 + \frac{3}{2}x & 0 & \sqrt{2} & 0 \\ 0 & 0 & 0 & 1 - \frac{3}{2}x & 0 & 0 \\ 0 & 0 & \sqrt{2} & 0 & -\frac{3}{2}x & 0 \\ 0 & \sqrt{2} & 0 & 0 & 0 & -1 - \frac{3}{2}x \end{pmatrix}. \quad (3.17)$$

The energy levels are obtained by diagonalizing the interaction Hamiltonian in eqns. 3.16 and 3.17

Hydrogen	Deuterium	
	$\nu_1^D = \frac{\nu_{HF}^D}{3}(1 + \frac{3}{2}x)$	
$\nu_1^H = \frac{\nu_{HF}^H}{4}(1 + 2x)$	$\nu_2^D = \frac{\nu_{HF}^D}{6}(-1 + \sqrt{(3x + 1)^2 + 8})$	
$\nu_2^H = \frac{\nu_{HF}^H}{4}(-1 + 2\sqrt{x^2 + 1})$	$\nu_3^D = \frac{\nu_{HF}^D}{6}(-1 + \sqrt{(3x - 1)^2 + 8})$	(3.18)
$\nu_3^H = \frac{\nu_{HF}^H}{4}(1 - 2x)$	$\nu_4^D = \frac{\nu_{HF}^D}{3}(1 - \frac{3}{2}x)$	
$\nu_4^H = \frac{\nu_{HF}^H}{4}(-1 - 2\sqrt{x^2 + 1})$	$\nu_5^D = \frac{\nu_{HF}^D}{6}(-1 - \sqrt{(3x - 1)^2 + 8})$	
	$\nu_6^D = \frac{\nu_{HF}^D}{6}(-1 - \sqrt{(3x + 1)^2 + 8})$	

Figure 3-11 shows plots of the hyperfine energy level as a function of the external magnetic

field. This figure illustrates that when the external field is turned off the energy levels become  $2F + 1$  degenerate, whereas at the non-zero external magnetic field each of these two levels split further into  $2F + 1$  levels.

Hydrogen states  $|1\rangle$  through  $|4\rangle$  and deuterium states  $|1\rangle$  through  $|6\rangle$  are the normalized eigenvectors of the interaction Hamiltonian,  $\mathcal{H}_{HF}^{H/D}$ . The wave functions are the linear combinations of states  $|F, m_F; m_I, m_S\rangle$  written in the so-called *Breit-Rabi basis* [124] as

Hydrogen	Deuterium
$ 1\rangle =  1, 1; \frac{1}{2}, \frac{1}{2}\rangle$	$ 1\rangle =  \frac{3}{2}, \frac{3}{2}; 1, \frac{1}{2}\rangle$
$ 2\rangle = \alpha 1, 0; -\frac{1}{2}, \frac{1}{2}\rangle + \beta 1, 0; \frac{1}{2}, -\frac{1}{2}\rangle$	$ 2\rangle = \alpha_+ \frac{3}{2}, \frac{1}{2}; 0, \frac{1}{2}\rangle + \beta_+ \frac{3}{2}, \frac{1}{2}; 1, -\frac{1}{2}\rangle$
$ 3\rangle =  1, -1; \frac{1}{2}, -\frac{1}{2}\rangle$	$ 3\rangle = \alpha_- \frac{3}{2}, -\frac{1}{2}; -1, \frac{1}{2}\rangle + \beta_- \frac{3}{2}, -\frac{1}{2}; 0, -\frac{1}{2}\rangle$
$ 4\rangle = \alpha 0, 0; -\frac{1}{2}, -\frac{1}{2}\rangle - \beta 0, 0; \frac{1}{2}, \frac{1}{2}\rangle,$	$ 4\rangle =  \frac{3}{2}, -\frac{3}{2}; -1, -\frac{1}{2}\rangle$
	$ 5\rangle = \alpha_- \frac{1}{2}, -\frac{1}{2}; 0, -\frac{1}{2}\rangle - \beta_- \frac{1}{2}, -\frac{1}{2}; -1, \frac{1}{2}\rangle$
	$ 6\rangle = \alpha_+ \frac{1}{2}, \frac{1}{2}; 1, -\frac{1}{2}\rangle - \beta_+ \frac{1}{2}, \frac{1}{2}; 0, \frac{1}{2}\rangle,$

where

$$\alpha = \sqrt{\frac{1}{2}\left(1 + \frac{x}{\sqrt{x^2+1}}\right)}$$

$$\beta = \sqrt{\frac{1}{2}\left(1 - \frac{x}{\sqrt{x^2+1}}\right)}$$

where

$$\alpha_{\pm} = \sqrt{\frac{1}{2}\left(1 + \frac{(3x\pm 1)}{\sqrt{(3x\pm 1)^2+8}}\right)}$$

$$\beta_{\pm} = \sqrt{\frac{1}{2}\left(1 - \frac{(3x\pm 1)}{\sqrt{(3x\pm 1)^2+8}}\right)}.$$
(3.19)

One can note from eqn. 3.19 that some eigenstates are “pure” states while some are functions of the external magnetic field.

The electron polarization,  $P_e$ , and the nuclear vector polarization,  $P_z$ , of an atom in an external magnetic field are defined as the expectation values of  $\langle S_z \rangle$  and  $\langle I_z \rangle$ , respectively. Also, in the case of deuterium one can define a *tensor polarization*,  $P_{zz}$ , as the expectation value of  $\langle (3I_z^2 - 2) \rangle$ . Using eqn. 3.19 the polarizations can be expressed in terms of the external magnetic field as

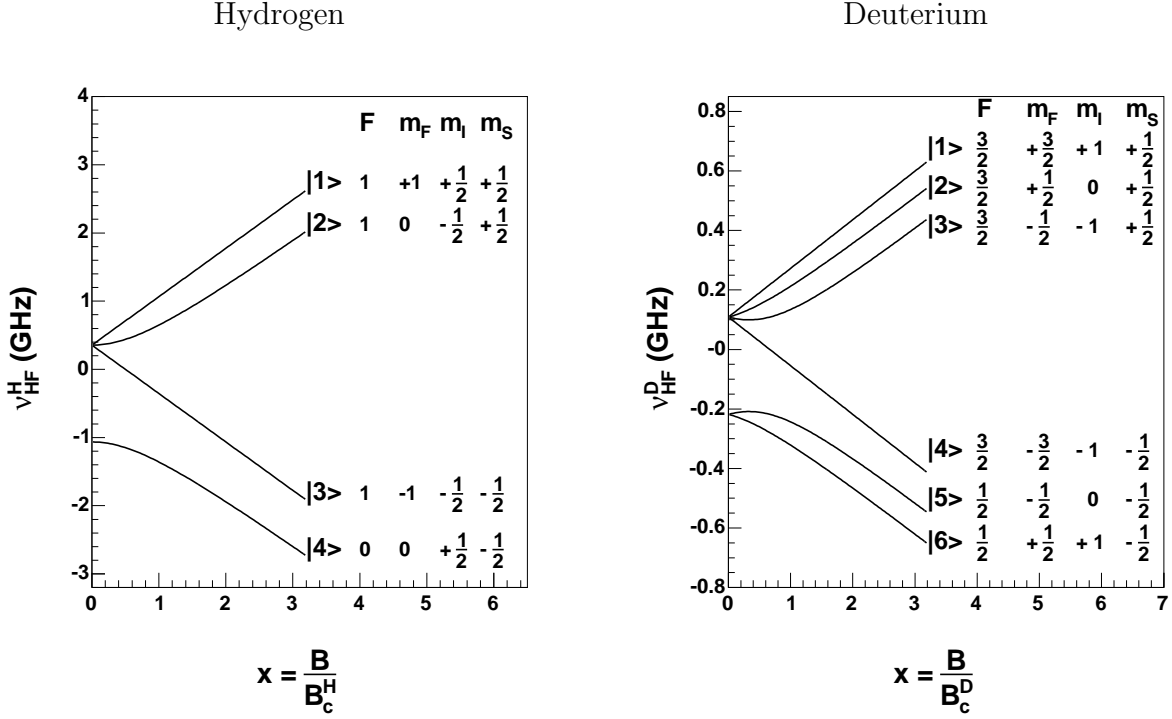


Figure 3-11: Hyperfine structure of hydrogen (left) and deuterium (right).

Hydrogen

$$P_e = N_1 - N_3 + (N_2 - N_4) \frac{x}{\sqrt{x^2+1}}$$

$$P_z = N_1 - N_3 + (N_4 - N_2) \frac{x}{\sqrt{x^2+1}}$$

Deuterium

$$P_e = (N_1 - N_4) + (N_2 - N_6)(\alpha_+^2 - \beta_+^2) + (N_3 - N_5)(\alpha_-^2 - \beta_-^2)$$

$$P_z = N_1 - N_4 + N_2\beta_+^2 - N_3\alpha_+^2 - N_5\beta_-^2 + N_6\alpha_-^2$$

$$P_{zz} = 1 - 3N_2\alpha_+^2 - 3N_3\beta_+^2 - 3N_5\alpha_-^2 - 3N_6\beta_-^2, \quad (3.20)$$

where  $N_k$  is the relative population of the  $|k\rangle$ th eigenstate.

The discussion of the nuclear polarization as a function of the atomic hyperfine state is important in the context of the atomic states injected into the target cell, since the atomic states that produce the best nuclear polarization at a given holding magnetic field should be selected for injection.

Figure 3-12 shows the electron polarization,  $P_e$ , and the nuclear polarization,  $P_z$ , for each hyperfine state of hydrogen. States  $|1\rangle$  and  $|3\rangle$  are independent of the static field. However, the polarizations of the  $|2\rangle$  and  $|4\rangle$  states grow as a function of the field. The holding field was

## Hydrogen

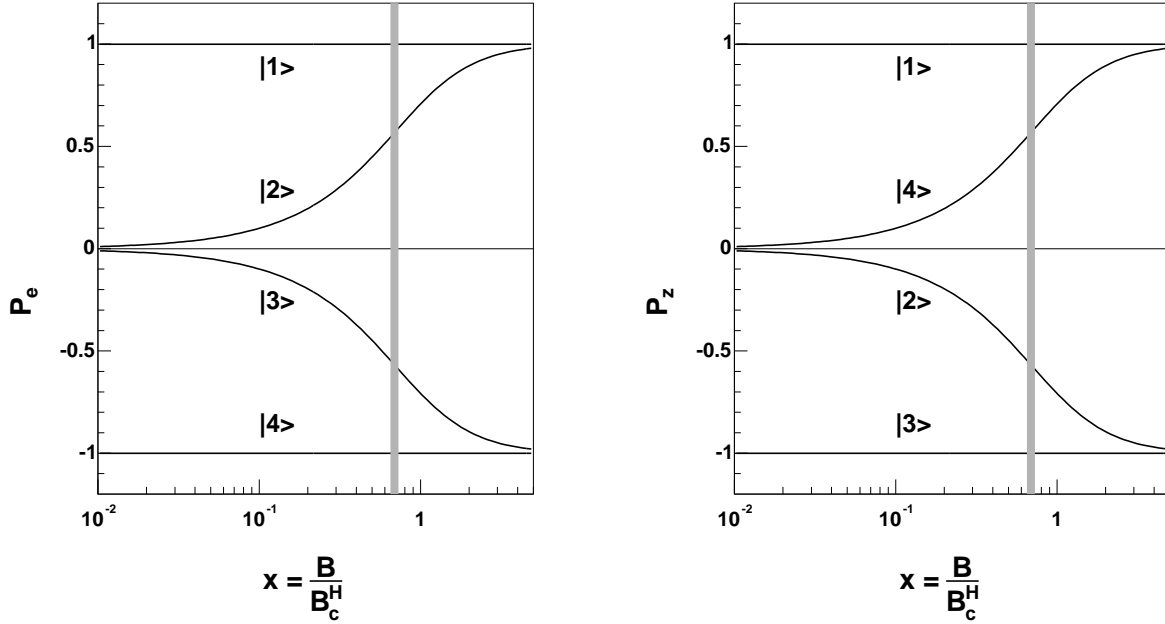


Figure 3-12: Electron (left) and nuclear vector (right) polarizations of each hydrogen hyperfine state as a function of the external magnetic field. The vertical band indicates the holding field in the BLAST target.

chosen to be  $\sim 450$  Gauss<sup>7</sup> indicated by a gray vertical band in the picture. Although both states  $|1\rangle$  and  $|4\rangle$  produce positive nuclear polarization, the holding field is not strong enough for state  $|4\rangle$  to have a high polarization. Thus, injecting both states  $|1\rangle$  and  $|4\rangle$  effectively dilutes the nuclear polarization. The analog applies to the negative nuclear polarization states. Due to this, a single state injection mode was chosen for the hydrogen target, i.e. the state  $|1\rangle$  is injected for  $P_z = 1$  and  $|3\rangle$  for  $P_z = -1$ .

Figures 3-13 and 3-14 show the electron polarization,  $P_e$ , the nuclear vector polarization,  $P_z$ , and the nuclear tensor polarization,  $P_{zz}$ , of the individual hyperfine states of deuterium. With the deuterium target, the holding field is high enough for a two state injection. The difference is due to a lower critical field in deuterium than in hydrogen (see eqn. 3.15). One can notice from the deuterium polarization plots that the states which produce vector polarization,  $P_z = \pm 1$ , also produce tensor polarization,  $P_{zz} = +1$ . This is an important aspect of the polarization scheme employed at BLAST.

<sup>7</sup>This is the highest field limit of the holding field magnet.

## Deuterium

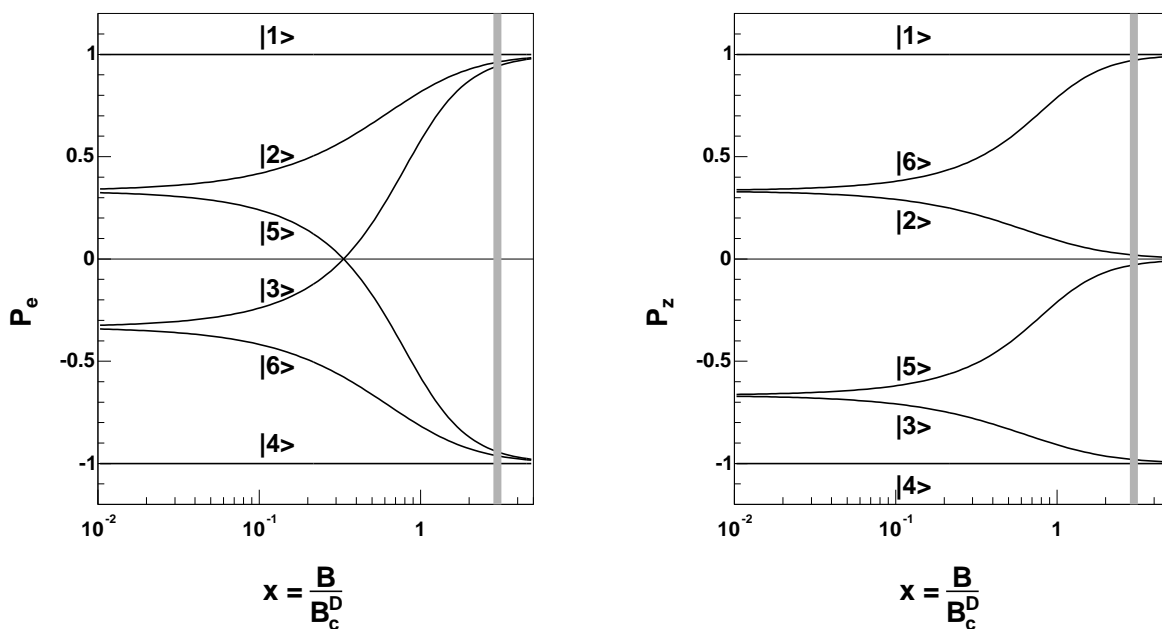


Figure 3-13: Electron (left) and nuclear vector (right) polarization of each deuterium hyperfine state deuterium as a function of the external magnetic field. The vertical band indicates the holding field in the target.

### 3.3.2 RF Transitions

The previous section described the hyperfine states in the external *static* magnetic field, where the population of each hyperfine state remains unchanged. However, when the external time-varying magnetic field is applied the hyperfine states can exchange their populations. This process is typically referred to as the hyperfine RF transitions.

There are two possible cases of the RF transitions. In the first case, the time-varying magnetic field is parallel to the static magnetic field, such that the total magnetic field is

$$\vec{B}(t) = (B_0 + B_{RF}\cos(\omega t))\hat{z}. \quad (3.21)$$

In this case the interaction Hamiltonian has the same matrix form as in eqns. 3.16 and 3.17, where  $x(t) = B(t)/B_c$  is now a function of time. This type of RF transition is called a  $\sigma$ -transition. The eigen-states have a time-dependent Breit-Rabi basis. Since only hydrogen states  $|2\rangle$  and  $|4\rangle$  are functions of an external magnetic field, the only possible RF  $\sigma$ -transition in hydrogen is  $|2\rangle - |4\rangle$ . Similarly, in deuterium, possible  $\sigma$ -transitions are  $|3\rangle - |5\rangle$  and

Deuterium

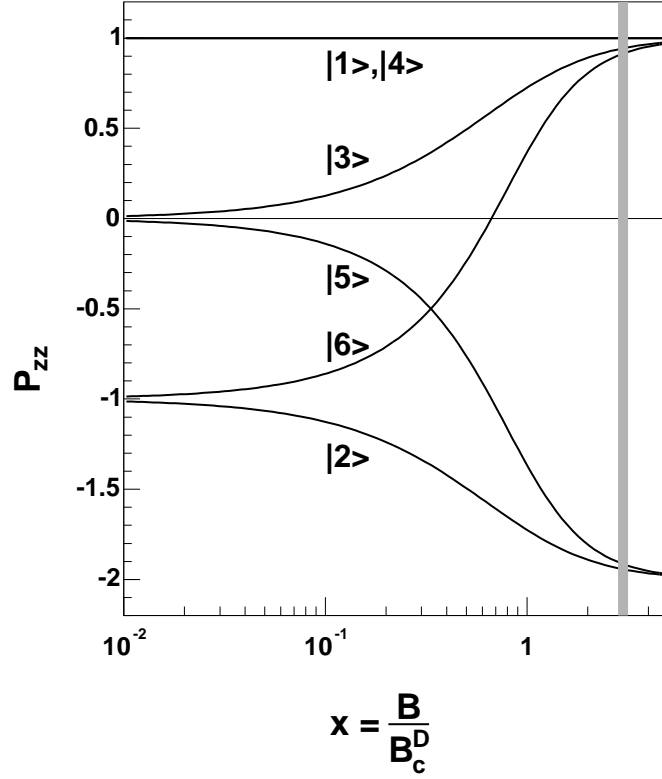


Figure 3-14: Nuclear tensor polarization,  $P_{zz}$  of each deuterium hyperfine state as a function of the external magnetic field. The vertical band indicates the holding field in the target.

$|2\rangle - |6\rangle$ . Accordingly, all RF  $\sigma$ -transitions satisfy the  $\Delta m_F = 0$  selection rule.

In the second case, the time-varying magnetic field is perpendicular to the static magnetic field, such that the total field has the following form

$$\vec{B}(t) = B_0 \hat{z} + B_{RF} \cos(\omega t) \hat{x}. \quad (3.22)$$

The interaction Hamiltonian corresponding to this field has a more complex form

$$H_{HF}^{H/D}(t) = h\nu_{HF}^{H/D} \left( \vec{I} \cdot \vec{S} + S_z \cdot \frac{B_z}{B_c^{H/D}} + \frac{1}{2} (S_+ + S_-) \cdot \frac{B_x(t)}{B_c^{H/D}} \right), \quad (3.23)$$

where  $S_+$  and  $S_-$  are the raising and lowering spin operators. Solving the time-dependent Schrödinger equation,

$$i\hbar \frac{d}{dt} |\Psi\rangle = H_{HF}^{H/D}(t) |\Psi\rangle, \quad (3.24)$$

with this Hamiltonian yields the frequencies at which the RF transitions occur as a function of the external static magnetic field. These RF transitions are called  $\pi$ -transitions. As such, RF  $\pi$ -transitions satisfy the  $\Delta m_F = \pm 1$  selection rule.

Both  $\sigma$ - and  $\pi$ -transitions have one frequency for the particular value of the external static magnetic field at which they occur. However, the atoms in the atomic beam spend different amounts of time in the magnetic field (both static and RF), due the Maxwellian profile of the velocity distribution. This fact limits the efficiency of the RF transitions. For this reason, the high frequency RF transitions are done in the *adiabatic* regime [125, 126].

In the adiabatic regime an atom passes through the static magnetic field,  $B_0$ , superimposed with a gradient and a high frequency time-varying magnetic field,  $B_{gr}$  and  $B_{RF}$ , respectively. The total magnetic field seen by an atom in case of the  $\pi$ -transition is

$$\vec{B}(y, t) = (B_0 + B_{gr}v_x t)\hat{z} + B_{RF}\cos(\omega t)\hat{x}, \quad (3.25)$$

where  $v_x$  is the velocity of an atom passing through the gradient field. The total static magnetic field ( $B_0 + B_{gr}x$ ) slowly (adiabatically) changes along the flight path of an atom.

Typically, the Schrödinger equation (eqn. 3.24) for the Hamiltonian with the magnetic field in eqn. 3.25 is solved numerically. However, R.J. Philpott [126] found an exact analytical solution for the case where there are only two hyperfine states exchanging their populations. In this simpler case the transition probability was found to be

$$P = 1 - \exp^{-2\pi\kappa}, \quad (3.26)$$

where  $\kappa$  is defined as

$$\kappa = \left| \frac{\mu_B g_S B_{RF}^2}{2 \frac{d(B_0 + B_{gr}v_x t)}{dt} \hbar} \right| = \left| \frac{\mu_B g_S B_{RF}^2}{2 B_{gr} v_x \hbar} \right|. \quad (3.27)$$

Hence, for the probability of an adiabatic transition,  $P$ , to be close to unity, the following adiabatic condition needs to be satisfied

$$B_{gr} \ll \frac{\mu_B g_S B_{RF}^2}{2 v_x \hbar}. \quad (3.28)$$

It follows that for a proper match between the gradient field,  $B_{gr}$ , and the RF field amplitude,

$B_{RF}$ , can provide close to 100% efficiency of an RF transition.

### Medium Field and Weak Field RF Transitions

The Medium Field Transition (MFT) and Weak Field Transition (WFT) are RF  $\pi$ -transitions. In the medium and weak field transition regimes the hyperfine states of the same multiplet exchange their populations. The possible  $\pi$ -transitions in hydrogen and deuterium are listed below.

<i>Hydrogen</i>	<i>Deuterium</i>	
$ 1\rangle \leftrightarrow  2\rangle$ (MFT1-2)	$ 1\rangle \leftrightarrow  2\rangle$ (MFT1-2)	(3.29)
$ 2\rangle \leftrightarrow  3\rangle$ (MFT2-3)	$ 2\rangle \leftrightarrow  3\rangle$ (MFT2-3)	
$ 2\rangle \leftrightarrow  3\rangle$ (MFT2-3)	$ 3\rangle \leftrightarrow  4\rangle$ (MFT3-4)	
	$ 5\rangle \leftrightarrow  6\rangle$ (MFT5-6)	

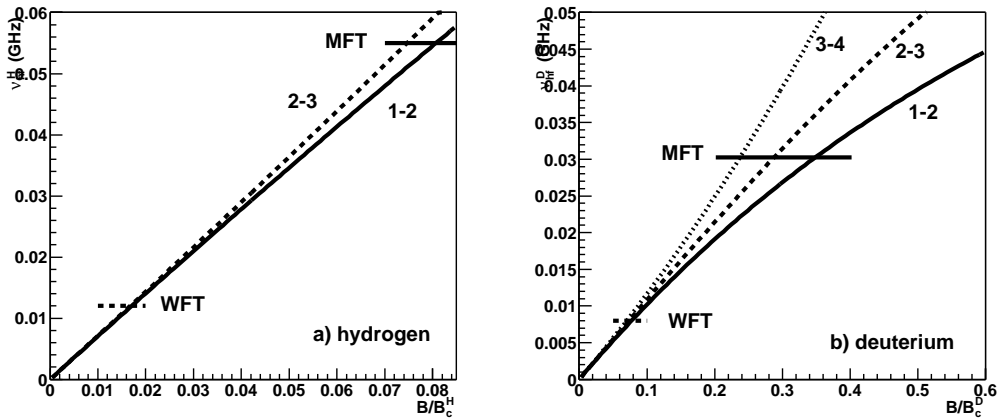


Figure 3-15: The frequency of the RF  $\pi$ -transitions in hydrogen (left) and deuterium (right) as a function of the static magnetic field. Horizontal lines indicate the frequency at which the MFT and WFT transition units are operated during the BLAST experiment. A negative gradient corresponds to the field seen by the atom changing from right to left, while a positive gradient corresponds to change from left to right.

Figure 3-15 shows the frequency of these transitions in the MFT and WFT units as a function of the static magnetic field. A choice of the positive gradient along the flight path of a particle induces a sequence of hydrogen RF transitions MFT2-3 followed by MFT1-2 and of deuterium RF transitions MFT3-4, MFT2-3, MFT1-2, respectively. The resulting

transition is MFT1-3 in hydrogen and MFT1-4 in deuterium. The negative gradient produces the hydrogen RF transition MFT2-3 and deuterium RF transition MFT3-4.<sup>8</sup> The MFT frequencies of the individual transitions are chosen so that the magnetic fields at which the transitions occur are well separated.

The WFT transition is operated at a lower frequency at which the static magnetic fields of the hyperfine transitions are not separated. The atoms passing through the WFT experience a static field at which all  $\pi$ -transitions are taking place at once<sup>9</sup>. Therefore, the WFT operates with a positive gradient along the atomic flight path, inducing the transition WFT1-3 in hydrogen and cascading WFT1-4 in deuterium. In fact, the WFT is typically used to induce hydrogen  $|1\rangle$ - $|3\rangle$  and deuterium  $|1\rangle,|2\rangle$ - $|3\rangle,|4\rangle$  transitions in the atomic beam, since the WFT requires a lower gradient field thus improving the transition efficiency.

### Strong Field RF Transition

The Strong Field Transition (SFT) refers to the RF  $\sigma$ -transition. The atoms passing through the SFT change their hyperfine state population between states in different multiplets ( $\Delta F = \pm 1$ ) with  $\Delta m_F = 0$ . Hence, possible RF  $\sigma$ -transitions in hydrogen and deuterium are

$$\begin{array}{ll}
 \textit{Hydrogen} & \textit{Deuterium} \\
 |2\rangle \leftrightarrow |4\rangle \text{ (SFT2-4)} & |2\rangle \leftrightarrow |6\rangle \text{ (SFT2-6)} \\
 & |3\rangle \leftrightarrow |5\rangle \text{ (SFT3-5)}.
 \end{array} \tag{3.30}$$

The condition in eqn. 3.28 also applies to the  $\sigma$ -transition. Therefore, a well-chosen gradient field is also important to the efficiency of the SFT transition. Figure 3-16 shows the frequencies of the RF  $\sigma$ -transitions in hydrogen and deuterium as a function of the external magnetic field. The two  $\sigma$ -transitions in deuterium are well separated. The SFT2-4 transition in hydrogen is not used in the BLAST polarization scheme while both the SFT2-6 and SFT3-5 transitions in deuterium are required for the target operation.

---

<sup>8</sup>It is assumed here that the hydrogen hyperfine states  $|3\rangle$  and  $|4\rangle$  and deuterium hyperfine states  $|4\rangle$ ,  $|5\rangle$  and  $|6\rangle$  have been rejected in the top sextupole system before entering the MFT unit. For details see section 3.3.3

<sup>9</sup>These are called *cascading transitions*.

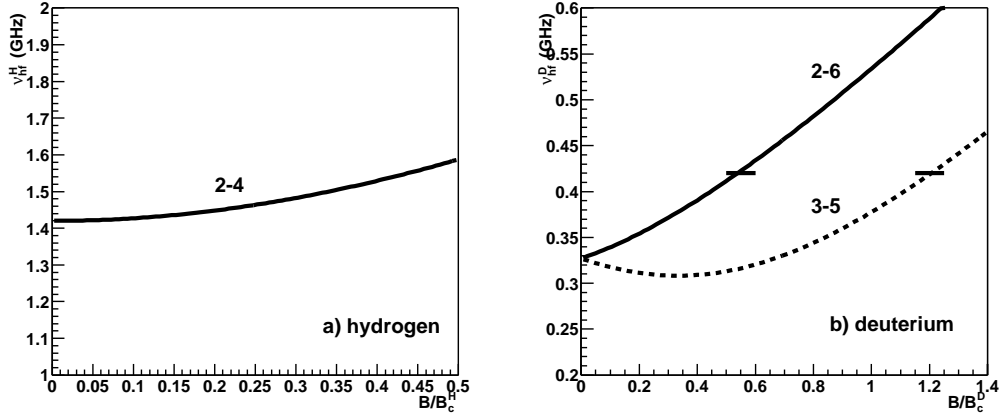


Figure 3-16: The frequency of SFT RF  $\sigma$ -transitions in hydrogen (left) and deuterium (right) as a function of the magnetic field. Horizontal lines indicate the frequency at which the SFT unit is operated.

### 3.3.3 Polarization States in the Target

As discussed before, the hydrogen atoms are injected into the target cell in the single state mode due to the limitation of the holding field magnet. Since the critical field of deuterium is significantly lower, both vector and tensor polarization states in the target are prepared using the two state injection.

The hydrogen atoms are ejected from the nozzle with all four hyperfine states equally populated by  $n_1, n_2, n_3, n_4$ . *Vector plus* and *vector minus* polarized hydrogen atomic beam is separately injected in the target cell after it undergoes a sequence of transitions. For the vector plus state the transition sequence is

$$\begin{pmatrix} n_1 \\ n_2 \\ n_3 \\ n_4 \end{pmatrix} \xrightarrow{6-pole} \begin{pmatrix} n_1 \\ n_2 \\ 0 \\ 0 \end{pmatrix} \xrightarrow{MFT} \begin{pmatrix} n_1 \\ 0 \\ n_3 \\ 0 \end{pmatrix} \xrightarrow{6-pole} \begin{pmatrix} n_1 \\ 0 \\ 0 \\ 0 \end{pmatrix}, \quad (3.31)$$

and for the vector minus state the sequence is

$$\begin{pmatrix} n_1 \\ n_2 \\ n_3 \\ n_4 \end{pmatrix} \xrightarrow{6-pole} \begin{pmatrix} n_1 \\ n_2 \\ 0 \\ 0 \end{pmatrix} \xrightarrow{MFT} \begin{pmatrix} n_1 \\ 0 \\ n_3 \\ 0 \end{pmatrix} \xrightarrow{6-pole} \begin{pmatrix} n_1 \\ 0 \\ 0 \\ 0 \end{pmatrix} \xrightarrow{WFT} \begin{pmatrix} 0 \\ 0 \\ n_3 \\ 0 \end{pmatrix}. \quad (3.32)$$

The unpolarized deuterium atomic beam exiting the nozzle has all six hyperfine states

equally populated by  $n_1, n_2, n_3, n_4, n_5, n_6$ . The beam of deuterium atoms becomes *vector plus*, *vector minus* and *tensor minus* polarized by passing through a sequence of transitions.

For the vector plus beam the transition sequence is

$$\begin{pmatrix} n_1 \\ n_2 \\ n_3 \\ n_4 \\ n_5 \\ n_6 \end{pmatrix} \xrightarrow{6-pole} \begin{pmatrix} n_1 \\ n_2 \\ n_3 \\ 0 \\ 0 \\ 0 \end{pmatrix} \xrightarrow{MFT} \begin{pmatrix} n_1 \\ n_2 \\ 0 \\ n_4 \\ 0 \\ 0 \end{pmatrix} \xrightarrow{6-pole} \begin{pmatrix} n_1 \\ n_2 \\ 0 \\ 0 \\ 0 \\ 0 \end{pmatrix} \xrightarrow{SFT} \begin{pmatrix} n_1 \\ 0 \\ 0 \\ 0 \\ 0 \\ n_6 \end{pmatrix}, \quad (3.33)$$

for the vector minus the sequence is

$$\begin{pmatrix} n_1 \\ n_2 \\ n_3 \\ n_4 \\ n_5 \\ n_6 \end{pmatrix} \xrightarrow{6-pole} \begin{pmatrix} n_1 \\ n_2 \\ n_3 \\ 0 \\ 0 \\ 0 \end{pmatrix} \xrightarrow{MFT} \begin{pmatrix} n_1 \\ n_2 \\ 0 \\ n_4 \\ 0 \\ 0 \end{pmatrix} \xrightarrow{6-pole} \begin{pmatrix} n_1 \\ n_2 \\ 0 \\ 0 \\ 0 \\ 0 \end{pmatrix} \xrightarrow{WFT} \begin{pmatrix} 0 \\ 0 \\ n_3 \\ n_4 \\ 0 \\ 0 \end{pmatrix}, \quad (3.34)$$

and for the tensor minus the transition sequence is

$$\begin{pmatrix} n_1 \\ n_2 \\ n_3 \\ n_4 \\ n_5 \\ n_6 \end{pmatrix} \xrightarrow{6-pole} \begin{pmatrix} n_1 \\ n_2 \\ n_3 \\ 0 \\ 0 \\ 0 \end{pmatrix} \xrightarrow{MFT} \begin{pmatrix} 0 \\ n_2 \\ n_3 \\ n_4 \\ 0 \\ 0 \end{pmatrix} \xrightarrow{6-pole} \begin{pmatrix} 0 \\ n_2 \\ n_3 \\ 0 \\ 0 \\ 0 \end{pmatrix} \xrightarrow{SFT} \begin{pmatrix} 0 \\ n_2 \\ 0 \\ 0 \\ n_5 \\ 0 \end{pmatrix}. \quad (3.35)$$

Table 3.3 has a compilation of the required transitions for all polarization states injected into the target cell at BLAST.

As noted before, the vector plus and vector minus states in deuterium are also a tensor plus state. Therefore, the experiments that require both vector and tensor polarized deuterium target can be run simultaneously with the sequence of  $P_z = +1, -1$  and  $P_{zz} = -2$  injected. In this “three-state” scheme the experiment requiring the tensor polarized target runs 100% of the time, while the experiment on the vector polarized target uses 2/3 of the total run time. Compared to the sequentially running of the vector and tensor polarization

	Hydrogen		Deuterium		
	Vector +	Vector -	Vector +	Vector -	Tensor -
MFT	$\pi_{2-3}$	$\pi_{2-3}$	$\pi_{3-4}$	$\pi_{3-4}$	$\pi_{1-4}$
SFT	off	off	$\sigma_{2-6}$	off	$\sigma_{3-5}$
WFT	off	$\pi_{1-3}$	off	$\pi_{1,2-3,4}$	off
$P_z$	+1	-1	1	-1	0
$P_{zz}$	-	-	1	1	-2

Table 3.3: RF transitions used in the ABS operation to produce vector polarized hydrogen and vector/tensor polarized deuterium atomic beams.

experiments this effectively increases the figure of merit for the vector polarization experiment by 30 % and for the tensor polarization experiment by a factor of 2. For example, if there are vector and tensor target experiments designed to run 1000 hours each, with the “three-state” scheme the tensor target experiment runs for 2000 hours and the vector target experiment runs for  $2/3 \times 2000$  hours.

## 3.4 The RF Transition Units

The operation of the RF units is controlled by a special sequencer program which manages the flipping of the polarization states in the target. During each polarization change which occurs every 5 minutes an RF unit magnet is cycled through the hysteresis loop before a new field value is set.

### 3.4.1 MFT

The Medium Field Transition Unit had to be redesigned to fit the BLAST specifications. In redesigning the new MFT unit, the problem of the strong magnetic field created by the BLAST toroid had to be addressed. In the region of the MFT the BLAST spectrometer field is  $\sim 2.2$  kG with a strong vertical gradient (solid curve in fig. 3-17).

The full TOSCA magnetic field calculation was used to study possible magnetic shielding schemes. The design was adopted in which a thick metal shield reduces the external BLAST magnetic field to  $\sim 1.3$  kG and a set of water cooled copper coils capable of generating fields inside of the MFT of up to 2 kG sets the correct static field (dashed curve in fig. 3-18).

However, due to a simulation flaw, the magnetic coils were heavily over designed. The

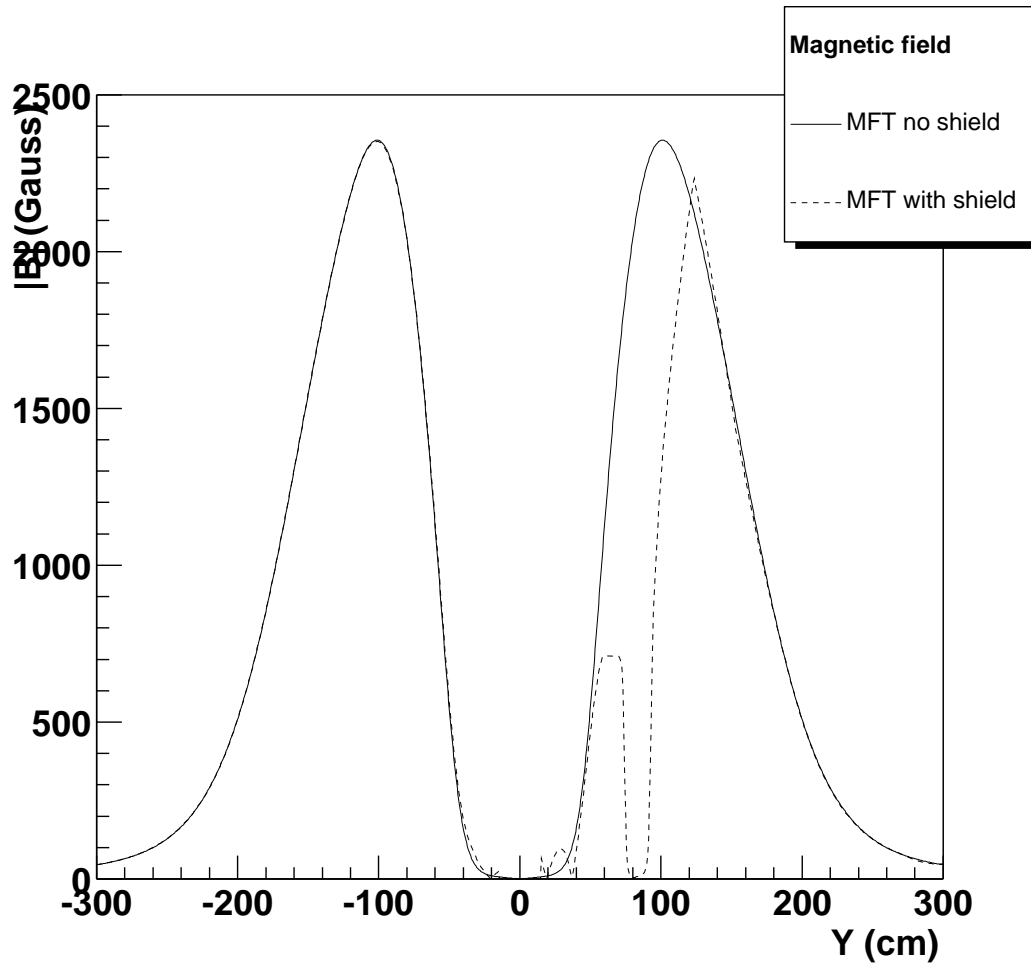


Figure 3-17: TOSCA model of the magnitude of the BLAST magnetic field along the path of the atomic beam. The atomic beam moves from right to left in this picture. The full curve is the field without the MFT shielding and the dashed curve is the field after the MFT shielding was put into the TOSCA model. The MFT unit is located between 70 and 90 cm in Y.

magnetic shield turned out to be more efficient in shielding the external BLAST field (down to  $\sim 200$  G) than expected. It is believed that the TOSCA simulations were performed with a lower grade steel than the one used to build the magnetic shield. Hence, the coils are operated at a significantly lower current than they were designed for. This, however, does not preclude the efficient operation of all RF transitions in the MFT. The reduction of the BLAST field by the magnetic shield of the MFT is localized only to the region of the MFT, as can be seen in fig 3-17 which shows the magnetic field profile along the flight path of the atomic beam predicted by TOSCA simulation.

After the BLAST field is canceled by the magnetic shield a small positive field gradient

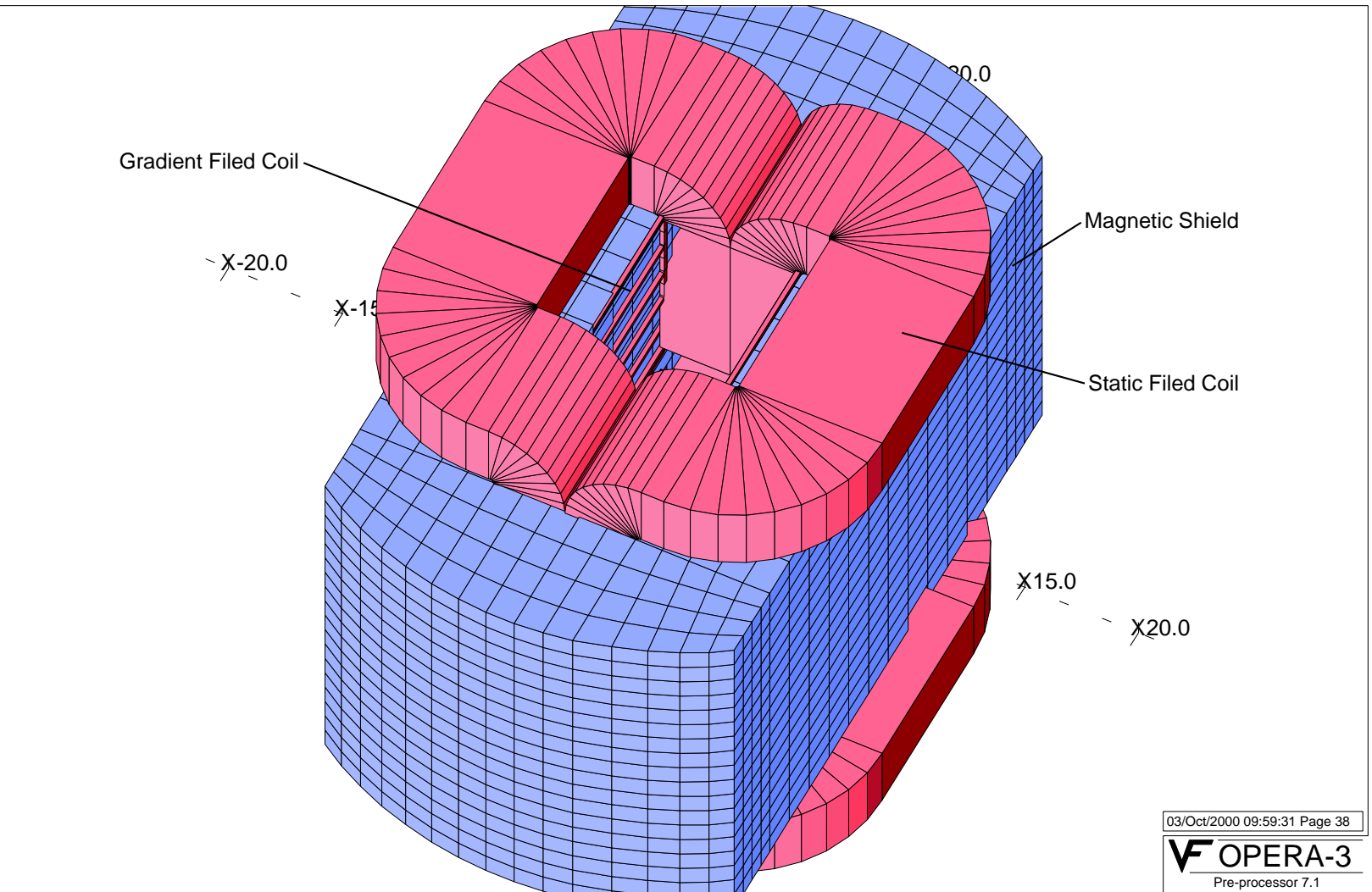


Figure 3-18: The TOSCA design of the MFT magnetic shield (blue) and magnetic coils (red). A heavy set of coils was needed to handle a large current. Gradient coils (in red) are seen on the walls of the magnetic shield. An RF coil fits inside.

along the flight path of the atomic beam remains. This small residual gradient is useful for some RF transitions in the MFT. At the same time the MFT unit is equipped with a set of gradient coils, which can easily reverse the residual positive gradient.

The RF field is fed into the MFT through the RF coil, which is 12 cm long solenoid with 6 turns and 3 cm in diameter. The time-varying magnetic field in the solenoid is parallel to the flight path of the atomic beam. The RF frequency is remotely controlled inside the RF power supply. A pick-up coil is used to monitor the amplitude of the RF field in the MFT (see fig 3-19).

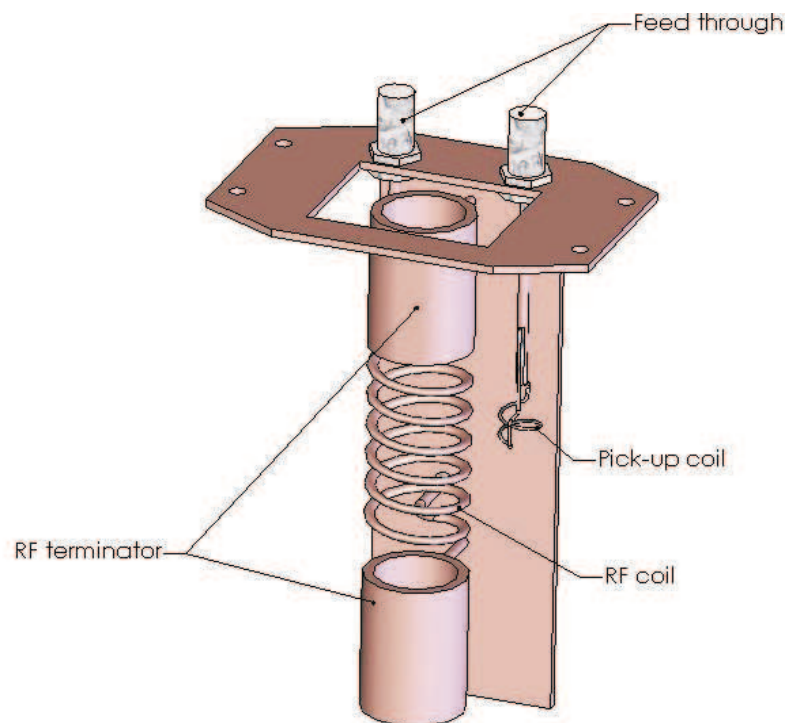


Figure 3-19: MFT RF unit which fits inside of the MFT magnet in fig. 3-18. The atomic beam is directed downward. Not shown is the magnetic field Hall probe which is located on the inside of the magnetic shield.

The static magnetic field created by the MFT coils is controlled by the PID loop. The magnetic field is set by the sequencer which controls flipping of the target polarization states. The current in the MFT coils is remotely adjusted while the Hall probe inside of the MFT unit measures the magnetic field. The rate of the current adjustment is proportional to the

difference between the set and measured fields. This PID loop operates until the field inside of the MFT is correctly established. The PID loop stays active to correct any drifts of the MFT static field away from the set value. The drifts of the static field in the MFT were observed to be large enough to completely move the RF transitions off resonance. With the PID loop on, the magnetic field is kept constant within 1 G.

### 3.4.2 WFT

The WFT unit is located in the lower part of the BLAST magnet, closer to the target (see fig 3-1). This means that the BLAST field in the WFT unit is significantly lower ( $\sim 300$  Gauss). A simple electromagnet is capable of producing a magnetic field large enough to cancel the external BLAST field and the field due to the target holding magnet. Due to this fact, the open geometry design of the WFT magnet was adopted from the NIKHEF design (see fig. 3-21). The WFT unit shares the static and gradient field coils with the SFT. The same PID loop mechanism that is used in the MFT is also used with the WFT/SFT magnet, resulting in a magnetic field stability of less than 1 Gauss for all transitions.

Similarly to the MFT, the RF field is fed into the RF coil, producing the time-varying magnetic field along the flight path of the atom beam essential to the  $\pi$ -transition. The pick-up coil is used to monitor the amplitude of the RF field in the WFT (see fig 3-20)

### 3.4.3 SFT

The high frequency RF field is used to induce SFT transitions in the deuterium atomic beam. The RF source for the SFT unit has a fixed frequency of 420 MHz. The RF power used to induce an SFT transition in deuterium is  $\sim 9$  Watts. This level of power output requires dynamic PID retuning capabilities as the RF conditions change inside of the cavity. The changes in the RF conditions arise from the thermal heating of the copper cavity. To limit the heating of the cavity the copper material of the cavity was silver-plated (see fig 3-20) .

The RF field in the SFT is created between two copper conductors inside of the RF cavity with a large Q-value. The time-varying magnetic field is oriented along the static field and perpendicular to the flight path of the deuterium atoms. The pick-up coil inside of the SFT is used for both monitoring of the RF amplitude and the PID control of the RF

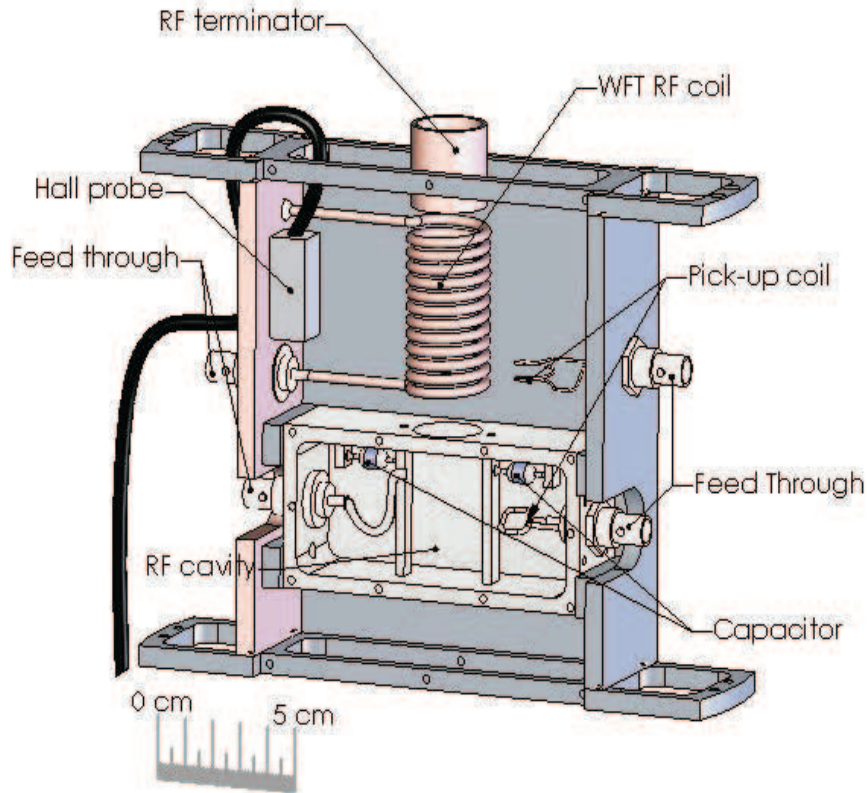
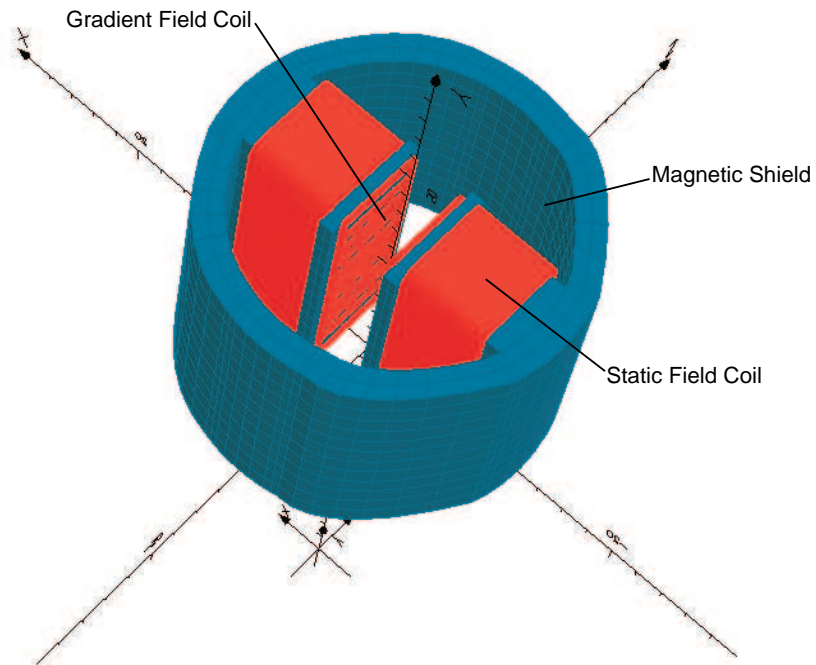


Figure 3-20: The WFT and SFT RF units share the same magnet shown in fig. 3-21. The top coil is the WFT RF coil and the box on the bottom is the silver plated SFT RF cavity. The atomic beam is directed from top to bottom.

tuning circuit.

### 3.5 The Scattering Chamber

The target scattering chamber was also received from NIKHEF. It consists of a holding field magnet capable of generating longitudinal and transverse magnetic fields, a target cell on a holder with a cooling system and thin aluminum windows. Since the target chamber is internal to the South Hall Ring, it shares vacuum with the ring. Thus, strong vacuum pumping is needed to ensure reliable beam operation. The aluminum windows have to be



## **V VECTOR FIELDS**

Figure 3-21: The TOSCA design of the SFT/WFT magnetic shield (blue) and magnetic coils (red). The gradient coils (in red) are seen on the walls of the magnetic shield. The RF cavities fit inside.

thin to reduce multiple scattering and energy loss of the particles exiting the target.

### **3.5.1 Gas in the Storage Cell**

The storage cell is used to increase the luminosity over the pure polarized atomic beam experiment while preserving the stored electron beam quality in the ring. The atomic beam is injected through an inlet tube into a cylindrical cell of a small diameter, fig. 3-22. The polarized atoms are confined by the cell around a stored electron beam thus increasing the probability of a scattering reaction.

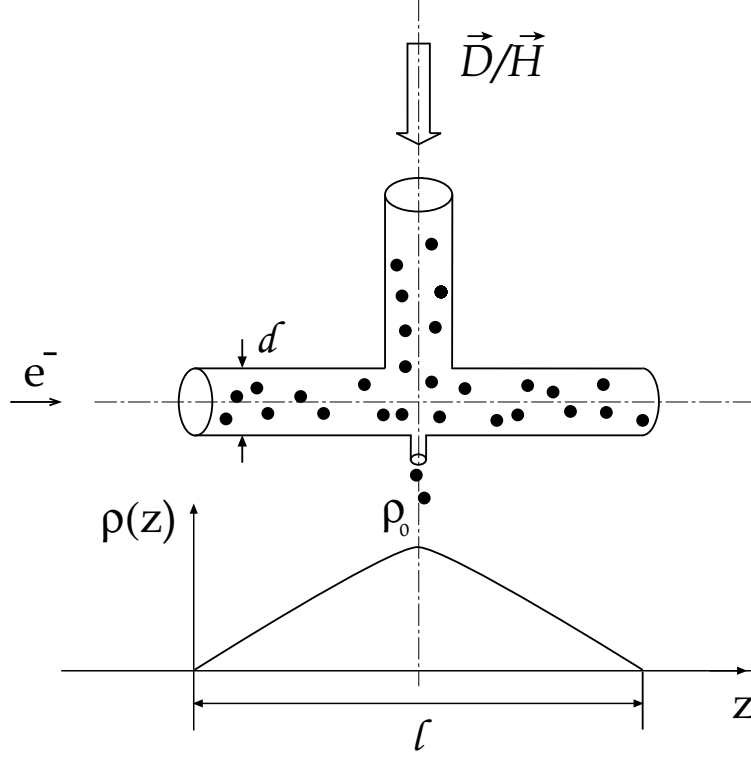


Figure 3-22: Schematic of the atomic beam injected into the storage cell. The polarized atomic beam is injected from the ABS into the inlet tube. The atoms diffuse in the cell until they are pumped out. The electron beam passes through the cell from left to right. A small hole at the bottom of the cell samples atoms injected into the cell. The density profile along the target cell is approximately triangular.

The density profile along the target cell ( $z$ -profile) is approximately triangular [127].

$$\rho(z) = \begin{cases} \frac{2\rho_0}{l}(z + l/2) & , z < 0 \\ \frac{2\rho_0}{l}(l/2 - z) & , z > 0 \end{cases} \quad (3.36)$$

$$\rho_0 = I_0/C_{tot},$$

where  $I_0$  is the intensity of the atomic beam into the cell,  $l$  is the length of the cell and  $C_{tot}$  is the total conductance of the cell. Since there are three openings in the cell<sup>10</sup> through which

<sup>10</sup>Two ends and the inlet tube. Plus there is a small exit hole straight below the inlet tube that samples atomic beam. However, its conductance is negligible.

the gas is pumped out,  $C_{tot}$  is written as

$$\begin{aligned}
C_{tot} &= C_{cell} + C_{inlet}, \\
C_{cell} &= 2C_0 \frac{d_{cell}^3}{l_{cell}/2} \sqrt{\frac{T_{cell}}{M}}, \\
C_{inlet} &= C_0 \frac{d_{inlet}^3}{l_{inlet}} \sqrt{\frac{T_{cell}}{M}},
\end{aligned} \tag{3.37}$$

where  $C_0 = 3.81 \times 10^3 \text{ cm}^3/\text{s}$  is the conductance constant,  $T_{cell}$  is the cell temperature in Kelvin and  $M$  is the atomic mass of the target gas in atomic mass units (amu). The factor of 2 in the equation for  $C_{cell}$  is due to the two open ends in the cell. The gas target thickness per unit area is thus

$$\rho_{tot} = \int_{-l/2}^{l/2} \rho(z) dz = \rho_0 \frac{l}{2}, \tag{3.38}$$

where  $\rho_0$  is defined in eqn. 3.36.

An increase in luminosity can be achieved by increasing the length of a cell,  $l$ . However, due to the limited length of the target magnet, only data collected within 20 cm from the center of the cell are useful in the analysis. Hence,  $l$  in eqn. 3.38 must remain constant and increasing the length of the cell would increase the luminosity purely due to the decrease in the total conductance,  $C_{tot}$ .

Three different cells were used during the commissioning and the production experiment. Table 3.4 lists the conductances and densities for a given flow for these three cells<sup>11</sup>.

	Cell #1		Cell #2		Cell #3	
	Cell	Inlet	Cell	Inlet	Cell	Inlet
Length, $l$ (mm)	400	125	600	125	600	150
Diameter, $d$ (mm)	15	11.9	15	11.9	15	11.9
Temperature, $T$ (K)	90	290	90	290	90	90
Conductance, $C$ ( $\times 10^3 \text{ cm}^3/\text{s}$ )	8.62	6.19	5.76	6.19	5.76	2.87
$C_{tot}$ ( $\times 10^3 \text{ cm}^3/\text{s}$ )	14.81		11.95		8.63	
$\rho_{tot}$ ( $\times 10^{-3} \text{ atoms}/\text{cm}^2$ )	$1.6I_0$		$2.51I_0$		$3.48I_0$	

Table 3.4: Three cells were used during this experiment. Listed here are cells' geometries, temperatures, conductances and density integrated over a whole length of the cell.  $I_0$  is the ABS flow into the cell.

<sup>11</sup>Conductances are listed for the deuterium atoms. Conductances for hydrogen are larger by a factor of  $\sqrt{2}$ .

The low conductance value in cell #3 was achieved by increasing the cell length and cooling the inlet tube. An increase in target thickness between cell #1 and #3 is a factor of 2.2. However, by factoring in a  $|z| < 20$  cut, the increase in thickness is 66%. Close to 90 % of all data used in this work were collected with cell #3.

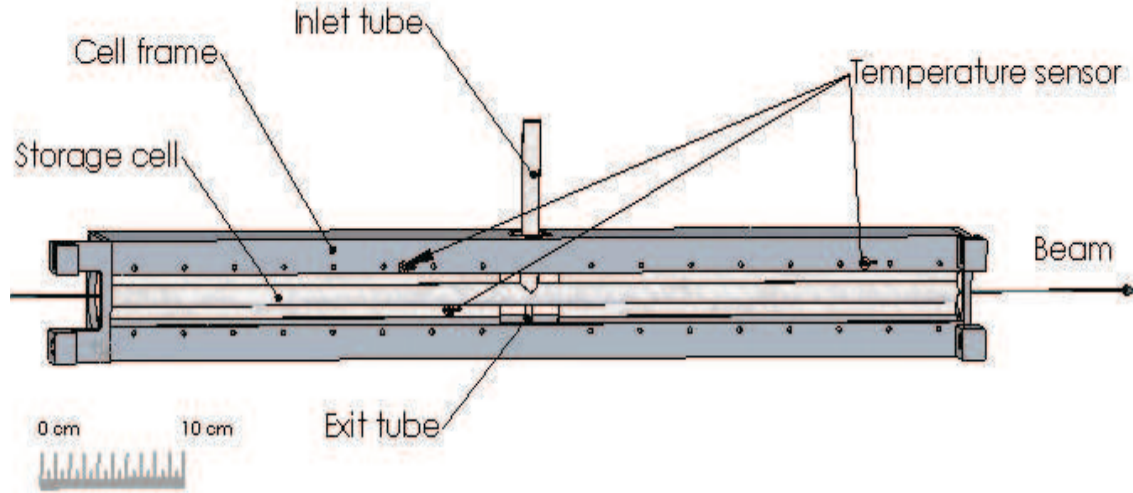


Figure 3-23: Storage cell on the frame. The temperature sensors are located on the cell and on the frame upstream and downstream from the center. An additional temperature sensor (not shown) is on the cryo cold head.

### 3.5.2 Polarized Atomic Gas in the Storage Cell

In a polarized target experiment the luminosity is not the only quantity that needs to be optimized. The Figure of Merit (FOM) of a polarization experiment is defined as

$$FOM = Polarization^2 \times Luminosity, \quad (3.39)$$

where *Polarization* could be vector,  $P_z$ , or tensor,  $P_{zz}$ , target polarization or in many cases a product of the beam and target polarizations. Therefore, preservation of a high polarization of atoms in the storage cell is of the highest priority.

Since no significant measurements were made to study different processes of polarization loss in the BLAST target, the following discussion of the depolarization mechanisms in the BLAST target will be purely qualitative and mostly based on the experiences from other internal target experiments.

### Depolarization Due to Recombination on the Wall

The time an atom spends in the cell is related to the conductance through the diffusive flow equations by

$$\tau_d = \frac{\pi d_{cell}^2 l_{cell}}{4C_{tot}}. \quad (3.40)$$

During the time  $\tau_d$  the atom collides with the cell walls on average  $\langle N \rangle$  times. The number of wall collisions experienced by an atom can be derived from the kinetic gas theory as [123]

$$\langle N \rangle = \frac{\pi d_{cell} l_{cell}}{8C_{tot}} \langle v \rangle, \quad (3.41)$$

where  $\langle v \rangle = \sqrt{\frac{k_B T}{M}}$  is the average thermal velocity of an atom. Using eqn. 3.37 one can see that the average number of bounces on the cell wall is purely a function of the cell geometry<sup>12</sup>

$$\langle N \rangle = \frac{3}{8} d_{cell} l_{cell} \left( \frac{l_{inlet}}{d_{inlet}^3} + \frac{l_{cell}}{d_{cell}^3} \right). \quad (3.42)$$

The rate of the volume recombination is negligible at the density inside the cell. The only time when the atoms can recombine is when they find themselves on the cell surface. Hence, the recombination rate is proportional to the number of the wall bounces. The recombination rate is also proportional to the dwell time of an atom on the cell wall during each bounce. This time can be expressed in terms of Arrhenius law [128] as

$$\tau_{dwell} = \tau_0 e^{\frac{E_b}{k_B T}}, \quad (3.43)$$

where  $E_b$  is the surface adsorption energy characteristic to the chemistry of the surface. Typically, the dwell time is on the order of  $\sim 10^{-10}$  sec, which is much less than the time the

---

<sup>12</sup>This equation assumes that temperature of the inlet tube is the same as the cell temperature, as in cell #3 setup.

atom spends between bounces. The recombination probability is parametrized as

$$P_r(T) = k_1 e^{\frac{T_1}{T}} + k_2 e^{-\frac{T_2}{T}}, \quad (3.44)$$

where the first term is due to an increase of the atom's dwell time at a lower temperature (Arrhenius law). The second term is interpreted as being due to the activation barrier needed to be overcome by an atom to recombine with chemically bound atoms on the surface of the cell. Hence, the recombination probability increases at a very low temperature due to the dwell time and it also increases at high temperature due to an effective lowering of the activation barrier.

No quantitative studies of the recombination were done with the ABS at BLAST. The operation of the ABS is optimized based on extensive experience from other polarized gas storage cell experiments at HERMES [129, 130], NIKHEF [131, 132] and Indiana [133]. It is generally believed that in order to reduce the dwell time of an atom on the surface of the cell (first term in equation 3.44), the cell should be coated with a layer of a Drifilm [134]. This decreases the probability of binding an atom with the cell surface since the Drifilm layer is chemically saturated and has no available bonds. Further increase of the cell surface binding energy comes from accumulated water molecules (in the form of ice) on the cell surface which originate from the dissociator (see section 3.1).

In order to reduce the second term in eqn. 3.44, the cell was cooled down to increase the activation barrier for the interactions between the atoms on the surface. However, this increases the dwell time of the atoms on the surface of the cell. Therefore, there is an optimal temperature that will lower the recombination rate, typically around 100 K. The cell temperature at BLAST is set to  $\sim 90$  K.

It is generally believed that once the atoms recombine into molecules they become completely depolarized. However, the NIKHEF ABS collaboration [131] found some evidence that the atoms do preserve their tensor polarization even after recombining into molecules. Also, the Indiana collaboration [133] observed that at room temperature with a sufficient magnetic holding field ( $\sim 6$  kG) nearly 40 % of the hydrogen atoms retain their vector polarization. The observation by the Indiana collaboration, however, is not applicable to the BLAST target, since the magnetic holding field is not strong enough to reproduce this effect.

## Depolarization Due to Wall Collisions

A wall collision is a chemical interaction in which an attractive potential between the cell surface and an atom makes that atom spend some time dwelling infinitesimally close to the surface. As first suggested by Bouchiat and Brossel [135], an electron in the atom interacts with any magnetic dipoles found on the cell surface and with the unpaired electrons through both spin exchange and Pauli exclusion interactions. The depolarization then occurs through induced transitions between different Zeeman and hyperfine levels. The probability of this transition is characterized by its frequency. The relaxation rate of a single spin is given as [134]

$$\nu_s = \frac{2}{3} \frac{\tau_{dwell}}{\tau_{dwell} + \tau_{bounce}} g_S^2 b^2 \tau_c \times \frac{1}{1 + \omega_s^2 \tau_c^2}, \quad (3.45)$$

where  $g_S$  is the gyro-magnetic ratio,  $b$  is the local magnetic field on the cell surface,  $\tau_{bounce}$  is the time between each surface collision,  $\omega_s$  is the Larmor frequency of the spin and  $\tau_c$  is the correlation time of the modulation.

In the strong magnetic field regime the electron spin is decoupled from the nuclear spin. Since the wall interactions affect mostly the electrons in the atom, the nuclear polarization relaxation is weak, as observed at HERMES [136].

In the weak magnetic field regime the electron spin is coupled to the nuclear spin. What is observed then is a  $\langle \vec{S} \cdot \vec{I} \rangle$  relaxation. Therefore, the nuclear polarization relaxes just as fast as the electron polarization. The time dependence of such relaxation was suggested by Bouchiat and Brossel [135] to be of the following form

$$\langle \vec{S} \cdot \vec{I} \rangle = \langle \vec{S} \cdot \vec{I} \rangle_0 e^{-t\nu_{hf}}, \quad (3.46)$$

where  $\nu_{hf}$  is defined in equation 3.45 as  $\nu_s$  with  $\omega_s$  becoming the frequency of a hyperfine transition,  $\omega_{hf}$ .

The BLAST target operates in the strong magnetic field regime when the polarized deuterium gas is in the target whereas the polarized hydrogen target is operated in the weak magnetic field regime.

## Spin Exchange Collisions

When the atoms collide with each other there is a finite probability for them to exchange their spins. The rate of the spin exchange collisions per unit time per unit volume is [128]

$$\nu_{se} = n\langle\sigma_{se}v\rangle, \quad (3.47)$$

where  $n$  is the number of atoms per unit volume,  $\sigma_{se}$  is the cross section for a spin-exchange collision and  $v$  is the velocity of an atom. Hence, there is a linear density dependence of the relaxation rate due to the spin exchange collisions.

In a physical internal target there is no way to separate the spin relaxation due to the wall collisions or spin exchange collisions. However, these processes are of different nature. Wall depolarizations have a strong temperature dependence in very low or very high temperature limits as well as a strong dependence on the quality of the cell and magnitude of the target holding field and the cell geometry. At the same time, wall depolarization has a small density dependence.

Spin exchange collisions, on the other hand, have an explicitly strong density dependence and a weak temperature dependence. In a diffusive flow, the density is an inverse function of the velocity of an atom. At the same time the spin diffusion rate due to spin exchange has a linear velocity dependence<sup>13</sup>. When this relaxation rate is integrated over the time an atom spends in the cell, a  $1/\sqrt{T}$  dependence exists. Hence, the spin exchange collision rate is relatively insensitive to the temperature of a cell.

In general, it is believed that the depolarization rate in the BLAST target is dominated by the wall effects (recombination and cell wall depolarization). This is important for a 60 cm cell, since the atoms diffusing along this cell would at some point cross zero magnetic field while still being in the cell. At this point they become completely depolarized. The part of the cell where the holding field crosses zero is not used in the data analysis. However, in the presence of a strong spin exchange rate the polarization along the whole cell would be negatively impacted due to the depolarized atoms at the edge of the cell having a finite probability to return back to the center and scatter off the polarized atoms. However, this

---

<sup>13</sup>An approximation is made here that  $\langle\sigma_{se}v\rangle \approx \sigma_{se}\langle v\rangle$ .

has not been observed when the performance of a 60 cm cell was compared with that of a 40 cm cell.

	Cell #1	Cell #2	Cell #3
Time in the cell, $\tau_d$ (ms)	44.1	60	73.6
Number of wall bounces, $\langle N \rangle$	1130	2323	2829
Time between wall bounces, $\tau_{bounce}$ ( $\mu$ s)	39	25.8	26.0

Table 3.5: For each cell used in the experiment the time the atom spends in the cell, the number of wall collisions and the time between wall collisions can be calculated from the diffusion flow equations.

Tabulated in table 3.5 are the characteristic quantities<sup>14</sup> of each cell that can be calculated from the diffusive flow equations. Unfortunately, due to the lack of available run time, the quantities specific to the quality of an individual cell, such as relaxation rates, were not measured. Looking at table 3.5 it is noticed that by going from cell #1 to cell #3 the number of wall bounces almost triples. One would thus expect an increase in the polarization loss in the longer cell. This is especially true for the case of polarized hydrogen gas in the target, since the magnetic holding field is too low to decouple the atomic and electric spins. However, as it will be shown in the target’s performance discussion (section 3.6.2), cell #3 turned out to produce the largest figure of merit. This points to the importance of the internal quality of a cell when considering its performance.

### 3.5.3 Target Magnetic Holding Field

The magnetic holding field for the atoms in the target is provided by a strong electromagnet. The requirement for the magnitude of the holding field is that it should be at least a few times larger than the critical field,  $B_c$ . The second requirement concerns the uniformity of the magnetic field along the target length. The atoms diffusing through the cell must constantly experience the uniform magnetic field in order to avoid depolarization.

The polarization direction of the target is defined by the direction of its holding field. The target magnet provides field only in the laboratory x-z plane. However, purely in-plane target polarization direction is sufficient for the experimental program at BLAST. All experimental asymmetries measured at BLAST have a strong dependence on the polarization

---

<sup>14</sup>These quantities are calculated for the deuterium target.

direction. Therefore, for a precision measurement the target field direction has to be well known and stable over the duration of the experiment. For this purpose, a high resolution two-dimensional Hall probe was installed in the scattering chamber to monitor the target holding field angle.

The holding field magnet had not been altered since it was shipped from NIKHEF [137] (see fig. 3-24). The magnet has an open geometry with the coils placed at the top and bottom

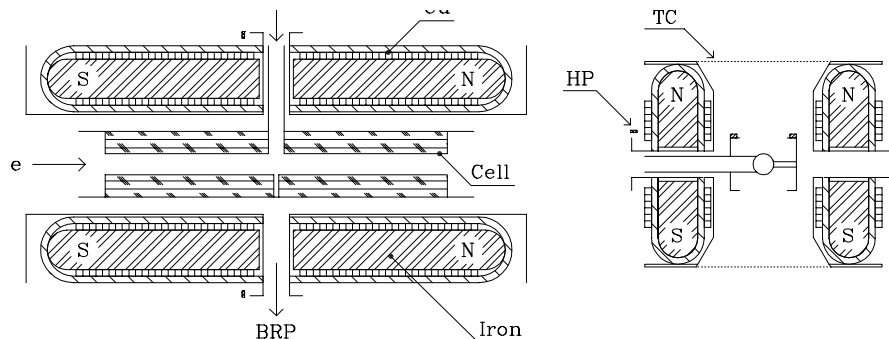


Figure 3-24: Holding field magnet as it was built at NIKHEF [137]. The magnet has not been modified for BLAST. Slight adjustments were made to the mounting of the storage cell. Also, the positions of the temperature (TC) and field (HP) probes were changed to provide more precise readings. The cell in the picture is 40 cm long. A 60 cm long cell was used in the experiment. The diagram is taken from the Ph.D. thesis by Zilu Zhou [119].

of the scattering chamber to allow space for the target windows on the sides. The water cooled copper coils are wound along the electron beam direction to provide the transverse field and perpendicular to the beam for the longitudinal field. The coils are designed so that there is room for the inlet tube on the top and the exit tube on the bottom allowing a sampling of the atomic beam for analysis with the Breit-Rabi Polarimeter (see section 3.5.4). The coils are wound around two steel plates, one on top and one on the bottom. The steel plates increase the strength of the holding field in the target region and at the same time make the field uniform along the cell length. Both plates have a small hole in the center for the inlet and outlet tubes. The discontinuity in the copper coils along with the holes in the steel plates create a slight non-uniformity in the transverse magnetic field at the center of the target (see fig. 3-25, right). Due to the influence of the transverse magnetic field on the orbit of the stored electron beam, two correction magnets were installed upstream and downstream of the target.

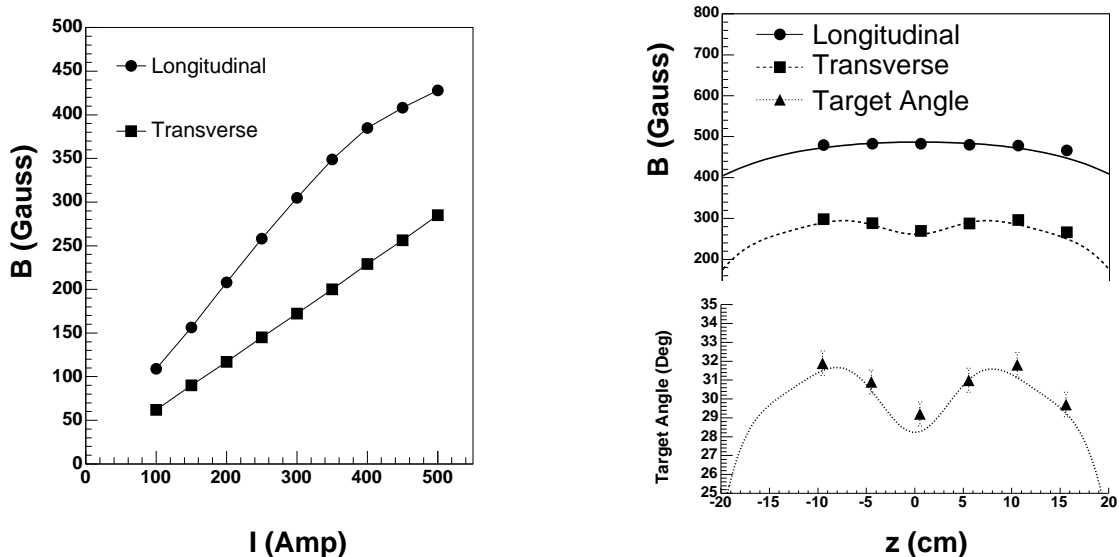


Figure 3-25: On the left is the field vs. current measurement of longitudinal (circles) and transverse (squares) holding field magnets. On the right is the data on longitudinal (circle) and transverse (squares) magnetic fields with the derived target angle (triangle) along the length of the target cell. The lines are from the TOSCA calculation.

Figure 3-25 shows a map of the target field measured before the target was installed into the South Hall Ring. The  $B$  vs.  $I$  curve (left) shows that there is little saturation in the transverse field magnet while the longitudinal field magnet starts to saturate around 400 A. Also, the full field strength of the transverse magnet is close to one half of the longitudinal magnet.

The longitudinal field is uniform around the center of the target and starts to vary more strongly at  $|z| > 15$  cm. The transverse field has a dip in the middle of the cell due to the break in the magnet coils and a hole in the steel. This dip is even more pronounced when the target polarization angle is calculated from the transverse and longitudinal fields. The magnetic field of the target magnet is modeled with TOSCA. The calculations agree with the data reasonably well.

### 3.5.4 Breit-Rabi Polarimeter

Historically, the atomic beams entering the storage cell were analyzed with a Quadrupole Mass Analyzer (QMA), similar to the one used in the dissociator studies described in section 3.1. However, the QMA does not function properly in the strong or even moderate ambient magnetic field. It is also impractical to take the QMA-based analyzing device outside of the BLAST field, since the distance from the target cell becomes so large that the signal-to-noise ratio in the QMA precludes any precise measurements. Instead, the Breit-Rabi Polarimeter

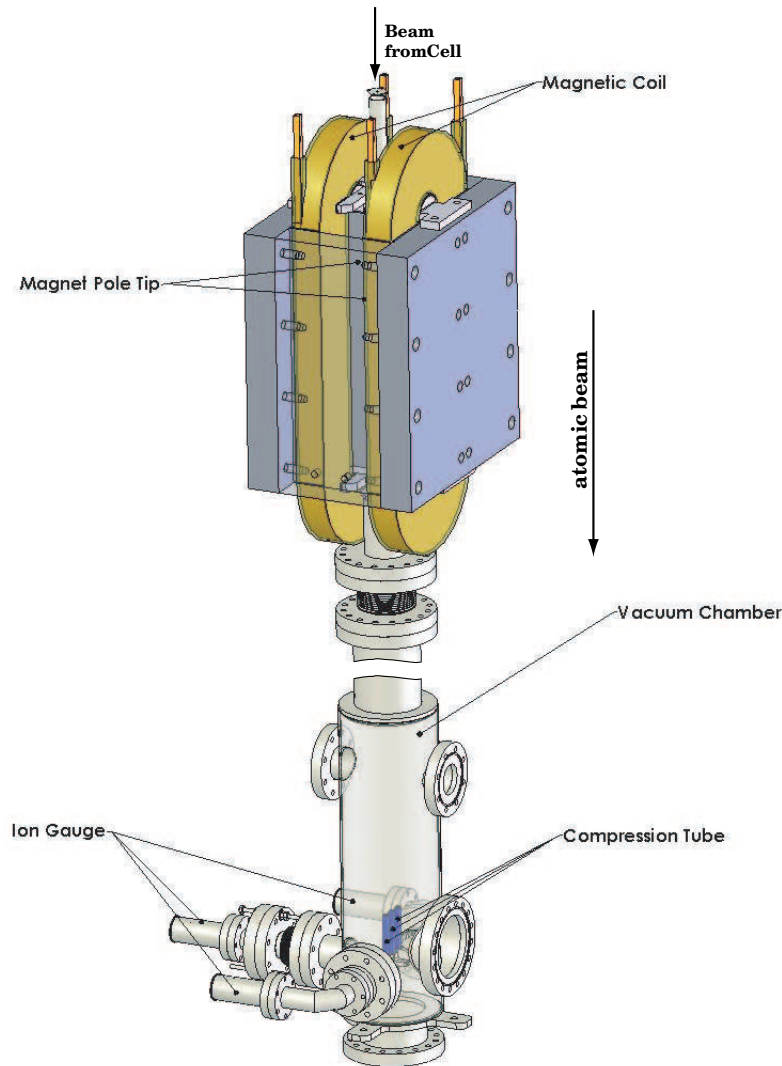


Figure 3-26: Breit-Rabi Polarimeter. To enhance the details the figure is not drawn to scale. The atomic beam is directed from top to bottom.

(BRP) is instrumented underneath the storage cell in a form of dipole magnet with a strong

and uniform gradient field. A small 2 mm aperture is placed at the entrance of the magnet to limit the acceptance of the atomic beam to the spatial resolution of three compression tubes. The aperture improves the signal-to-noise ratio significantly. The atomic beam is deflected in the strong gradient field of the BRP in a similar fashion to the sextupole magnets (see section 3.2). Three compression tubes (CT) equipped with ion vacuum gauges are installed 1.5 m below the magnet to sample the deflected beams. The central CT collects both the atomic and molecular gas with the BRP magnet off. When the BRP magnet is on the left and right CTs are sampling the deflected atomic beams. The atomic beam polarization can be monitored during the experiment by using the signals in the left and right CTs. By comparing the central CT signal with the ABS sextupoles in the atomic beam to the signal with the sextupoles moved out of the atomic beam, the atomic fraction of the beam as it leaves the nozzle,  $\alpha_{H/D}$ , is measured.

Since it only samples the central trajectories of the atomic beam, the BRP set-up is not designed to measure the absolute polarization of the target with a great certainty. Also, the BRP is not sensitive to the polarization of the atoms stored in the cell. The polarization of the atoms in the cell can be different from the polarization of the atomic beam injected in the cell due to the various depolarizing mechanisms in the cell described in section 3.5.2. The absolute polarization of the target is measured by the electron scattering reaction. However, together with electron scattering, the BRP provides a good monitor of the relative strength of the atomic states in the ABS.

The BRP also provides a good method to tune the RF transition units with the BLAST field on. A static field scan is performed for all RF units to determine the location of the hyperfine transitions needed to polarize the atomic beam (see fig. 3-27 for example).

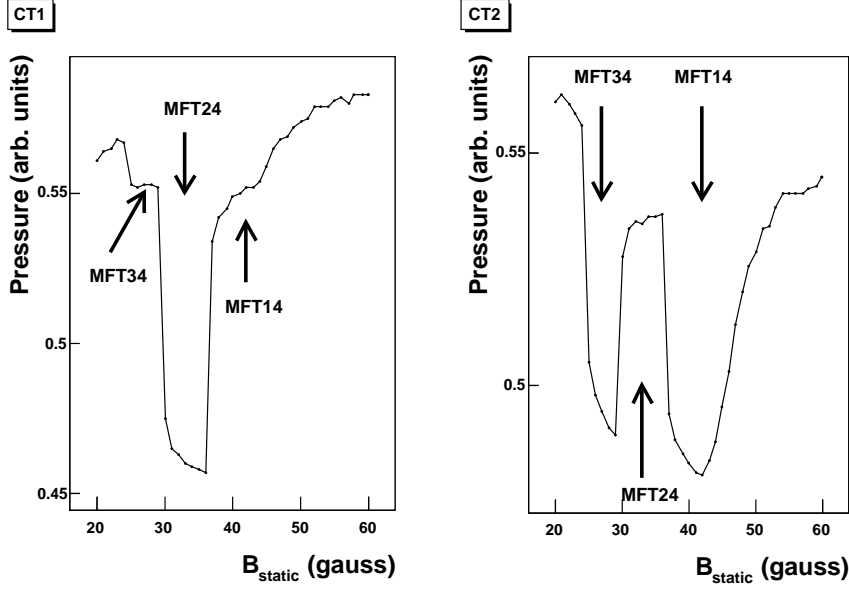


Figure 3-27: MFT static field scan with the SFT2-6 transition turned on for the atomic deuterium beam. Compression tube, CT1 (left) samples hyperfine states with  $m_S = -\frac{1}{2}$ . The CT2 (right) samples  $m_S = +\frac{1}{2}$  states. MFT 3-4, 2-4 and 1-4 transitions are clearly discernible.

## 3.6 ABS Performance

### 3.6.1 Intensity

The ABS intensity is a strong function of the pumping speed along the path of the polarized atoms. The atomic beam intensity is parametrized as [138]

$$I(Q) = I_0 \cdot Q \cdot e^{-Q/Q_0}, \quad (3.48)$$

where  $Q$  is the flow into the dissociator,  $I_0$  is the intensity in the absence of rest gas scattering and  $Q_0$  is the beam attenuation parameter which is a function of the rest gas density in the ABS chambers. The intensity  $I_0$  is a function of the ABS parameters, such as the degree of dissociation, geometry of the nozzle-skimmer-collimator system, sextupole transition probability, etc. In the case of the BLAST ABS the atomic beam attenuation is dominated by the rest gas scattering and intra-beam scattering is negligible. When the ABS was originally assembled at BLAST the production of a high intensity atomic beam was significantly limited by the vacuum pumping. The vacuum components were redesigned and assembled

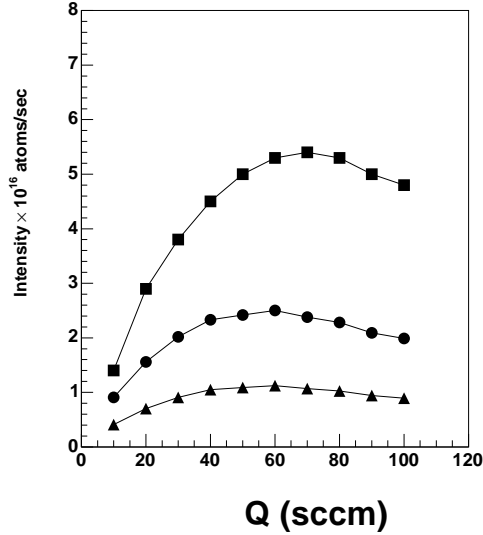


Figure 3-28: Attenuation of the Atomic Beam in the ABS as a function of the gas flow into the dissociator. The measurements were performed on the two state hydrogen target in the old ABS pumping configuration with the BLAST field on (triangles) and off (circles) and the new pumping configuration (squares) with the BLAST field on.

into the final configuration. The intensity measurements were performed with the ABS in its original low pumping speed and in the final high pumping speed configurations by injecting hydrogen into the target in two state mode (see fig. 3-28). Also, the sextupole magnets were not shielded from the BLAST magnetic field in the original configuration. In the final set-up the sextupole magnet strength was improved and the magnets were shielded from the BLAST field. The measurements were performed with the storage cell replaced by a compression tube equipped with an ion vacuum gauge. The intensity was measured with the RF transition units off<sup>15</sup>. The results of these measurements are collected in table 3.6. The

Configuration	BLAST field	$I_0$ (atoms/s/sccm)	$Q_0$ (sccm)	$I_{max}$ (atoms/s)
Old	on	$4.65 \times 10^{16}$	57.4	$1.25 \times 10^{16}$
Old	off	$1.03 \times 10^{17}$	57.4	$2.5 \times 10^{16}$
New	on	$1.75 \times 10^{17}$	73.3	$5.4 \times 10^{16}$

Table 3.6: ABS intensity measurements for the hydrogen gas in two state injection mode.

<sup>15</sup>In this configuration all  $m_S = +\frac{1}{2}$  states are injected into the target. Correspondingly, during the experiment, when the RF transitions are used, the hydrogen and deuterium intensities would be down by 1/2 and 1/3, respectively.

effect of the BLAST field on the focusing in the sextupole system can be seen by comparing the intensity,  $I_0$ , with the BLAST spectrometer on and off. The difference between  $I_0$  in the old and new configurations is due to the stronger sextupole magnets used in the new configuration. A significant improvement in  $Q_0$  between the old and new ABS configurations was achieved by improving the overall pumping speed. No significant difference was observed between the intensity measured with the BLAST field on and off in the new ABS configuration, due to the shielding of the sextupole magnets.

The atomic density in the storage cell was determined with the known elastic scattering reaction. The average target thickness achieved with cell #3 during the experiment is estimated to be  $\approx 4.5 \times 10^{13}$  atoms/cm<sup>2</sup> for both hydrogen (1 state injection) and deuterium (2 states). This thickness corresponds to an atomic beam intensity of  $\approx 2.6 \times 10^{16}$  atoms/s. A precise determination of the target density is not possible, since it requires an exact knowledge of the detector efficiencies. The average intensity for hydrogen is in line with the expected value from  $I_{max}$  in table 3.6, whereas for deuterium the average intensity is somewhat lower, mainly due to the non-optimal ABS running conditions in the beginning of the run<sup>16</sup>.

### 3.6.2 Polarization

As mentioned before, the target polarization is measured by means of electron scattering reactions. The precision of the vector polarization measurement from electron scattering is limited by the precision of the electron beam polarization measurement using the Compton polarimeter. The precision of the deuterium tensor polarization,  $P_{zz}$ , measurement is limited by the systematics of the  $T_{20}$  measurement.

The target polarization was monitored daily during the experiment (see figs. 3-29, 3-30 and 3-31). With cell #3 placed in the target the vector and tensor polarizations have remained stable over the course of the experiment. The overall polarizations quoted in this section have been achieved with cell #3. The vector polarization in deuterium is about 10 % larger than the vector polarization of hydrogen. This is expected considering that the

---

<sup>16</sup>The hydrogen experiment followed a long deuterium run. The running conditions were being improved in the course of the deuterium run. The optimal ABS running conditions were achieved by the time of the hydrogen target running.

Target	Reaction	$P_z$	$P_{zz}$
Hydrogen	${}^1\vec{H}(\vec{e}, e'p)$	78 % $\pm$ 4 %	-
Deuterium	${}^2\vec{H}(\vec{e}, e'p)n$ and ${}^2\vec{H}(\vec{e}, e' {}^2H)$	86 % $\pm$ 4 %	68 % $\pm$ 6 %

Table 3.7: Vector and tensor polarization results. The uncertainties in the vector polarization,  $P_z$ , of the hydrogen and deuterium targets are mostly determined by the systematic uncertainty of the Compton polarimeter measurement. The tensor polarization,  $P_{zz}$ , uncertainty is determined by the systematic uncertainties in the  $T_{20}$  measurement.

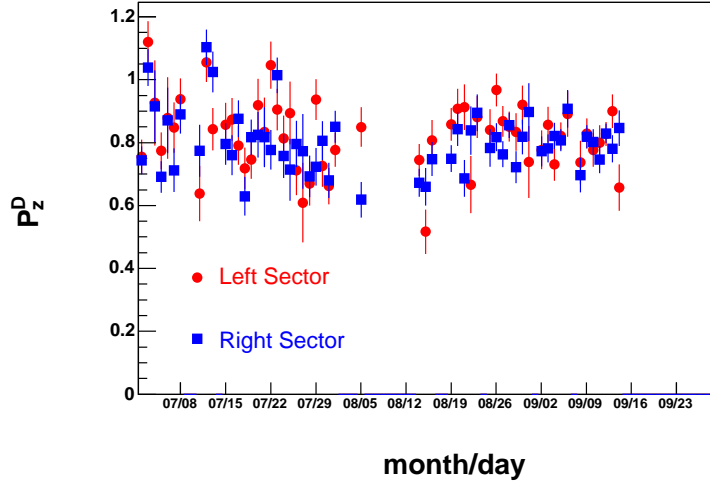


Figure 3-29: Vector polarization,  $P_z$ , of the deuterium target measured each day of the experiment with an electron scattered into the left and right sectors separately. The error bars are purely statistical.

magnetic holding field of the target is better suited for the critical field of deuterium. In fact, it is somewhat surprising to measure such high  $P_z$  in hydrogen considering the inadequate magnitude of the holding field. This kind of performance with the hydrogen target could only be explained by a cell of a very high quality.

The deuterium tensor polarization,  $P_{zz}$ , is about 15 % lower than the vector polarization. This may be due to the electron depolarization in the cell having a greater effect on the tensor polarization. An atom has to go from a state with  $m_I = 1$  to a state with  $m_I = -1$  in the same hyperfine multiplet to completely vector depolarize while it only has to go to a state with  $m_I = 0$  for a complete tensor depolarization. However, this has not yet been investigated in great detail.

Overall, the BLAST target performed exceptionally well. The figure-of-merit achieved

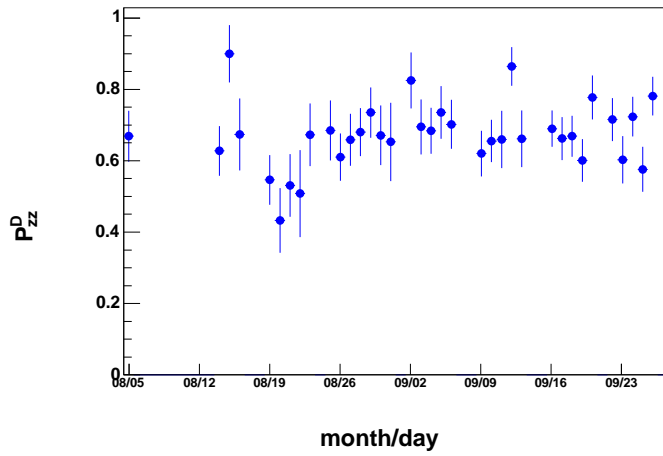


Figure 3-30: Tensor polarization,  $P_{zz}$ , of the deuterium target measured each week of the experiment with left and right sectors combined. The error bars are purely statistical.

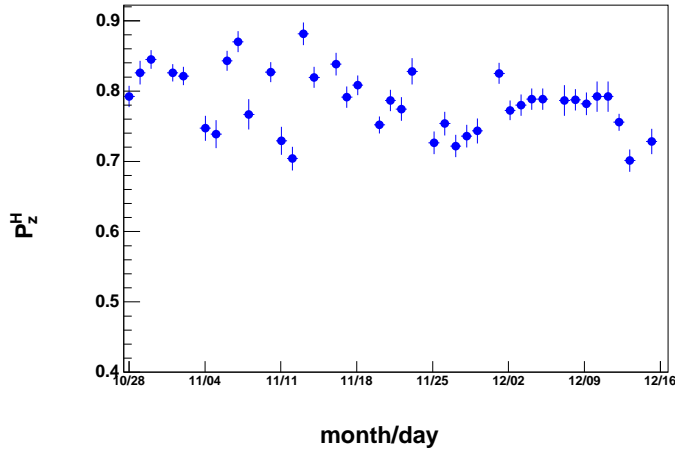


Figure 3-31: Vector polarization,  $P_z$ , of the hydrogen target measured each day of the experiment with left and right sectors combined. The error bars are purely statistical.

with cell #3 is somewhat bigger than projected in the proposals. It is almost a factor of three greater than the NIKHEF FOM with deuterium gas in the target and factor of ten greater with the hydrogen gas.

# Chapter 4

## The BLAST Experiment

### 4.1 The Stored Polarized Electron Beam in the South Hall Ring

The South Hall Ring (SHR) is located at the Bates Linear Accelerator Center. Polarized electrons extracted from the laser driven GaAs crystal are accelerated to an energy of up to 1 GeV. The acceleration is achieved by the 500 MeV linear accelerator. The 500 MeV beam is recirculated into the linac to nearly double the energy to 1 GeV. The electron beam is then injected into the South Hall Ring.

SHR Parameter	Value	
Energy Range	300-1000	MeV
Circumference	190.204	m
Revolution Frequency	1.576	MHz
Bend Radius	9.144	m
Stored Current	$\geq 100$	mA
Internal Duty Factor	99	%
Injection Frequency	1-1000	Hz
RF Frequency	2.856	GHz
Harmonic Number	1812	

Table 4.1: SHR Design Parameters

The South Hall Ring operates either as a storage ring for the internal target experiment (BLAST) or as a pulse stretcher ring to produce nearly CW beam for the external target experiments. In a storage mode, currents in excess of 200 mA are achieved by means of

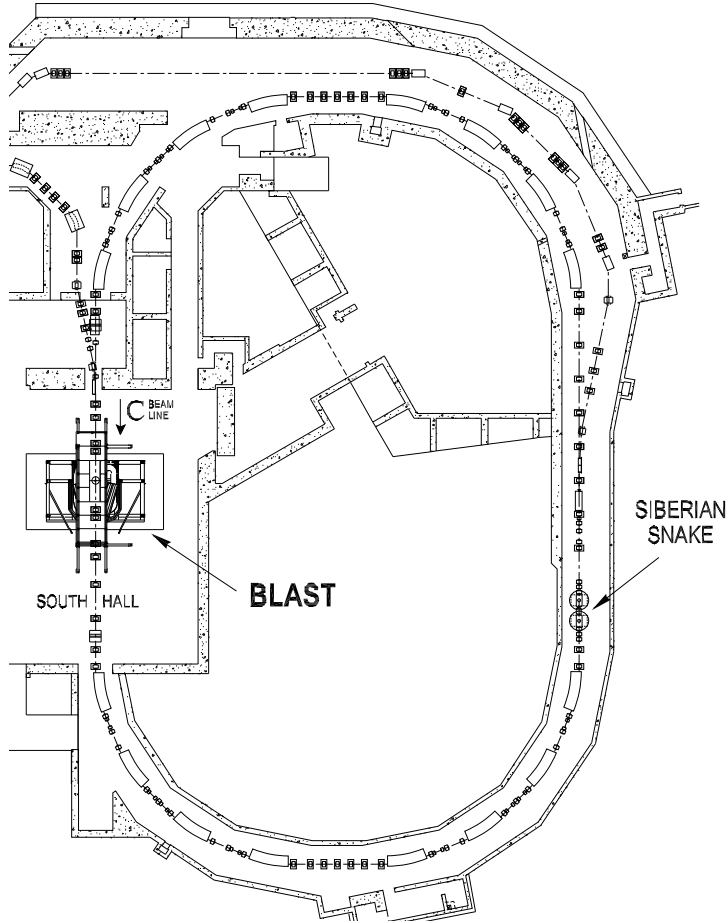


Figure 4-1: South Hall Ring. The electron beam is circulating counter clockwise.

stacking beam pulses of a few mA at an injection rate of about 10 Hz [139].

A beam tune was found to accommodate the storage cell in the center of the west straight section of the ring (see fig. 4-1). The small diameter of the storage cell requires a low  $\beta$ -function of the beam in order to limit scattering from the cell walls and beam lifetime loss. To further limit scattering of the beam from the target cell walls, a tungsten collimator with the inner diameter slightly smaller than the diameter of the storage cell was placed at the upstream end of the cell. The collimator also helps to protect the target cell Drifilm coating from damage caused by the electron beam and the synchrotron radiation.

The current in the ring is measured with a zero-flux DC current transformer (LDCCT). The LDCCT is designed for non-destructive measurements of electron beam currents. It has a frequency response from DC to 100kHz, an absolute accuracy of 0.05%, and is routinely calibrated. A 16 bit ADC digitizes the output and broadcasts the EPICS value in units

of mA. This signal is digitally filtered to a final bandwidth of approximately 0.5 Hz. The technology used is a saturatable core primary winding. A secondary winding is injected with a known level sine signal. Pickup electronics on the primary winding measure the level of the resultant second harmonic product. This level is related to the DC flux through the primary core [140].

The electrons in the beam are longitudinally polarized. To prevent polarization loss due to the electron spin precession around its momentum vector, a Siberian snake was installed in the east straight section of the ring (see fig. 4-1). The snake flips the spin vector to the opposite side of the momentum vector so that the  $g - 2$  precession in the north arc of the ring cancels the precession in the south arc.

The beam polarization is monitored by the Compton polarimeter [141]. The Compton polarimeter exploits the spin asymmetry of the backscattered circularly polarized light. The circularly polarized light is produced by a high intensity laser. The electron beam upstream of the target scatters the circularly polarized laser light at a very small angle. The backscattered light travels in a straight path and exits the beam pipe when the electron beam is bent in a dipole magnet. A set of absorbers, sweep magnet and charged particle veto counters are designed to reduce charged particle and synchrotron light backgrounds. The energy spectrum of the backscattered photons is measured by a CsI calorimeter (see fig. 4-2). The

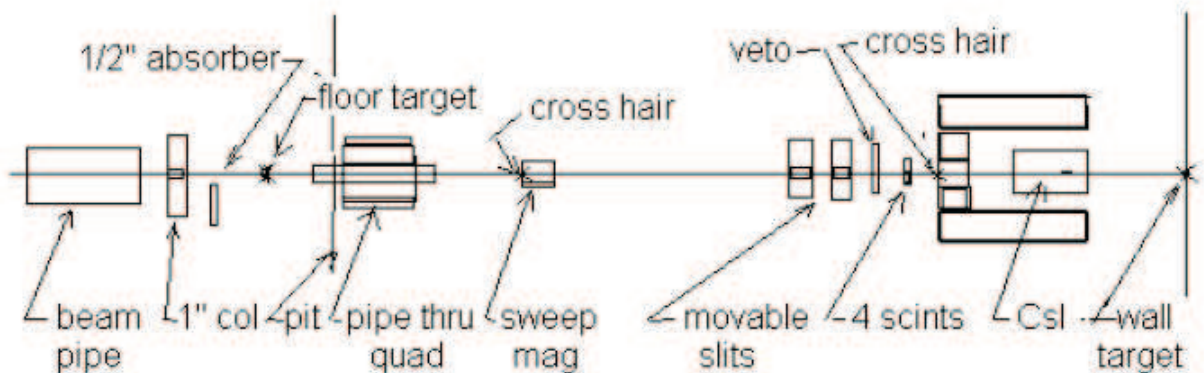


Figure 4-2: Flight path of the backscattered light.

beam polarization is measured during BLAST data taking, thus reducing helicity-dependent

systematic uncertainties of the experiment. The average polarization during the experiment was measured by the Compton polarimeter to be  $65 \pm 4\%$ . The uncertainty in this measurement is dominated by the internal systematic uncertainties of the Compton polarimeter.

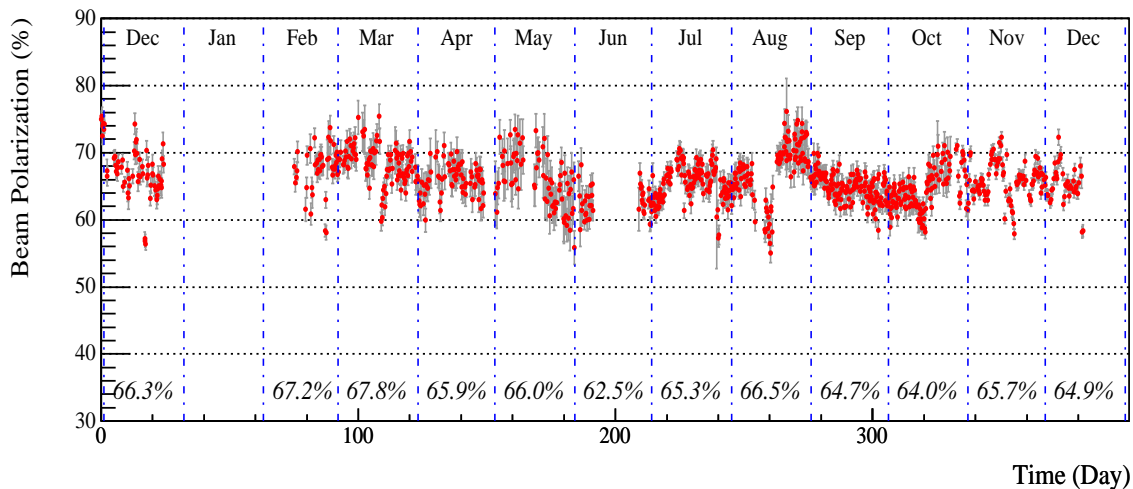


Figure 4-3: Polarization of the stored electron beam measured each day over the 2004 BLAST running period.

Overall, the polarized source, linac and the SHR have performed exceptionally well consistently delivering high intensity and high polarization electron beam for the experiment (see fig. 4-3). This is especially significant considering the challenges to the beam quality from the internal target operating in the SHR. The combination of the collimator and storage cell limits the conductance of the ring. The gas in the storage cell becomes ionized and increases the emittance of the beam. The target magnetic holding field steers the electron beam. All of these challenges were overcome by the operations group at Bates.

## 4.2 The BLAST Toroid Magnet

The Bates Large Acceptance Spectrometer Toroid magnet consists of eight copper conductor coils arranged symmetrically around the beam line (see fig. 4-4). The toroidal magnetic field generated by the coils provides curvature to the charged particle trajectories for precise tracking and momentum determination. The coils are made of 1.5'' square copper hollow conductors, with 26 turns in each coil. The operating current of a coil is 6731 A, creating a

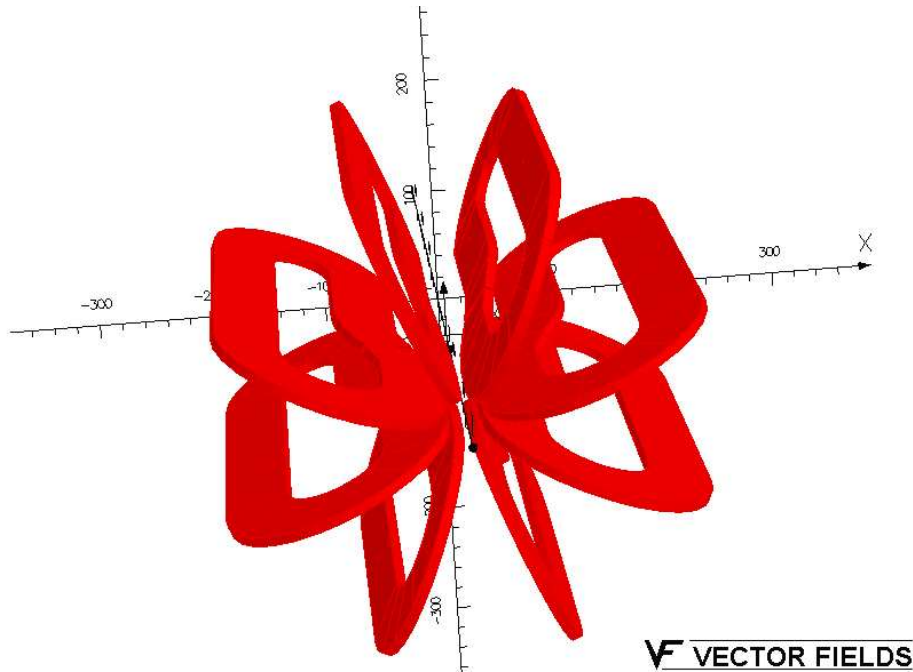


Figure 4-4: BLAST Toroidal Magnet

maximum field of 3.8 kG.

The magnetic field produced by the BLAST magnet was carefully mapped in the target and detector regions [142] to provide a three-dimensional field map used in the reconstruction of charged particle tracks. The measurements were then compared to Biot-Savart calculations with ideal coil locations. Figure 4-5 shows a scan of the vertical component of the magnetic field along the axis perpendicular to the beam axis (x-axis) at  $y = 0$  and  $z = 0$ . The measurements are in relatively good agreement with the Biot-Savart calculations. The deviations of  $\leq 5\%$  are mostly due to shifts of the coils from the ideal positions, and the presence of magnetic materials in the field.

### 4.3 The BLAST Detector

The BLAST detector is designed to accommodate the geometry of the BLAST toroidal spectrometer magnet. The drift chambers in the left and right sectors fit between two neighboring spectrometer coils. The entrance window of the smallest drift chamber is positioned near the aluminum windows of the target chamber. The Čerenkov detectors are located behind the drift chambers. The Time-of-Flight (TOF) scintillators are located behind the Čerenkov

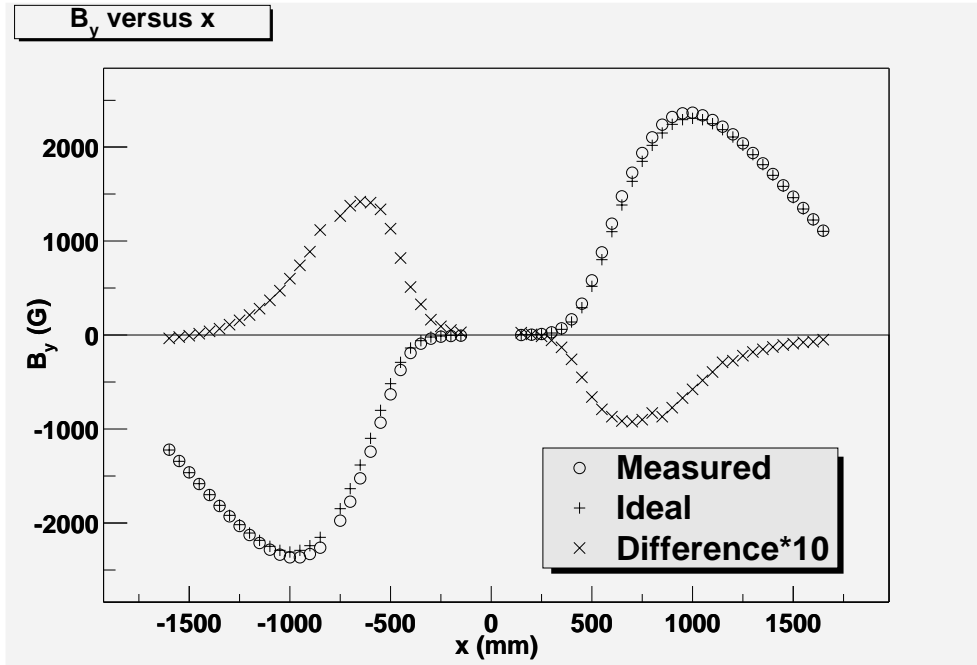


Figure 4-5: Vertical component of the magnetic field along along the axis perpendicular to the beam axis (x-axis) at  $y = 0$  and  $z = 0$ .

counters. The drift chambers, Čerenkov and TOF detectors are all mounted on a detector subframe which can be moved out of the region of the BLAST coils for servicing, or to allow work on the target. The neutron detectors are mounted on their own support frame a few meters away from the target (see fig. 4-6).

All detector and drift chamber high voltage is supplied by remotely controlled high voltage modules in a Lecroy 1458 HP mainframe. The high voltage is controlled using the EPICS slow control system, the same system that operates the South Hall Ring. This allows for a smooth integration of the high voltage controls with the beam injection software. The integrated control package is named “Automatic Ring Fill Software” (ARFS). ARFS allows for the safe, automatic injection of the electron beam into the South Hall Ring. To avoid the damage to the detectors from the injection flash, the detector high voltages are lowered automatically before the fill is dumped. Once the detector voltages are lowered the ring control gets an “OK” to dump stored beam and fill the ring again. After the ring is filled, the high voltages are raised again. The data acquisition is inhibited while the high voltages are down. All this is done without any involvement of an operator, which improves the efficiency of the experiment and reduces the data acquisition dead time.

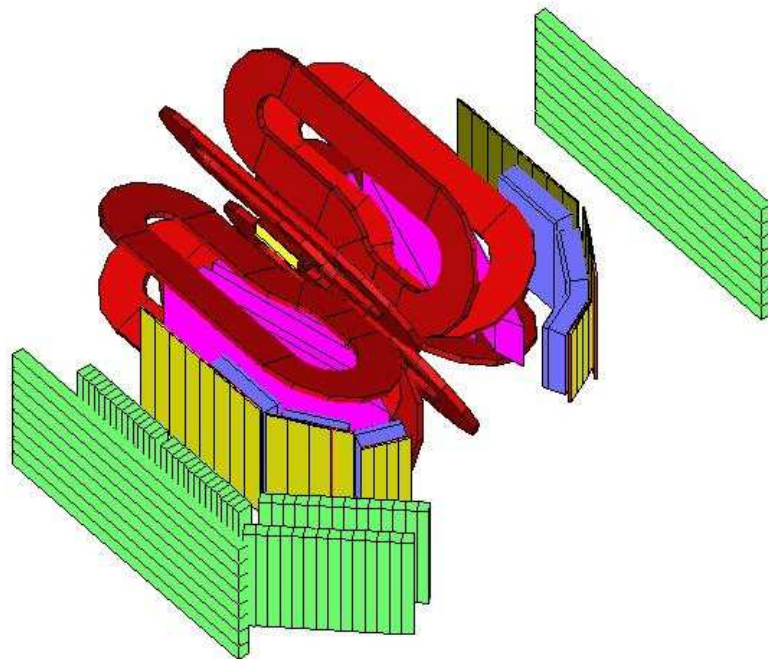
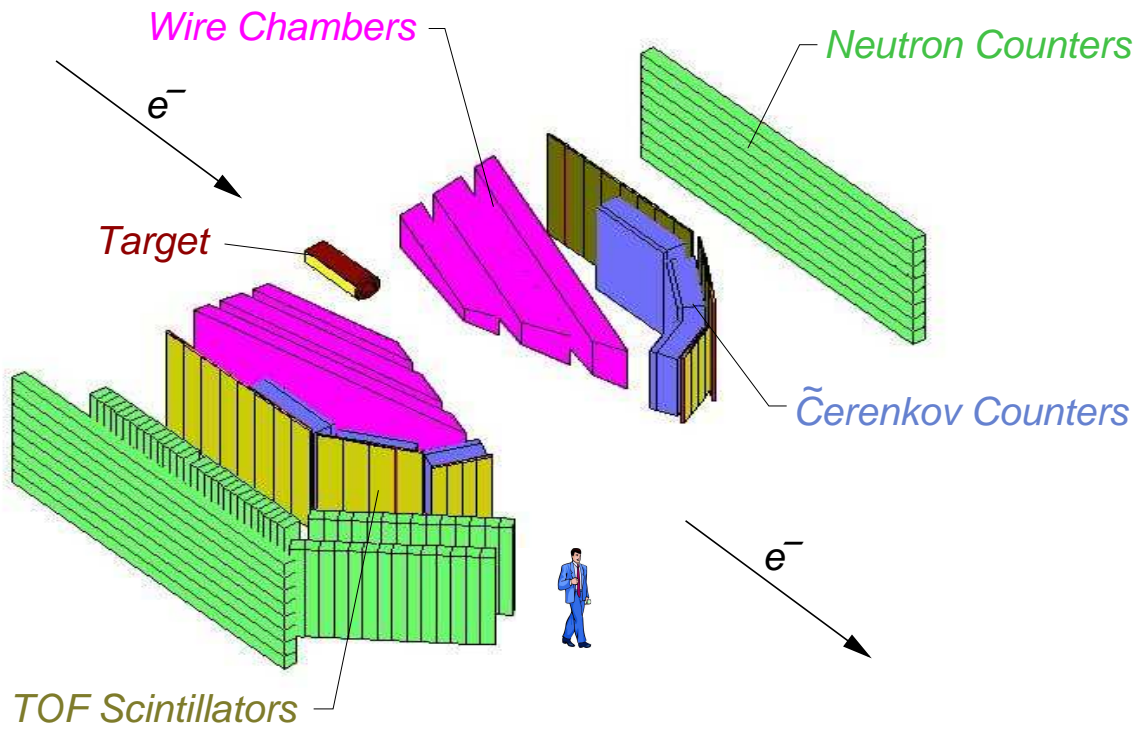


Figure 4-6: Schematic layout of the BLAST Detector without the spectrometer coils (top) and with them (bottom).

### 4.3.1 The Drift Chambers

The BLAST detector is equipped with a set of drift chambers in the left and right sectors. Each set consists of three chambers of a compound trapezoidal shape with a common gas volume. The shape is chosen to fit inside of the BLAST coils. The geometrical acceptance of the three wire chambers define the acceptance of the BLAST detector. The total acceptance is  $\sim 512$  msr per sector (see fig. 4-7).

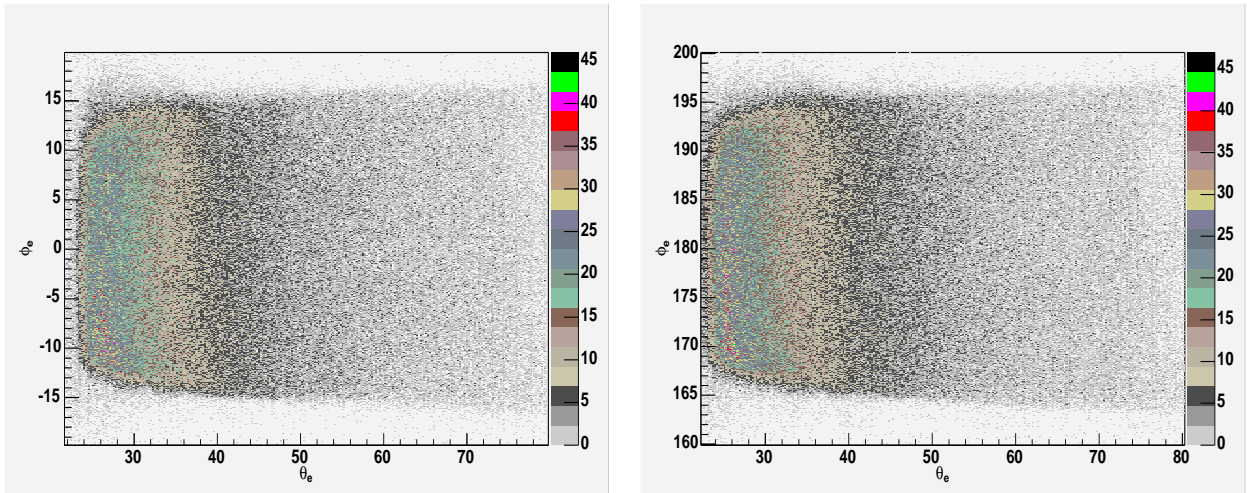


Figure 4-7: Electron geometrical acceptance ( $\phi_e$  vs.  $\theta_e$ ) of the BLAST detector in the left sector (left) and right sector (right).

Each drift chamber consists of 2 super layers with 3 layers of sense wires in each super layer. The sense wires are tilted at a stereo angle ( $\pm 5^\circ$ ) with respect to the vertical direction. As a charged particle traverses the drift chamber gas volume (80:20 He:Isobutane), it liberates electrons by ionization. These electrons propagate towards the sense wires in the electric field produced by the high voltage on the field wires. In the vicinity of the sense wires an avalanche of ionization is produced which induces a signal on the wire. The position of a particle in the drift chamber is reconstructed from the time it takes the ionization electrons to reach the sense wire and a known time-to-distance<sup>1</sup> function. The sense wires in the neighboring layers are staggered by 0.5 mm in order to resolve the left-right ambiguity, i.e. to determine from which side of the wire the ionization electrons came from. The vertical position reconstruction is allowed by the stereo angle of the sense wires.

<sup>1</sup>Time-to-distance function refers to the time it takes an ionization electron in the gas to travel a certain distance. The time-to-distance relation is a function of gas mixture, magnetic field, etc.

However, spatial coordinates (and hence scattering angles) are not sufficient for the reconstruction of most scattering reactions (they are enough for elastic scattering). The momentum reconstruction is needed as well. In a magnetic field a charged particle experiences a  $\vec{v} \times \vec{B}$  force. The solution of this drift equation is the curved track with a radius proportional to the known magnetic field strength and the momentum of the charged particle. The BLAST drift chambers are designed so that the track curvature measurement is determined by three clusters of points. Each cluster measurement of a track stub has an accuracy of  $\epsilon$ . The intrinsic momentum resolution in the absence of multiple scattering is then

$$\frac{\Delta p}{p} = \frac{8p}{0.3L_0} \frac{1}{\int Bdl} \sqrt{(\epsilon_1/2)^2 + (\epsilon_2/2)^2 + (\epsilon_3/2)^2}, \quad (4.1)$$

where  $p$  is the momentum of the particle,  $L_0$  is the length of the track and  $\int Bdl$  is the integral of the magnetic field along the particle's path. The accuracies  $\epsilon$  are defined as  $\epsilon_i = \frac{\sigma_i}{\sqrt{N}}$ , where  $\sigma_i$  is the intrinsic position resolution in the wire chambers and  $N$  is the number of measurements.

### 4.3.2 Reconstruction Resolution of the Drift Chambers

The resolutions of the reconstructed variables in the drift chamber were studied with elastic electron scattering on the hydrogen. The kinematics in the elastic scattering are determined by only one out of four kinematic variables<sup>2</sup> in the final state, as the beam energy and particle masses are well known. Since all four are measured, the system of equations is overdetermined. The momentum of the electron,  $p_e$  and the angle of the proton,  $\theta_p$  are expressed in terms of the electron angle,  $\theta_e$  as

$$p_e = \frac{\mathcal{E}}{1 + 2\frac{\mathcal{E}}{M_p} \sin^2\left(\frac{\theta_e}{2}\right)} \quad (4.2)$$

$$\theta_p = \sin^{-1} \left( \frac{1}{1 + \tan^2\left(\frac{\theta_e}{2}\right) \left(\frac{\mathcal{E}}{M_p} + 1\right)} \right)^{\frac{1}{2}}, \quad (4.3)$$

---

<sup>2</sup>The kinematic variables reconstructed by the drift chambers are  $\phi_e, \theta_e, p_e, \phi_p, \theta_p, p_p$ . Of them  $\phi_e$  and  $\phi_p$  drop out of the kinematical relations.

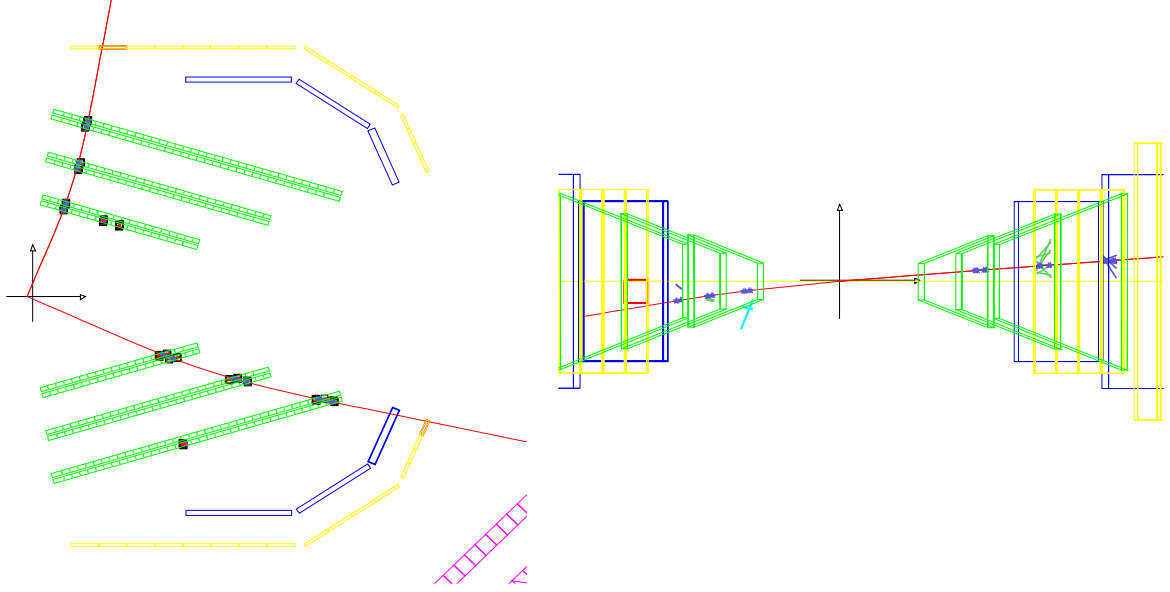


Figure 4-8: Single Event Display (nsd) of a typical e-p elastic event. In the top view (left) the electron beam is traveling from left to right. The scattered electron is bent towards the beam, while protons are bent away from the beam. The three hit clusters, one in each drift chamber, are clearly visible in the top view. The coplanarity of the event is seen in the front view (right). In the front view the beam is directed out of the page.

where  $\mathcal{E}$  is the electron beam energy and  $M_p$  is the proton mass. The differences between the measured and calculated  $p_e$  and  $\theta_p$  are histogrammed to study the resolution of the drift chamber reconstruction (see fig. 4-9). The widths of these histograms are approximately related to the resolutions of the reconstructed variables as

$$\Delta f(p_e - p_e(\theta_e)) \approx \Delta p_e \quad (4.4)$$

$$(\Delta f(\theta_e - \theta_p(\theta_e)))^2 \approx (\Delta\theta_p)^2 + (\Delta\theta_e)^2 \quad (4.5)$$

$$(\Delta f(\phi_e - \phi_p))^2 = (\Delta\phi_p)^2 + (\Delta\phi_e)^2 \quad (4.6)$$

$$(\Delta f(z_e - z_p))^2 = (\Delta z_p)^2 + (\Delta z_e)^2, \quad (4.7)$$

where the last two equations stem from the coplanarity and the single vertex in the elastic scattering (see fig. 4-10). The results of the resolution measurements for the electron are compiled in table 4.2<sup>3</sup> along with the original design values [143]. The projected resolution is based on the 130  $\mu\text{m}$  intrinsic wire resolution and the Monte Carlo studies of the

<sup>3</sup>The values are extracted using the approximation that the electron resolution is the same as the proton's. In fact the proton resolution is slightly better.

	Design	Measured
$\Delta p_e$	2 %	3 %
$\Delta \theta_e$	0.3°	0.45°
$\Delta \phi_e$	0.5°	0.56°
$\Delta z_e$	1.0 cm	1.0 cm

Table 4.2: Resolutions of the electron kinematic quantities measured by the BLAST detector.

multiple scattering.

The resolutions in the drift chamber achieved to date are close to the design values. Further improvements to the resolution are possible with a better understanding of the drift chamber time-to-distance relations and constants.

### 4.3.3 Čerenkov Detectors

The Čerenkov detectors in BLAST are used to discriminate between the electron and  $\pi^-$  tracks in the drift chamber. At high pion energy the time resolution of the BLAST spectrometer is not good enough to separate the mass of the pion from that of the electron using just the time-of-flight and momentum information.

There are four Čerenkov counters in each sector<sup>4</sup>. The first, most forward detector contains 7 cm thick radiator silica aerogel with index of refraction,  $n=1.02$ . The other two counters contain 5 cm of radiator with  $n=1.03$ . The smallest, most forward counter has six 5-inch PMTs (Photonis XP4500B). The second counter contains eight PMTs and the largest most backward detector has twelve PMTs. The size (width $\times$ height $\times$ depth) of the largest Čerenkov detector is  $100\times 150\times 19$  cm<sup>3</sup>. All Čerenkov PMTs were shielded with iron to avoid loss of efficiency due to the BLAST magnetic field.

A relativistic charged particle emits light in a material if the velocity of this particle is greater than the speed of light in the material. The angle of the emitted light cone is defined as [144]

$$\cos(\theta_c) = \frac{1}{n\beta}, \quad (4.8)$$

where  $\beta$  is the ratio of the charged particle's velocity to the speed of light and  $n$  is the index of refraction of the radiator material. The number of the photoelectrons emitted by a

---

<sup>4</sup>The fourth Čerenkov is used in front of the Back Angle Detector scintillators (BATs) and not considered in this work.

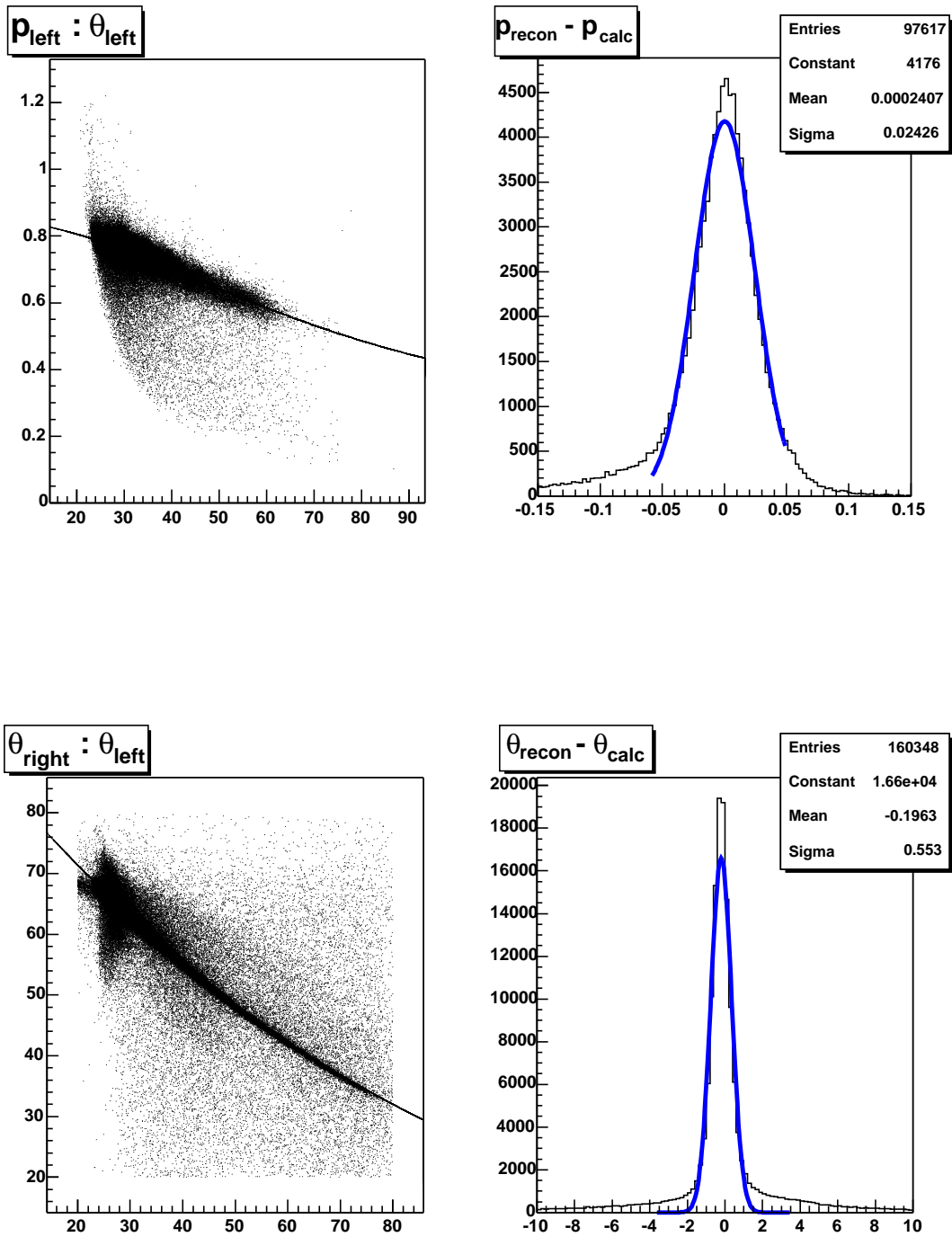


Figure 4-9: Plot of momentum (top) and polar angle (bottom) resolutions measured with elastic e-p scattering.

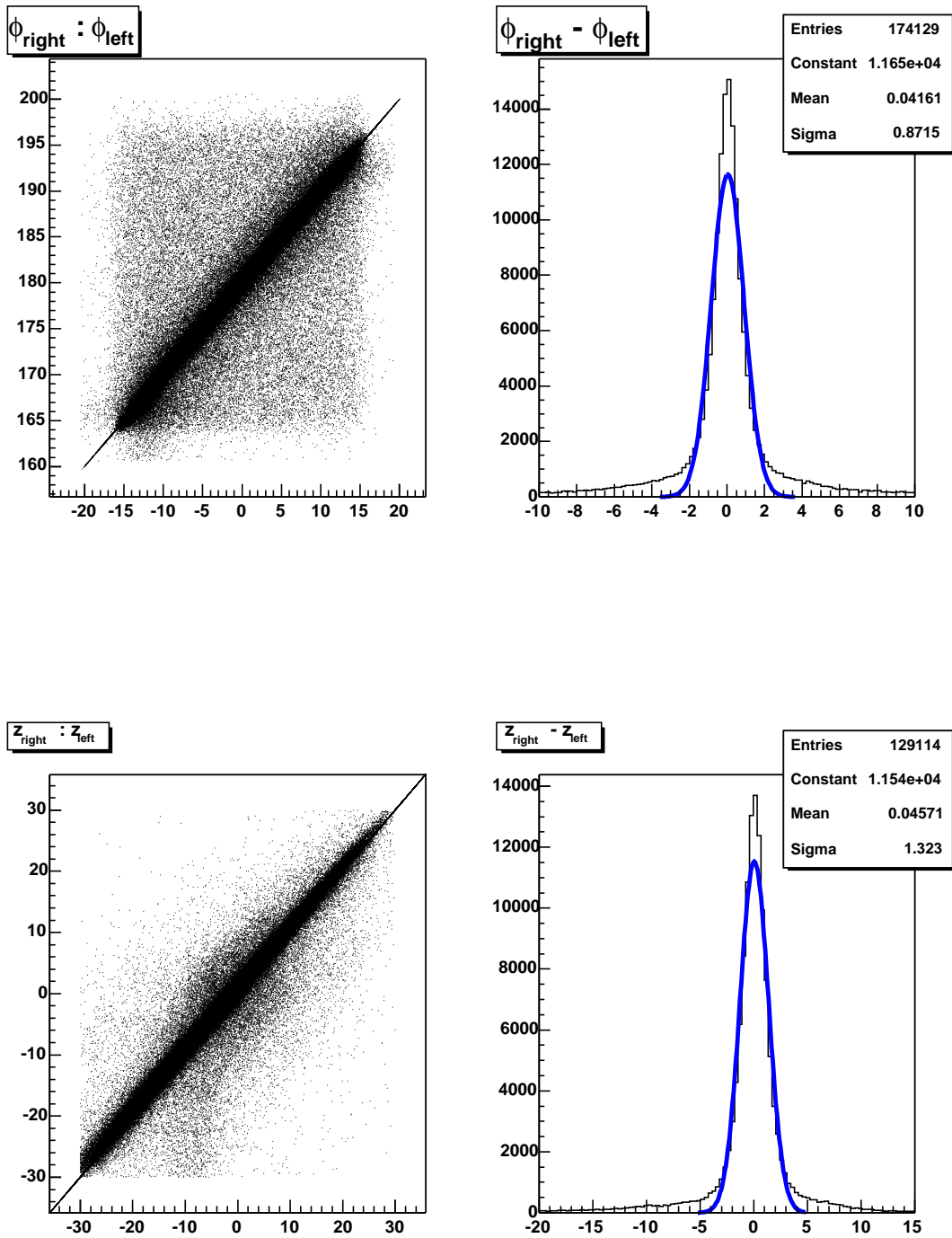


Figure 4-10: Plot of azimuthal angle (top) and vertex (bottom) resolutions measured with the elastic e-p scattering.

radiating particle is [145]

$$N_{p.e.} \propto L\epsilon_{det}\sin^2\theta_c \quad (4.9)$$

where  $L$  is the path length of the particle in the radiating material,  $\epsilon_{det}$  is the detection probability and  $\theta_c$  is defined in eqn. 4.8.

The photoelectron signal response of the BLAST Čerenkov counters was modeled using Monte Carlo methods [146] with a Poisson event generator. The ADC spectrum of the Čerenkov detector was obtained by summing over the events in the PMT that passed the trigger threshold. An ADC spectrum calculated by Monte Carlo for a multiplicity of 4 PMTs is shown in fig. 4-11. The average number of photoelectrons that trigger an event was found to be 2.8.

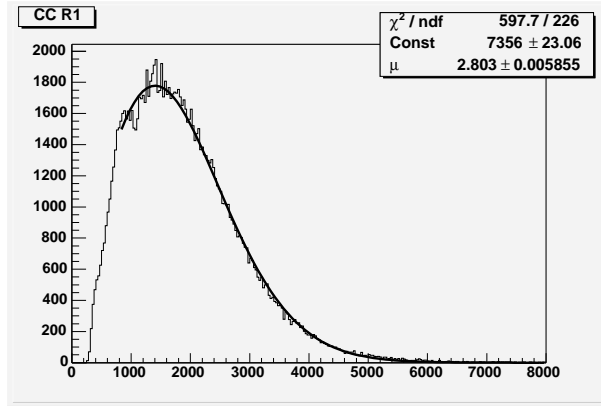


Figure 4-11: A simulated ADC event distribution of a Čerenkov counter fitted by a Poisson distribution with  $\mu = 2.8$ .

The efficiency of the Čerenkov counter for the electron detection was obtained using the elastic electron scattering on hydrogen. The elastic electrons are identified using the drift chamber information with a set of cuts defined by the elastic kinematics. The efficiencies of the Čerenkov counters are plotted as a function of the TOF scintillator number (see fig. 4-12), located directly behind the Čerenkov counters. There are four TOFs per Čerenkov. The efficiency for electron detection was found to be  $\sim 85\%$  for all Čerenkov detectors. Each Čerenkov counter shows a lower efficiency at its upstream edge, since electrons are bent in and miss the fourth TOF.

The effect of the Čerenkov cut on the determination of  $G_E^n$  was investigated. It was found that the Čerenkov cut has no statistically significant effect on the extracted value of

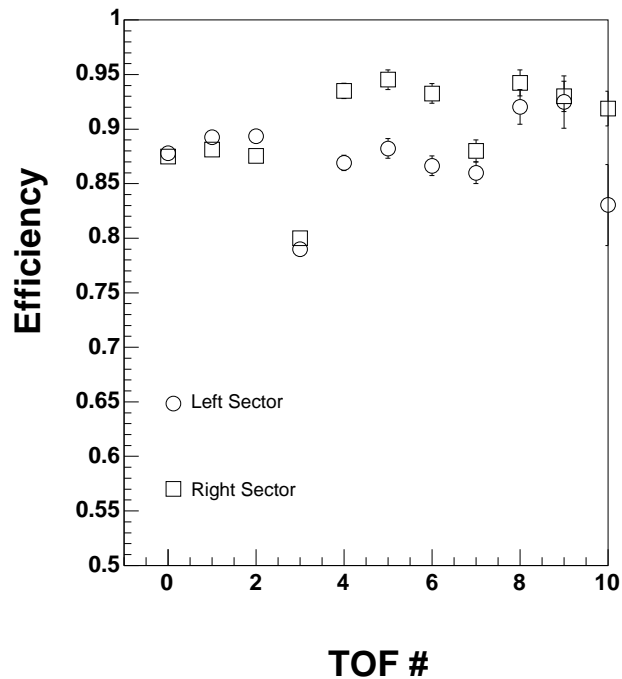


Figure 4-12: The Čerenkov efficiency for electron detection as a function of the TOF number. The low efficiency values at TOF #3, #7 (off scale) and #10 are due to an edge-of-acceptance effect.

$G_E^n/G_M^n$ . This is mostly due to the fact that there have to be two pions in the final state in order for a  $\pi^-$  to be detected in coincidence with a neutron. A product of the cross section and the geometrical phase space for this type of reaction is orders of magnitude lower than the quasielastic scattering. Therefore, the Čerenkov counter information was not used in the final analysis.

#### 4.3.4 Time-of-Flight Scintillators

The Time-of-Flight (TOF) scintillation detectors provide timing information for the particle track reconstruction and identification. Although, the position information from the TOFs is redundant to the drift chamber reconstruction, it is useful for consistency checks of the drift chamber performance.

The time information from the TOFs is used for the particle identification at BLAST.

At 400 MeV kinetic energy, the time separation at the TOFs between the pion and proton is  $\sim 6$  ns. At 200 MeV, the proton reaches a TOF  $\sim 8$  ns ahead of an elastic deuteron. These times are well above the intrinsic time resolutions ( $\sim 750$  ps) of the TOFs, thus providing a good particle identification.

The TOF wall in each sector consists of sixteen Bicron BC-408 scintillators. Each scintillator is 2.5 cm thick. The front four scintillators are 120 cm tall and 15 cm wide and the other twelve are 180 cm in length and 26 cm in width. The TOF scintillators are equipped with 3" photo-multiplier tubes (PMT) at both ends. The geometrical acceptance of the TOF wall matches the acceptance of the drift chambers.

The TOF scintillators are equipped with a flasher system, which consists of a laser, splitter box and optic fibers. The laser light is split and attenuated in the splitter box and then fed into the optic fibers which are coupled directly to the TOFs. The flasher system provides a good consistency check of the TOF detector gain changes and timing shifts during the experiment.

### 4.3.5 Neutron Detector System

#### Neutron Detector Geometry

The neutron detector system was optimized for measurement of the perpendicular vector asymmetry. The target angle was set at  $32^\circ$  pointing into the beam left sector (see fig. 4-13). Hence, the three-momentum transfer vector,  $\vec{q}$ , in perpendicular kinematics points into the right sector. The right sector was instrumented with five neutrons walls: one OHIO wall<sup>5</sup> and four LADS walls<sup>6</sup>. One OHIO wall was positioned in the left sector to measure electron-neutron coincidence events in the parallel kinematics. The vector asymmetry in the parallel kinematic regime was used to check the consistency of the product of the beam and target polarizations,  $hP_z$  (see section 5.8.2).

Compiled in table 4.3 are the dimensions of each neutron wall. The total solid angle of the neutron detectors is 244 msr to beam left and 366 msr to beam right. However, the average effective detector thickness in the beam right sector is three times the effective thickness in

---

<sup>5</sup>Constructed by Ohio University

<sup>6</sup>Large Acceptance Detector System from PSI, most recently used at Jefferson Laboratory

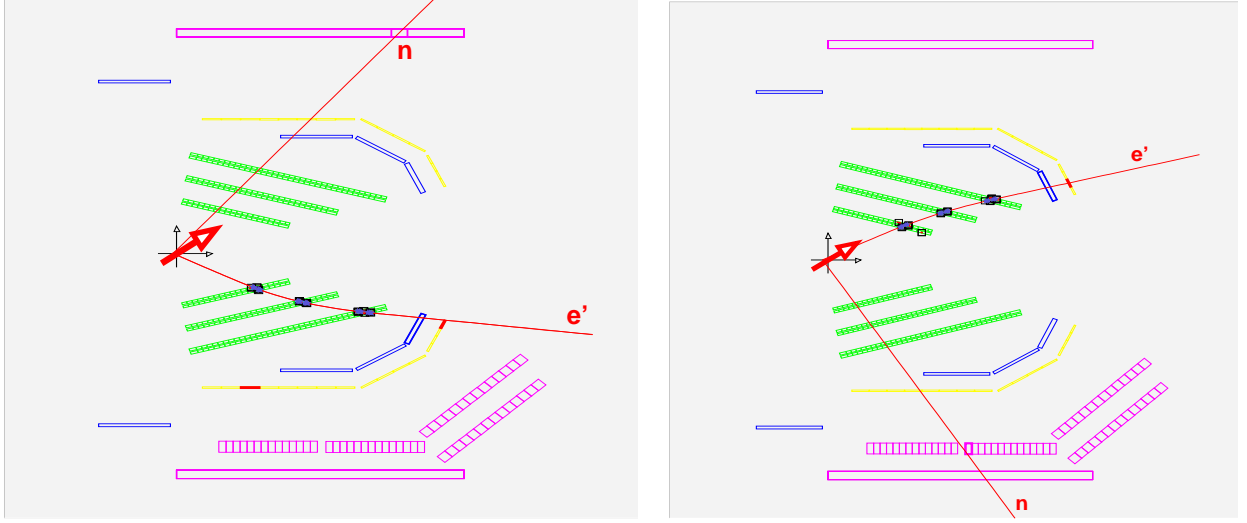


Figure 4-13: Single event display of a  ${}^2\vec{H}(\vec{e}, e', n)p$  event in the BLAST acceptance in parallel (left) and perpendicular (right) kinematics. The scattered electron track bends into the beam pipe. The neutron track is a straight line between the vertex defined by the electron track and the position of a hit in the neutron counter. The neutron detection was enhanced in the perpendicular kinematics regime.

the left sector.

### Time Calibration of the Neutron Detectors

The time-to-digital converter (TDC) start for the neutron counter signal is defined as the electron's time of flight to the TOF plus the light propagation time inside of the scintillator and the delay time in the electronics. The stop is the sum of the neutral particle's time of flight, the light propagation time and the neutron detector's electronics delays. Mathematically the start and stop times of a neutron detector TDC are defined as

$$\begin{aligned}
 t_{start}^n &= T^e + T_{sc}^{tof} + T_{el}^{tof} \\
 t_{stop}^n &= T^n + T_{sc}^n + T_{el}^n,
 \end{aligned}
 \tag{4.10}$$

where  $T^i$  is the physical time of flight of the particle and  $T_{sc}^i$  is the light propagation time in each detector. Each detector has a photo-multiplier tube at both ends of the scintillator. The light propagation time  $T_{sc}^i$  is different for each end of the scintillator, depending on where the particle hits the scintillator. However, for a *mean-timed* TDC signal this value

Sector	Wall	# of detectors	orientation	thickness (cm)	length (cm)	width (cm)
Left	Ohio	8	horizontal	10	400	22.5
Right	Ohio	8	horizontal	10	400	22.5
Right	L20L	14	vertical	20	160	13.7
Right	L20R	14	vertical	20	160	13.7
Right	L15L	14	vertical	15	160	9.3
Right	L15R	14	vertical	15	160	9.3

Table 4.3: Geometrical dimensions of neutron detectors in each neutron wall. Orientation refers to the orientation of the largest dimension. Thickness refers to the width of a detector material seen by a neutron incident perpendicular to the detector. The effective thickness is dependent upon the angle of an incident neutron.

is constant. The difference between  $T_{sc}^i$  at each end gives the particle's incident position in the detector. Therefore, the time-of-flight and the position as measured by the TDCs are defined as

$$\begin{aligned}
TOF^n &= \frac{1}{2}(TDC(0) + TDC(1)) = (T^n - T^e) + (T_{sc}^n - T_{sc}^{tof}) + (T_{el}^n - T_{el}^{tof}) \\
POS^n &= \frac{1}{2}(TDC(0) - TDC(1)) = \frac{1}{2}(T_{sc}^n(0) - T_{sc}^n(1)),
\end{aligned} \tag{4.11}$$

where  $TDC(i)$  is the TDC value at each end of a scintillator. The momentum of a neutral particle is calculated from the value of  $T^n$  in eqn. 4.11. The only unknown in this equation is the relative time offset due to the electronics delay,  $T_{el}^n - T_{el}^{tof}$ . Typically, these values are different for each TOF-neutron detector combination. Two methods were used to obtain these values.

The first method involves a flasher system with the laser light being delivered to all TOFs and neutron detectors simultaneously. The precision of this method depends on the synchronization of the laser splitter output slots, all optic fibers going to the detectors being of the same length, the precise knowledge of the position of the optic fibers couplers on each scintillator and the knowledge of the speed of light inside the detector material. Then eqn. 4.11 can be solved for  $T_{el}^n$  with  $T^n - T^e = 0$  and  $POS^n = 0$  (since an attempt was made to put all fiber optic cables into the middle of a scintillator). However, as it turned out, the laser flashers were not synchronous, not all fiber optic cables were of the same length and the measured speed of light inside of the plastic scintillator material strongly deviated from the assumed values<sup>7</sup>.

---

<sup>7</sup>This was especially true in the case of LADS detectors, where the speed of light varied by 10% from

A new method was developed by Chris Crawford [147] to find proper time offsets,  $T_{el}^n$  using cosmic events. This method was first used by Chris to find time offsets for all TOFs. The knowledge of the TOF offsets allows one to find a time offset for all neutron detectors with respect to just one TOF. The relative time of a cosmic particle passing through both the TOF and the neutron detector can be defined as

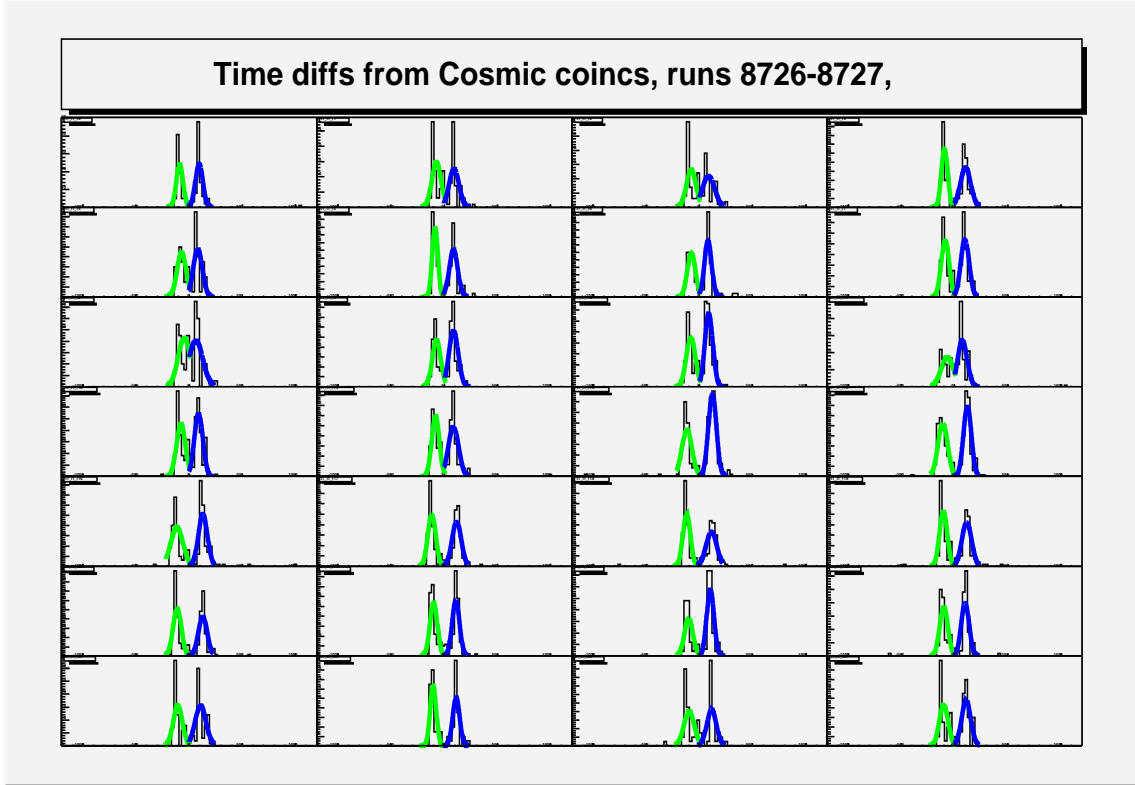


Figure 4-14: Neutron detector timing calibration using cosmic rays. Each peak is fitted with a Gaussian. The timing offsets were applied to center Gaussian peaks around channel zero. The green Gaussian corresponds to the particle traveling from a TOF to a neutron counter and the blue Gaussian corresponds to a Neutron counter to TOF path.

$$TDC_{tof} - TDC_n = \begin{cases} T_{sc}^n - T_{sc}^{tof} + T_{el}^n - T_{el}^{tof} - 1000 + TOF_{cosmic} & , \text{ TOF} \rightarrow \text{Neutron} \\ T_{sc}^n - T_{sc}^{tof} + T_{el}^n - T_{el}^{tof} - 1000 - TOF_{cosmic} & , \text{ Neutron} \rightarrow \text{TOF} \end{cases} \quad (4.12)$$

where  $TDC_i$  is the *mean-time* average of the TDC values at two ends of a scintillator, as defined in eqn. 4.11,  $TOF_{cosmic}$  is the time it takes a cosmic particle to travel between a neutron detector and a TOF, and 1000 is an arbitrary location of a TOF's *self-timing* peak detector to detector and deviated up to 30% from the expected values.

(see section 4.4). Since the travel time of a cosmic particle from a TOF to a Neutron counter equals the travel time between a Neutron counter and a TOF, a histogram of eqn. 4.12 should be ideally centered around zero. If it is not, then the amount it takes to center the spectrum around zero corresponds to the time offset for this particular neutron detector (see fig. 4-14).

The above procedure is used to determine the sum of two time offsets at each end of a detector. In order to determine the individual offsets, the position spectrum defined in eqn. 4.11 was used with the same cosmic data (see fig. 4-15). The center of the position spectrum provides the second equation needed to solve for the individual time offsets. Since the whole length of a neutron detector is illuminated equally by the cosmic rays, the cosmic events provide a good reconstruction of the physical detector length. The comparison between the reconstructed size and the actual size of a detector gives a good determination of the velocity of light in the scintillator.

Since the cosmic data were collected only intermittently during the experiment, the flasher timing information was used to monitor run-to-run timing changes.

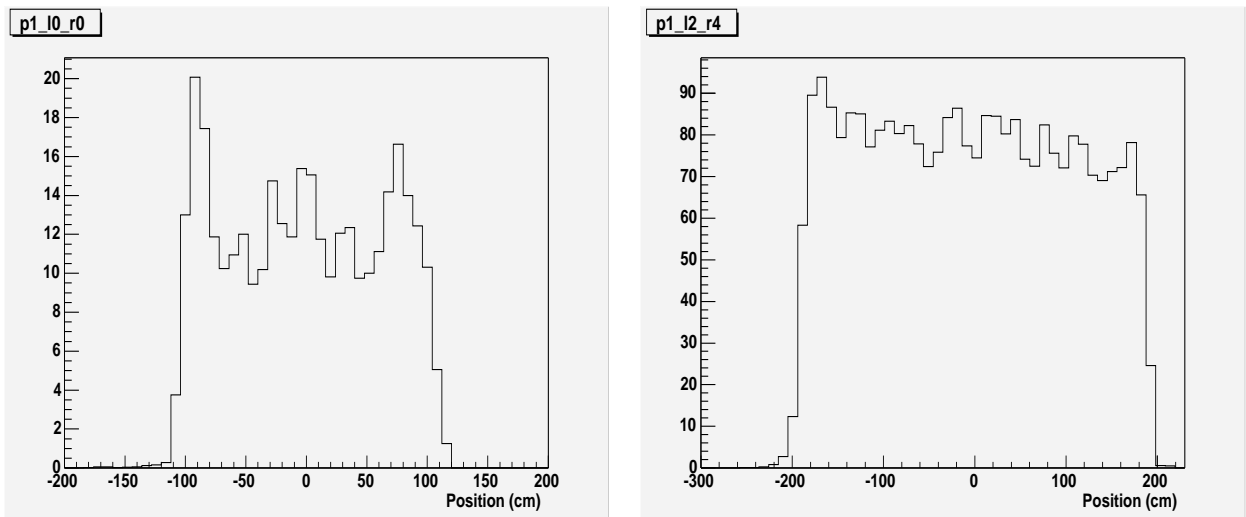


Figure 4-15: The Reconstructed position of cosmic events inside of a typical LADS detector (left) and typical OHIO detector (right). In this picture a uniform speed of light inside of a scintillator was assumed to be  $V_{cs} = 14.7$  cm/ns. This value reconstructs the length of the OHIO wall very well, whereas it overestimates the length of a LADS detector by 25%. The speed of light was adjusted individually for each neutron detector.

## Neutron TDC Calibration

The linearity of each TDC channel was verified to a sub-nanosecond level by introducing a known amount of time delay. The deviation of the slope from the assumed slope of  $50 \frac{psec}{count}$  was at most  $2 \frac{psec}{count}$  in some channels. Since individual neutron PMT signals are digitized in the *leading-edge* discriminators, a significant pulse height dependence of the TDC value was observed. This is due to a *time-walk effect*, where larger signals trigger a leading-edge discriminator a few nano-seconds sooner than the smaller signals. To correct all TDC spectra for this effect, a set of timing measurements was made using a signal from the laser flasher with variable attenuation (see fig.4-16). A fit to the TDC vs. ADC curve was made using the following form,

$$TDC^i = \frac{p_0^i}{\sqrt{ADC^i - ADC_{ped}^i - p_1^i}}, \quad (4.13)$$

where  $ADC_{ped}^i$  is the pedestal value for an individual ADC, and  $p_0^i$  and  $p_1^i$  are the fit parameters determined for the individual TDC channels. The stability of the ADC pedestals was closely monitored during the experiment to reduce errors in calculating the walk effect.

## 4.4 The BLAST Trigger

The detector signals are routed from the experimental hall into a radiation-safe tunnel, where the readout electronics are located. Each PMT signal is split in to two signals by a splitter-delay module<sup>8</sup>. The delayed output of the splitter goes directly to a FASTBUS ADC (Lecroy 1881 M) module for an integrated charge measurement. The prompt output of the splitter is fed to a discriminator module (Lecroy 3412 constant fraction discriminator for TOFs, Lecroy 3420 leading edge discriminators for Čerenkov and in-house built leading edge discriminator for all Neutron counters). The output of the discriminator module is split into multiple signals. One discriminator output goes to the VME scaler modules for counting rate measurements in real time. The second output of the discriminator module is delayed and used for the individual TDC “stops”. The third discriminator output of an individual PMT is ANDed with the discriminated signal from the PMT at the opposite end of

---

<sup>8</sup>The outputs of the Čerenkov PMTs are added together before the splitter-delay box.

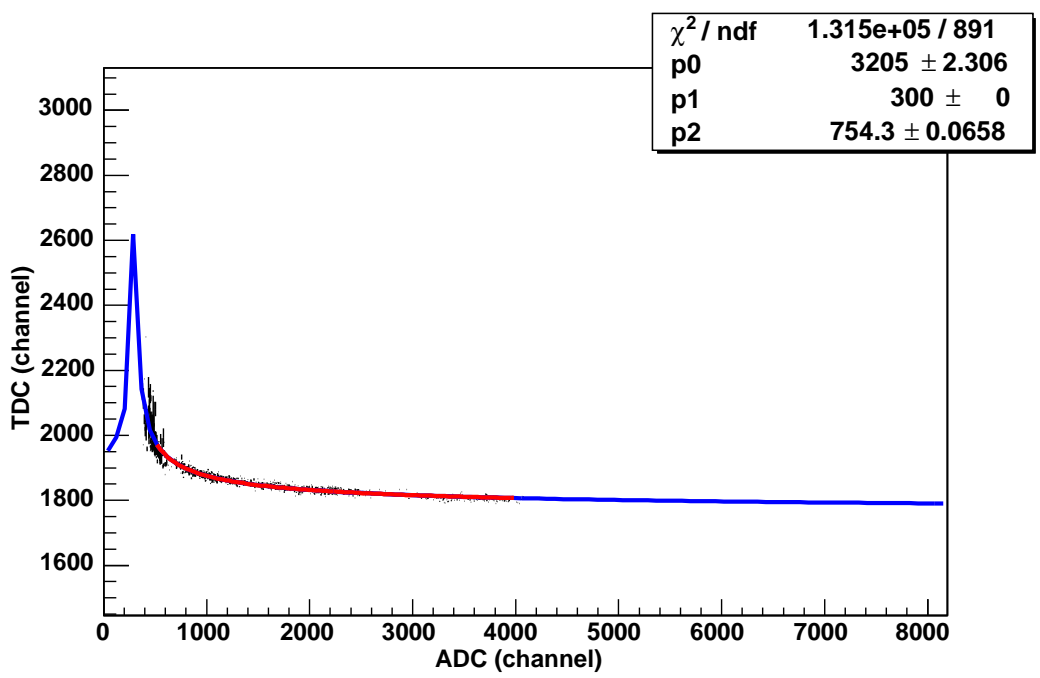


Figure 4-16: Time-walk correction for one of the neutron counters. In red is the region in which the fit of eqn. 4.13 is performed. The peak close to zero ADC channel is the analytical continuation of eqn. 4.13. This type of fit was done for all neutron detector PMTs.

a scintillator. The AND from each detector is ORed together with the rest of the scintillators in the detector subpart<sup>9</sup> (TOFs, Neutron Counters, etc.). The ORs are then fed into the programmable sector logic unit (MLU), which is capable of building up to  $2^{16}$  different logic combinations from its 16 inputs. The outputs of the sector MLUs are connected into the cross sector MLU (XMLU) unit. The XMLU is programmed for various left-right sector trigger combinations constituting a *first level trigger*.

The majority of all events that pass the first level trigger requirement leave no track in the drift chambers. These events are most likely from the electromagnetic showers originating in the collimator at the upstream end of the target cell. A *second level trigger* was instrumented to reduce the count rate due to the trackless events. The second level trigger constitutes an AND of at least one wire hit in each of the three wire chambers. Table 4.4 describes the definitions of all trigger types used during the experiment. The hierarchy of the triggers in table 4.4 is top to bottom. For example, if an event satisfies both trigger types #1 and #7, the event is assigned to trigger #1 and so on. The trigger rates are lowered by a factor of

<sup>9</sup>In case of TOFs only 5 through 16 are ORed. TOFs 1 through 4 are used as individual detector subparts.

20 with the addition of the second level trigger. The total second level trigger rate is  $\sim 200$  Hz. The trigger rate is dominated by trigger #7 (inclusive electron scattering). The overall dead time is  $\sim 15\%$ .

Trigger	minimal definition	prescale	1st/2nd level rates
# 1	$\text{TOF}_l \& \text{TOF}_r$	1	$\sim 32/2$ (Hz)
# 2	$(\text{TOF}_l \& !\text{TOF}_r \& \text{NC}_r) \parallel (\text{TOF}_r \& !\text{TOF}_l \& \text{NC}_l)$	1	$\sim 1100/66$ (Hz)
# 3	$(\text{TOF}_l \& \text{TOF}_l \& \text{CC}_l) \parallel (\text{TOF}_r \& \text{TOF}_r \& \text{CC}_r)$	10	$\sim 87/5$ (Hz)
# 4	$(\text{TOF}_l \& \text{TOF}_l) \parallel (\text{TOF}_r \& \text{TOF}_r)$	100	$\sim 235/14$ (Hz)
# 5	$(\text{TOF}_l \& \text{BAT}_r \& \text{CC}_{bat}) \parallel (\text{TOF}_r \& \text{BAT}_l \& \text{CC}_{bat})$	1	$\sim 16/1$ (Hz)
# 6	$(\text{TOF}(12-15)_l) \parallel (\text{TOF}(12-15)_r)$	1000	$\sim 760/46$ (Hz)
# 7	$(\text{TOF}(0-11)_l \& \text{CC}_l) \parallel (\text{TOF}(0-11)_r \& \text{CC}_r)$	3	$\sim 3200/192$ (Hz)
# 8	Flasher	1	1/na (Hz)

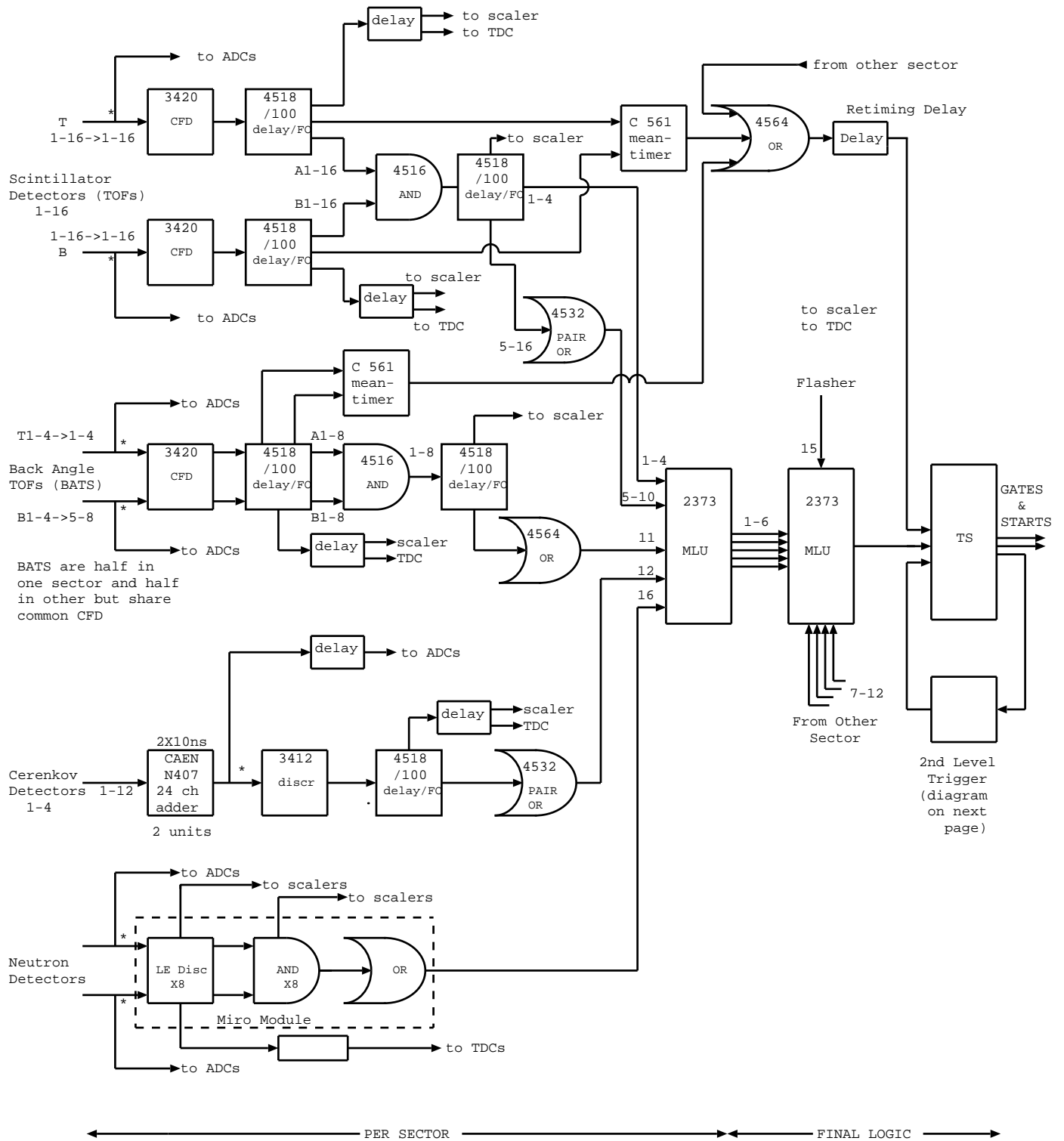
Table 4.4: BLAST trigger definitions in XMLU and rates after the prescaling. Minimal definition is defined as a minimum requirement needed for an event to be defined as a particular trigger type. TOF: TOF detector, NC: Neutron counters (Ohio walls or LADS), CC: Čerenkov detector, BAT: Backward Angle Detectors, “l” and “r” subscripts refer to the left and right sectors in BLAST, respectively and “bat” subscript refers to the special Čerenkov instrumented in front of the Backward Angle Detectors.

All scintillator TDCs operate in a *common start* mode where the start is defined by the trigger out of the XMLU, with the start time given by the earliest TOF mean time. In a typical BLAST coincidence event, the scattered electron triggers the TOF scintillator before a hadron triggers a TOF or a Neutron Counter in the opposite sector. In this way, the timing signal from the electron always shows up as a sharp *self-timing* peak in the TDC spectrum. The hadron timing is measured in relation to the electron self-timing peak. This is done to give a stable reference time for the drift chambers.

A copy of the phototube TDC start signal is delayed to provide a common stop to the drift chamber TDCs which work in common-stop mode.

## 4.5 Charge Particle Veto

As mentioned before, a neutron event (trigger #2 in table 4.4) is defined as a hit in a Neutron counter and necessarily no hit in the TOF scintillator in the same sector. Typically, the experiments of this kind rely on a thin scintillator as a veto for charged particle [113]. However, even the most efficient thin scintillators are not 100% efficient. Since the  ${}^2\vec{H}(\vec{e}, ep)n$  rate is



note: \* all analog signal division in matched impedance passive splitters

Figure 4-17: BLAST first level trigger logic diagram

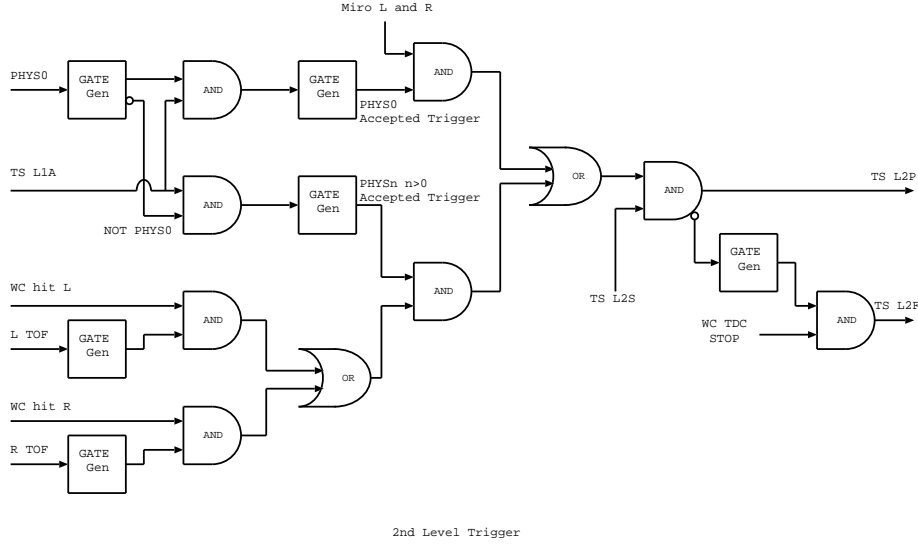


Figure 4-18: BLAST second level trigger logic diagram

an order of magnitude larger than the  ${}^2\vec{H}(\vec{e}, en)p$  rate<sup>10</sup>, even a small veto inefficiency can result in a sizable proton contamination. The proton background has a negative asymmetry. Thus, its contribution would dilute the positive neutron asymmetry.

The advantage of the BLAST detector is that all of its acceptance is covered by the large gas volume of the drift chambers. A charged particle ionizes the gas with close to 100 % probability. The ionization electrons in the gas are collected by an average of 18 wires. The probability of a single wire to produce a signal is better than 98 %. Thus, the probability of at least one wire hit when a proton passes through the drift chambers is better than 99.9%. By adding the drift chamber information into the neutron event identification, the charged particle veto efficiency is greatly improved. A possible background due to misidentified protons is investigated in section 5.6.2.

## 4.6 BLAST Monte-Carlo

The BLAST experiment was simulated with a GEANT Monte Carlo code, BLASTMC. BLASTMC uses an event generator, DGEN, based on H. Arenhövel’s electro-disintegration formalism [79]. The electro-disintegration events were evenly generated in a five dimensional phase space of variables,  $\phi_e$ ,  $\phi_{cms}$ ,  $\theta_{cms}$ ,  $\omega$  and  $\theta_e$ . The sixth variable in which the events

<sup>10</sup>This ratio is even larger when the neutron detection efficiency is factored in.

were simulated is the reaction vertex along the target cell. The vertex was generated with a triangular distribution function, following the target density distribution function. A map of the target holding field was used to calculate the target polarization angle at each vertex. The generated events were then propagated through the BLAST acceptance simulated with a GEANT software package. All detector hits and deposited energies were recorded into the event list. The event list was then sorted according to hit pattern, i.e. single electron hits, electron-proton coincidence, electron-neutron coincidence, etc. For each event a spin dependent cross section (see eqn. 2.72) was assigned as a weight. This cross section has an explicit dependence on  $\phi_e$  and  $\phi_{cms}$  (eqns. 2.75-2.79). The dependence of the cross section on the other three variables is hidden in the structure functions,  $f_{\mu\mu}$ . These structure functions were calculated by Arenhövel on a grid of variables  $\theta_{cms}$ ,  $\omega$  and  $\theta_e$  relevant to the BLAST acceptance (see fig. 4-19).

For each point on the  $\omega$ - $\theta_e$  plane a calculation of the structure function was done over the full range of  $\theta_{cms}$ ,  $0^\circ < \theta_{cms} < 180^\circ$ . The structure functions were determined for an event at an arbitrary  $(\theta_{cms}, \omega, \theta_e)$  point in the acceptance by interpolating the calculations on the grid using a cubic spline.

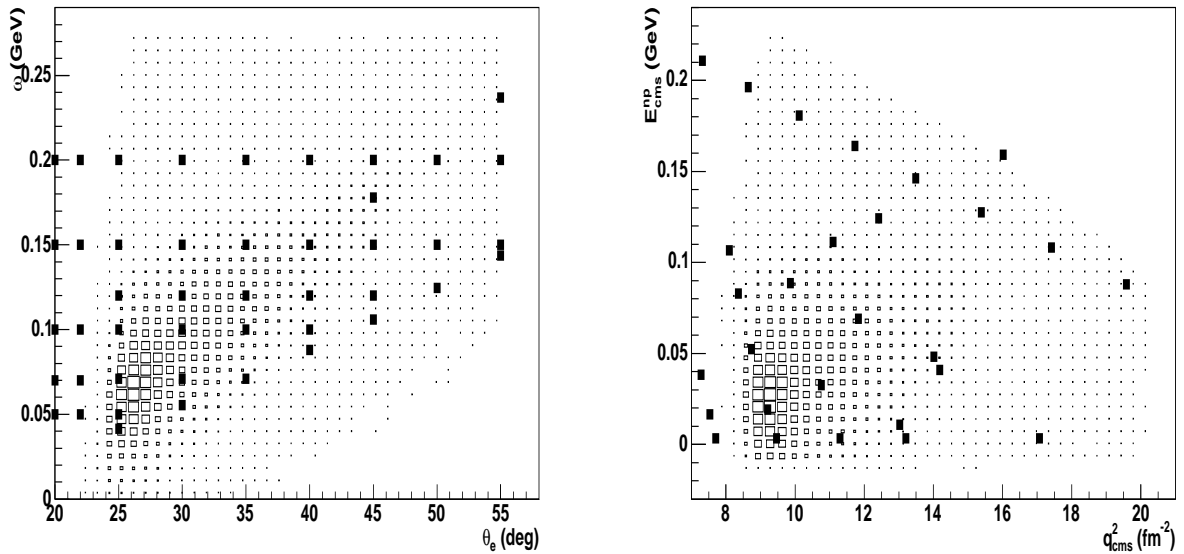


Figure 4-19: Plot of the BLAST kinematic acceptance with points at which Arenhövel's deuterium electro-disintegration calculation are available. A calculation grid in the  $\omega$ - $\theta_e$  plane (left) is regularized. Calculations, however, are done in the center of mass phase-space (right) where the grid is not as regular.

The momenta and angles of an electron, proton and neutron registered in the event list were convoluted with Gaussian functions whose widths match the realistic detector resolutions. All other kinematic quantities were then re-calculated from the convoluted quantities in the event list, similarly to how it is done with the reconstruction in the physical experiment.

The BLASTMC code uses GEANT to simulate the BLAST neutron detection volume. The neutron detection in GEANT is calculated from the neutron-proton elastic scattering in plastic detector material. The n-p elastic cross sections, which are related to the neutron detection efficiencies, are contained in the FLUKA component of the GEANT software. The neutron detection efficiency in GEANT is estimated on the average to be  $\sim 1\%$  per 1 cm of material.

The electron-neutron coincidence rate is proportional to the luminosity of the experiment, the average cross section in a particular kinematic bin, and the size of the phase space of this bin. The calculated coincidence rate can thus be expressed as

$$\mathcal{R} = \mathcal{L} \times \langle \sigma_j \rangle \times \Omega_j, \quad (4.14)$$

where  $\mathcal{L}$  is the luminosity,  $\langle \sigma_j \rangle$  is an average cross section in the  $j$ th bin and  $\Omega_j$  is the acceptance of this bin<sup>11</sup>. The average cross section can be calculated using Monte Carlo methods from a large ensemble of  $\sigma^i$  inside of a bin [148] as

$$\langle \sigma_j \rangle = \frac{\sum_i^{N_j} \sigma_j^i}{N_j}, \quad (4.15)$$

where  $N_j$  is the number of events in an individual bin. Here, the Monte Carlo integral is done over an ensemble of cross section values for events that have passed through the GEANT model of the BLAST acceptance and were registered as a hit. The advantage of this is that the very complicated BLAST acceptance as well as the neutron detection efficiency are folded into the average cross section calculation.

Since a “white” generator is used, the density of generated events is constant over the

---

<sup>11</sup>The bin acceptance is not purely geometrical, but also includes the physical BLAST acceptance.

whole generator phase space. This results in a very useful relation,

$$\frac{\Omega_j}{\Omega_{tot}} = \frac{N_j}{N_{tot}}, \quad (4.16)$$

where  $\Omega_{tot}$  and  $N_{tot}$  are the total volume and number of events generated respectively. All BLASTMC calculations in this work have been made with a white generator where,  $N_{tot} = 10$  million events were generated in a five dimensional volume,  $\Omega_{tot} = 0.245 \text{ GeV} \times \text{sr}^2$ . Using this equality, eqn. 4.14 becomes

$$\mathcal{R} = \mathcal{L} \times \frac{\sum_i^{N_j} \sigma_j^i}{N_{tot}} \times \Omega_{tot}. \quad (4.17)$$

Equation 4.17 helps to estimate the total rate from the electro-disintegration of deuterium in BLAST as a function of kinematic quantities ( $Q^2$ ,  $p_m$ , etc.) without analytically knowing the detector acceptance. However, the rate estimation is subject to relatively poor knowledge of the luminosity. Also, the GEANT model with an ideal detection efficiency is only an approximation to the physical BLAST detector.

The polarization observables measured at BLAST are independent of the precise knowledge of the luminosity or (to the first order) efficiency of the detector. The acceptance averaged, spin dependent asymmetries are expressed in terms of the coincidence rate in eqn. 4.17 as

$$\mathcal{A} = \frac{\mathcal{R}(+) - \mathcal{R}(-)}{\mathcal{R}(+) + \mathcal{R}(-)} = \frac{\sum_i^{N_j(+)} \sigma_j^i(+)-\sum_i^{N_j(-)} \sigma_j^i(-)}{\sum_i^{N_j^{tot}} \sigma_j^i}, \quad (4.18)$$

where  $N_j^{tot} = N_j(+) + N_j(-)$ .

Suppose now that the efficiency of the BLAST detector is overestimated in GEANT by a small amount,  $\epsilon$ . Then the number of events in the BLASTMC in each bin is  $N' = (1 + \epsilon)N$ , where  $N$  is the correct number of events. Since the efficiency is not dependent on the target spin or beam helicity, the eqn. 4.18 is rewritten as

$$\begin{aligned} \mathcal{A}' &= \frac{\sum_i^{(1+\epsilon)N_j(+)} \sigma_j^i(+)-\sum_i^{(1+\epsilon)N_j(-)} \sigma_j^i(-)}{\sum_i^{(1+\epsilon)N_j^{tot}} \sigma_j^i} = \frac{\mathcal{A} + \mathcal{A}(\epsilon)F(\epsilon)}{1 + F(\epsilon)}, \\ F(\epsilon) &= \frac{\sum_i^{\epsilon N_j^{tot}} \sigma_j^i}{\sum_i^{N_j^{tot}} \sigma_j^i}, \end{aligned} \quad (4.19)$$

where  $\mathcal{A}(\epsilon)$  is the asymmetry from the overestimated events. If the geometrical acceptance of the GEANT model is close to the physical acceptance, it is safe to say that  $\mathcal{A} = \mathcal{A}(\epsilon)$ . This means that  $\mathcal{A}' = \mathcal{A}$  and the efficiency of the detector cancels out in the spin asymmetry calculation. It is important, however, to simulate the geometrical acceptance of the BLAST detector in the GEANT model correctly.

# Chapter 5

## Data Analysis

### 5.1 Overview of the Experiment

This work is based on 1200 hours of polarized electron beam scattering from the polarized deuterium target in the South Hall Ring. The time averaged stored current in the ring in which the data acquisition was alive was 95 mA. The total accumulated charge was 420 kC, 40 kC of which were taken with cell #2; the rest were taken with cell #3. The maximum injected current increased over the course of the experiment from  $\sim 100$  mA to  $\sim 140$  mA with an average beam lifetime of  $\sim 20$  min. The target cell temperature was kept constant at  $\sim 90$  K. The polarized deuterium gas flow was  $\sim 2.5 \times 10^{16}$  atoms/s corresponding to a target density of  $\sim 4.5 \times 10^{13}$  atoms/cm<sup>2</sup>. Some amount of time was allocated to collect data on the empty and unpolarized gas targets to estimate background rates, false asymmetries and various other experimental systematics.

The data were taken on both vector and tensor polarized targets. Vector plus and minus and tensor minus (vector zero) polarized atomic beams were injected an average 1/3 of the total run time ( $\sim 400$  hours) each. The measurement of the cross section in one target polarization state continuously for the prolonged period of time would introduce systematic uncertainties in the asymmetry stemming from slow variations in the running conditions (beam, target, detector, etc.). To reduce these systematic errors the target polarization state was changed every 5 min. A sequencer program randomly selected a state from a set of three polarization states to be injected into the target. The detector's data acquisition

start date	05/26/04
finish date	10/15/04
total charge	420 kC
run time	1228 hours
beam energy, $E_e$	0.850 GeV
average beam current, $\langle I_e \rangle$	95 mA
average beam polarization, $\langle P_e \rangle$	$\approx 65\%$
average beam lifetime, $\langle \tau_e \rangle$	$\approx 20$ min
target angle, $\theta_D$	$32^\circ$
atomic beam flow, $I_0$	$2.6 \times 10^{16}$ atoms/sec
cell temperature, $T_{cell}$	$\approx 90$ K
target density, $\rho_{tot}$	$4.5 \times 10^{13}$ atoms/cm <sup>2</sup>
target vector polarization, $P_z$	$\approx 80\%$
electron geometrical acceptance per sector, $\Omega_e^{exp}$	461 msr
neutron geometrical acceptance (right sector), $\Omega_n^{exp}$	366 msr
neutron efficiency, $\epsilon_n$	$\sim 0.3$
electronics dead time	$\sim 15\%$
total luminosity, $\mathcal{L}_{tot}$	$1.32 \times 10^{38}$ cm <sup>-2</sup>
average ${}^2\vec{H}(\vec{e}, e'n)$ coincidence rate, $\langle \mathcal{R}_n \rangle$	0.1 Hz

Table 5.1: Summary of the experimental parameters. See text for details.

system was inhibited during the target polarization flip. The beam helicity was reversed at the source before each ring fill.

Both beam and target helicity information were digitized on an event-per-event basis in an ADC used as a bit register. Figure 5-1 shows the target polarization states as a function of time reconstructed from the bit register ADC.

The beam helicity and the target polarization state information were registered in an input register and read out with the scalers every second. The beam current in the ring was measured by the LDCCT. An output of the LDCCT was sent to a voltage-to-frequency converter and those pulses were sent to two scaler channels. One channel was ungated and the other was inhibited by “experiment busy” signal which is the combination of “run not in progress”, “front end modules busy”, “HV not all in good state” and “target no defined” signals. The inhibited current in the scalers was integrated to determine the accumulated charge for each beam and target helicity combination (6 in all). Both LDCCT and scalers were carefully calibrated. The calibrations were periodically checked over the course of the experiment.

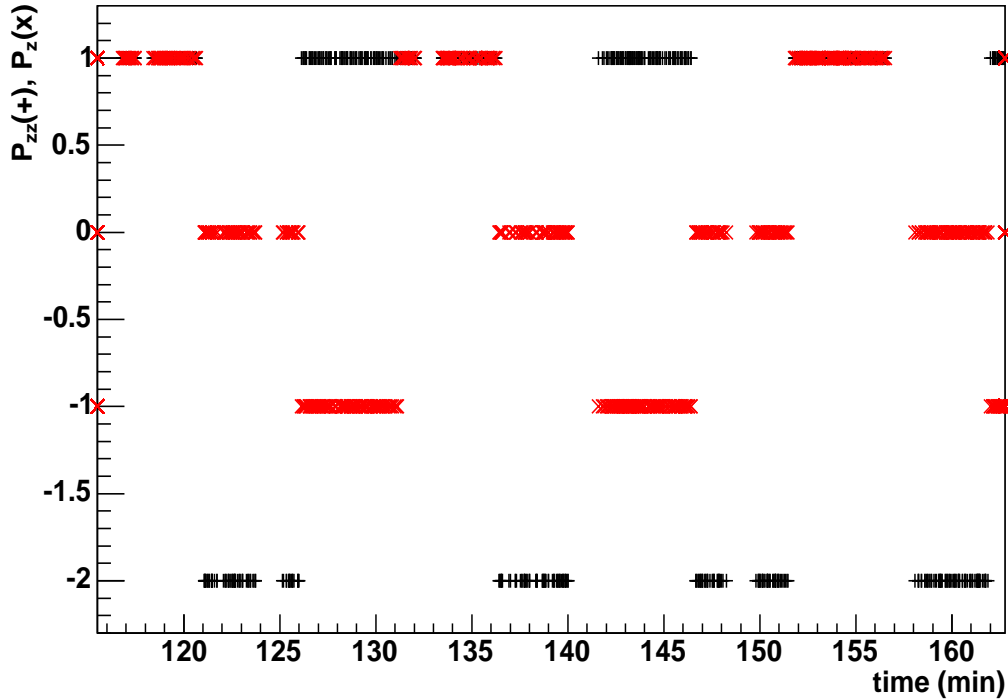


Figure 5-1: Target polarization states as a function of time. The polarization state was changed every 5 min. The tensor polarization (black +) has a value of -2 when the vector polarization (red x) has a value of 0. When a vector state of +1 or -1 is injected, the tensor polarization is 1. Breaks in the data correspond to periods of time when the DAQ was inhibited due to beam injection, detector voltage trips, etc.

## 5.2 Identification of the ${}^2\vec{H}(\vec{e}, e'n)p$ events

Since the same event identification procedure was applied to the data in each  $Q^2$  bin, it is sufficient to discuss the  ${}^2\vec{H}(\vec{e}, e'n)p$  event identification in the “super bin”, where all data are combined into one  $Q^2$  bin.

The  ${}^2\vec{H}(\vec{e}, e'n)p$  event identification starts with particle identification in each sector. The electron is easily identifiable as a relativistic particle creating an in-bending track in the drift chambers. The neutron is identified as a slow particle which fires a neutron bar, and leaves no wire hits in the drift chambers and deposits no energy in the thin plastic trigger scintillator (TOF). After the coincidence particles are identified, additional kinematic and data quality cuts are applied to the data. Below is the summary of the most significant cuts used.

### 5.2.1 Vertex cuts

The vertex of an individual event is determined from the reconstruction of the electron track. The purpose of a vertex cut is to ensure that the event comes from scattering on the gas in the target. The majority of the background rate in trigger #2 comes from electromagnetic showers. The primary source of these showers is the collimator upstream of the target. The vertex cut is an effective way to remove shower events produced at the collimator from the data sample.

The target cell is 60 cm long and has a triangular density profile. However, due to the length limitation of the target holding field magnet, the cut has to be made tighter, at  $\pm 20$  cm to avoid unpolarized background from the atoms in the zero holding field region.

The discussion of the data in the rest of this chapter assumes that the vertex cut has been applied.

### 5.2.2 Neutron-photon separation

There are two kinds of neutral particles detected by the neutron counters that leave no hits in the drift chambers and no deposited energy in the TOFs at BLAST. One is a neutron and the other is a high energy photon. Either particle in coincidence with an electron would produce trigger #2. The photons at BLAST have two major sources. One is the decay of  $\pi^0$  produced by the inelastic electron scattering. The lifetime of the  $\pi^0$  is  $\sim 10^{-4}$  ns, which means that the two gammas are produced immediately at the scattering vertex. The second source is an electromagnetic shower produced by the beam hitting the target cell holder. Since the reconstruction of the x and y coordinates of the vertex is limited at BLAST, the reconstructed electron from the shower appears to originate in the cell.

The gammas are relativistic particles, whereas the neutrons are much slower. Based on the relative velocities, a time-of-flight separation of the neutrons from fast gammas is possible. Figure 5-2 (left) shows the time spectrum produced by a neutral track in the right sector, less the time it would take a relativistic particle to reach the neutron detector.

The peak at zero represents a neutral particle traveling with the speed of light (gamma). The neutron reaches the detector 20 ns later, indicated by the position of the second peak. Since no other cuts have been applied so far, the source of the neutrons can be quasielastic

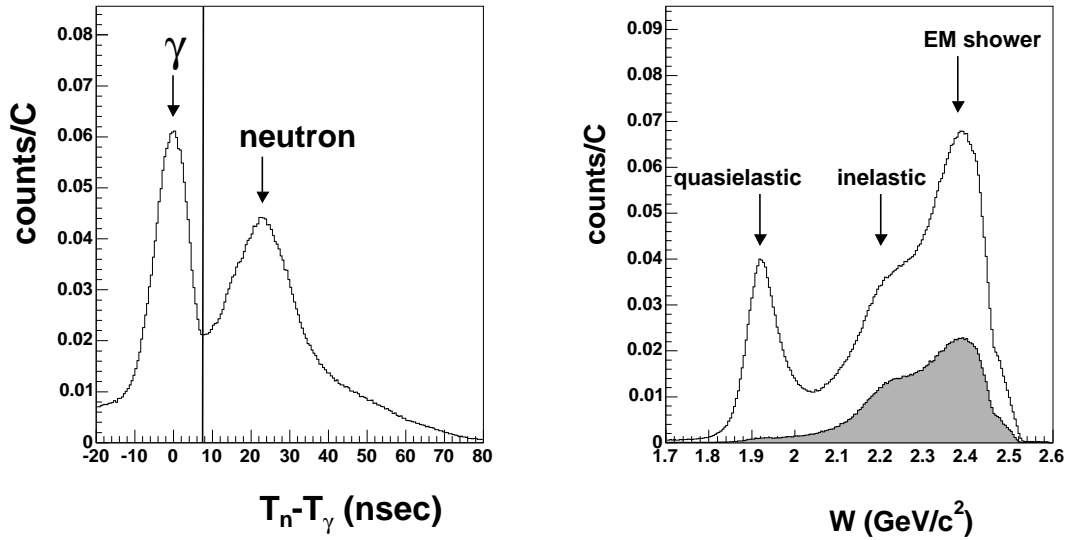


Figure 5-2: Plotted in the left panel is the time-of-flight spectrum of a neutral particle in which zero is the time at which photons reach the detector. The vertical line is a rough cut applied to separate neutron from gamma particles. Plotted in the right panel is the invariant mass of the final state defined in eqn. 2.69. The white spectrum represents all events and the shaded spectrum represents the gamma events. The quasielastic, inelastic and electromagnetic shower regions are identified.

scattering from the target gas and the target material,  $\pi^+$  or  $\pi^0$  production from deuterium, or random coincidences. A cut is applied at  $\sim 7.5$  nsec to separate slower neutrons from the relativistic gammas.

Figure 5-2 (right) shows the invariant mass of the final system, as defined in eqn. 2.69. The white spectrum represents all events. The shaded spectrum is what is left from the white spectrum after the gamma events are selected. The high energy photon events are mostly in the inelastic and electromagnetic shower kinematic regions. The neutron time-of-flight cut would remove these inelastic and shower events from the data sample. However, the comparison of two spectra shows that not all non-quasielastic events are removed with the neutron time-of-flight cut, meaning that at least half of all non-quasielastic events are underneath the neutron time peak. This is not unexpected. Other cuts are applied to further clean up the data.

### 5.2.3 Electron Quasielastic Cut

In the quasi-free scattering approximation, an electron elastically scatters from the neutron inside of the deuteron, while the proton is a spectator in the reaction. The quasi-free approximation is kinematically defined as

$$\sqrt{(\omega + M_n)^2 - \vec{q}^2} - M_n = 0, \quad (5.1)$$

where,  $\omega$  and  $\vec{q}$  are the energy and the three-momentum of the virtual photon respectively, and  $M_n$  is the mass of the neutron. Any deviation from this equality is due to the nucleon Fermi motion in the deuteron nucleus. Since quasielastic scattering dominates the total differential cross section, the histogram of eqn. 5.1 is expected to have a pronounced quasielastic peak.

Figure 5-3 is a histogram of equation 5.1 after the neutron time-of-flight cut is applied. The peak around zero corresponds to quasielastic scattering. The width of this peak is determined by the Fermi motion inside of the deuteron ( $\sim 75$  MeV/c) convoluted with the electron momentum resolution ( $\sim 23$  MeV/c).

A cut is applied around the quasielastic peak in fig. 5-3 to separate the pure quasielastic events from the inelastic and electromagnetic shower background.

### 5.2.4 Missing Mass Cut

The energy and momentum of the undetected recoil system are defined in equation 2.64. In a pure electro-disintegration reaction the undetected recoil system is in its ground state, i.e. the mass of the recoil system has an on-shell definition,

$$M_m^2 = E_m^2 - p_m^2 \quad (5.2)$$

In the case of deuteron break-up with a neutron detected in the final state, the mass of a recoil system is expected to be equal to the mass of the proton. In the ideal detector case, histogramming the difference of the calculated missing mass and the mass of the proton would produce a delta function.

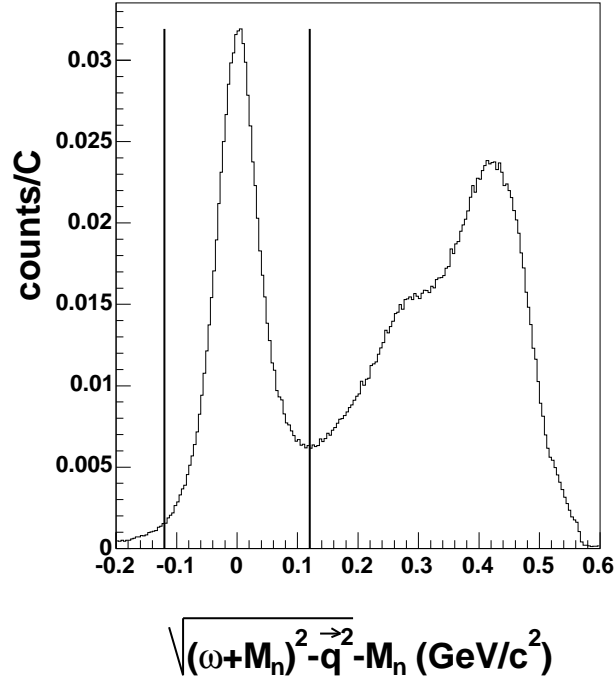


Figure 5-3: Histogram of the quasi-free neutron knock-out kinematics after the neutron time-of-flight cut. The vertical lines represent the cut around the quasielastic peak. This cut provides good background rejection from inelastic and shower events.

Thus, the advantage of the missing mass cut is that the width of the  $M_m - M_p$  spectrum is determined purely by a convolution of the electron and the neutron momentum resolutions and not by the kinematics of the reaction<sup>1</sup>. The full width at half maximum (FWHM) of the peak in figure 5-4 is  $\sim 60$  MeV/c<sup>2</sup>.

The cuts are applied to the data in each run to determine  ${}^2\vec{H}(\vec{e}, e'n)p$  yields per run. As expected, the yields have a Gaussian distribution (see fig. 5-5 (right)). The arbitrary cut of  $3 \times \sigma$  is used to throw out those runs with extremely high or low yields (marked with red markers in fig. 5-5 (left)).

<sup>1</sup>Actually, there is a slight spreading due to radiative processes.

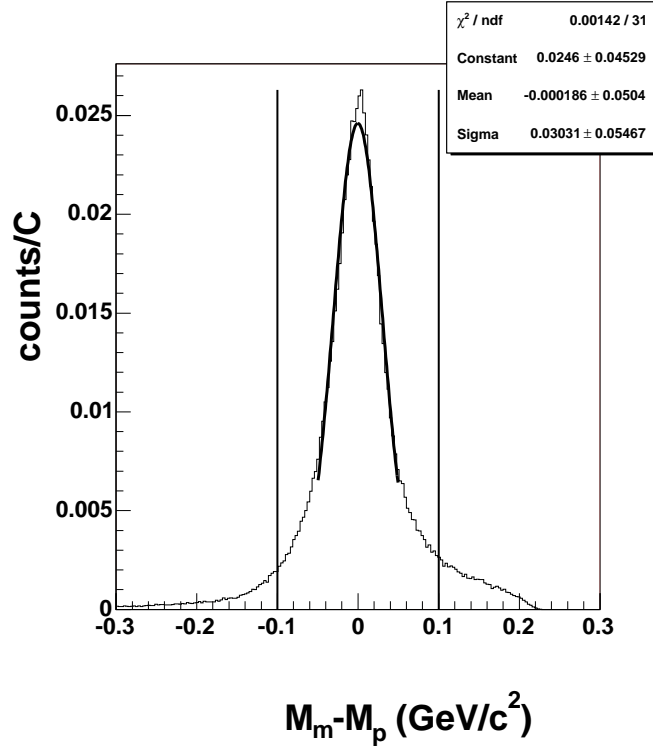


Figure 5-4: Missing mass spectrum of quasielastic events. Both neutron time-of-flight and quasielastic cuts have been applied. Vertical lines represent the cut used to isolate two body break-up events.

### 5.3 $Q^2$ Bin Selection

The decision on binning the data in  $Q^2$  is based on a desire to isolate  $Q^2$  regions of interest while having enough statistics in each bin to make a statistically significant measurement. The first point represents the best possible measurement at the lowest  $Q^2$  allowed by the BLAST acceptance. Four other data points are selected to optimally measure  $G_E^n$  in a region where the maximum of the neutron electric form factor is observed.

Five  $Q^2$  bins are chosen to be  $\langle Q^2 \rangle = 0.14, 0.20, 0.29, 0.38$  and  $0.50$   $(\text{GeV}/c)^2$ . Higher momentum transfer data are also available, but their analysis is outside of the scope of this work.

Table 5.2 lists the number of  ${}^2\vec{H}(\vec{e}, e'n)p$  events in each momentum transfer bin after the cuts are applied. The neutrons are contained equally in all six beam and target spin combinations. However, only four of these combinations contribute to the vector asymmetry.

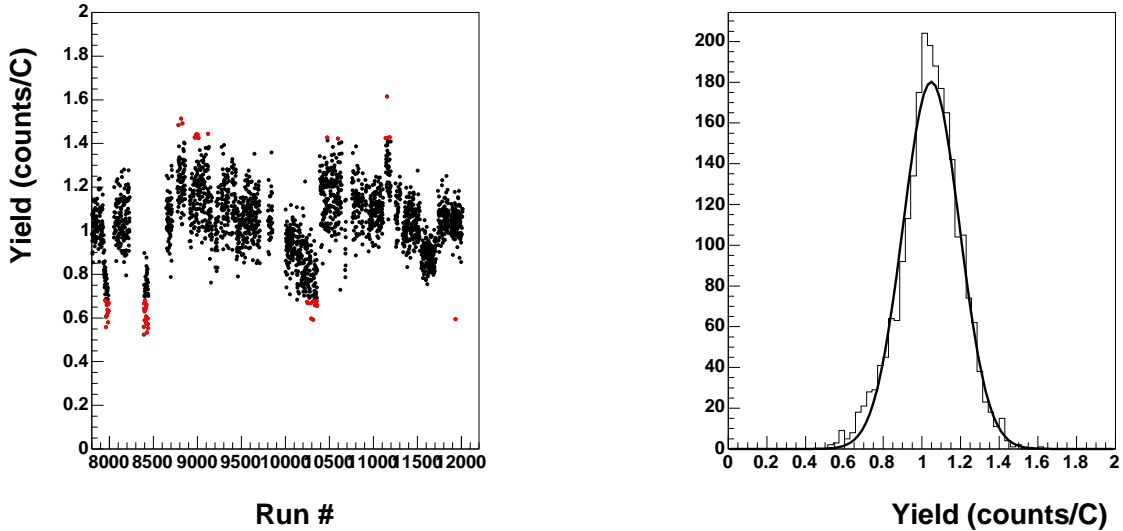


Figure 5-5: Neutron yields per run (left) and a histogram of yields (right). The mean neutron yield is  $1.05 \pm 0.11$  counts/C. A  $3 \times \sigma$  yield cut is applied to each run. In red are the yields that do not pass this cut. These runs are thrown out.

Therefore, only 2/3 of the events listed in table 5.2 are used in the  $G_E^n$  analysis.

## 5.4 Reconstructed Kinematic Variables

Figures 5-6 through 5-11 show a set of reconstructed kinematic variables compared to the BLASTMC predictions. The data are normalized to the total charge in the six spin state combinations. The BLASTMC curves are arbitrarily normalized to the data. Some kinematic correction had to be applied to the reconstructed data to achieve good agreement with the BLASTMC shapes. The source of these corrections is currently being investigated. The BLAST acceptance in the azimuthal angle of the electron,  $\phi_e$ , is narrower than predicted by the BLASTMC. This is primarily due to the inefficiency of the wire chambers at the edge of the  $\phi$ -acceptance. However, this inefficiency has no effect on the final result, since all inefficiencies drop out in the asymmetry to first order.

The missing mass peak in figs. 5-7, 5-9 and 5-11 is wider than the BLASTMC indicates. In fact the difference in the width grows as a function of  $Q^2$ . This difference is attributed to

cut	$\langle Q^2 \rangle = 0.14 \text{ (GeV/c)}^2$	$\langle Q^2 \rangle = 0.20 \text{ (GeV/c)}^2$	$\langle Q^2 \rangle = 0.29 \text{ (GeV/c)}^2$	$\langle Q^2 \rangle = 0.38 \text{ (GeV/c)}^2$	$\langle Q^2 \rangle = 0.50 \text{ (GeV/c)}^2$
-20cm < z < 20cm	818126	587193	333864	133472	109188
quasielastic	191215	123050	50758	24657	14875
missing mass	136206	94342	40144	18727	8096
neutron angle	115137	88435	39126	18478	7990

Table 5.2: Number of (e,e'n) events remaining for each  $Q^2$  bin after cuts. The first cut on the vertex is explained in section 5.2.1, the quasielastic cut in section 5.2.3 and the missing mass cut in section 5.2.4. The cut on neutron angle is necessary to remove events from a part of a neutron detector which is not covered by veto counters.

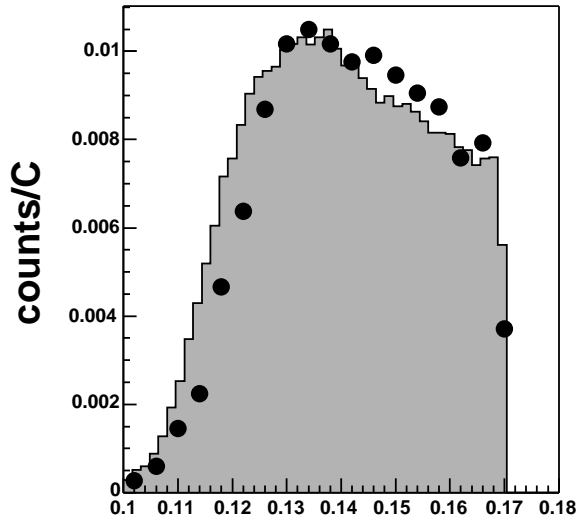
the radiative effects that at this moment are not accounted for in the BLASTMC. However, as will be shown, this is a small source of systematic uncertainty.

## 5.5 Raw Experimental Asymmetry

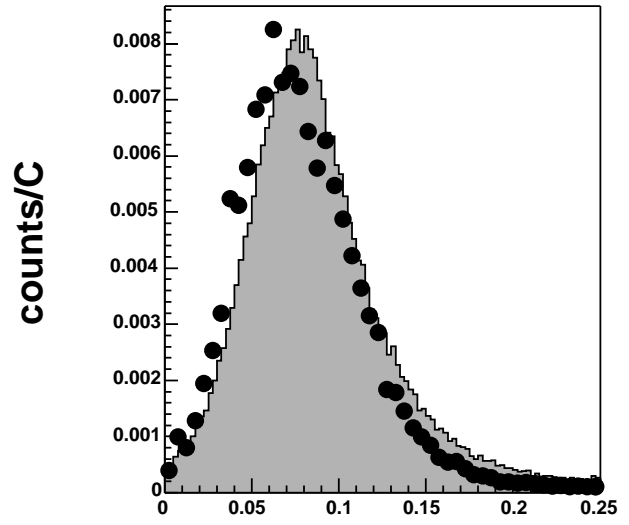
In the experimental asymmetry determination the number of neutrons is measured per unit charge for each of six combinations of beam and target polarizations. A yield column vector,  $n(h, P_z, P_{zz})$  has the following components

$$n(h, P_z, P_{zz}) = \begin{pmatrix} n(1, 1, 1) \\ n(1, -1, 1) \\ n(1, 0, -2) \\ n(-1, 1, 1) \\ n(-1, -1, 1) \\ n(-1, 0, -2) \end{pmatrix}. \quad (5.3)$$

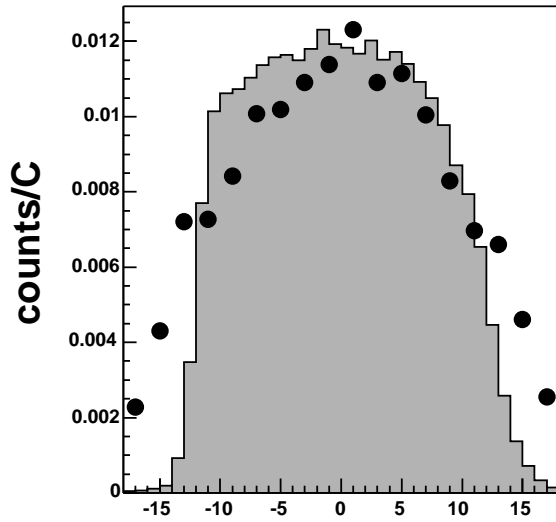
All five asymmetries defined in eqns. 2.75-2.79 can be represented as linearly independent combinations of six yields in equation 5.3. In matrix form these asymmetries are expressed as



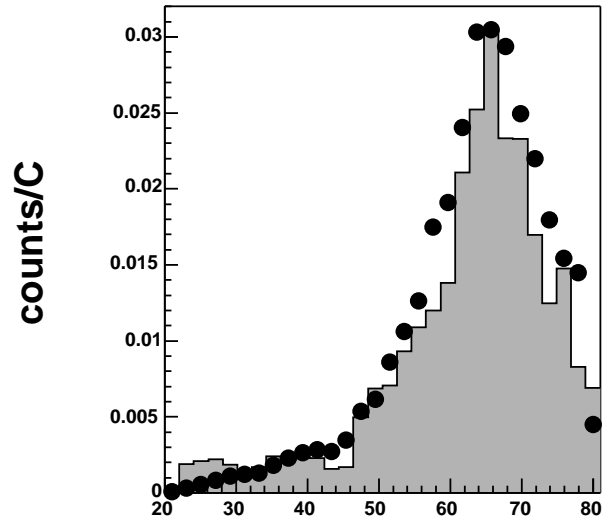
$Q^2$  (GeV/c)<sup>2</sup>



$\omega$  (GeV)



$\phi_e$  (deg)



$\theta_n$  (deg)

Figure 5-6: Reconstructed kinematic variables in the  $Q^2 = 0.14$  (GeV/c)<sup>2</sup> bin from the data (filled histogram) and from the BLASTMC (black dots). In the top left panel is the reconstructed  $Q^2$ . The top right panel shows the reconstructed energy of the virtual photon,  $\omega$ . The lower left panel shows an azimuthal angle of the scattered electron,  $\phi_e$ . In the lower right panel is the reconstructed polar angle of the detected neutron,  $\theta_n$ .

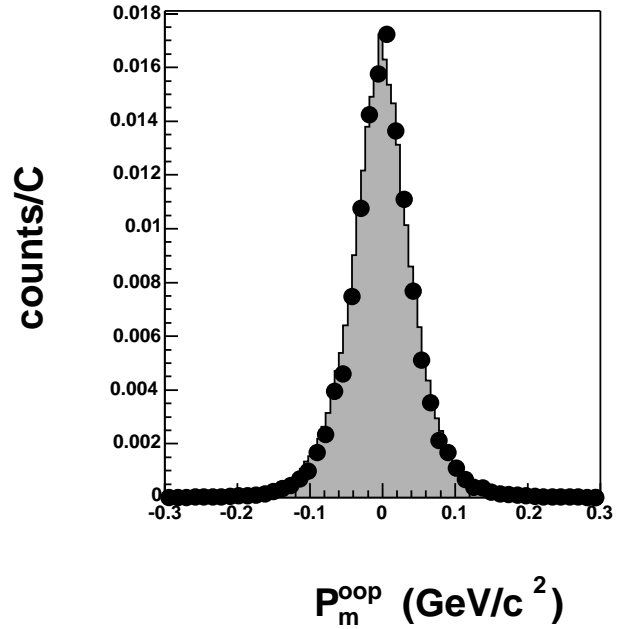
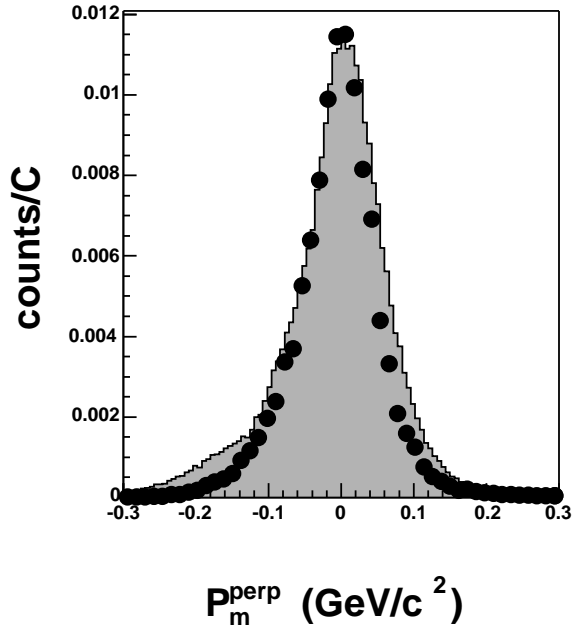
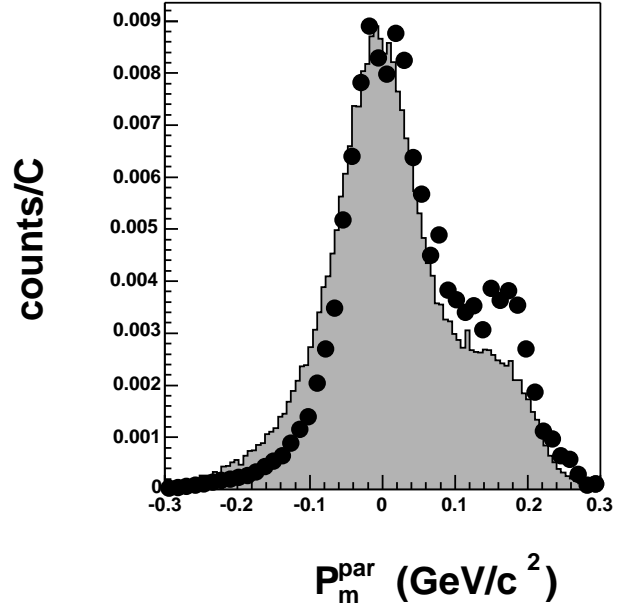
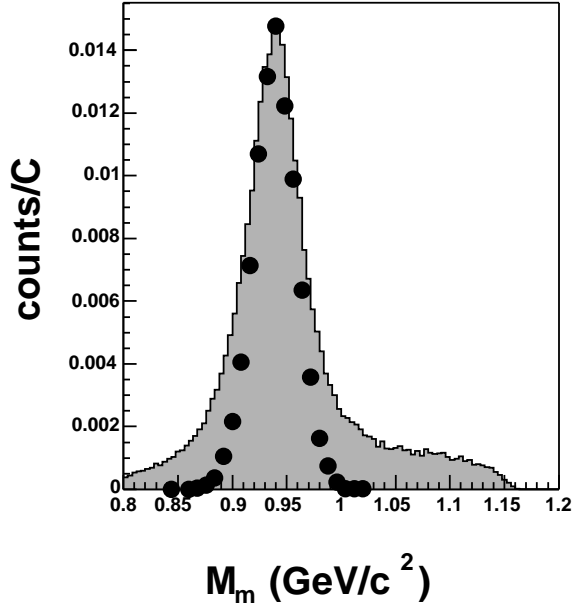
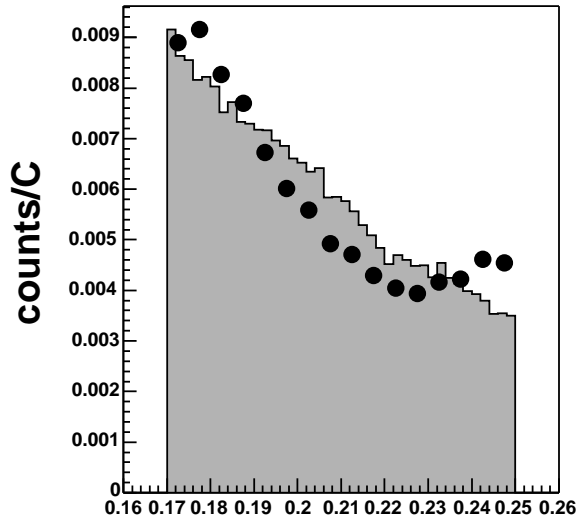
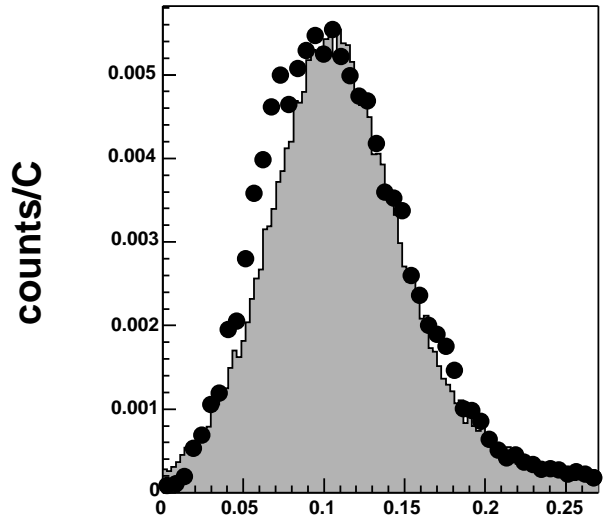


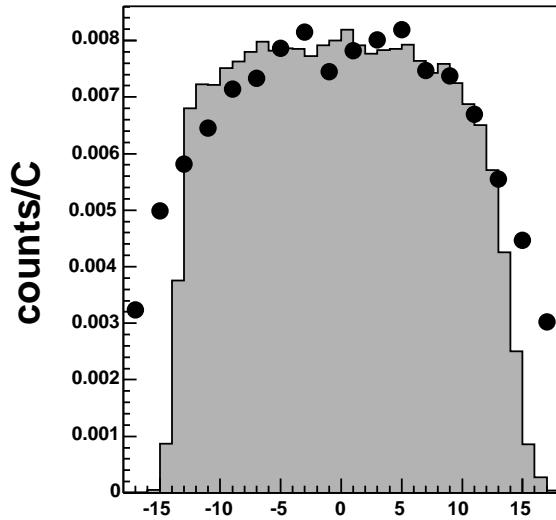
Figure 5-7: Reconstructed missing variables in the  $Q^2 = 0.14 \text{ (GeV}/c)^2$  bin from the data (filled histogram) and from the BLASTMC (black dots). In the top left panel is the reconstructed missing mass. The top right panel shows the component of the reconstructed missing momentum parallel to the momentum transfer vector,  $p_m^{\text{par}}$ . The bottom left panel shows the component of the reconstructed missing momentum perpendicular to the momentum transfer vector,  $p_m^{\text{perp}}$ . The bottom right panel shows the component of the reconstructed missing momentum pointing out of the scattering plane,  $p_m^{\text{oop}}$ .



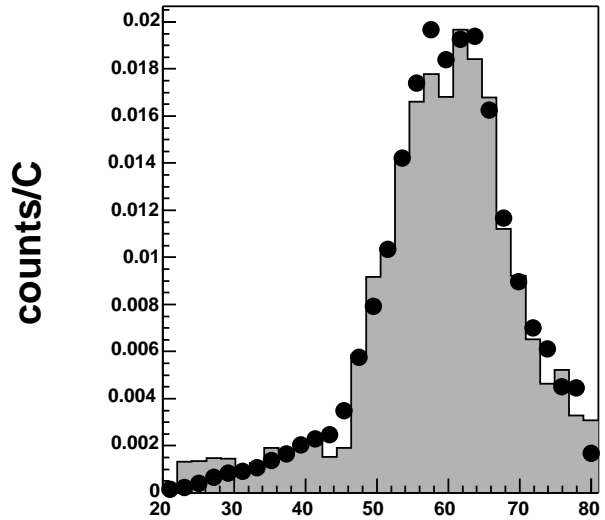
$Q^2 \text{ (GeV/c)}^2$



$\omega \text{ (GeV)}$



$\phi_e \text{ (deg)}$



$\theta_n \text{ (deg)}$

Figure 5-8: Reconstructed kinematic variables in the  $Q^2 = 0.20 \text{ (GeV/c)}^2$  bin from the data (filled histogram) and from the BLASTMC (black dots). In the top left panel is the reconstructed  $Q^2$ . The top right panel shows the reconstructed energy of the virtual photon,  $\omega$ . The lower left panel shows an azimuthal angle of the scattered electron,  $\phi_e$ . In the lower right panel is the reconstructed polar angle of the detected neutron,  $\theta_n$ .

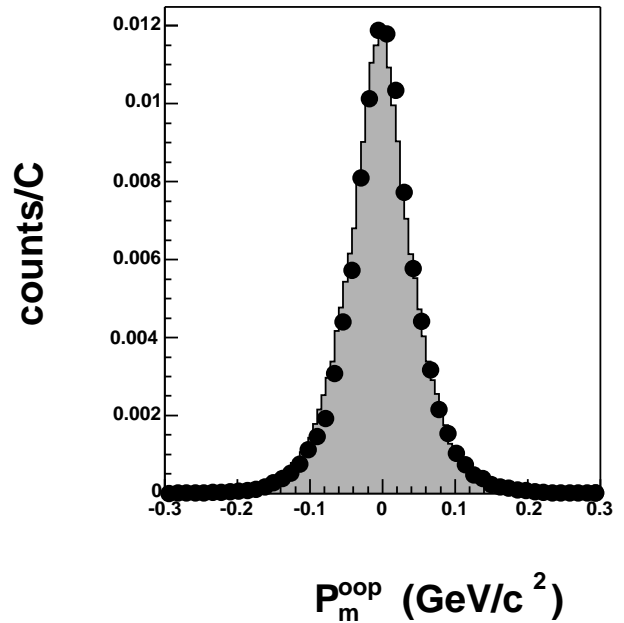
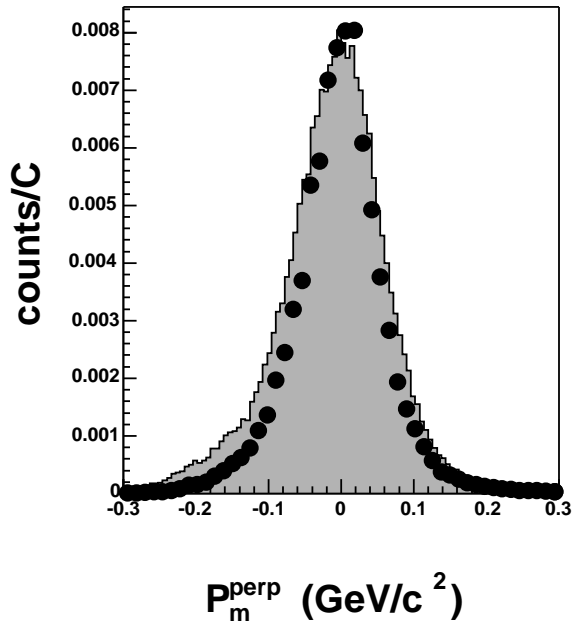
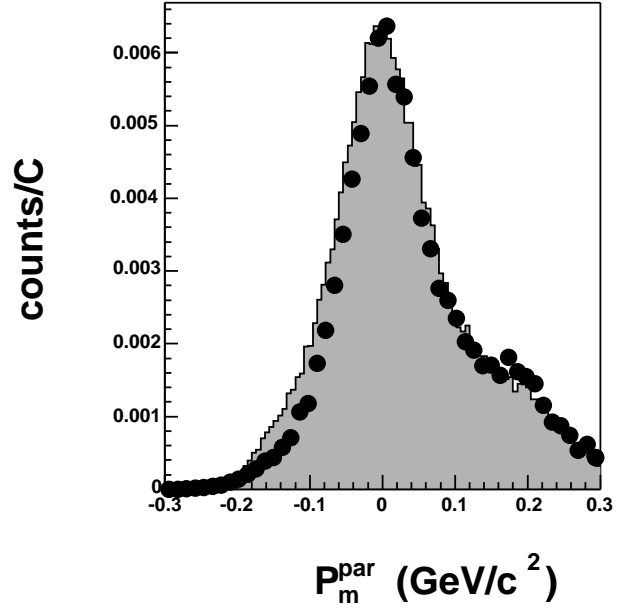
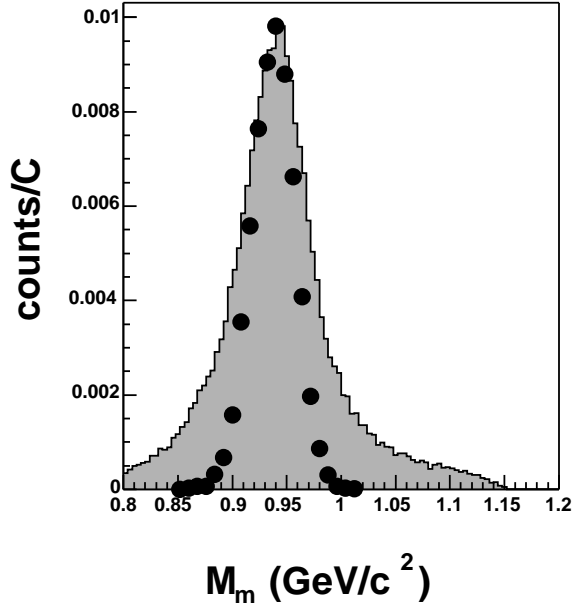


Figure 5-9: Reconstructed missing variables in the  $Q^2 = 0.20$  ( $\text{GeV}/c^2$ ) bin from the data (filled histogram) and from the BLASTMC (black dots). In the top left panel is the reconstructed missing mass. The top right panel shows the component of the reconstructed missing momentum parallel to the momentum transfer vector,  $p_m^{\text{par}}$ . The bottom left panel shows the component of the reconstructed missing momentum perpendicular to the momentum transfer vector,  $p_m^{\text{perp}}$ . The bottom right panel shows the component of the reconstructed missing momentum pointing out of the scattering plane,  $p_m^{\text{oop}}$ .

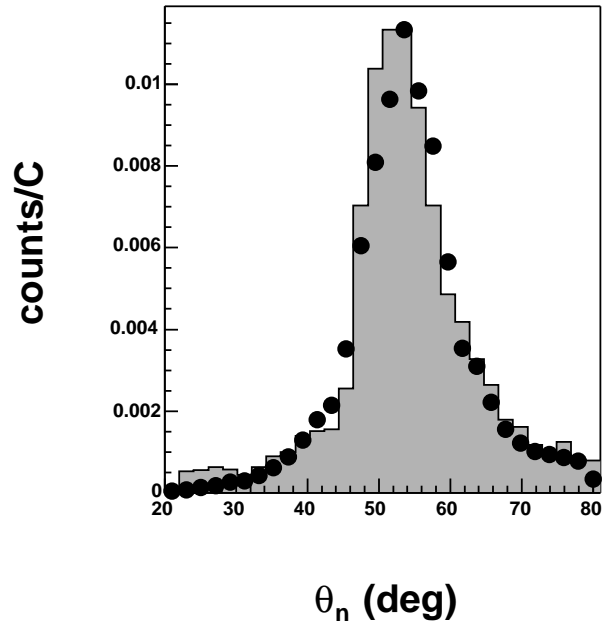
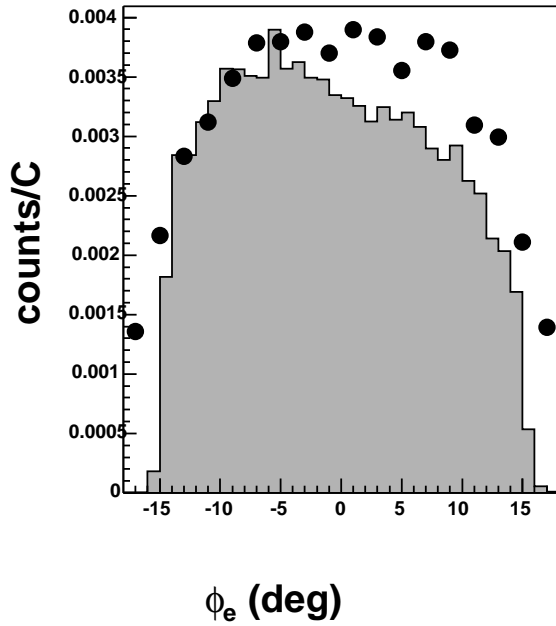
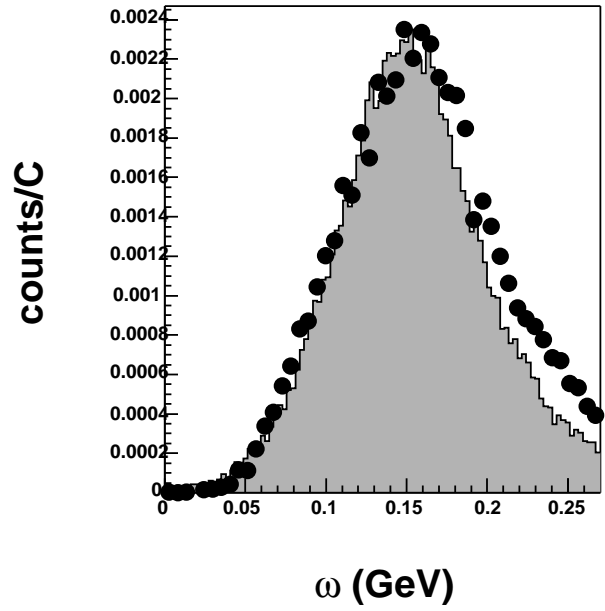
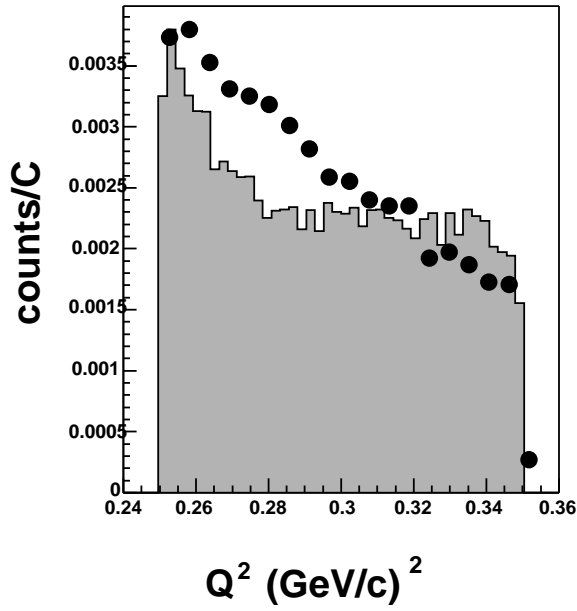


Figure 5-10: The reconstructed kinematic variables in the  $Q^2 = 0.29 \text{ (GeV/c)}^2$  bin from the data (filled histogram) and from the BLASTMC (black dots). In the top left panel is the reconstructed  $Q^2$ . The top right panel shows the reconstructed energy of the virtual photon,  $\omega$ . The lower left panel shows an azimuthal angle of the scattered electron,  $\phi_e$ . In the lower right panel is the reconstructed polar angle of the detected neutron,  $\theta_n$ .

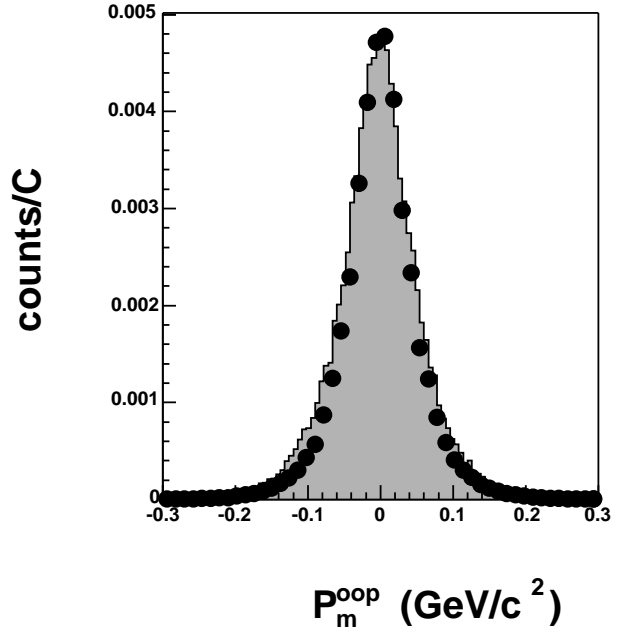
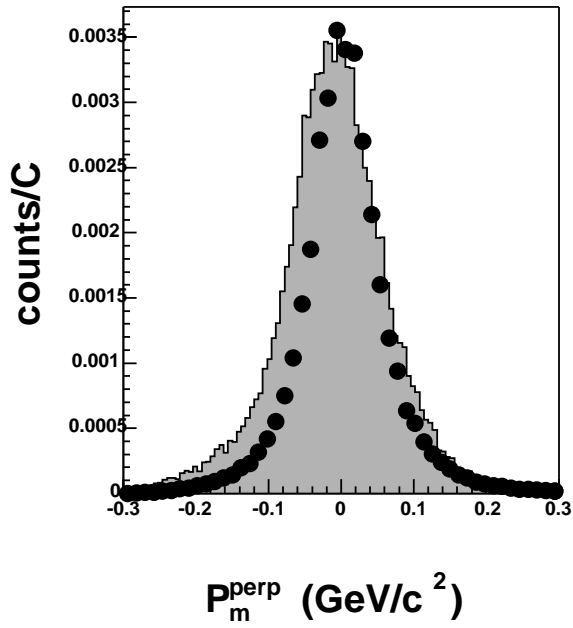
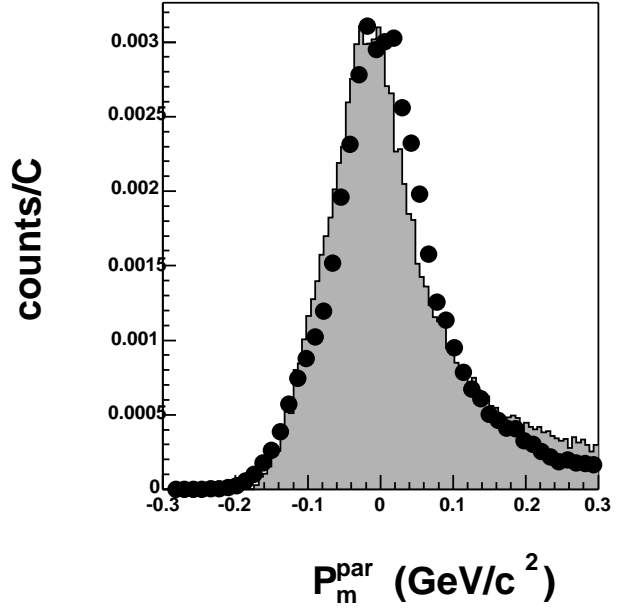
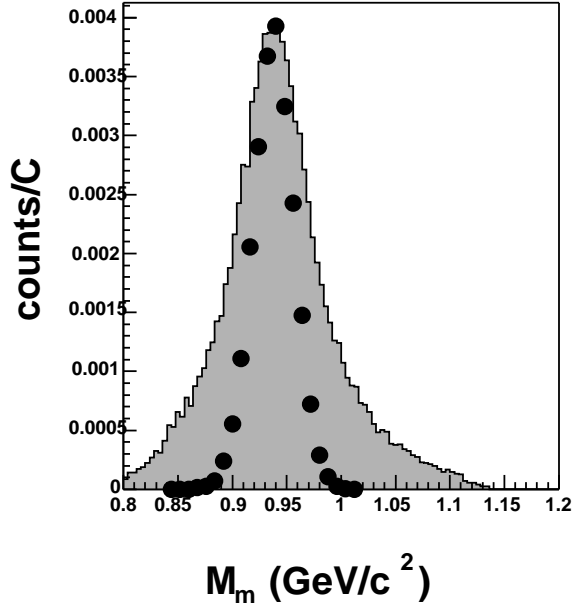


Figure 5-11: Reconstructed missing variables in the  $Q^2 = 0.29$  ( $\text{GeV}/c$ )<sup>2</sup> bin from the data (filled histogram) and from the BLASTMC (black dots). In the top left panel is the reconstructed missing mass. The top right panel shows the component of the reconstructed missing momentum parallel to the momentum transfer vector,  $p_m^{\text{par}}$ . The bottom left panel shows the component of the reconstructed missing momentum perpendicular to the momentum transfer vector,  $p_m^{\text{perp}}$ . The bottom right panel shows the component of the reconstructed missing momentum pointing out of the scattering plane,  $p_m^{\text{oop}}$ .

$$\begin{pmatrix} hA_e \\ P_z A_d^V \\ P_{zz} A_d^T \\ hP_z A_{ed}^V \\ (hP_{zz} A_{ed}^T) \end{pmatrix} = \frac{1}{n_{tot}} \begin{bmatrix} 1 & 1 & 1 & -1 & -1 & -1 \\ \sqrt{\frac{3}{2}} & -\sqrt{\frac{3}{2}} & 0 & \sqrt{\frac{3}{2}} & -\sqrt{\frac{3}{2}} & 0 \\ \sqrt{\frac{1}{2}} & \sqrt{\frac{1}{2}} & -\sqrt{2} & \sqrt{\frac{1}{2}} & \sqrt{\frac{1}{2}} & -\sqrt{2} \\ \sqrt{\frac{3}{2}} & -\sqrt{\frac{3}{2}} & 0 & -\sqrt{\frac{3}{2}} & \sqrt{\frac{3}{2}} & 0 \\ \sqrt{\frac{1}{2}} & \sqrt{\frac{1}{2}} & -\sqrt{2} & -\sqrt{\frac{1}{2}} & -\sqrt{\frac{1}{2}} & \sqrt{2} \end{bmatrix} \begin{pmatrix} n(1, 1, 1) \\ n(1, -1, 1) \\ n(1, 0, -2) \\ n(-1, 1, 1) \\ n(-1, -1, 1) \\ n(-1, 0, -2) \end{pmatrix} \quad (5.4)$$

where  $n_{tot}$  is the total number of events in all helicity states.

The polarization observable used to extract  $G_E^n$  is  $A_{ed}^V$  in perpendicular kinematics, corresponding to the electron being scattered into the left sector of the BLAST detector. From eqn. 5.4,  $A_{ed}^{V,exp}$  is explicitly written as<sup>2</sup>

$$A_{ed}^{V,exp} = \frac{1}{hP_z} \sqrt{\frac{3}{2}} \left( \frac{n(1, 1) + n(-1, -1) - n(1, -1) - n(-1, 1)}{n_{tot}} \right) \quad (5.5)$$

Figure 5-12 shows the raw asymmetry plots,  $A_{ed}^{V,exp}$ , where the electron is detected in the left sector for each  $Q^2$  kinematics bin.

## 5.6 Background Corrected Asymmetry

The raw asymmetries in fig. 5-12 are subject to small corrections due to the unpolarized and possibly polarized backgrounds. The possibilities of such backgrounds and their size are investigated in this section.

### 5.6.1 Unpolarized Background from the Target Cell

The unpolarized background mostly comes from the electron beam scattering from the walls of the storage cell. The resulting reaction is the quasielastic scattering on aluminum,  $^{27}Al(e, e'n)^{26}Al$ . This reaction is in many ways similar to the  $^2H(e, e'n)p$  reaction. The only difference is that the Fermi momentum is higher in aluminum than in deuterium. The

<sup>2</sup>The  $P_{zz} = 1$  is dropped from all  $n(h, P_z, 1)$  yields in this equation.

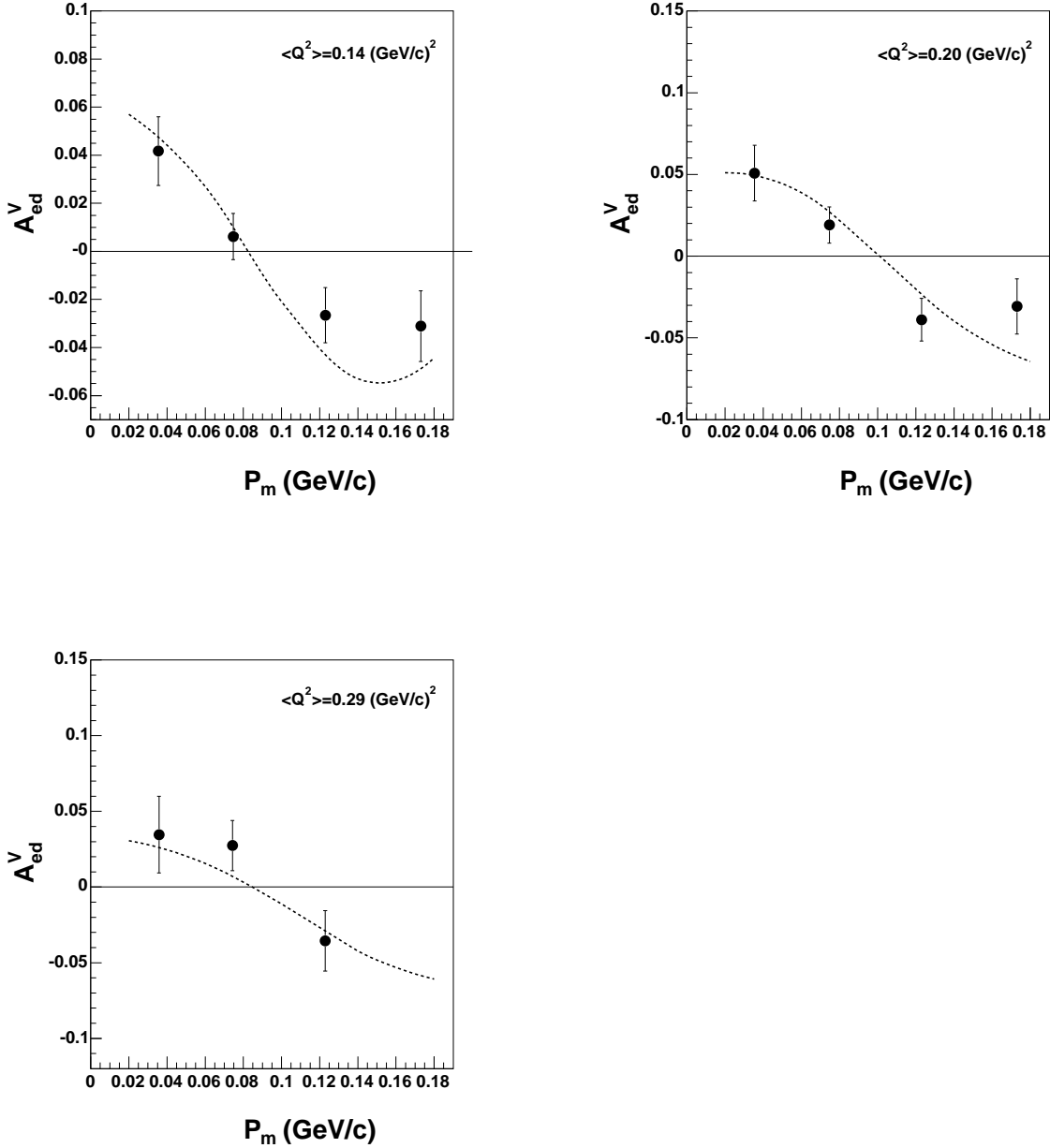


Figure 5-12: Plot of the beam-target vector asymmetry,  $A_{ed}^V$  not corrected for the unpolarized or polarized background in the  $Q^2 = 0.14$  (top left),  $0.20$  (top right) and  $0.29$  (bottom)  $(\text{GeV}/c)^2$  bins, respectively as a function of missing momentum,  $p_m$ . The dashed curve is the BLASTMC calculation with the Galster form factor for  $G_E^n$ .

background from quasielastic scattering on the aluminum cell is unpolarized since the cell itself is not polarized.

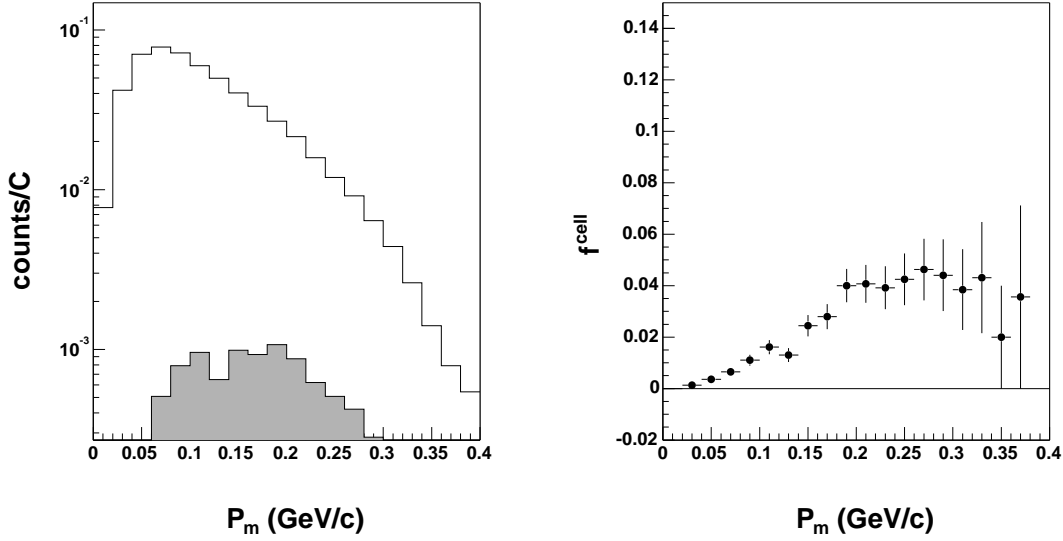


Figure 5-13: In the left panel is the yield from the cell wall scattering (shaded curve) compared to the yield of real quasielastic scattering from deuterium (clear curve). In the right panel is the ratio of the yields plotted as a function of missing momentum.

In the presence of the unpolarized background, the vector asymmetry,  $A_{ed}^{V,exp}$  in eqn. 5.5 is rewritten as

$$A_{ed}^{V,back} = \frac{1}{hP_z} \sqrt{\frac{3}{2}} \left( \frac{n(1,1) + n(-1,-1) - n(1,-1) - n(-1,1)}{n_{tot} + n_{cell}} \right), \quad (5.6)$$

where  $n_{cell}$  is the rate from the empty target.  $n_{cell}$  was measured during dedicated empty target running. The background-uncorrected asymmetry,  $A_{ed}^{V,back}$  in eqn. 5.6 is related to the true experimental asymmetry,  $A_{ed}^{V,exp}$  by

$$A_{ed}^{V,exp} = A_{ed}^{V,back} (1 + f^{cell}), \quad (5.7)$$

where  $f^{cell}$  is the ratio of the cell wall quasielastic events to the deuterium quasielastic events

$$f^{cell} = n_{cell}/n_{tot}. \quad (5.8)$$

Figure 5-13 shows the function  $f^{cell}$  measured with the empty cell. The data from all  $Q^2$  bins are combined in this measurement to improve statistics. It is assumed that the background conditions do not vary strongly as a function of the momentum transfer, since the quasielastic scattering on aluminum cross section has the same  $Q^2$  dependence as scattering on the deuteron. The maximum of  $f^{cell}$  function in the  $p_m$  region of interest is on the order of 4 %.

## 5.6.2 Polarized Background

A possible source of polarized background is from  ${}^2\vec{H}(\vec{e}, e'p)n$  events misidentified as  ${}^2\vec{H}(\vec{e}, e'n)p$  events. Since the electron-proton coincidence rate is an order of magnitude higher than the electron-neutron rate, a small charged particle veto inefficiency can be a significant contributor to the polarized background. This contribution becomes even more significant considering that the  ${}^2\vec{H}(\vec{e}, e'p)n$  asymmetry is on the average three times larger than the  ${}^2\vec{H}(\vec{e}, e'n)p$  asymmetry and has the opposite sign.

The proton veto inefficiency can be investigated using elastic electron-proton scattering on the polarized hydrogen target. The measured rate from the hydrogen target can then be compared to the rate from the empty cell. However, a distinction has to be made between the enhancement of the detected neutrons coming from the misidentified protons and the enhancement coming from the beam blowup effect. The beam blowup effect is due to the spreading of the electron beam diameter in the presence of the gas in the target. When the beam spreads, the electrons in the beam have a higher probability to scatter on the aluminum cell walls. A distinction can be made because, unlike the protons inside of the aluminum cell, the protons inside of the hydrogen are vector polarized. By building the vector asymmetry from these events one can determine the size of the polarized proton background.

Similarly to the unpolarized background correction in eqn. 5.7, the polarized background correction is written as

$$A_{ed}^{V,exp} = A_{ed}^{V,pol.back} (1 + f^p) (1 + f^{h,cell}) - A^{V,p} f^p (1 + f^{h,cell}), \quad (5.9)$$

where  $A^{V,pol.back}$  is the raw asymmetry measured in the presence of the polarized background,

$A^{V,p}$  is the proton asymmetry,  $f^{h,cell}$  is defined in eqn. 5.8 where  $n_{cell}$  is now the number of cell events in the presence of the hydrogen gas and  $f^p$  is the ratio of the misidentified proton event rate,  $n_{mis,p}$  to the neutron event rate defined as

$$f^p = n_{mis,p}/n_{tot}, \quad (5.10)$$

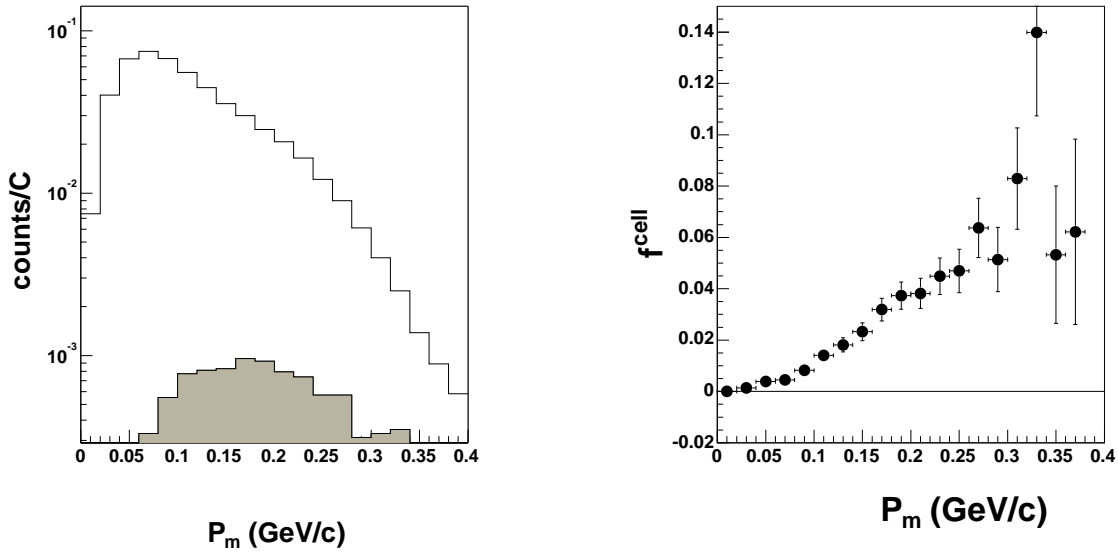


Figure 5-14: In the left panel the yield from the cell wall scattering in the presence of the hydrogen gas (shaded curve) is compared to the yield of real quasielastic scattering from deuterium (clear curve). In the right panel is the ratio of the yields plotted as a function of missing momentum.

It is estimated that  $f^p$  ( $< 0.1$  %) is negligible in comparison with  $f^{h,cell}$ . The estimate of  $f^p$  comes from the veto efficiency estimates, a very small vector asymmetry of the background events and the absence of a significant difference between  $f^{h,cell}$  and  $f^{cell}$ . In the following analysis,  $f^p$  defined in eqn. 5.10 is neglected. With this assumption, eqn. 5.9 looks identical to eqn. 5.7. The  $f^{cell}$  function with the presence of hydrogen gas in the cell is plotted in fig. 5-14. This function is almost identical to the function measured with the empty cell. From these two functions one can calculate the *beam blow up factor*.

The beam blow up factor, which can be defined as the ratio between  $f^{cell}$  and  $f^{h,cell}$  is

very close to unity,  $\sim 1.05$ . The minimal beam blow up due to the gas in the storage cell can possibly be explained by the collimator at the upstream end of the cell with its inner diameter smaller than the diameter of the cell.

The correction function  $f^{h,cell}$  determined with the hydrogen in the cell is applied to the raw vector asymmetries in fig. 5-12. Figure 5-15 shows the background-corrected vector polarization observable,  $A_{ed}^V(\frac{\pi}{2}, 0)$  in comparison to the BLASTMC calculation. The background-corrected asymmetry values are listed in table 5.3.

$\langle Q^2 \rangle$ (GeV/c) <sup>2</sup>	$\langle p_m \rangle$ (GeV/c)	$A^{exp}$	$\Delta A_{stat}^{exp}$	$\Delta A_{sys}^{exp}$
0.14	0.0355	0.0418	0.0143	0.0016
	0.0747	0.0062	0.0096	0.0002
	0.1230	-0.0270	0.0115	0.0010
	0.1730	-0.0320	0.0147	0.0012
0.20	0.0354	0.0509	0.0171	0.0020
	0.0749	0.0192	0.0111	0.0007
	0.1231	-0.0395	0.0131	0.0015
	0.1729	-0.0316	0.0169	0.0012
0.29	0.0358	0.0347	0.0254	0.0013
	0.0743	0.0276	0.0166	0.0010
	0.1229	-0.0361	0.0200	0.0014
0.38	0.0350	-0.0283	0.0340	0.0007
	0.0733	-0.0296	0.0249	0.0007
	0.1217	-0.0876	0.0345	0.0022
	0.1724	0.0166	0.0475	0.0004
0.50	0.0378	-0.1960	0.0880	0.0049
	0.0761	-0.0539	0.0459	0.0013
	0.1231	-0.0676	0.0503	0.0017
	0.1737	-0.1045	0.0636	0.0026

Table 5.3: Extracted background corrected  $A_{ed}^V(\frac{\pi}{2}, 0)$  values. The systematic uncertainty is due to the uncertainty of the beam and target polarization product,  $hP_z$ .

The systematic uncertainties quoted in table 5.3 are due to the uncertainty in the measurement of the beam and target polarization product,  $h \cdot P_z$ . The source of this and other systematic uncertainties will be discussed in section 5.8.

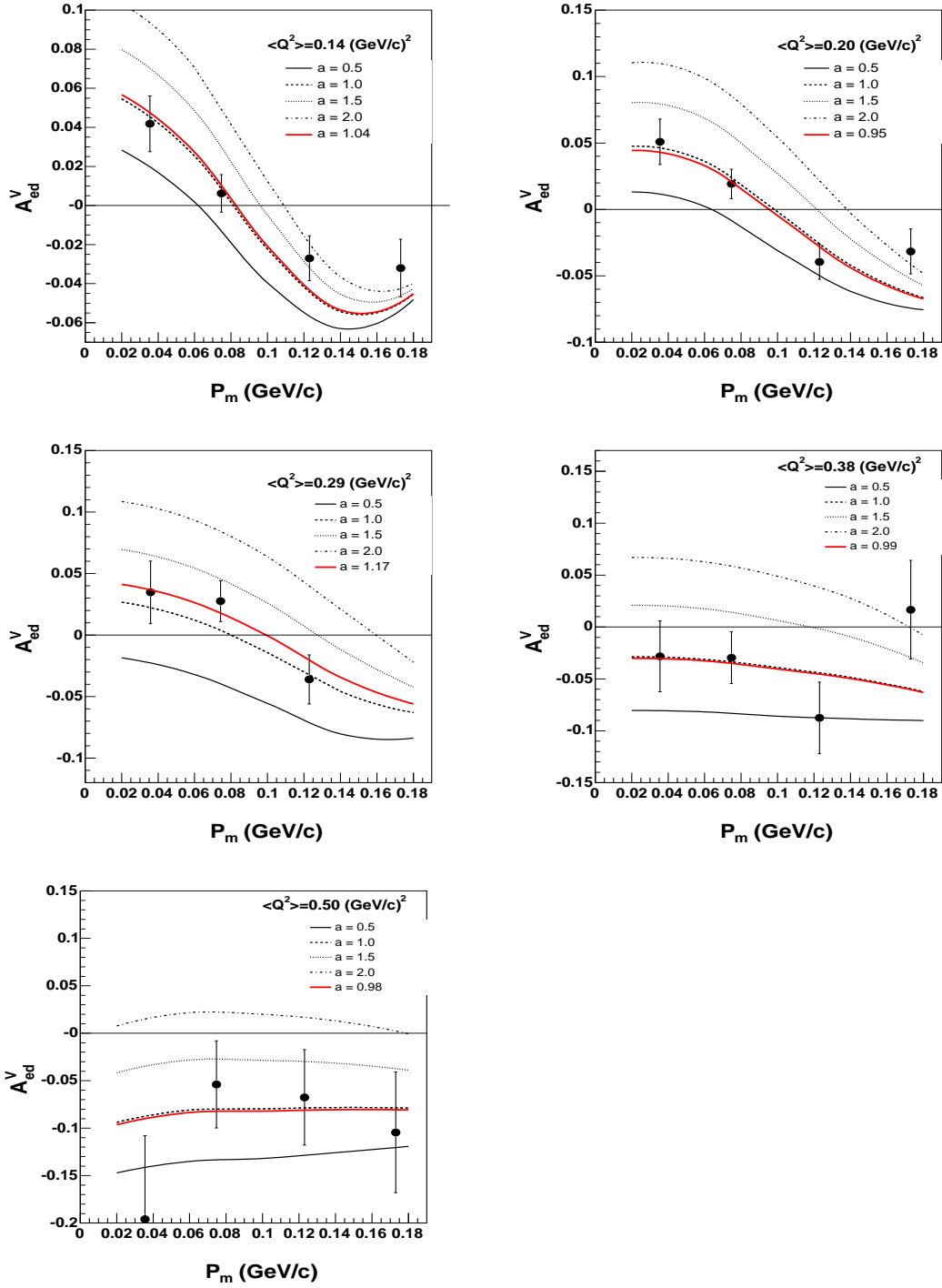


Figure 5-15: Plot of the vector asymmetry corrected for the unpolarized background for  $Q^2 = 0.14$  (top-left),  $0.20$  (top-right),  $0.29$  (middle-left),  $0.38$  (middle-right) and  $0.50$  (bottom)  $(\text{GeV}/c)^2$  bins as a function of the missing momentum,  $p_m$ . The curves are the BLASTMC calculation with various values of the neutron form factor,  $a$ , in units of Galster form factor. The thick, red line represents the best fit to the data. The error bars shown on the plot are purely statistical. The effect of the systematic errors will be discussed in section 5.8.

## 5.7 Extraction of $G_E^n/G_M^n$ from the Background Corrected Asymmetry

The background corrected asymmetry,  $A_{ed}^V(\frac{\pi}{2}, 0)$  is compared to the calculation of this polarization observable in BLASTMC with various values of the parameter  $a$  defined in the Platchkov parametrization (see eqn. 2.63) with  $b = 5.6$ , such that

$$G_E^n = a \frac{\mu_n \tau}{1 + 5.6\tau} \frac{1}{(1 + Q^2/0.71)^2}. \quad (5.11)$$

A chi-square  $\chi_k^2(a_k)$  is calculated for each set of neutron electric form factors based on the BLASTMC simulations. The values of  $\chi_k^2(a_k)$  are expressed in terms of the asymmetry values as

$$\chi_k^2(a_k) = \sum_i \frac{(A_i^{exp} - A_i^{theory})^2}{(\sigma_i^{exp})^2}, \quad (5.12)$$

where  $k$  is the  $\langle Q^2 \rangle$  bin,  $A_i^{exp}$  and  $A_i^{theory}$  are the experimental and theoretical asymmetries in the  $i^{th}$   $p_m$  bin and  $\sigma_i^{exp}$  is the experimental uncertainty in each bin.

The  $\chi_k^2(a_k)$  is expected to be parabolic around the minimum [149]. Hence,  $\chi_k^2(a_k)$  is parametrized as

$$\chi_k^2(a_k) = \tau_{min} + \frac{(a_k - \tau_1)^2}{(\tau_2 + a_k \tau_3)^2}, \quad (5.13)$$

where  $\tau_{min}$  and  $\tau_1, \tau_2, \tau_3$  are the parabolic fit parameters. The minimum of the  $\chi_k^2(a_k)$  corresponds to the parameter  $a_k^{min}$  of the theoretical model used in BLASTMC that best describes the experimental data. Thus,  $G_E^n/G_D^n = a_k^{min} \cdot (\mu_n \tau)/(1 + b\tau)$  corresponds to the best value of the neutron form factor ratio. The uncertainty of the  $a_k^{min}$  in this method is defined as

$$\chi_k^2(a_k^{min} + \Delta a_k^{min}) = \chi_k^2(a_k^{min}) + 1, \quad (5.14)$$

where  $\Delta a_k^{min}$  is the uncertainty of the parameter  $a_k^{min}$ . The  $\chi^2$  minimization is shown in fig. 5-16. The results of this procedure are collected in table 5.4 The quantity  $\chi_{min}^2/ndf$  is the minimum of the  $\chi^2$  fit in fig 5-16 divided by the number of degrees of freedom. The  $\chi_{min}^2/ndf$  in the second  $Q^2$  bin is slightly greater than 1. This is primarily due to the value of the vector asymmetry  $A_{ed}^V(Q^2 = 0.20)$  in the last last missing momentum bin (see top-right

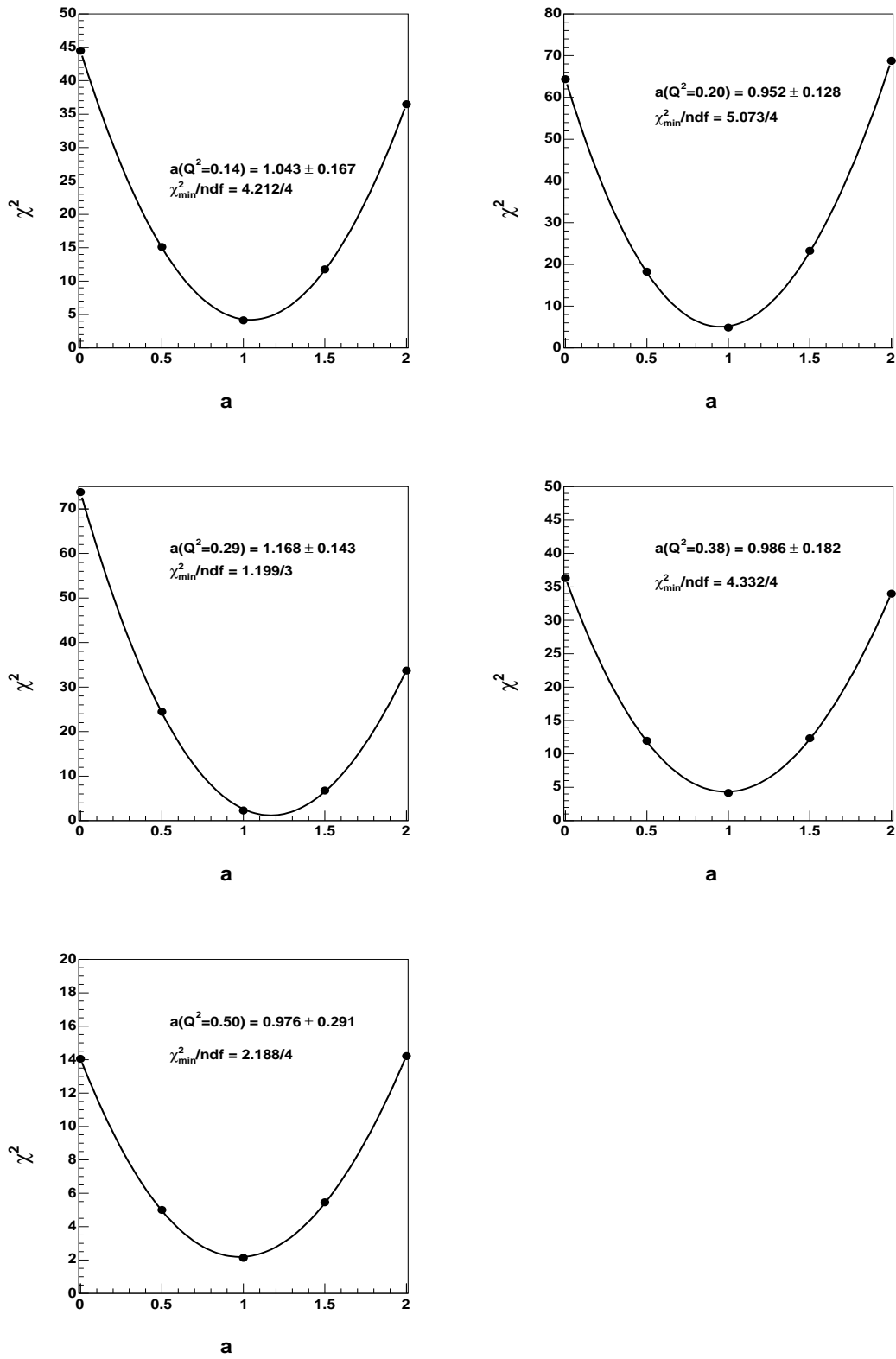


Figure 5-16:  $\chi^2$  fit for the best value of  $G_E^n$  in units of Galster for the momentum transfers of  $Q^2 = 0.14$  (top-left),  $0.20$  (top-right),  $0.29$  (middle-left),  $0.38$  (middle-right) and  $0.50$  (bottom) (GeV/c)<sup>2</sup>.

$\langle Q^2 \rangle$ (GeV/c) <sup>2</sup>	$G_E^n/G_D^n$	$\Delta G_E^n/G_D^n(stat)$	$\Delta G_E^n/G_D^n(sys)$	$\chi_{min}^2/ndf$
0.14	0.0438	0.0070	0.0031	1.05
0.20	0.0463	0.0062	0.0036	1.27
0.29	0.0624	0.0076	0.0039	0.40
0.38	0.0537	0.0099	0.0040	1.08
0.50	0.0519	0.0155	0.0039	0.55

Table 5.4: Measured values of  $G_E^n/G_D^n$  with the statistical and systematic uncertainties. The source of the systematic uncertainties are discussed in section 5.8.

panel in fig. 5-15) being more than one sigma away from the extracted average value (thick red line). However, the expected error due to this data point is small and will be accounted for in the discussion of the systematic uncertainties.

## 5.8 Systematic Uncertainties

The sources of the systematic uncertainties presented in table 5.4 are discussed in this section. The systematic uncertainties in this experiment are dominated by the precision in the knowledge of the target polarization angle. The second largest contribution is from the determination of the product of the beam and target polarizations. Other systematic contributions are negligible in comparison with the first two. Table 5.5 shows the relative contributions with the overall systematic uncertainty.

Source	Uncertainty in % of Galster
Target Polarization Angle (see 5.8.1)	5 %
Beam-Target Polarization (see 5.8.2)	2.5 %
Reconstruction (see 5.8.3)	2.0 %
Cut Dependence (see 5.8.5)	2.0 %
$G_M^n$ (see 5.8.4)	1.5 %
False Asymmetry (see 5.8.7)	1 %
Radiative Corrections (see 5.8.6)	1 %
Total	6.6 %

Table 5.5: Contributions to the overall systematic uncertainty of the  $G_E^n$  measurement. The total uncertainty is calculated by adding the individual contributions in quadrature.

The systematic uncertainties contribute equally in all five  $Q^2$  bins. Following is the discussion of each individual systematic uncertainty source.

### 5.8.1 Target Polarization Angle

The angle of the target polarization,  $\theta_d$  is fixed by the direction of the holding field magnet. However, the target polarization angle with respect to the momentum transfer vector,  $\theta_d^*$  varies within the BLAST acceptance (see fig. 5-17). Hence, the kinematics of the experiment deviate from the  $\vec{S} \perp \vec{q}$  requirement.

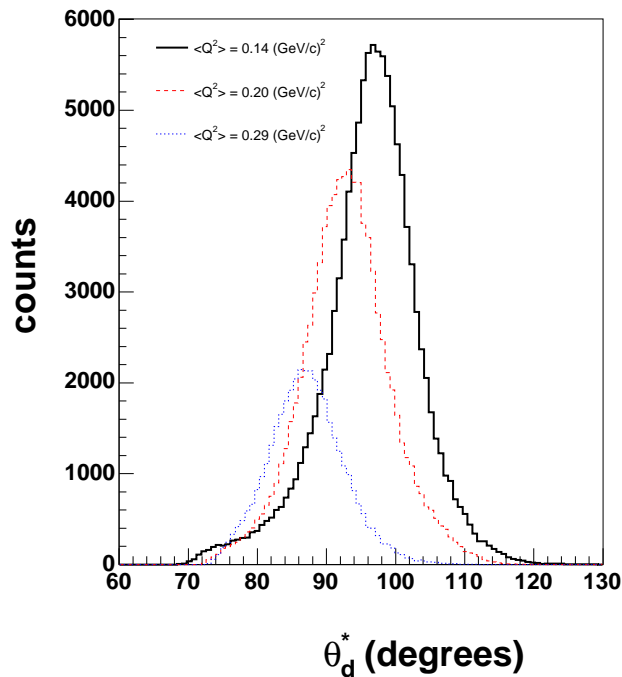


Figure 5-17: Plot of  $\theta_D^*$  for  $\langle Q^2 \rangle = 0.14$  (GeV/c)<sup>2</sup> (solid),  $\langle Q^2 \rangle = 0.20$  (GeV/c)<sup>2</sup> (dashed) and  $\langle Q^2 \rangle = 0.29$  (GeV/c)<sup>2</sup> (dotted) bins.

If the kinematics are not exactly perpendicular, the parallel asymmetry proportional to  $(G_M^n)^2$  starts to contribute to the overall asymmetry. Since  $G_E^n$  is only a few percent of  $G_M^n$ , any contribution from parallel asymmetry is significant, even when multiplied by the cosine of an angle close to 90°. To test the sensitivity of the measurement to the target polarization angle, the neutron electric form factor was extracted with the assumption of two different polarization angles. The effect of the target polarization angle on  $G_E^n$  measurement was found to be  $\sim 12$  % (of Galster) per degree.

The target holding field was mapped with the BLAST toroid field on. The precision in spin angle due to these measurements is on the order of 1 degree. The best measurement of the polarization angle is done using the tensor polarization observable in elastic electron-deuteron scattering<sup>3</sup>. The tensor asymmetry in this reaction has the opposite sign in the left and right sector. In the tensor analysis the target polarization angle is varied until the extracted deuterium tensor polarization,  $P_{zz}$  is equal in both sectors (see fig. 5-18 left).

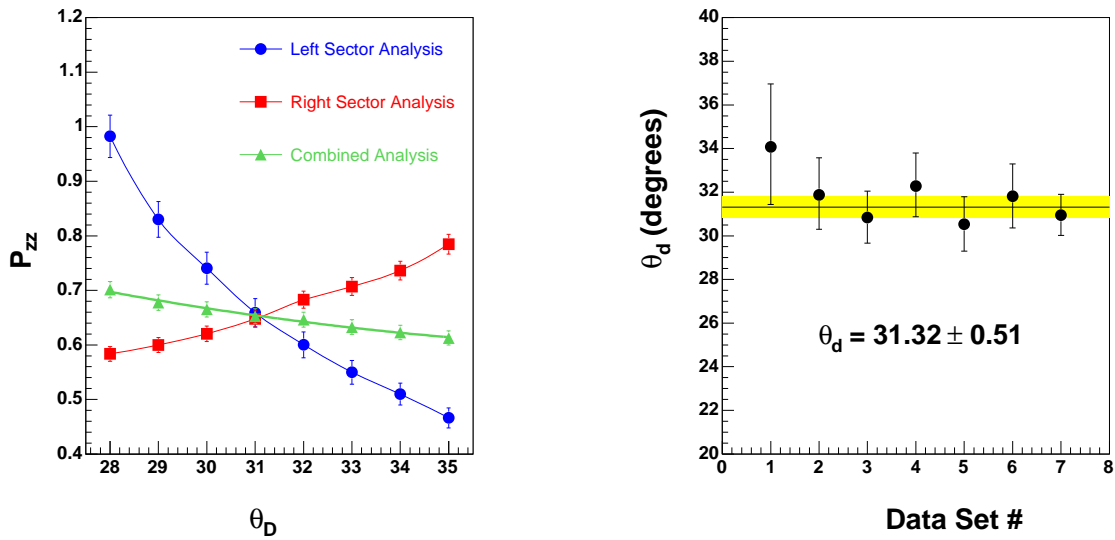


Figure 5-18: Target angle calculation using the elastic tensor asymmetry. The target angle is at the crossing point of the  $P_{zz}$  calculation from the left sector (circles), right sector (squares). The average target polarization spin angle is found for seven data sets in the right panel.

The extraction of the target polarization angle is split into seven data sets for this analysis (see fig. 5-18 right). The data in the first set were collected with the cell #2, all other data sets will cell # 3. The average target polarization angle is found to be [150]  $\theta_d = 31.32^\circ \pm 0.51^\circ$ . The uncertainty of this measurement is almost purely statistical.

The target polarization angle determined using tensor polarization is in remarkable agreement with the angle calculation from the holding field map (see fig. 5-19), which produces the elastic cross section averaged value of the target angle of  $\theta_d = 31.4^\circ \pm 1.0^\circ$ . The uncertainty in this value is dominated by the systematic uncertainty of the magnetic field

<sup>3</sup>As mentioned before, the tensor and the vector polarization observables are measured simultaneously.

measurement. The values of  $G_E^n$  are extracted with the polarization angle taken from the field map and from the tensor asymmetry<sup>4</sup>. The difference between two methods is  $\sim 2\%$ . The final values of  $G_E^n$  reported in this work are extracted with the target polarization angle

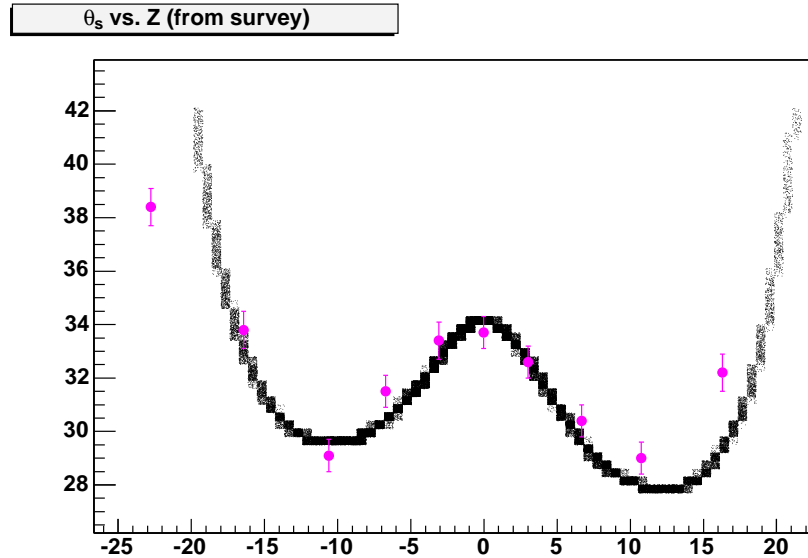


Figure 5-19: Elastic scattering luminosity weighted target spin angle profile along  $z$  (dark band) plotted with the calculated target angle from the  $P_{zz}$  measurements (points). Data from  $|z| < \pm 20$  cm are used in the analysis.

calculated from the holding field map. However, the tensor analysis provides confidence that the polarization angle is properly determined. The uncertainty in the target polarization angle from the combination of the two methods corresponds to a 5% systematic uncertainty in the determination of  $G_E^n$ .

## 5.8.2 Product of the Beam and Target Polarizations

The product of the beam and target vector polarizations,  $hP_z$  is extracted from quasielastic electron scattering reaction with a proton detected in the final state. As mentioned before, the calculation of this reaction channel is less sensitive to the uncertainties in reaction mechanisms at the quasielastic peak. The cross section for this reaction is large enough to limit the statistical uncertainty of  $hP_z$  to below 1%. Figure 5-20 shows the vector polarization

<sup>4</sup>The target polarization angle from the field map varies along the length of the storage cell, while the angle from the tensor analysis is assumed constant over the whole length of the target.

observables in spin-perpendicular and parallel kinematics,  $A_{ed}^V(\frac{\pi}{2}, 0)$  and  $A_{ed}^V(0, 0)$ , respectively. The polarization product was extracted in bins of  $Q^2 < 0.35$  (GeV/c)<sup>2</sup> with a missing momentum below 0.15 GeV/c. The resulting  $hP_z$  is measured to be [151]

$$hP_z^{proton} = 0.52 \pm 0.0035(stat.) \pm 0.02(syst.).$$

A large systematic uncertainty is due to the variation of the  $hP_z$  over the full  $Q^2$  range.

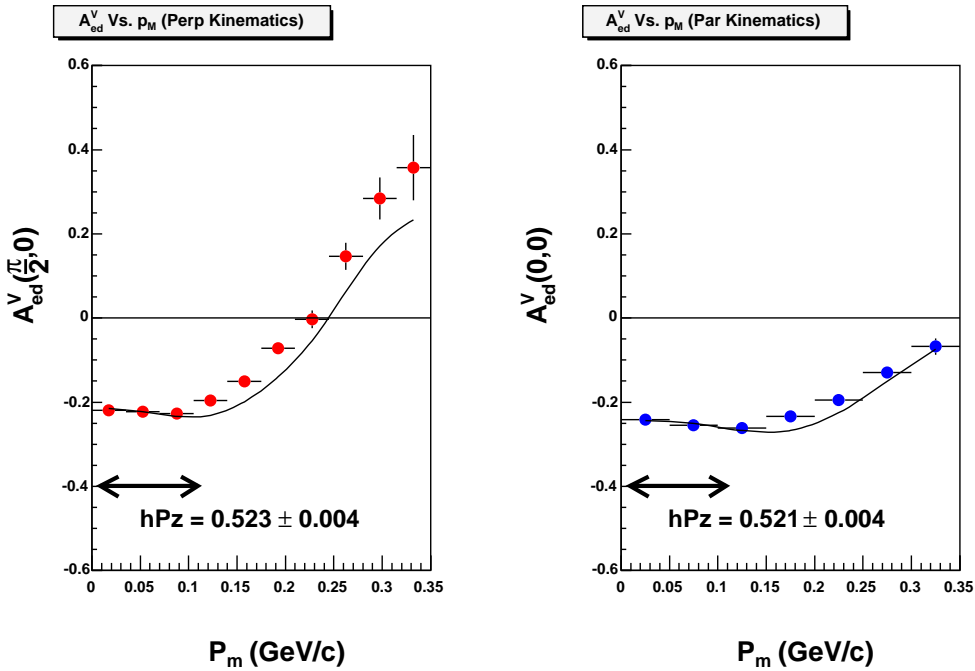


Figure 5-20: Extraction of the product of the beam and target vector polarizations,  $hP_z$  using exclusive quasielastic scattering on deuterium with the detected proton. The values of the  $hP_z$  from the perpendicular (left) and parallel (right) kinematics include statistical error only.

In order to check the consistency of this measurement, a vector asymmetry in parallel kinematics from electron-neutron quasielastic scattering is used to extract an alternative value of the  $hP_z$ . In spin-parallel kinematics the vector polarization observable,  $A_{ed}^V(0, 0)$  is sensitive to a purely kinematic quantity, since  $G_M^n$  dominates over  $G_E^n$  in both the numerator and denominator.

The extraction of  $hP_z$  using the detected neutron is done in the same  $Q^2$  range. However, the fit is carried out over a greater missing momentum range, since the uncertainty of this

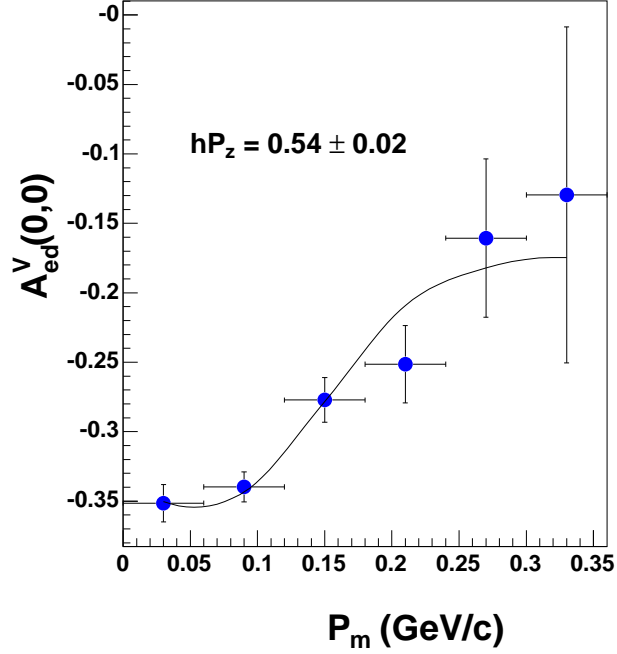


Figure 5-21: Extraction of the product of the beam and target vector polarizations,  $hP_z$  using exclusive quasielastic scattering on deuterium with the neutron detected in the final state. The value of  $hP_z$  from spin-parallel kinematics includes the statistical error only.

determination is dominated by the statistical errors. The value of  $hP_z$  is

$$hP_z^{neutron} = 0.54 \pm 0.02(stat.) \pm 0.01(syst.),$$

where the systematic uncertainty is due to the reaction mechanism dependence of the  $A_{ed}^{V,theory}(0,0)$  calculation. A good agreement between  $hP_z$  from the two methods is found.

The value of  $hP_z^{proton}$  is used to determine  $G_E^n$ . The overall error on  $hP_z$  contributes an uncertainty of  $\pm 2.5\%$  to the value of  $G_E^n$ .

### 5.8.3 Reconstruction

The systematic shifts in the reconstruction of the missing momentum,  $p_m$ , in which the fit for the best value of  $G_E^n$  is performed is a potential source of an error. Since the size of each

bin in missing momentum is much larger than the resolution of the kinematic quantities the uncertainties due to the resolution are negligible. The systematic misreconstruction however, is important, especially when the asymmetry changes sign. When the shifts in the reconstruction are large enough, the events in one bin with a positive asymmetry can be wrongly assigned to another bin with the negative asymmetry effectively diluting the asymmetry in both bins. This *bin drift* was reduced with the kinematic corrections discussed above. However, some bin drift effects still possibly persist at large missing momentum. The effect of these bin drifts is rather small. The magnitude of the uncertainty due to the bin drifts is estimated by considering the effect of the  $p_m > 0.1$  (GeV/c)<sup>2</sup> bins on the final value of  $G_E^n$  and an estimation of the degree to which the bin drift is present in the data. The contribution of the uncertainty due to the reconstruction to the total systematic uncertainty is estimated to be  $\sim 2.0$  %.

#### 5.8.4 Value of $G_M^n$

A good parametrization of the neutron magnetic form factor is needed in order to extract the value of  $G_E^n$  from the form factor ratio measurements listed in table 5.4. This is needed because Arenhövel’s calculations use a dipole parametrization of the  $G_M^n$ . However,  $G_M^n$  is known to deviate up to 5 % from the dipole form in the  $Q^2$  region of interest (see fig. 5-22).

In their recent paper [103] Friedrich and Walcher parametrized a dip region of  $G_M^n$  by a Gaussian form. The full parametrization consists of the two dipole forms for the “inner” and the “outer” charge distributions and the afore-mentioned Gaussian form,

$$G_M^n = \frac{a_0^{out}}{(1 + Q^2/a_1^{out})^2} + \frac{a_0^{in}}{(1 + Q^2/a_1^{in})^2} + a_0^\pi \left(1 - \frac{1}{6}Q^2/a_1^\pi\right) e^{-\left(\frac{Q^2}{4a_1^\pi}\right)} \quad (5.15)$$

Figure 5-22 shows a comparison of the Friedrich and Walcher parametrization and the world’s data. The authors did not include data measured by Markowitz [32] and Bruins [33] in their fit<sup>5</sup>. The uncertainty of the fit is on the order of 1.5 %, which directly contributes to the overall systematic uncertainty of  $G_E^n$  calculation.

---

<sup>5</sup>Both of these data sets used absolute cross section measurements, thus introducing large systematic uncertainty from the neutron detector efficiency.

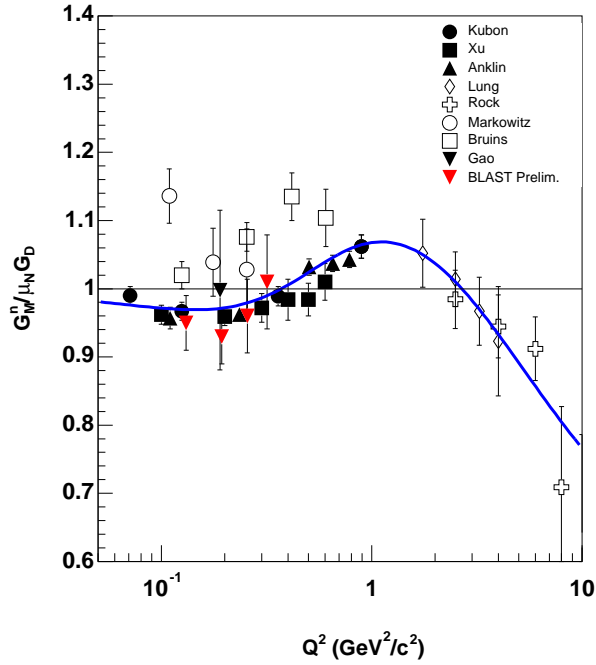


Figure 5-22: Parametrization by Friedrich and Walcher of the neutron magnetic form factor,  $G_M^n$  (solid curve). The data are the same as in fig 2-3. In addition the preliminary data from the inclusive analysis at BLAST performed by Nikolas Meitanis [152].

### 5.8.5 Cut Dependence

The cut dependencies arise from a possible enhancement of some kinematic region, where the asymmetries would differ from calculated values, by applying the cuts to the data. These dependencies of the extracted value of  $G_E^n$  on the kinematic cuts are studied by varying the cut on the missing mass,  $M_m$ . Figure 5-23 shows the values of  $G_E^n$  as a function of the width of the missing mass cut in units of  $\text{MeV}/c^2$ , for each  $Q^2$  bin. A small variation is observed over a large range of the cut width. The variation is statistically insignificant. The missing mass cut in the final value of  $G_E^n$  extraction was chosen to be  $100 \text{ MeV}/c^2$  which corresponds to anywhere from 3.5 to 3 sigma of the missing mass peak. The contribution of the cut dependence on the overall systematic error is estimated to be 2.0 %.

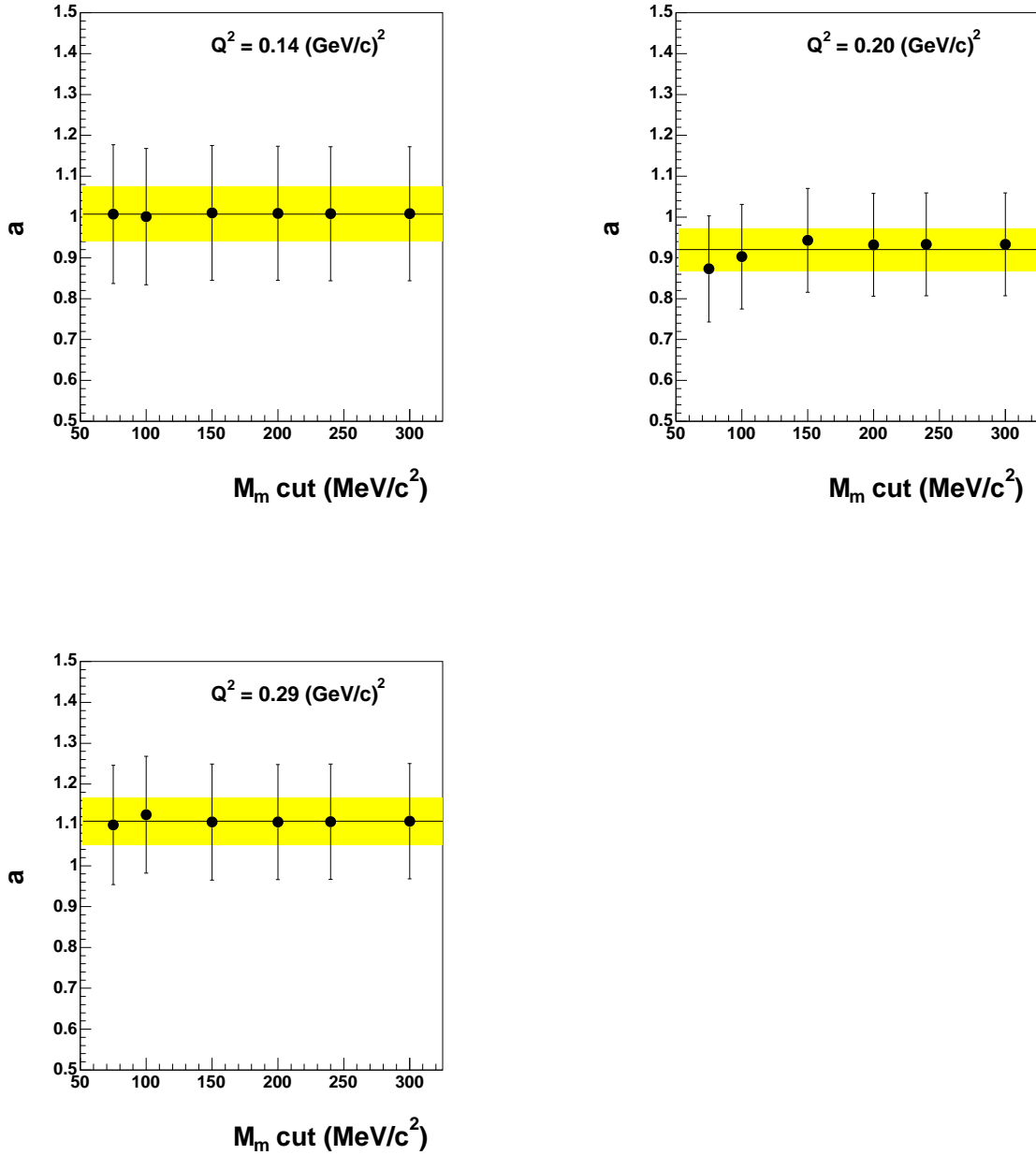


Figure 5-23: Missing mass cut dependence of  $G_E^n$  (in units of Galster) in momentum transfer bins of  $Q^2 = 0.14$  (top-left),  $0.20$  (top-right),  $0.29$  (bottom)  $(\text{GeV}/c)^2$ . The line represents an average value and the yellow band is an error around the mean, assuming that each  $G_E^n$  value is statistically uncorrelated.

### 5.8.6 Radiative Corrections

The radiative corrections are needed to account for QED correction to the tree-level diagram (see fig. 2-1) where the initial or scattered electron radiates a real or virtual photon, thus changing the kinematics of the reaction. In terms of the radiative corrections the observed cross section is written as [153]

$$\sigma_{obs} = (1 + \delta)\sigma_0 + \sigma_R, \quad (5.16)$$

where  $\sigma_0$  is the unradiated cross section,  $\delta$  is the factorized correction and  $\sigma_R$  is the unfactorized bremsstrahlung contribution to the cross section.

The factorized correction,  $\delta$  is usually large, resulting in a large radiative correction to the observed cross section. However,  $\delta$  cancels exactly in the expression for the asymmetry expressed as

$$\Delta A_R = A_R - A_0 = \frac{(1 + \delta)\sigma_0^p + \sigma_R^p}{(1 + \delta)\sigma_0^u + \sigma_R^u} - \frac{\sigma_0^p}{\sigma_0^u}, \quad (5.17)$$

where  $A_R$  and  $A_0$  are the asymmetries with and without radiative corrections applied,  $\sigma^u$  and  $\sigma^p$  are unpolarized and polarized cross sections, respectively. The relative difference can be written in terms of  $\delta^{u,p} = \sigma_R^{u,p}/\sigma_0^{u,p}$  as

$$\Delta_R = \frac{\Delta A_R}{A_0} = \frac{\delta^p - \delta^u}{1 + \delta + \delta^u} \quad (5.18)$$

Figure 5-24 shows the parameter  $\Delta_R$  in eqn. 5.18 for the case of the spin-perpendicular kinematics. The calculation was done for e-p elastic scattering using MASCARAD code developed by Afanasev et al. [154]. However, this calculation is applicable to quasielastic scattering on deuterium in the PWBA formalism. The difference between the radiated and non-radiated asymmetry is less than 1 %. Due to the smallness of the radiative effects in the polarization observable, the radiative corrections have not been implemented at this point. The systematic uncertainty due to the radiative effects is estimated to be  $\sim 1$  %.

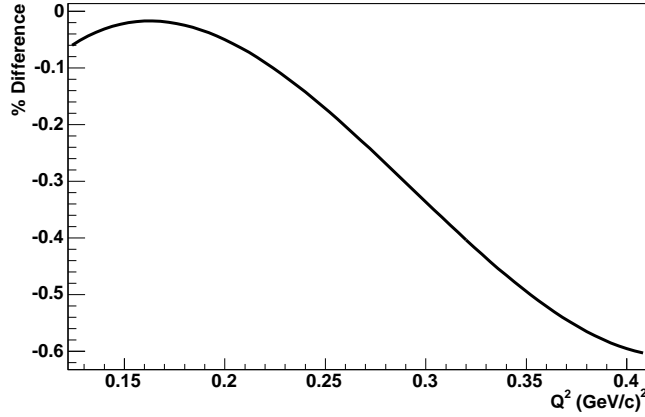


Figure 5-24: Effect of the radiative corrections on beam-target vector polarization observable in the spin-perpendicular kinematics,  $A_{e,p}^{\perp}$ .

### 5.8.7 False Asymmetries

As mentioned previously, the asymmetries,  $A_e$ ,  $A_d^V$  and  $A_{ed}^T$  are expected to be small. The possible reasons for these asymmetries not being zero could be incorrect determination of the accumulated charge in each helicity state or, in case of  $A_e$ , incorrect averaging over the out-of-plane angles. All these uncertainties can contribute to the overall systematic uncertainty in the measurement.

Figure 5-25 shows the plots of these three asymmetries in the perpendicular kinematics. For these plots the data was combined over the combined  $Q^2$  range considered in this work, to reduce the statistical uncertainty. It is assumed that the false asymmetry in each  $Q^2$  bin is equal to the false asymmetry in the combined  $Q^2$  bin. The values of the average false asymmetries are following

$$\begin{aligned}
 A_e &= (-1.489 \pm 3.374) \times 10^{-3} \\
 A_d^V &= (-5.140 \pm 3.201) \times 10^{-3} \\
 A_{ed}^T &= (-2.446 \pm 5.021) \times 10^{-3}.
 \end{aligned}$$

All false asymmetries are small and consistent with zero. The contribution from the false asymmetry to the overall systematic error of the measurement is estimated to be less than 1 %.

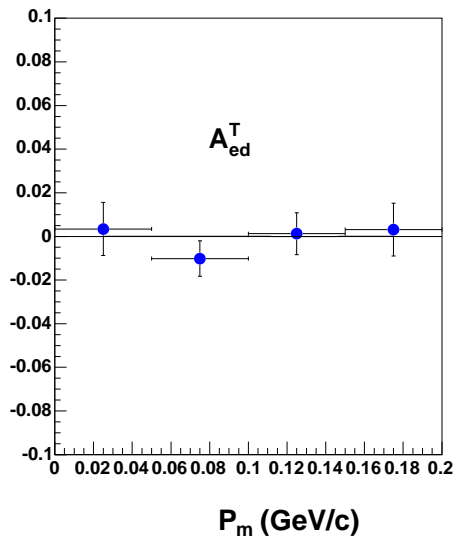
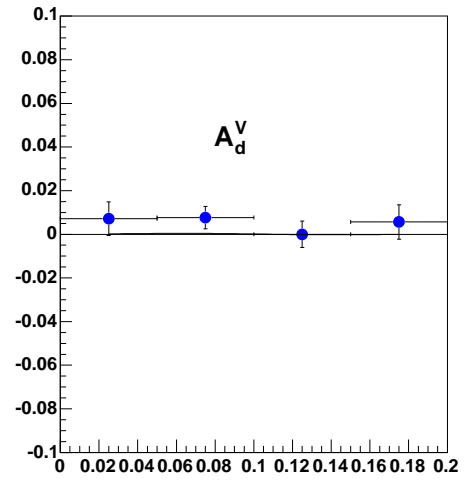
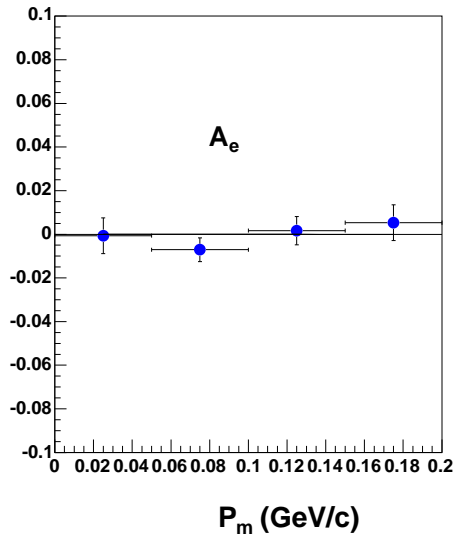


Figure 5-25: False asymmetries,  $A_e$  (top-left),  $A_d^V$  (top-right) and  $A_{ed}^T$  (bottom) in the spin-perpendicular kinematics.

# Chapter 6

## Discussion and Conclusion

### 6.1 Discussion of the Results

#### 6.1.1 Phenomenological Fit

The values of  $G_E^n$  obtained in this work are consistent with the previous data. The determination of the electric form factor of the neutron at  $Q^2 = 0.14$  (GeV/c)<sup>2</sup> is the lowest  $Q^2$  measurement ever performed. This value of  $G_E^n$  is in good agreement with the previous lowest  $Q^2$  measurement at 0.15 (GeV/c)<sup>2</sup> [117]. Both of these values are in good agreement with the Platchkov parametrization, where  $a^{platchkov}$  is fixed at 0.906 to match the slope at  $Q^2 = 0$  determined by thermal neutron scattering [77] and where the global fit parameter,  $b^{platchkov} = 3.47$  (see blue solid curve in fig. 6-1).

However, the Platchkov parametrization is too rigid to describe the behavior of  $G_E^n$  as a function of  $Q^2$ . This is illustrated by the high precision data recently obtained at high  $Q^2$  at Jefferson Lab Hall C [105]. If  $a^{platchkov}$  is fixed to match the experimentally determined charge radius of the neutron, then the Platchkov parametrization completely underestimates the size of  $G_E^n$  at large  $Q^2$  and produces a large  $\chi^2$  of 17.6<sup>1</sup>. If the Platchkov parametrization is fit to the Hall C points at  $Q^2 = 1.13, 1.45$  (GeV/c)<sup>2</sup>, thus predicting the high  $Q^2$  behavior, it underestimates the slope at  $Q^2 = 0$  by a significant amount.

Recently, the Mainz A1 collaboration [107] used a different  $G_E^n$  parametrization suggested by Friedrich and Walcher [103] to better match both low and high  $Q^2$  behaviors. The

---

<sup>1</sup>The  $\chi^2$  is calculated with the data set which includes the values measured in this work.

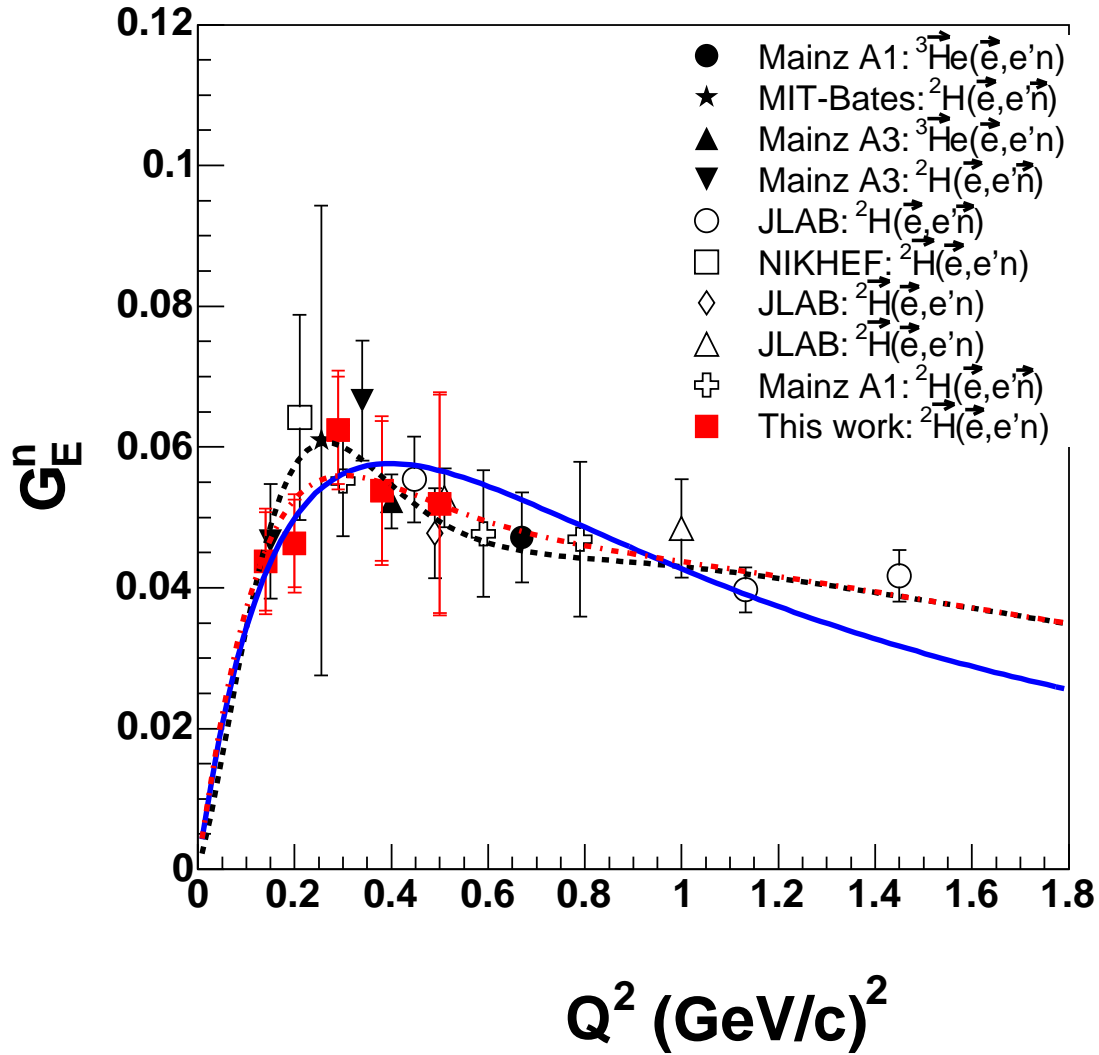


Figure 6-1: The world's  $G_E^n$  data plotted together with the new results from this work. The statistical and systematic uncertainties are added in quadrature. The solid curve is a fit to the Platchkov parametrization (eqn. 2.63) with the slope at  $Q^2 = 0$  corresponding to the measured neutron charge radius ( $a = 0.906$  and  $b = 3.47$ ). The dashed black curve is the fit of the Friedrich and Walcher parametrization performed by the A1 collaboration [107]. The dot-dashed red curve is the new fit of the same parametrization done in this work (see table 6.1).

parametrization includes a smooth contribution consisting of the sum of two dipole functions normalized to produce  $G_E^n(Q^2 = 0) = 0$  and a bump contribution parametrized by a sum of two Gaussians,

$$G_E^n = \frac{a_{10}}{(1 + Q^2/a_{11})^2} + \frac{a_{20}}{(1 + Q^2/a_{21})^2} + a_b Q^2 \left( e^{-\frac{1}{2} \left( \frac{Q-Q_b}{\sigma_b} \right)^2} + e^{-\frac{1}{2} \left( \frac{Q+Q_b}{\sigma_b} \right)^2} \right), \quad (6.1)$$

where  $a_{20} = -a_{10}$  for the normalization at zero. The value of  $Q_b$  determines the position of the bump and the value of  $\sigma_b$  corresponds to its width. Since the bump part in eqn. 6.1 is not entirely a function of  $Q^2$ , a proper symmetrization is done by addition of two Gaussians. The magnitude of the bump is dominated by the value of the first Gaussian,  $e^{-\frac{1}{2} \left( \frac{Q-Q_b}{\sigma_b} \right)^2}$ , since both  $Q$  and  $Q_b$  are positive definite. Friedrich and Walcher postulated that the smooth dipole term would correspond to the constituent quark core and the bump describes the pion cloud around the core.

The fit of this parametrization performed by the A1 collaboration matches well to the existing data with a  $\chi^2$  significantly lower than that obtained with the refitted Platchkov parametrization (see black dashed line fig. 6-1). The A1 fit is successful in describing the high  $Q^2$  behavior predicted by the Jefferson Lab Hall C data. However, the value of this fit at  $Q^2 = 0.2$  (GeV/c)<sup>2</sup> is one sigma and a half away from the value of the second  $Q^2$  point measured in this work. Also, the original A1 fit does not reproduce the correct slope at  $Q^2 = 0$  predicted by the experimentally determined neutron charge radius. Using eqn. 6.1 the charge radius of the neutron is defined as<sup>2</sup>

$$-\frac{1}{6} \langle r_n^2 \rangle = \frac{dG_E^n}{dQ^2} \Big|_{Q^2=0} = -2 \left( \frac{a_{10}}{a_{11}} + \frac{a_{20}}{a_{21}} \right) + 2a_b e^{-\frac{Q_b^2}{2\sigma_b^2}} \quad (6.2)$$

Accordingly, the contribution to the neutron charge radius from the smooth term is rather small ( $\sim 30$  %). Thus, the charge radius is dominated by the bump term in the parametrization.

A new BLAST parametrization is introduced, where  $a_b$  is fixed by the charge radius (see red dot-dashed line in fig 6-1). The parameters found in the BLAST fit are listed in table

---

<sup>2</sup>Note that this requirement correlates the contributions from the individual uncertainties of the smooth and bump parts to the total uncertainty of the fit.

	$a_{10}$	$a_{11}$ (GeV/c) <sup>2</sup>	$a_{20}$	$a_{21}$ (GeV/c) <sup>2</sup>	$a_b$ (GeV/c) <sup>-2</sup>	$Q_b$ (GeV/c)	$\sigma_b$ (GeV/c)	$\langle r_n^2 \rangle$ fm <sup>2</sup>	$ndf$	$\chi^2/ndf$	$\chi^2_{total}$
BLAST 1.0	1.27(1.9)	1.73(fixed)	-1.27(fixed)	1.54(1.2)	0.224(fixed)	0.20(2.6)	0.24(2.9)	-0.115(fixed)	14	0.464	6.48
A1 [107]	1.2974	1.7301(fixed)	-1.2974	1.5479	0.19426	0.3421	0.16758	-0.052	13	0.597	7.76

Table 6.1: Comparison between the global phenomenological fits to the world's  $G_E^n$  data performed in this work and performed by A1 collaboration. The errors of the last significant digits are quoted in parentheses. The  $\chi^2$  calculation for A1 fit includes the results from this work.

6.1. A marginally better  $\chi^2$  is achieved in the BLAST fit, while preserving the correct slope at zero momentum transfer. The comparison in table 6.1 between the new and A1 fits shows that the smooth term in the parametrization is the same in the new fit, while the contribution from the bump is significantly different. The new fit finds that the amplitude of the bump (determined by  $a_b$ ) is larger, the bump maximum (determined by the  $Q_b$ ) occurs at a lower  $Q$  and the bump is significantly more spread out according to the width parameter,  $\sigma_b$ .

Figure 6-2 shows the relative contributions from the smooth dipole and the Gaussian bump. The slope at low  $Q^2$  is dominated by the contribution from the bump. This means that the charge radius of the neutron is determined by the properties of the pion cloud. At high  $Q^2$ , which corresponds to a small distance in coordinate space,  $G_E^n$  is dominated by the dipole form corresponding to the constituent quark core. This fact also preserves the asymptotic behavior predicted by pQCD calculations. This situation is consistent with the pion cloud picture of the neutron charge distribution.

The recent data from Hall C drastically improved the precision of the parametrization at high  $Q^2$ , thus shrinking the error band around the BLAST fit. The precision of the fit at medium  $Q^2$  is determined by the spread of the existing world's data. The precision at extremely low  $Q^2$  is constrained by the knowledge of the neutron charge radius,  $\langle r_n^2 \rangle$  (see fig. 6-3).

Figure 6-4 shows a ratio of the  $G_E^n$  data to the best Platchkov parametrization with the fixed slope at  $Q^2 = 0$  (solid blue line in fig. 6-1). The data hint at an oscillatory behavior in the low and medium  $Q^2$  ranges and the asymptotic deviation from Galster at  $Q^2 > 1$  (GeV/c)<sup>2</sup>. However, more precise data at low  $Q^2$  as well as additional data at very high  $Q^2$  are needed.

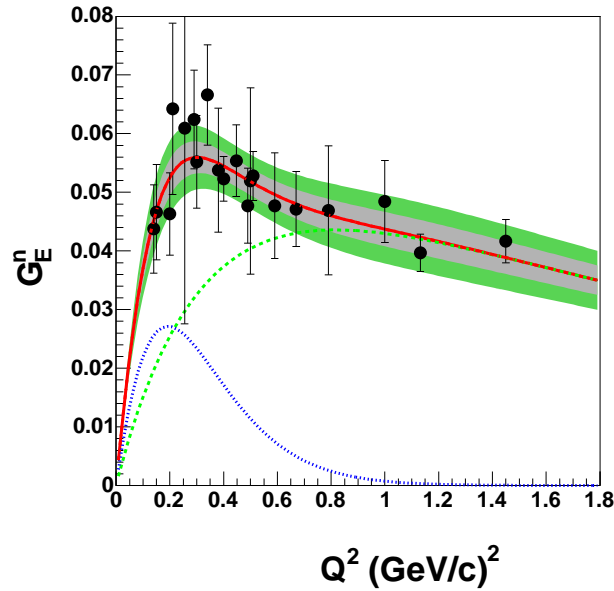


Figure 6-2: Contributions to  $G_E^n$  from parts of the phenomenological parametrization (see eqn. 6.2). The green dashed curve is the smooth contribution to the parametrization. The blue dotted curve is the bump contribution. The solid red line is the total. The gray and green bands are one- and two-sigma error bands. The black points are the world's data.

### 6.1.2 Charge Density of the Neutron

Relativity plays a central role in the understanding of the nucleon's charge distribution. In fact the transfer of momentum in the scattering process necessarily involves two reference frames and hence one cannot simply work with the charge operator in the nucleon's rest frame [155]. In a simplistic non-relativistic model the charge distribution in the coordinate space would be constructed as a Fourier transform of the Sachs form factors in the Breit frame to provide a qualitative understanding of the charge structure of the neutron. In particular, while not actually the neutron's charge distribution, it is interesting to examine the Fourier transform of the parametrization in eqn. 6.1. The smooth part of this parametrization has an exponential analytical form. However, the contribution due to the bump can only be determined numerically.

Figure 6-5 shows the contributions to the Fourier transform from the smooth and bump terms in the parameterization. The core at the short distance is dominated by the dipole

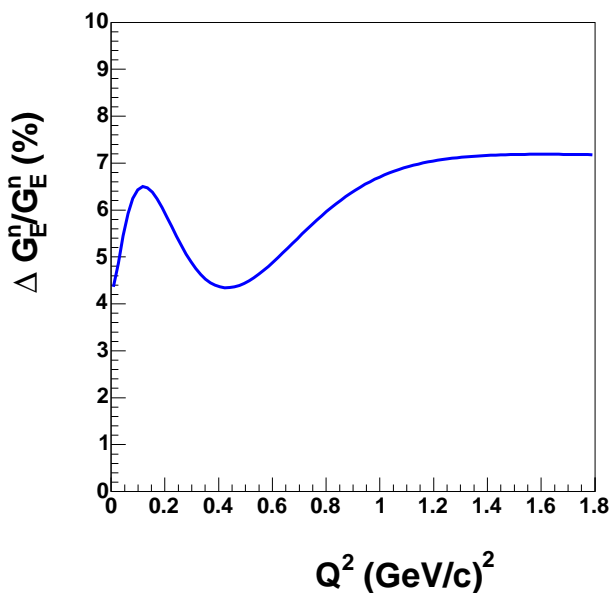


Figure 6-3: Precision of the BLAST fit,  $\Delta G_E^n/G_E^n$ .

content of the parametrization. If the core is connected to the constituent quark distribution, then the positive up quarks, with charge of  $+\frac{2}{3}$  are located centrally in the neutron, whereas the negative down quarks, with charge of  $-\frac{1}{3}$  are pushed to the edge of the neutron. The pion cloud due to the bump content of the parametrization has positive and negative components. The pion cloud dominates the distribution at large distances.

The full charge density distribution is plotted in fig. 6-6. It is compared with that calculated with the original Galster parametrization<sup>3</sup>. The positive content of the core appears to be more on the inside than what is predicted by the Galster parametrization. This difference is driven by the recent high  $Q^2$  data from Jefferson Lab being significantly above the Galster parametrization. At the same time, the negative part of the distribution extends further out than the “Galster” prediction.

The positive part of the pion cloud almost exactly cancels the negative part of the core. Thus, in the BLAST parametrization the neutron appears to consist of the very narrow positive core distribution and the diffuse negative pion cloud, which extends to very large

<sup>3</sup>In the context of this discussion the Galster parametrization is the special case of the Platchkov parametrization with  $a^{platchkov} = 1$ , which explicitly violates the slope at  $Q^2 = 0$ .

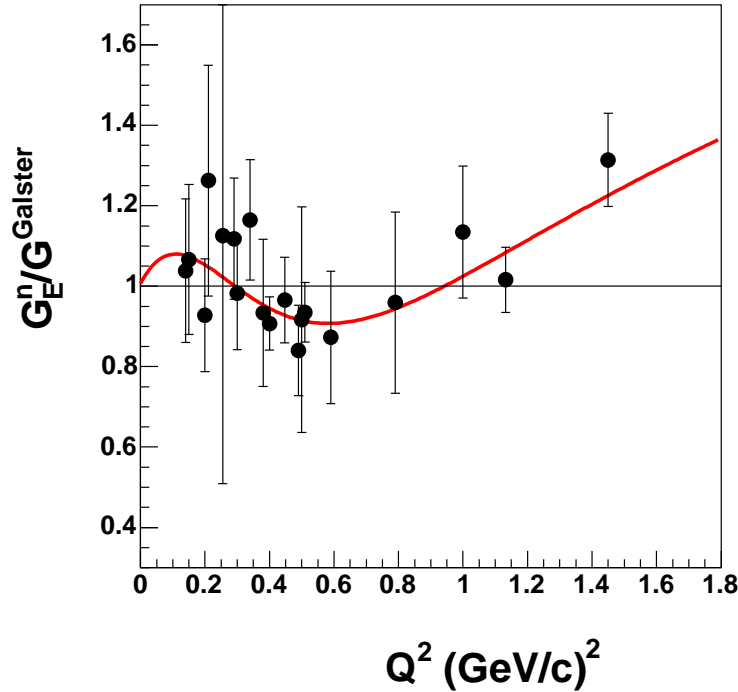


Figure 6-4: Ratio of the world's data (black points) and fit 1 in table 6.1 to the refitted Platchkov form (solid blue line in fig. 6-1.)

distances.

This discussion is purely qualitative since it does not take the relativistic effects into account. The more sophisticated Fourier transforms of the Sachs form factors can be devised to account for at least some aspects of the relativistic effects. One such scheme was suggested by J. Kelly [156].

The precision of the fit of eqn. 6.1 is significantly improved with the new BLAST data. There is a significant improvement in understanding of the neutron charge distribution in comparison to the original Galster parametrization. This can be clearly seen in the close up plot of the charge distribution at small distances (see fig. 6-6 right).

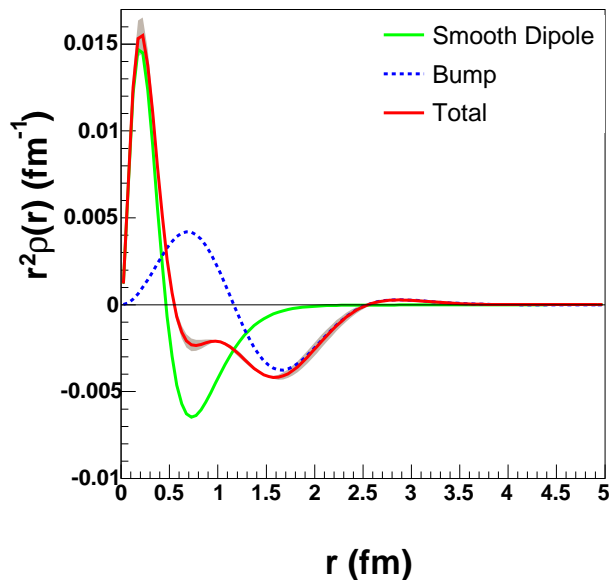


Figure 6-5: Relative contributions to the charge density of the neutron from the smooth (solid red line) and bump (dashed blue line) parts.

### 6.1.3 Nucleon Effective QCD Models

Figure 6-7 shows a blowup of a low  $Q^2$  region of the  $\mu_n G_E^n / G_M^n$  plot along with the results from this work. The new data indicate some disagreement with most QCD effective field models at low  $Q^2$ . The only model that is in good agreement with the data in this work is the diquark model, which is in disagreement with the data at higher momentum transfer (see discussion in section 2.5.9).

It is clear that the data indicate a structure at low  $Q^2$  which is not yet correctly understood in terms of the effective QCD field models.

## 6.2 Conclusion

The electric form factor of the neutron has been measured at five four-momentum transfer points of 0.14, 0.20, 0.29, 0.38 and 0.50  $(\text{GeV}/c)^2$  using a stored polarized electron beam and a polarized gas internal target with the BLAST detector at the MIT-Bates Linear Accelerator Center. Good agreement with the previous world's data was found. The parametrization

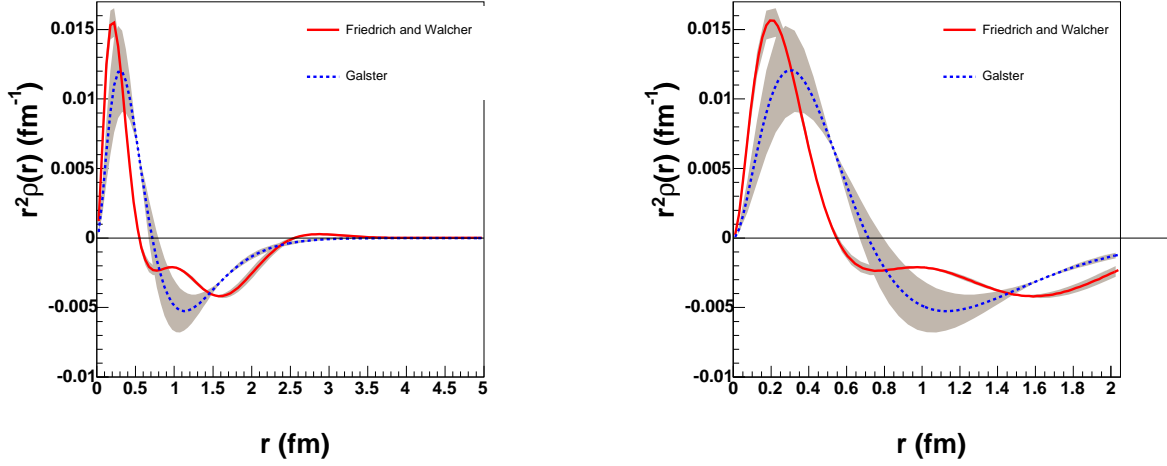


Figure 6-6: Charge density of the neutron calculated from the fit to parametrization in eqn. 6.1 (solid red line with gray error band) and from the original Galster parametrization (dashed blue line with gray error band). On the right is the blowup at  $r < 2.0$  fm.

suggested by Friedrich and Walcher was used to fit the data with slope at  $Q^2 = 0$  fixed to the measured value of the neutron charge radius. The data point at  $0.14 \text{ (GeV}/c)^2$  is the lowest  $Q^2$  point ever measured using polarized electron scattering. This data point is expected to improve the precision of the strange form factor measurements at low four momentum transfer.

The BLAST experiment is currently in phase II of its experimental program. Based on preliminary estimates the neutron data sample at BLAST will be doubled, thus further reducing the statistical uncertainties. The systematic uncertainties, particularly due to the knowledge of the target holding field, are expected to be significantly reduced.

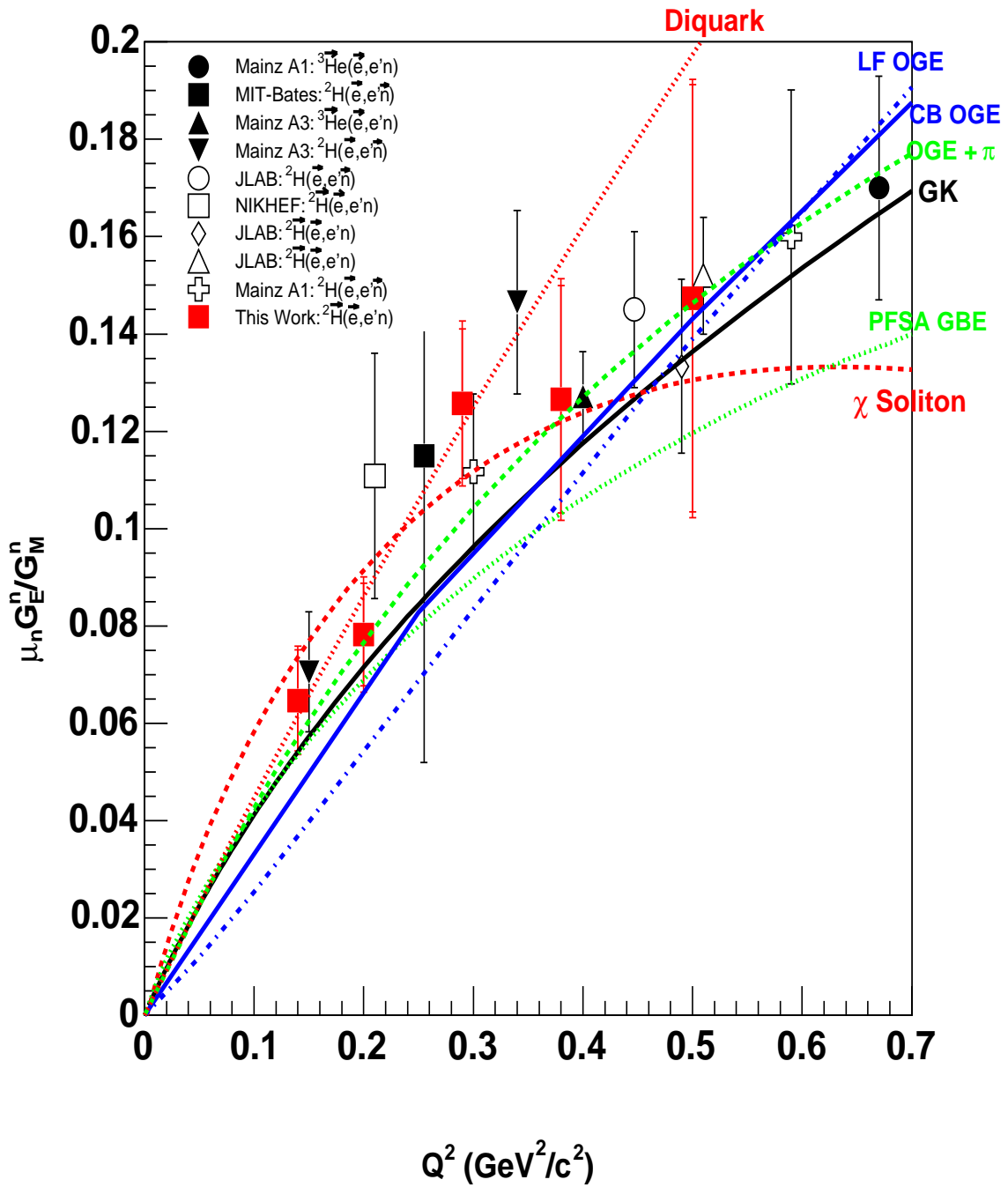


Figure 6-7: Plot of  $\mu_n G_E^n / G_M^n$  from fig. 2-20 enhanced in the low  $Q^2$  region. The data points and curves are explained in fig. 2-20 and the red squares are the results of this work.

# Appendix A

## Boosts and Rotations at BLAST

### A.1 Variable Naming Convention

There are two reference frames which are relevant to the kinematic analysis of the electro-disintegration of deuterium at BLAST. The first is the laboratory frame, in which the target is at rest. The second such frame is the center-of-mass frame, in which the sum of all momenta in the final state is equal to zero.

There are also two coordinate systems. The first coordinate system is the BLAST system. The unit vectors in this frame are defined as

$+\hat{z}^B$	$\equiv$	in the direction of electron beam
$+\hat{y}^B$	$\equiv$	directed upward
$+\hat{x}^B$	$\equiv$	$\hat{y}^B \times \hat{z}^B$

The second coordinate system is the “q-vector”, where the momentum transfer vector defines the  $\hat{z}$  direction. Following the Madison convention the unit vectors in this system are defined as

$+\hat{z}^Q$	$\equiv$	$\vec{q}^B /  \vec{q} $
$+\hat{y}^Q$	$\equiv$	$(\vec{k}^B \times \vec{k}'^B) / ( k  k' )$
$+\hat{x}^Q$	$\equiv$	$\hat{y}^Q \times \hat{z}^Q,$

where  $\vec{q}^B$  is the momentum transfer three-vector, and  $\vec{k}^B$  and  $\vec{k}'^B$  are the initial and final

momenta of the electron, respectively.

All kinematic variables in this appendix come with following letters denoting the two inertial frames and two coordinate systems

L	≡	laboratory frame
C	≡	center-of-mass frame
B	≡	BLAST coordinate system
Q	≡	q-vector coordinate system

## A.2 Kinematic Variable Listing

Listed in this section are all kinematic variables relevant to the electro-disintegration of deuterium reaction. The following kinematic variables are defined in the scattering plane, defined as the plane perpendicular to the  $+\hat{y}^Q$  axis.

$\epsilon^L$	$\equiv$	energy of the initial electron in the lab frame
$k^L$	$\equiv$	three-momentum of the initial electron in lab frame
$\epsilon'^L$	$\equiv$	energy of the scattered electron in the lab frame
$k'^L$	$\equiv$	three-momentum of the scattered electron in the lab frame
$\theta_{e'}^{L,B}$	$\equiv$	polar angle of the scattered electron in the lab frame and BLAST coordinate system
$\phi_{e'}^{L,B}$	$\equiv$	azimuthal angle of the scattered electron in the lab frame and BLAST coordinate system
$\omega^L$	$\equiv$	energy of the virtual photon in the lab frame
$q^L$	$\equiv$	three-momentum magnitude of the virtual photon in the lab frame
$\theta_q^{L,B}$	$\equiv$	polar angle of the virtual photon in the lab frame and BLAST coordinate system
$\phi_q^{L,B}$	$\equiv$	azimuthal angle of the virtual photon in the lab frame and BLAST coordinate system

The kinematic variables of the initial and final hadronic system are defined as

$\epsilon_p^L$	$\equiv$	energy of the recoil proton in the lab frame
$p_p^L$	$\equiv$	three-momentum magnitude of the recoil proton in the lab frame
$\theta_p^{L,B}$	$\equiv$	polar angle of the recoil proton in the lab frame and BLAST coordinate system
$\phi_p^{L,B}$	$\equiv$	azimuthal angle of the recoil proton in the lab frame and BLAST coordinate system
$\epsilon_p^C$	$\equiv$	energy of the recoil proton in the center-of-mass frame
$p_p^C$	$\equiv$	three-momentum magnitude of the recoil proton in the center-of-mass frame
$\theta_p^{C,Q}$	$\equiv$	polar angle of the recoil proton in the center-of-mass frame and Q coordinate system
$\phi_p^{C,Q}$	$\equiv$	azimuthal angle of the recoil proton in the center-of-mass frame and Q coordinate system
$\epsilon_n^L$	$\equiv$	energy of the recoil neutron in the lab frame
$p_n^L$	$\equiv$	three-momentum magnitude of the recoil neutron in the lab frame
$\theta_n^{L,B}$	$\equiv$	polar angle of the recoil neutron in the lab frame and BLAST coordinate system
$\phi_n^{L,B}$	$\equiv$	azimuthal angle of the recoil neutron in the lab frame and BLAST coordinate system
$\epsilon_n^C$	$\equiv$	energy of the recoil neutron in the center-of-mass frame
$p_n^C$	$\equiv$	three-momentum magnitude of the recoil neutron in the center-of-mass frame
$\theta_n^{C,Q}$	$\equiv$	polar angle of the recoil neutron in the center-of-mass frame and Q coordinate system
$\phi_n^{C,Q}$	$\equiv$	azimuthal angle of the recoil neutron in the center-of-mass frame and Q coordinate system

Finally, there are a few remaining kinematic quantities that are useful to understanding the formalism in which the differential cross section of the electro-disintegration is calculated. These quantities are defined as

$p_m^L$	$\equiv$	three-momentum magnitude of the missing momentum in the lab frame
$p_m^C$	$\equiv$	three-momentum magnitude of the missing momentum in the center-of-mass frame
$\epsilon_{np}^C$	$\equiv$	total energy of the recoil proton and neutron in the center-of-mass frame
$T_{np}^C$	$\equiv$	total kinetic energy of the recoil proton and neutron in the center-of-mass frame
$q^C$	$\equiv$	three-momentum magnitude of the virtual photon in the center-of-mass frame

### A.3 Kinematic Relations

All kinematic information measured in the experiment is in the lab frame and in the BLAST coordinate system. The scattered electron's four-momentum vector is written as<sup>1</sup>

$$K' = \left( \epsilon'^L, \epsilon'^L \left[ \sin\theta_{e'}^{L,B} \cos\phi_{e'}^{L,B} \hat{x}^B + \sin\theta_{e'}^{L,B} \sin\phi_{e'}^{L,B} \hat{y}^B + \cos\theta_{e'}^{L,B} \hat{z}^B \right] \right) \quad (\text{A.1})$$

The four-momentum of a detected hadron (proton or neutron) is defined in the similar fashion as

$$P'_p = \left( \epsilon_p^L, k_p^L \left[ \sin\theta_p^{L,B} \cos\phi_p^{L,B} \hat{x}^B + \sin\theta_p^{L,B} \sin\phi_p^{L,B} \hat{y}^B + \cos\theta_p^{L,B} \hat{z}^B \right] \right), \quad (\text{A.2})$$

and

$$P'_n = \left( \epsilon_n^L, k_n^L \left[ \sin\theta_n^{L,B} \cos\phi_n^{L,B} \hat{x}^B + \sin\theta_n^{L,B} \sin\phi_n^{L,B} \hat{y}^B + \cos\theta_n^{L,B} \hat{z}^B \right] \right) \quad (\text{A.3})$$

These are all of the kinematic variables measured by the BLAST detector. All other quantities have to be calculated from them.

---

<sup>1</sup>This equation is written in ultra-relativistic approximation, where the mass of the electron is neglected.

From Eqn. (A.1), the energy transfer in the lab frame is defined as

$$\omega^L = \epsilon^L - \epsilon'^L, \quad (\text{A.4})$$

and the four-momentum transfer squared<sup>2</sup> is then

$$Q^2 \equiv 4\epsilon^L \epsilon'^L \sin^2(\theta_{e'}^{L,B}/2) \quad (\text{A.5})$$

The polar and azimuthal angles of the three-momentum transfer is given in eqn. (A.1) as

$$\cos\theta_q^{L,B} = \frac{\epsilon^L - \epsilon'^L \cos\theta_{e'}^{L,B}}{q^L} \quad (\text{A.6})$$

$$\phi_q^{L,B} = \phi_{e'}^{L,B} + \pi \quad (\text{A.7})$$

The Lorentz boost into the center-of-mass system is govern by a set of kinematic quantities. One such quantity is the total four-momentum squared of the final system, otherwise known as Mandelstam variable,  $s$ , defined as

$$s \equiv (P_p^\mu + P_n^\mu)^2 \quad (\text{A.8})$$

Using the four-momentum conservation,  $s$  is given in the lab frame as

$$s = (\epsilon_p^L + \epsilon_n^L)^2 - (\vec{p}_p^L + \vec{p}_n^L)^2 = (\omega^L + m_d)^2 - (q^L)^2, \quad (\text{A.9})$$

where  $m_d$  is the mass of the deuteron. However, in the center-of-mass frame,  $s$  is simply equal to the square of the total center-of-mass energy, since the total momentum is zero.

$$s = (\epsilon_p^C + \epsilon_n^C)^2 \quad (\text{A.10})$$

Using the fact that in the center-of-mass frame  $p_p^C = p_n^C \equiv p^C$ , it can then be shown that

---

<sup>2</sup>Note that that  $Q^2 \equiv (q^L)^2 - (\omega^L)^2 \geq 0$ .

$$p_p^C = p_n^C \equiv p^C = \frac{([s - (m_p + m_n)(m_p + m_n)][s - (m_p - m_n)(m_p - m_n)])^{1/2}}{4s}, \quad (\text{A.11})$$

where  $m_p$  and  $m_n$  are the respective masses of the proton and neutron.

Hence, the momentum of a hadron in the center-of-mass system can be determined using only kinematic information from the scattered electron.

A convenient variable often used in calculations of the electro-disintegration of deuterium is the kinetic energy of the center-of-mass system [79]. This variable can be simply expressed in terms of the Mandelstam variable  $s$  as

$$T_{np}^C = \sqrt{s} - m_p - m_n, \quad (\text{A.12})$$

where  $m_p$  and  $m_n$  are masses of the proton and neutron, respectively.

## A.4 Lorentz Transformations

Transforming kinematic variables from the (L,B) to the (C,Q) system is done by applying Lorentz rotations and boosts. The rotation matrix in question (which is denoted by  $\mathcal{R}$ ) maps a three-momentum vector in the (L,B) system into the (L,Q) system, such that

$$\begin{pmatrix} p_x^{L,Q} \\ p_y^{L,Q} \\ p_z^{L,Q} \end{pmatrix} = \mathcal{R} \begin{pmatrix} p_x^{L,B} \\ p_y^{L,B} \\ p_z^{L,B} \end{pmatrix} \quad (\text{A.13})$$

where any three-component vector in the (L,B) system is given by

$$\begin{aligned} \vec{p}^L &= p_x^{L,B} \hat{x}^B + p_y^{L,B} \hat{y}^B + p_z^{L,B} \hat{z}^B \\ &= p^L \left[ \sin \theta_p^{L,B} \cos \phi_p^{L,B} \hat{x}^B + \sin \theta_p^{L,B} \sin \phi_p^{L,B} \hat{y}^B + \cos \theta_p^{L,B} \hat{z}^B \right]. \end{aligned} \quad (\text{A.14})$$

The same vector in the (L,Q) system is given by

$$\begin{aligned}
\vec{p}^L &= p_x^{L,Q} \hat{x}^Q + p_y^{L,Q} \hat{y}^Q + p_z^{L,Q} \hat{z}^Q \\
&= p^L \left[ \sin \theta_p^{L,Q} \cos \phi_p^{L,Q} \hat{x}^Q + \sin \theta_p^{L,Q} \sin \phi_p^{L,Q} \hat{y}^Q + \cos \theta_p^{L,Q} \hat{z}^Q \right]. \quad (\text{A.15})
\end{aligned}$$

As was mentioned before, the  $\hat{z}$  direction in the (L,Q) system is defined by the direction of  $\vec{q}$  in the (L,B) system, thus  $\hat{z}^Q$  can be written as

$$\hat{z}^Q \equiv \vec{q}^L / |\vec{q}^L| = \left[ \sin \theta_q^{L,B} \cos \phi_q^{L,B} \hat{x}^B + \sin \theta_q^{L,B} \sin \phi_q^{L,B} \hat{y}^B + \cos \theta_q^{L,B} \hat{z}^B \right] \quad (\text{A.16})$$

By definition, the y-component of a three-vector in the (L,Q) system is  $\hat{y}^Q \equiv \hat{k}^L \times \hat{k}'^L$ . However, this equation can be expressed more conveniently as  $\hat{y}^Q = \hat{z}^Q \times \hat{z}^B$ . Using eqn. (A.16),  $\hat{y}^Q$  is defined in terms of the q-vector's polar and azimuthal angles as

$$\hat{y}^Q = \sin \phi_q^{L,B} \hat{x}^B - \cos \phi_q^{L,B} \hat{y}^B. \quad (\text{A.17})$$

Since  $\hat{x}^Q \equiv \hat{y}^Q \times \hat{z}^Q$ , the x-component in the (L,Q) system is written as

$$\hat{x}^Q = -\cos \theta_q^{L,B} \cos \phi_q^{L,B} \hat{x}^B - \cos \theta_q^{L,B} \sin \phi_q^{L,B} \hat{y}^B + \sin \theta_q^{L,B} \hat{z}^B. \quad (\text{A.18})$$

From eqns. (A.16), (A.17), and (A.18)  $\mathcal{R}$  is written in the matrix form as

$$\mathcal{R} = \begin{bmatrix} -\cos \theta_q^{L,B} \cos \phi_q^{L,B} & -\cos \theta_q^{L,B} \sin \phi_q^{L,B} & \sin \theta_q^{L,B} \\ \sin \phi_q^{L,B} & -\cos \phi_q^{L,B} & 0 \\ \sin \theta_q^{L,B} \cos \phi_q^{L,B} & \sin \theta_q^{L,B} \sin \phi_q^{L,B} & \cos \theta_q^{L,B} \end{bmatrix} \quad (\text{A.19})$$

The polar and azimuthal angles of any vector in (L,Q) system can be defined in terms of the angles of this vector in the (L,B) system and in terms of the q-vector angles as

$$\begin{aligned}
\cos \theta_p^{L,Q} &= \hat{p}^L \cdot \hat{z}^Q = \frac{p_z^{L,Q}}{p^L} \\
&= \cos \theta_p^{L,B} \cos \theta_q^{L,B} + \sin \theta_p^{L,B} \sin \theta_q^{L,B} \cos \left( \phi_q^{L,B} - \phi_p^{L,B} \right), \quad (\text{A.20})
\end{aligned}$$

and

$$\begin{aligned}
\tan \phi_p^{L,Q} &= p_y^{L,Q} / p_x^{L,Q} \\
&= \sin \theta_p^{L,B} \sin (\phi_q^{L,B} - \phi_p^{L,B}) / \\
&\quad \left[ \cos \theta_p^{L,B} \sin \theta_q^{L,B} - \sin \theta_p^{L,B} \cos \theta_q^{L,B} \cos (\phi_q^{L,B} - \phi_p^{L,B}) \right]. \quad (\text{A.21})
\end{aligned}$$

The Lorentz boost into the center-of-mass system, (C,Q) is along the  $\hat{z}^Q$  direction. Thus, only the vector components along  $\hat{z}^Q$  are boosted, whereas vector components perpendicular to  $\hat{z}^Q$  are not. The Lorentz boost has the following matrix form

$$\begin{pmatrix} \epsilon^C \\ p_x^{C,Q} \\ p_y^{C,Q} \\ p_z^{C,Q} \end{pmatrix} = \begin{bmatrix} \gamma & 0 & 0 & -\gamma\beta \\ 0 & 1 & 0 & 0 \\ 0 & 0 & 1 & 0 \\ -\gamma\beta & 0 & 0 & \gamma \end{bmatrix} \begin{pmatrix} \epsilon^L \\ p_x^{L,Q} \\ p_y^{L,Q} \\ p_z^{L,Q} \end{pmatrix}, \quad (\text{A.22})$$

where  $\gamma \equiv (1 - \beta^2)^{-1/2}$ . The Lorentz boost parameter  $\beta$  is calculated from definition of the center-of-mass frame. The sum of all momenta in the final state equals to the momentum of the virtual photon. In the center-of-mass frame this sum is identically zero. Therefore, one gets that

$$(p_{(p+n)}^z)^{C,Q} = 0 = \gamma \left[ q^L - \beta (\omega^L + m_d) \right]. \quad (\text{A.23})$$

It follows that  $\beta$  and  $\gamma$  are functions of the virtual photon's momentum and energy,

$$\beta = \frac{q^L}{\omega^L + m_d}, \quad (\text{A.24})$$

$$\gamma = \frac{\omega^L + m_d}{\sqrt{(\omega^L + m_d)^2 - (q^L)^2}}, \quad (\text{A.25})$$

$$q^C = \frac{m_d q^L}{\sqrt{(\omega^L + m_d)^2 - (q^L)^2}}. \quad (\text{A.26})$$

Using eqns. (A.24) and (A.25) in (A.22), the final form of the Lorentz boost becomes

$$\begin{pmatrix} \epsilon^C \\ p_x^{C,Q} \\ p_y^{C,Q} \\ p_z^{C,Q} \end{pmatrix} = \frac{\omega^L + m_d}{\sqrt{(\omega^L + m_d)^2 - (q^L)^2}} \begin{bmatrix} 1 & 0 & 0 & -\frac{q^L}{\omega^L + m_d} \\ 0 & 1 & 0 & 0 \\ 0 & 0 & 1 & 0 \\ -\frac{q^L}{\omega^L + m_d} & 0 & 0 & 1 \end{bmatrix} \begin{pmatrix} \epsilon^L \\ p_x^{L,Q} \\ p_y^{L,Q} \\ p_z^{L,Q} \end{pmatrix}. \quad (\text{A.27})$$

Since only the components along the q-vector are effected by the Lorentz boost, the azimuthal angle in the (L,Q) system does not change its value. That is,

$$\phi_p^{C,Q} = \phi_p^{L,Q}. \quad (\text{A.28})$$

The polar angle in the (C,Q) system can be expressed as

$$\cos \theta_p^{C,Q} = \frac{\gamma}{p^C} [p^L \cos \theta_p^{L,Q} - \beta \epsilon^L], \quad (\text{A.29})$$

where

$$(p^C)^2 = (p^L \sin \theta_p^{L,Q})^2 + \gamma^2 (p^L \cos \theta_p^{L,Q} - \beta \epsilon^L)^2. \quad (\text{A.30})$$

## A.5 Jacobians and Cross Sections

The experimental measurement of the differential cross section for the reaction  $e + d \rightarrow e + p + n$  is in the (L,B) system. In general, the differential cross sections is a function of five variables,

$$\sigma^{exp} = \frac{d^5 \sigma}{d\omega^L d\Omega_{e'}^{L,B} d\Omega_N^{L,B}}, \quad (\text{A.31})$$

where  $N$  represents the detected nucleon and  $\Omega_{e'}$  and  $\Omega_N$  are the respective solid angles of the detected scattered electron and nucleon.

However, the theoretical differential cross section is calculated in the (C,Q) system. As such, the theoretical cross sections can be written as

$$\sigma^{theory} = \frac{d^5 \sigma}{d\omega^L d\Omega_{e'}^{L,B} d\Omega_N^{C,Q}}. \quad (\text{A.32})$$

In order to compare the measured cross section observables with the BLASTMC predictions  $\sigma^{theory}$  in (C,Q) has to be transformed into the (L,B) frame, by the following formula

$$\sigma^{exp} = \sigma^{theory} \frac{\partial \Omega_N^{C,Q}}{\partial \Omega_N^{L,B}}, \quad (\text{A.33})$$

where  $\partial \Omega_N^{C,Q} / \partial \Omega_N^{L,B}$  is the Jacobian. The property of the Jacobian is such that,

$$\frac{\partial \Omega_N^{C,Q}}{\partial \Omega_N^{L,B}} = \left( \frac{\partial \Omega_N^{L,Q}}{\partial \Omega_N^{L,B}} \right) \left( \frac{\partial \Omega_N^{C,Q}}{\partial \Omega_N^{L,Q}} \right). \quad (\text{A.34})$$

However, since the rotations do not change the unit solid angle, it follows that

$$\left( \frac{\partial \Omega_N^{L,Q}}{\partial \Omega_N^{L,Q}} \right) = 1.$$

Thus, the Jacobian becomes

$$\frac{\partial \Omega_N^{C,Q}}{\partial \Omega_N^{L,B}} = \det \begin{pmatrix} \frac{\partial \cos \theta_N^{C,Q}}{\partial \cos \theta_N^{L,Q}} & \frac{\partial \phi_N^{C,Q}}{\partial \cos \theta_N^{L,Q}} \\ \frac{\partial \cos \theta_N^{C,Q}}{\partial \phi_N^{L,Q}} & \frac{\partial \phi_N^{C,Q}}{\partial \phi_N^{L,Q}} \end{pmatrix} = \frac{\gamma \left( 1 - \frac{\beta \epsilon_N^L}{p_N^L} \cos \theta_N^{L,Q} \right)}{\left[ \sin^2 \theta_N^{L,Q} + \gamma^2 \left( \cos \theta_N^{L,Q} - \frac{\beta \epsilon_N^L}{p_N^L} \right)^2 \right]^{3/2}}, \quad (\text{A.35})$$

where  $p_N^L$  and  $\cos \theta_N^{L,Q}$  are the momentum and polar angle of the detected nucleon.

# Bibliography

- [1] J. Chadwick. *Nature*, 129:312, 1932.
- [2] W. Heisenberg. *Z. Phys.*, 77, 1932.
- [3] W. Heisenberg. *Z. Phys.*, 78:154, 1932.
- [4] Von R. Frisch and O. Stern. *Z. Phys.*, 85:4, 1933.
- [5] H.C. Urey et al. *Phys. Rev.*, 39:164, 1932.
- [6] J. Chadwick and M. Goldhaber. *Nature*, 134:237, 1934.
- [7] J.D. Bjorken and S.D. Drell. *Relativistic Quantum Mechanics*. McGraw-Hill, New York, 1964.
- [8] N.F. Mott. *Proceedings of the Royal Society of London*, 124(794):425, 1925.
- [9] N.F. Mott. *Proceedings of the Royal Society of London*, 132(827):429, 1932.
- [10] M.N. Rosenbluth. *Phys. Rev.*, 79(4):615, 1950.
- [11] F.J. Ernst, R.G. Sachs, and K.C. Wali. *Phys. Rev.*, 119(3):1105, 1960.
- [12] N. Isgur. *Phys. Rev. Lett.*, 83:272, 1999.
- [13] L.L. Foldy. *Phys. Rev.*, 87:688, 1952.
- [14] G. G. Simon, C. Schmitt, F. Borkowski, and V. H. Walther. Absolute electron proton cross-sections at low momentum transfer measured with a high pressure gas target system. *Nucl. Phys.*, A333:381–391, 1980.

- [15] L. E. Price et al. Backward-angle electron-proton elastic scattering and proton electromagnetic form-factors. *Phys. Rev.*, D4:45–53, 1971.
- [16] C Berger, V. Burkert, G. Knop, B. Langenbeck, and K. Rith. Electromagnetic form-factors of the proton at squared four momentum transfers between  $10 \text{ fm}^{-2}$  and  $50 \text{ fm}^{-2}$ . *Phys. Lett.*, B35:87, 1971.
- [17] L. Andivahis et al. Measurements of the electric and magnetic form-factors of the proton from  $Q^2 = 1.75 \text{ (GeV/c)}^2$  to  $8.83 \text{ (GeV/c)}^2$ . *Phys. Rev.*, D50:5491–5517, 1994.
- [18] G. Höhler. *Nuclear Physics*, B114:505–534, 1976.
- [19] K.M. Hanson et al. *Phys. Rev. D*, 8:753, 1973.
- [20] T. Janssens et al. *Phys. Rev.*, 114:922, 1966.
- [21] W. Bartel et al. Measurement of proton and neutron electromagnetic form-factors at squared four momentum transfers up to  $3 \text{ (GeV/c)}^2$ . *Nucl. Phys.*, B58:429–475, 1973.
- [22] R. C. Walker et al. Measurements of the proton elastic form-factors for  $1 \text{ (GeV/c)}^2 \leq Q^2 \leq 3 \text{ (GeV/c)}^2$  at SLAC. *Phys. Rev.*, D49:5671–5689, 1994.
- [23] A. F. Sill et al. Measurements of elastic electron - proton scattering at large momentum transfer. *Phys. Rev.*, D48:29–55, 1993.
- [24] Samuel S.M. Wong. *Introductory Nuclear Physics*. Prentice Hall, Englewood Cliffs, New Jersey, 1990.
- [25] G. Kubon et al. Precise neutron magnetic form factors. *Phys. Lett.*, B524:26–32, 2002, nucl-ex/0107016.
- [26] W. Xu et al. The transverse asymmetry  $A_{T'}$  from quasielastic polarized  ${}^3\vec{H}e(\vec{e}, e')$  process and the neutron magnetic form factor. *Phys. Rev. Lett.*, 85:2900–2904, 2000, nucl-ex/0008003.
- [27] W. Xu et al. PWIA extraction of the neutron magnetic form factor from quasi-elastic  ${}^3\vec{H}e(\vec{e}, e')$  at  $Q^2 = 0.3 \text{ (GeV/c)}^2$  to  $0.6 \text{ (GeV/c)}^2$ . *Phys. Rev.*, C67:012201, 2003, nucl-ex/0208007.

- [28] H. Anklin et al. Precision measurement of the neutron magnetic form-factor. *Phys. Lett.*, B336:313–318, 1994.
- [29] H. Anklin et al. Precise measurements of the neutron magnetic form factor. *Phys. Lett.*, B428:248–253, 1998.
- [30] A. Lung et al. *Phys. Rev. Lett.*, 70:718, 1993.
- [31] Stephen Rock et al. Measurement of elastic electron - neutron cross-sections up to  $Q^2 = 10(\text{GeV}/c)^2$ . *Phys. Rev. Lett.*, 49:1139, 1982.
- [32] P. Markowitz et al. Measurement of the magnetic form-factor of the neutron. *Phys. Rev.*, C48:5–9, 1993.
- [33] E. E. W. Bruins et al. Measurement of the neutron magnetic form-factor. *Phys. Rev. Lett.*, 75:21–24, 1995.
- [34] H. Gao et al. Measurement of the neutron magnetic form-factor from inclusive quasi-elastic scattering of polarized electrons from polarized  $^3\text{He}$ . *Phys. Rev.*, C50:546–549, 1994.
- [35] J. Jourdan, I. Sick, and J. Zhao. Comment on "measurement of the neutron magnetic form factor". *Phys. Rev. Lett.*, 79:5186, 1997.
- [36] T.W. Donnelly and A.S. Raskin. *Annals of Physics*, 169:247–351, 1986.
- [37] A.S. Raskin and T.W. Donnelly. *Annals of Physics*, 91:78–142, 1989.
- [38] Hartmuth Arenhovel, Winfried Leidemann, and Edward L. Tomusiak. *Z. Phys. A: Atomic Nuclei*, 331:123–138, 1988.
- [39] B.D. Milbrath et al. *Phys. Rev. Lett.*, 80:452, 1998.
- [40] B.D. Milbrath et al. *Phys. Rev. Lett.*, 82:2221, 1999.
- [41] O. Gayou et al. *Phys. Rev. C*, 64:64, 2001.
- [42] O. Gayou et al. Measurement of  $G_E^p/G_M^p$  in  $\vec{e}p \rightarrow e\vec{p}$  to  $Q^2 = 5.6 (\text{GeV}/c)^2$ . *Phys. Rev. Lett.*, 88:092301, 2002, nucl-ex/0111010.

- [43] M. K. Jones et al.  $G_E^p/G_M^p$  ratio by polarization transfer in  $\vec{e}p \rightarrow e\vec{p}$ . *Phys. Rev. Lett.*, 84:1398–1402, 2000, nucl-ex/9910005.
- [44] T. Pospischil et al. Measurement of  $G_E^p/G_M^p$  via polarization transfer at  $Q^2 = 0.4$  (GeV/c)<sup>2</sup>. *Eur. Phys. J.*, A12:125–127, 2001.
- [45] J. Arrington. Are recoil polarization measurements of  $G_E^p/G_M^p$  consistent with Rosenbluth separation data? 2002, nucl-ex/0205019.
- [46] J. Arrington. Extraction of two-photon contributions to the proton form factors. 2004, hep-ph/0408261.
- [47] M. Garçon and J. W. Van Orden. The deuteron: Structure and form factors. *Adv. Nucl. Phys.*, 26:293, 2001, nucl-th/0102049.
- [48] J. L. Forest et al. Femtometer toroidal structures in nuclei. *Phys. Rev.*, C54:646–667, 1996, nucl-th/9603035.
- [49] R. Gilman and Franz Gross. Electromagnetic structure of the deuteron. *J. Phys.*, G28:R37–R116, 2002, nucl-th/0111015.
- [50] R. Machleidt. The high-precision, charge-dependent Bonn nucleon-nucleon potential (CD-Bonn). *Phys. Rev.*, C63:024001, 2001, nucl-th/0006014.
- [51] R. B. Wiringa, V. G. J. Stoks, and R. Schiavilla. An accurate nucleon-nucleon potential with charge independence breaking. *Phys. Rev.*, C51:38–51, 1995, nucl-th/9408016.
- [52] Raymond G. Arnold, Carl E. Carlson, and Franz Gross. *Phys. Rev.*, 23:363, 1981.
- [53] J. Ball. Private Communication.
- [54] C. D. Buchanan and R. Yearian. *Phys. Rev. Lett.*, 15:303, 1965.
- [55] J. E. Elias et al. *Phys. Rev.*, 177:2075, 1969.
- [56] D. Benaksas et al. *Phys. Rev.*, 148:1327, 1966.
- [57] R. Arnold et al. *Phys. Rev. Lett.*, 35:776, 1975.

- [58] S. Platchkov et al. *Nuclear Physics*, A510:740–758, 1990.
- [59] S. Galster et al. *Nuclear Physics B*, 32:221, 1971.
- [60] R. Cramer et al. *Z. Phys. C*, 29:513, 1985.
- [61] G. G. Simon et al. *Nuclear Physics A*, 364:285, 1981.
- [62] D. Abbott et al. *Phys. Rev. Lett.*, 82:1379, 1999.
- [63] L. C. Alexa et al. *Phys. Rev. Lett.*, 82:1374, 1999.
- [64] Hartmuth Arenhovel, Frank Ritz, and Thomas Wilbois. *Phys. Rev. C*, 61, 2000.
- [65] S. Auffret et al. *Phys. Rev. Lett.*, 54:649, 1985.
- [66] P. E. Bosted et al. *Phys. Rev. C*, 42(1):38, 1990.
- [67] D. Abbott et al. Phenomenology of the deuteron electromagnetic form factors. *Eur. Phys. J.*, A7:421–427, 2000, nucl-ex/0002003.
- [68] B. Boden et al. *Z. Phys. C*, 49:175, 1991.
- [69] M. Bouwhuis et al. *Phys. Rev. Lett.*, 82:3755, 1999.
- [70] V.F. Dmitriev et al. *Phys. Lett.*, 157B:143, 1985.
- [71] M. Ferro-Luzzi et al. *Phys. Rev. Lett.*, 77:2630, 1996.
- [72] M. Garcon et al. *Phys. Rev. C*, 49:2516, 1994.
- [73] R. Gilman et al. *Phys. Rev. Lett.*, 65:1733, 1990.
- [74] M.E. Schultze et al. *Phys. Rev. Lett.*, 52:597, 1984.
- [75] B.B. Voitsekovskiy et al. *JETP Lett.*, 43:733, 1986.
- [76] Michael J. Moravcsik and Pranab Chosh. *Phys. Rev. Lett.*, 32(6):321, 1974.
- [77] S. Kopecki et al. *Phys. Rev. Lett.*, 74:2427, 1995.

- [78] R. Schiavilla and I. Sick. Neutron charge form factor at large  $Q^2$ . *Phys. Rev.*, C64:041002, 2001, nucl-ex/0107004.
- [79] Hartmuth Arenhovel, Winfried Leidemann, and Edward L. Tomusiak. *Phys. Rev. C*, 46:455, 1992.
- [80] Hartmuth Arenhovel, Winfried Leidemann, and Edward L. Tomusiak. *Few Body Syst.*, 28:147–188, 2000.
- [81] Hai-yan Gao. Nucleon electromagnetic form factors. *Int. J. Mod. Phys.*, E12:1–40, 2003, nucl-ex/0301002.
- [82] B. Plaster. *The Neutron Electric Form Factor to  $Q^2 = 1.45 (GeV/c)^2$* . PhD thesis, Massachusetts Institute of Technology, 2004.
- [83] S. J. Brodsky and G.R Farrar. *Phys. Rev.*, D11:1309, 1975.
- [84] G. Peter Lepage and Stanley J. Brodsky. Exclusive processes in perturbative quantum chromodynamics. *Phys. Rev.*, D22:2157, 1980.
- [85] J. W. Negele et al. Insight into nucleon structure from lattice calculations of moments of parton and generalized parton distributions. *Nucl. Phys. Proc. Suppl.*, 128:170–178, 2004, hep-lat/0404005.
- [86] Gerald V. Dunne, Anthony W. Thomas, and Stewart V. Wright. Chiral extrapolation: An analogy with effective field theory. *Phys. Lett.*, B531:77–82, 2002, hep-th/0110155.
- [87] J. D. Ashley, D. B. Leinweber, Anthony W. Thomas, and R. D. Young. Nucleon electromagnetic form factors from lattice QCD. *Eur. Phys. J.*, A19:9–14, 2004, hep-lat/0308024.
- [88] M. Gockeler et al. Nucleon electromagnetic form factors on the lattice and in chiral effective field theory. *Phys. Rev.*, D71:034508, 2005, hep-lat/0303019.
- [89] H. W. Hammer, Ulf-G. Meissner, and D. Drechsel. Dispersion-theoretical analysis of the nucleon electromagnetic form factors: Inclusion of time-like data. *Phys. Lett.*, B385:343–347, 1996, hep-ph/9604294.

- [90] H. W. Hammer and Ulf-G. Meissner. Updated dispersion-theoretical analysis of the nucleon electromagnetic form factors. *Eur. Phys. J.*, A20:469–473, 2004, hep-ph/0312081.
- [91] Manfred Gari and W. Krumpelmann. Semiphenomenological synthesis of meson and quark dynamics and the electromagnetic structure of the nucleon. *Z. Phys.*, A322:689–693, 1985.
- [92] M. F. Gari and W. Kruempelmann. Vector meson nucleon couplings at space - like momentum transfer. *Phys. Rev.*, D45:1817–1820, 1992.
- [93] Dmitri Diakonov and Victor Yu. Petrov. Nucleons as chiral solitons. 2000, hep-ph/0009006.
- [94] T.H.R. Skyreme. *Nucl. Phys.*, 31:556, 1962.
- [95] G. Holzwarth. Electromagnetic form factors of the nucleon in the chiral soliton model. 2002, hep-ph/0201138.
- [96] Fabio Cardarelli and Silvano Simula. SU(6) breaking effects in the nucleon elastic electromagnetic form factors. *Phys. Rev.*, C62:065201, 2000, nucl-th/0006023.
- [97] Silvano Simula. Relativistic quark models. 2001, nucl-th/0105024.
- [98] R. F. Wagenbrunn, S. Boffi, W. Klink, W. Plessas, and M. Radici. Covariant nucleon electromagnetic form factors from the goldstone-boson exchange quark model. *Phys. Lett.*, B511:33–39, 2001, nucl-th/0010048.
- [99] S. Boffi et al. Covariant electroweak nucleon form factors in a chiral constituent quark model. *Eur. Phys. J.*, A14:17–21, 2002, hep-ph/0108271.
- [100] Gerald A. Miller. Light front cloudy bag model: Nucleon electromagnetic form factors. *Phys. Rev.*, C66:032201, 2002, nucl-th/0207007.
- [101] Murat M. Kaskulov and Peter Grabmayr. Effect of gluon-exchange pair-currents on the ratio  $\mu_p G_E^p / G_M^p$ . *Phys. Rev.*, C67:042201, 2003, nucl-th/0302037.
- [102] Murat M. Kaskulov and Peter Grabmayr. The electric form factor of the neutron and its chiral content. *Eur. Phys. J.*, A19:157–161, 2004, nucl-th/0308015.

- [103] J. Friedrich and T. Walcher. *Euro. Phys. Jour.*, A17:607, 2003.
- [104] Bo-Qiang Ma, Di Qing, and Ivan Schmidt. Electromagnetic form factors of nucleons in a light-cone diquark model. *Phys. Rev.*, C65:035205, 2002, hep-ph/0202015.
- [105] R. Madey et al. Measurements of  $G_E^n/G_M^n$  from the  ${}^2H(\vec{e}, e'\vec{n}){}^1H$  reaction to  $Q^2 = 1.45$  (GeV/c) $^2$ . *Phys. Rev. Lett.*, 91:122002, 2003, nucl-ex/0308007.
- [106] G. Warren et al. Measurement of the electric form factor of the neutron at  $Q^2 = 0.5$  (GeV/c) $^2$  and  $1.0$  (GeV/c) $^2$ . *Phys. Rev. Lett.*, 92:042301, 2004, nucl-ex/0308021.
- [107] D. I. Glazier et al. Measurement of the electric form factor of the neutron at  $Q^2 = 0.3 - 0.8$ (GeV/c) $^2$ . 2004, nucl-ex/0410026.
- [108] F. E. Maas et al. Measurement of strange quark contributions to the nucleon's form factors at  $Q^2 = 0.230$  (GeV/c) $^2$ . *Phys. Rev. Lett.*, 93:022002, 2004, nucl-ex/0401019.
- [109] J. Becker et al. *Euro. Phys. Jour. A*, 6:329–344, 1999.
- [110] J. Golak, G. Ziemer, H. Kamada, H. Witala, and Walter Gloeckle. Extraction of electromagnetic neutron form factors through inclusive and exclusive polarized electron scattering on polarized  ${}^3He$  target. *Phys. Rev.*, C63:034006, 2001, nucl-th/0008008.
- [111] D. Rohe et al. *Phys. Rev. Lett.*, 83(21):4257, 1999.
- [112] J. Bermuth et al. The neutron charge form factor and target analyzing powers from  ${}^3He(\vec{e}, e'n)$  scattering. *Phys. Lett.*, B564:199–204, 2003, nucl-ex/0303015.
- [113] I. Passchier et al. *Phys. Rev. Lett.*, 82:4988, 1999.
- [114] H. Zhu et al. A measurement of the electric form-factor of the neutron through  $\vec{d}(\vec{e}, e'n)p$  at  $Q^2 = 0.5$  (GeV/c) $^2$ . *Phys. Rev. Lett.*, 87:081801, 2001, nucl-ex/0105001.
- [115] T. Eden et al. *Phys. Rev. C*, 50(4):1749, 1994.
- [116] M. Ostrick et al. *Phys. Rev. Lett.*, 83(2):276, 1999.
- [117] C. Herberg et al. *Euro. Phys. Jour. A*, 5:131–135, 1999.

- [118] W. Meyer. Ammonia as a polarized solid target material: A review. *Nucl. Instrum. Meth.*, A526:12–21, 2004.
- [119] Z. Zhou. PhD thesis, University of Wisconsin at Madison, 2000.
- [120] Evgeni Tsentelovich. The Atomic Beam Source at BLAST. In *Proceeding of a Polarized Sources and Targets Conference*, 2004.
- [121] A. Vassiliev et al. *Review of Scientific Instruments*, 71:3331, 2000.
- [122] D.J. Larson, P.A. Valberg, and N.F. Ramsey. *Phys. Rev. Lett.*, 23:1369–1372, 1969.
- [123] Christian Baumgarten. *Studies of Spin Relaxation and Recombination at the HERMES Hydrogen/Deuterium Gas Target*. PhD thesis, Ludwig-Maximilians Universität München, 2000.
- [124] I. Rabi, S. Millman, P. Kusch, and J. Zacharias. *Phys. Rev.*, 55:526, 1939.
- [125] A. Abragam and J.M Winter. *Phys. Rev. Lett.*, 1:374, 1958.
- [126] R. J. Philpott. *Nuclear Instrumentation and Methods*, A259:317–323, 1987.
- [127] A. Roth. *Vacuum Technology*. North-Holland, Amsterdam, 1982.
- [128] D.R Swenson and L.W. Anderson. *Nuclear Instrumentation and Methods*, B29:627–642, 1988.
- [129] C. Baumgarten et al. *Euro. Phys. Jour. B*, 18:37, 2002.
- [130] C. Baumgarten et al. *Nuclear Instrumentation and Methods*, 496:277, 2002.
- [131] J. F. J. van den Brand et al. Evidence for nuclear tensor polarization of deuterium molecules in storage cells. *Phys. Rev. Lett.*, 78:1235–1238, 1997.
- [132] H.J. Bulten, Z.-L. Zhou, et al. *Phys. Rev. A*, 58(2):1146, 1998.
- [133] T. Wise et al. Nuclear polarization of hydrogen molecules from recombination of polarized atom. *Phys. Rev. Lett.*, 87:2701, 2001.

- [134] L.W. Anderson and D.R Swenson. *Nuclear Instrumentation and Methods*, B12:157, 1985.
- [135] M.A. Bouchiat and J. Brossel. *Phys. Rev.*, 147:41, 1966.
- [136] Bernd Braun. *Spin Relaxation of Hydrogen and Deuterium in Storage Cells*. PhD thesis, Ludwig-Maximilians Universitat Munchen, 1995.
- [137] Z. L. Zhou et al. Tensor analyzing powers for quasi-elastic electron scattering from deuterium. *Phys. Rev. Lett.*, 82:687–690, 1999, nucl-ex/9809002.
- [138] H. Kolster. ABS Status Report, PAC 29. Technical report, MIT-Bates, 2004.
- [139] The MIT-Bates. South hall ring technical design report. Technical report, MIT-Bates, 1994.
- [140] D. Cheever. Private Communication.
- [141] W. A. Franklin et al. The MIT-Bates South Hall Ring: a Unique Instrument for Studying Polarization. In *Spin2004 Conference Proceedings*. World Scientific, 2004.
- [142] K. Dow et al. Private Communication.
- [143] The BLAST Collaboration. Bates large acceptance spectrometer toroid technical design report. Technical report, MIT-Bates, 2000.
- [144] J.D. Jackson. *Classical Electrodynamics*. John Wiley & Sons, New York, 1962.
- [145] Particle Data Group. *Euro. Phys. Jour. A*, 3:1–794, 1998.
- [146] R. Alarcon et al. Private Communication.
- [147] C. Crawford. *Precision Measurement of the Proton Electric to Magnetic Form Factor Ratio with BLAST*. PhD thesis, MIT, 2005.
- [148] William H. Press, Saul A. Teukolsky, and Brian P. Flannery. *Numerical Recipes in C*. Cambridge Press, Cambridge, 1996.

- [149] P.R. Bevington and D.K. Robinson. *Data Reduction and Error Analysis for the Physical Sciences*. McGraw-Hill Higher Education, New York, 2003.
- [150] C. Zhang. *Tensor Analyzing Powers in Elastic Electron-Deuteron Scattering Below 1GeV*. PhD thesis, MIT, 2005.
- [151] A. Maschinot. *Analysis of Scattered Protons in Deuteron Electrodisintegration with a Polarized Electron Beam and an Internal Vector/Tensor Polarized Target at BLAST*. PhD thesis, MIT, 2005.
- [152] N. Meitanis. *Measurement of the neutron magnetic form factor from quasielastic  $D(e, e')$  at BLAST*. PhD thesis, MIT, 2005.
- [153] I. Akushevich, A. Ilyichev, and N. Shumeiko. Radiative effects in scattering of polarized leptons by polarized nucleons and light nuclei. 2001, hep-ph/0106180.
- [154] A. Afanasiev, I. Akushevich, and N. Merenkov. *Phys. Rev. D*, 64:113009, 2001.
- [155] W. Donnelly. Private Communication.
- [156] James J. Kelly. Nucleon charge and magnetization densities from Sachs form factors. *Phys. Rev.*, C66:065203, 2002, hep-ph/0204239.